PRECLINICAL ASSESSMENT OF FUNCTIONAL AND STRUCTURAL CONNECTIVITY IN STROKE AND TRAUMATIC BRAIN INJURY UTILIZING ADVANCED MAGNETIC RESONANCE IMAGING AND HIGH-CONTENT HISTOLOGICAL NEUROIMAGING

by

KELLY MARIE SCHEULIN

(Under the Direction of Franklin Delano West)

ABSTRACT

Despite the devastating global impact of ischemic stroke and traumatic brain injury (TBI), there are few Food and Drug Administration approved treatments. This can be largely attributed to the lack of testing in translational models in the preclinical phase. Therefore, further investigation of stroke and TBI pathophysiology is warranted in a large animal model with similar brain anatomy and physiology to the human brain. Utilizing magnetic resonance imaging (MRI) and high-content histological neuroimaging in a translational porcine model, the current studies aim to identify key cellular and structural changes caused by a permanent middle cerebral artery occlusion that impact stroke recovery and determine how brain functional networks are affected after TBI. The inclusion of stroke lesion location when predicting functional outcomes is likely to improve prognostic ability as there is a direct relationship between brain structures and function. A porcine MRI brain atlas was registered to identify stroke lesion location, and

correlations between infarcted brain structures and functional gait data were completed to evaluate the predictive capacity of individual brain structure lesion on neurological outcome. This approach identified neuroanatomical structures involved in motor coordination and function that were prognostic of overall gait outcomes and identified potential targets for therapeutic intervention to facilitate optimal recovery. Functional MRI can be employed to measure network changes after injury and provide early prognosis of functional outcomes, including motor, cognitive, and behavioral deficits. Brain activation maps were evaluated following TBI and compared to healthy control brain networks. Functional connectivity disruptions of brain networks were observed and able to be traced to individual affected anatomical structures. While many of these noninvasive neuroimaging modalities provide spatial and temporal information on tissue composition and brain activity, post-mortem histological assessment can provide deeper quantitative analysis of cell-to-cell interactions following an ischemic stroke. Significant differences in the morphology of microglia/macrophages, astrocytes, neurons, neuronal precursors, and vasculature cells were found in stroked brains compared to healthy controls, designating a stroke cell morphological fingerprint. These neuroimaging techniques can be employed to develop personalized patient recovery, disease progression, rehabilitation, and therapeutic intervention plans.

INDEX WORDS: ischemic stroke, traumatic brain injury, magnetic resonance imaging (MRI), resting-state functional MRI (rs-fMRI), large animal porcine model, high-content histological imaging analysis

PRECLINICAL ASSESSMENT OF FUNCTIONAL AND STRUCTURAL CONNECTIVITY IN STROKE AND TRAUMATIC BRAIN INJURY UTILIZING ADVANCED MAGNETIC RESONANCE IMAGING AND HIGH-CONTENT HISTOLOGICAL NEUROIMAGING

by

KELLY MARIE SCHEULIN

B.S.A., University of Georgia, 2017

B.S.A., University of Georgia, 2017

A Dissertation Submitted to the Graduate Faculty of The University of Georgia in Partial Fulfillment of the Requirements for the Degree

DOCTOR OF PHILOSOPHY

ATHENS, GEORGIA

2021

PRECLINICAL ASSESSMENT OF FUNCTIONAL AND STRUCTURAL CONNECTIVITY IN STROKE AND TRAUMATIC BRAIN INJURY UTILIZING ADVANCED MAGNETIC RESONANCE IMAGING AND HIGH-CONTENT HISTOLOGICAL NEUROIMAGING

by

KELLY MARIE SCHEULIN

Major Professor: Franklin D. West
Committee: Kara L. Dyckman
Steven L. Stice
Qun Zhao

Electronic Version Approved:

Ron Walcott
Dean of the Graduate School
The University of Georgia
May 2021

ACKNOWLEDGEMENTS

There is a long list of individuals who have made this experience worth-while and truly unforgettable, through the good... and the hard times. First, I would like to thank my family, Mom, Dad, and Megan. Thank you for being so supportive through it all and understanding why I couldn't ever stay long or even come home at all for many holidays. Also thank you to Gamma and Papa, for keeping me going with pictures of gumbo and texts on all things Pensacola. And maybe most of all, Chase. You have been so patient and kind over this degree program. Thank you for your endless support and always keeping me fed (tacos on tacos). I really don't know how I would have done this without you. Special shout out to my supportive boys who provided endless cuddles when cuddles were necessary, KJ and Koda. Also thank you Abby, I will miss having you as a roomie but know I appreciate you and our friendship so much! I would also like to thank Fuel Hot Yoga and their amazing instructors for keeping me sane and providing an outlet over the past couple of years.

Moving into the lab, first and foremost I would like to extend a million thank yous to the best boss out there, Frank. We made it through all the pig politics, rounds of editorial reviews, and dumpster fires. Thank you for having high expectations, but also being very understanding. The entire lab culture was a big reason I decided to join the West Lab (and friends) and for that, I thank Holly, Emily, Erin, Madelaine, Beth, Monika, Soo, Sydney, Savi, Madison, Christina, Julie, and Xi. You girls make the world go 'round and have each played a very special role in making my experience through this

PhD memorable. Thank you to Sam, Brian, and Greg—I thoroughly enjoyed working with each of you and publishing our manuscripts together; I am excited to see how your careers progress— you're going to do BIG THINGS! Meghan, thanks for being my yoga buddy, Taq del Sol partner, and friend. Our amazing undergraduate researchers deserve a big hug for all their hard work, there are too many to name, but honestly, these studies could not have been done without you. Kim, thank you for your MRI expertise, patience, and inspiring stories in front of the magnet. Gina, Jenny, and Ethan—I would not have survived the stroke study without your help, so thank you for going the extra mile. Finally, thank you to my committee, Drs. Stice, Zhao, and Dyckman, from the pig study collaborations to the endless MRI analysis questions, thank you all for your guidance and support over the years.

TABLE OF CONTENTS

Page

CHAPTER 1

INTRODUCTION

Traumatic brain injury (TBI) is a worldwide socio-economic problem and is regularly referred to as a "silent epidemic" because the side effects are often hard to diagnose and present over time [1]. TBI is defined as an external mechanical force to the head that can leave patients with lifelong disabilities, including impaired intellectual ability, sensorimotor function, and memory. The Centers for Disease Control and Prevention estimates that TBI accounts for 30.5% of all injury-related deaths in the United States [2]. Stroke is also a worldwide socio-economic problem and is considered the fifth leading cause of death and first leading cause of long-term disability in the United States [3]. Of the different types of strokes, 87% are ischemic in nature, which occurs when a blood vessel in the brain is obstructed leading to a significant decrease or total loss of cerebral perfusion [4]. Despite prevalence of these neural injuries and the many failed phase III clinical trials, there is no Food and Drug Administration (FDA) approved treatment for TBI [5], and there are few approved options for ischemic stroke, tissue plasminogen activator (tPA) and thrombectomy clot removal, but they come with significant limitations [4]. While many patients present with similar Glasgow Coma Scale (GCS) or modified Rankin Scale (mRS)/National Institutes of Health Stroke Scale (NIHSS)/Barthel Index (BI) scores at admission, individual brain injuries are typically unique, complex, and heterogenous [6-8]. It is likely and reasonable that a patient with a diffuse injury will need an entirely different therapeutic approach and rehabilitation

intervention as compared to a patient with a focal injury. Due to the heterogenous nature of brain injuries, clinical medicine needs adequate tools to evaluate brain injuries and create personalized treatment plans for patients. This highlights the need for advanced neuroimaging tools to be more frequently implemented in clinical cases and preclinical studies to further evaluate disease pathophysiology. In the context of brain injuries, magnetic resonance imaging (MRI) and histological high-content imaging (HCI) analysis techniques can provide information on disease pathophysiology, progression, and recovery.

Often it is difficult for patients and their families to understand and conceptualize the magnitude or the specific effects manifested after brain injury. Noninvasive tools, including MRI and functional MRI (fMRI), can help provide insight for the patient and their loved ones to have an estimated idea of what recovery will look like including length of time and what physical manifestations to expect. Especially when regarding pediatric brain injuries, it is difficult for a child to understand an injury that they cannot see. Similar to a broken arm, the brain also needs time to heal and be exercised. MRI can shed a light into what rehabilitation plans are best for each individual injury. While histological approaches are only applicable to preclinical studies, with the exception of few life-long clinical studies, the HCI technique in preclinical studies can support MRI findings throughout the study and provide insight into cell-to-cell interactions. HCI can provide conclusions on a cellular level. In order to effectively help at the clinical level in practice and in evaluating clinical trial therapeutic efficacy, these neuroimaging tools must be established and properly vetted in a translational preclinical model.

Modeling stroke and TBI in the preclinical setting is challenging due to heterogenous results between preclinical rodent studies and successful human clinical trials [9]. The disparity between successful therapeutic testing in rodents and the litany of failed human clinical trials warrants the assessment of functional and structural disruptions due to brain injury in a gyrencephalic brain that may provide a more translational model for testing therapeutics and understanding disease progression. To further this point, the stroke community has formed a consortium, the Stroke Therapy Academic Industry Roundtable (STAIR), which developed criteria recommendations for preclinical studies in an attempt to advance the translation from the bench to the bedside [10]. These criteria largely apply to preclinical TBI models as well. The criteria recommend testing therapeutics in multiple animal models, notably a gyrencephalic model as the second species. Additional recommendations include preclinical testing in both sexes and considering multiple endpoints of both histological and behavioral outcomes. However, despite the implementation of the STAIR criteria in preclinical stroke research, there are still few options for stroke therapies that provide pharmacological neuroprotection. This void can be attributed to the failure of the preclinical brain injury field to abide by these recommendations. Very few treatments to date have been tested in gyrencephalic brains, as the majority of therapeutics still go from mice to men. Due to the similar anatomy and physiology of the pig brain to the human brain, the pig serves as a valuable large animal model for studying brain injuries and may bridge the gap between rodent models and human clinical trials [11, 12]. In addition, the pig is also a useful pediatric neural injury model, as the piglet has significant parallels to children in terms of development and brain pathophysiology. Piglets exhibit a similar

pattern of brain development to humans that follows an analogous pattern of neurogenesis as infants, including neuroblast migration from the subventricular zone, as well as similar temporal myelination, and comparable innate immunity [11, 13-18]. Using the translational pig model can therefore provide insight into overall functional and structural pathway development and may serve as a step in the translational framework to study neural diseases and injuries.

Predicting stroke patient functional outcomes based on acute MRI information has significant clinical value in determining prognosis and potential course of treatment. The inclusion of stroke lesion location when predicting functional outcomes is likely to improve prognostic ability as there is a direct relationship between brain structures and function [19, 20]. However, stroke location is under assessed in predicting functional outcomes with traditional metrics such as lesion volumes and midline shifts being more heavily used preclinically and clinically [21-23]. The aim of the first study was to characterize lesion location in a reproducible middle cerebral artery occlusion (MCAO) stroke model and relate the lesion topology findings to functional outcomes.

Children who experience moderate-to-severe TBI at a young age may have associated long-term deficits when compared to their peers [24]. With disruptions to existing neural networks, normal developmental and learning processes can be hindered. Strong functional connections that support learning and memory are vital in the developing brain. Brain circuitry undergoes a functional weakening following injury [25]. Determining the location of the injury in relation to functional networks can tell us whether two parts of the brain are communicating properly, or if the brain has lost a connection to other body parts. There is currently a void in the neuroscience field in translational models utilizing

fMRI technology and the work presented herein starts to fill that void by being one of the first large animal studies to evaluate brain network disruptions following TBI.

Brain ischemia causes disruptions and injury in many cell types in the brain including neurons, glial cells, and blood vessels [26]. Histological findings provide a deeper cellular look to inform analyses and interpretations made in the context of noninvasive neuroimaging studies of brain functional and structural connectivity in various disease states. HCI provides an unbiased approach while increasing translatability of findings across the spectrum from rodent to human brains. A critical need in the stroke field is a deeper understanding of microscale cellular morphological changes that may result in more predictive studies of neural injuries and recovery patterns. The final study investigated the interactions between 5 major cell types in the ischemic and healthy porcine brain, including neurons, microglia/macrophages, astrocytes, blood vessels, and neuronal precursor cells.

As the neuroscience field progresses with new therapeutic options for brain injury patients, it is vital to keep the same momentum going with neuroimaging modalities to evaluate the safety, efficacy, and effectiveness of future therapies. The studies that comprise this dissertation sought to characterize 1) stroke lesion topology using advanced neuroimaging techniques including lesion mapping by structural MRI and relate those findings to functional outcomes, 2) functional network disruptions following a TBI using resting-state and task-based fMRI, and 3) regionally specific morphological alterations of immune and neural cells following stroke by quantitative HCI. Collectively, the work presented in this dissertation progressed advanced neuroimaging techniques including MRI and HCI in a translational preclinical model in an effort to better the standard of preclinical

research, hasten the speed of therapeutic development, and ultimately bring more options to stroke and TBI patients.

References

1. Maas, A.I., N. Stocchetti, and R. Bullock, *Moderate and severe traumatic brain injury in adults.* Lancet Neurol, 2008. **7**(8): p. 728-41.
2. Faul M, X.L., Wald MM, Coronado VG, *Traumatic Brain Injury in the United States: Emergency Department Visits, Hospitalizations and Deaths 2002–2006.* Centers for Disease Control and Prevention, National Center for Injury Prevention and Control, 2010.
3. *Stroke Facts*. 2020 [cited 2021 February 4]; Available from: https://www.cdc.gov/stroke/facts.htm.
4. Barthels, D. and H. Das, *Current advances in ischemic stroke research and therapies.* Biochim Biophys Acta Mol Basis Dis, 2020. **1866**(4): p. 165260.
5. McDonald, S.J., et al., *The effect of concomitant peripheral injury on traumatic brain injury pathobiology and outcome.* J Neuroinflammation, 2016. **13**(1): p. 90.
6. Saatman, K.E., et al., *Classification of traumatic brain injury for targeted therapies.* J Neurotrauma, 2008. **25**(7): p. 719-38.
7. Harrison, J.K., K.S. McArthur, and T.J. Quinn, *Assessment scales in stroke: clinimetric and clinical considerations.* Clin Interv Aging, 2013. **8**: p. 201-11.
8. DeWitt, D.S., et al., *Pre-Clinical Testing of Therapies for Traumatic Brain Injury.* J Neurotrauma, 2018. **35**(23): p. 2737-2754.
9. Xiong, Y., A. Mahmood, and M. Chopp, *Animal models of traumatic brain injury.* Nat Rev Neurosci, 2013. **14**(2): p. 128-42.
10. Fisher, M., et al., *Update of the stroke therapy academic industry roundtable preclinical recommendations.* Stroke, 2009. **40**(6): p. 2244-50.
11. Conrad, M.S., R.N. Dilger, and R.W. Johnson, *Brain growth of the domestic pig (Sus scrofa) from 2 to 24 weeks of age: a longitudinal MRI study.* Dev Neurosci, 2012. **34**(4): p. 291-8.
12. Rice, D. and S. Barone, Jr., *Critical periods of vulnerability for the developing nervous system: evidence from humans and animal models.* Environ Health Perspect, 2000. **108 Suppl 3**: p. 511-33.
13. Dobbing, J. and J. Sands, *Comparative aspects of the brain growth spurt.* Early Hum Dev, 1979. **3**(1): p. 79-83.
14. Pond, W.G., et al., *Perinatal ontogeny of brain growth in the domestic pig.* Proc Soc Exp Biol Med, 2000. **223**(1): p. 102-8.
15. Paredes, M.F., et al., *Extensive migration of young neurons into the infant human frontal lobe.* Science, 2016. **354**(6308).
16. Costine, B.A., et al., *The subventricular zone in the immature piglet brain: anatomy and exodus of neuroblasts into white matter after traumatic brain injury.* Dev Neurosci, 2015. **37**(2): p. 115-30.
17. Flynn, T.J., *Developmental changes of myelin-related lipids in brain of miniature swine.* Neurochem Res, 1984. **9**(7): p. 935-45.
18. Fairbairn, L., et al., *The mononuclear phagocyte system of the pig as a model for understanding human innate immunity and disease.* J Leukoc Biol, 2011. **89**(6): p. 855-71.

19. Cheng, B., et al., *Influence of stroke infarct location on functional outcome measured by the modified rankin scale.* Stroke, 2014. **45**(6): p. 1695-702.
20. Payabvash, S., et al., *Acute Ischemic Stroke Infarct Topology: Association with Lesion Volume and Severity of Symptoms at Admission and Discharge.* AJNR Am J Neuroradiol, 2017. **38**(1): p. 58-63.
21. Schiemanck, S.K., et al., *Relationship between ischemic lesion volume and functional status in the 2nd week after middle cerebral artery stroke.* Neurorehabil Neural Repair, 2005. **19**(2): p. 133-8.
22. Schiemanck, S.K., et al., *Ischemic lesion volume correlates with long-term functional outcome and quality of life of middle cerebral artery stroke survivors.* Restor Neurol Neurosci, 2005. **23**(3-4): p. 257-63.
23. Lovblad, K.O., et al., *Ischemic lesion volumes in acute stroke by diffusion-weighted magnetic resonance imaging correlate with clinical outcome.* Ann Neurol, 1997. **42**(2): p. 164-70.
24. Schachar, R., et al., *Attention deficit hyperactivity disorder symptoms and response inhibition after closed head injury in children: do preinjury behavior and injury severity predict outcome?* Dev Neuropsychol, 2004. **25**(1-2): p. 179-98.
25. Green, C., et al., *Sensorimotor Functional and Structural Networks after Intracerebral Stem Cell Grafts in the Ischemic Mouse Brain.* J Neurosci, 2018. **38**(7): p. 1648-1661.
26. Jayaraj, R.L., et al., *Neuroinflammation: friend and foe for ischemic stroke.* J Neuroinflammation, 2019. **16**(1): p. 142.

CHAPTER 2

LITERATURE REVIEW:

RESTING-STATE FUNCTIONAL MAGNETIC RESONANCE IMAGING PROVIDES OBJECTIVE MARKERS OF BRAIN INJURY AND PREDICTS EMOTIONAL, COGNITIVE, AND PHYSICAL CLINICAL MANIFESTATIONS

1. Introduction

The majority of the brain's energy consumption is devoted to intrinsic communications related to brain metabolism and not directly associated with an external task or stimulus [1]. 60-80% of the brain's energy is consumed when no task is present [2]. During a task-positive event or an external stimulus, the brain's energy consumption only increases by less than 5% from the baseline functional activity. Resting-state functional magnetic resonance imaging (rs-fMRI) is capable of acquiring signal and identifying functional areas at rest that are responsible for this major energy consumption. In conjunction with rs-fMRI, diffusion tensor imaging (DTI) can provide insight on the structural connectivity and overall organization of brain networks. This noninvasive technology allows brain function and architecture data to be collected from various populations including non-verbal populations, such as infants, sedated subjects, comatose patients, and animals, leading to objective diagnostic and prognostic information. rs-fMRI is capable of characterizing normal and abnormal brain function in a variety of clinical and preclinical applications. In this review, we will examine pioneering studies in the rs-fMRI field, the structural core of resting-state connectivity,

and clinical applications of rs-fMRI in stroke and traumatic brain injury (TBI). In addition, we will explore how brain injury can impact functionally linked brain regions and preclinical models evaluating functional connectivity after brain injury.

2. The complex balance of neuronal activity within the brain: functional connectivity

The brain is a vast network of neurons generating spontaneous fluctuations at all times. Since its inception in 1992, functional magnetic resonance imaging (fMRI) has been well accepted as a noninvasive modality to study brain function [3-5]. Even at rest, the human brain still operates and consumes a large amount of energy. Resting state signals are consistent low frequency fluctuations between 0.01-0.08 Hz [6]. In rs-fMRI, these low frequency fluctuations are based on the hemodynamic response of the vascular system at the sites of neuronal activation and are portrayed by blood oxygen level-dependent (BOLD) signals [7]. Whole brain activation maps for sensory and cognitive function can be constructed with high spatial resolution utilizing these techniques. Brain function is compartmentally organized to specific structures of the brain which reside within unique functional networks, each with its own specialization. In the context of functional neuroimaging, it is claimed that the highly correlated low frequency temporal fluctuations represent cortico-cortical connections, otherwise referred to as functional connectivity of the whole brain [8, 9].

Functional connectivity is defined as a temporally coupled neurophysiological activity originating from brain regions that are spatially separated [10, 11]. The brain is comprised of highly organized intrinsic activity at rest where all systems and networks work within a tight and balanced environment [12]. In the instance of a brain injury, such as TBI or stroke, this balance can be offset by brain lesioning or the effects of the secondary injury cascade (e.g., inflammation, reactive oxygen species (ROS) damage, etc.) causing the manifestation of functional deficits. For example, if a stroke patient were to present with a primary motor cortex lesion in their left brain hemisphere, hemiplegia will likely be present on the right side of the body. These deviations being so sensitive to lesion location imply the preexisting presence of "balance" within a healthy brain.

Biswal et al first investigated motor function with regard to rs-fMRI after studying the transfer of function in the motor cortex and found a high degree of temporal correlation within regions of the sensorimotor cortex and other regions associated with motor function in both hemispheres that were activated after hand movement had stopped [13, 14]. They concluded that these continuous low frequency fluctuations were a manifestation of ongoing functional connectivity and information processing between these regions during rest [8, 15, 16]. Further evaluation of other well-known resting state networks (RSNs) was conducted after Biswal and colleagues presented their pioneering findings, including identification of resting-state signals with brain regions responsible for sensorimotor function, language processing, executive functioning, auditory and visual processing, memory, and task-irrelevant processing (the default mode network (DMN)) [15-24]. It was determined that coherent fluctuations in the brain networks at rest are spontaneously communicating within themselves and that these resting-state

functional networks or low frequency BOLD fluctuations provide a more general representation of human brain function than compared to when a task stimulus is present [25]. De Luca and colleagues posed the alternative possibility that the fMRI signal fluctuations that we know as RSNs may actually be due to vascular changes that are not directly related to cortical neuronal activity (e.g., cerebral hemodynamics) [26-28]. While this has been largely refuted in the fMRI literature [14, 29], we posit that vascular changes do play a role in constructing the fMRI signal, but it is indeed due to neuronal activity and brain metabolism as a direct consequence of local neurotransmitter release [30]. De Luca et al concluded that RSNs are related to functionally relevant neuronal activity by demonstrating asymmetrical hemispheric differences in the motor cortices in response to a unilateral motor task [26]. Furthermore, Biswal, Kylen, and Hyde suggested that the significant BOLD signal correlation between the right and left sensorimotor cortices was much stronger compared to the corresponding perfusion signal indicating that resting connectivity was not due to vascular effects alone [14]. To show that fMRI signal follows neuronal function, Richter and colleagues conducted an fMRI study of the time-course of cognition and the hemodynamic response utilizing a “mental rotation” task, where the subject was shown a 3D block image, then a subsequent rotated 3D block image, and had to determine whether or not it was the same block image [31]. The amount of time it took the subject to make the decision was correlated to the period of the fMRI signal activation, indicating that fMRI signal activation or the hemodynamic response closely follows on-going neuronal function.

These studies demonstrated that rs-fMRI can be utilized to infer neuronal activity in healthy and clinical populations. As the field progresses and now finds clinical

significance within disease states by relating aberrant rs-fMRI findings to relevant clinical variables, the translatability of functional connectivity conclusions become more attainable and therefore more reproducible. Additionally, the original rs-fMRI studies mainly investigated connectivity between cortical brain regions, but today subcortical connections are being implemented into the analysis since they also play a major role in functional connectivity. This review will discuss the fields more recent advances in the subsequent sections with an underlying theme evaluating brain injuries. Since 1992, great advances have been made in the field of rs-fMRI including advanced analysis techniques (beyond the scope of this review) and complementary sequences, such as DTI, to aid in the understanding of the dynamic interconnected network of the brain.

3. The support skeleton for functional brain networks: white matter tracts

Structural connectivity refers to the presence of an axonal connection between two distinct brain regions. RSNs are composed of spatially separated brain regions. In order to effectively communicate within a network, information is passed along bundles of millions of axons that directly connect groups of neurons to each other. In the brain, white matter tracts are commonly referred to as information highways that pass on information between two regions. Diffusion of water molecules in the brain is restricted along the orientation of the fiber tracts and occurs more readily than in an unrestricted environment. DTI is frequently used to assess the structural composition of the white matter tracts in the brain by evaluating the integrity of the cell membranes and myelin sheaths water molecules flow through. DTI sequences also measure the water molecule movement direction and fiber orientation, which can provide information on whole brain

connectivity, including functional connectivity. Notably, in injury models, DTI data can reveal locations of structural reorganization and recovery, which can support fMRI findings of functional network reorganization after an injury such as a TBI. It should be distinguished that DTI provides a probabilistic direction of a fiber's orientation between two regions, but many studies have found encouraging results correlating structural and functional connectivity.

A review by Damoiseaux and Greicius summarizes whether functional connectivity reflects structural connectivity in the brain [32]. They concluded that functional regions do seem to communicate via white matter tracts due to the correlation between increased fiber strength (fractional anisotropy value) between two regions of interest known to be associated with a RSN and increased BOLD signal within those brain regions. Functional connectivity is also observed between regions where there is few or no fiber tracts connecting the two brain regions. This phenomenon is hypothesized to be mediated through indirect fiber tracts by a third brain region serving as a relay point. However, Damoiseaux and Greicius also claim that we need to be wary of false negatives in DTI. Their findings further support the theme that RSNs are of neuronal origin. The first study that directly compared functional and anatomical connectivity was published by Koch and colleagues in 2002 [33]. They found that low functional connectivity rarely occurs in combination with high anatomical connectivity, but high functional connectivity can occur in combination with low anatomical connectivity indicating that functional centers can either be directly or indirectly linked, respectively, by fiber tracts in the brain. Further studies were conducted to determine if DTI could inform rs-fMRI by separating large functional centers into distinct subclusters. Greicius et al investigated the structural

connections between the DMN using tractography [34]. Major findings from this study concluded that tractography can be utilized to determine probabilistic locations (e.g., ventral vs caudal) of where the white matter tracts interact on structures such as the posterior cingulate cortex within the DMN. Furthermore, functional connectivity does not always reflect structural connectivity as they found that there were no fiber tracts detected between the medial prefrontal cortex and the medial temporal lobe. To reiterate our point from above, this suggests that the two regions may be mediated through a third-party region within the DMN or that there could be an error in the DTI analysis methods. Many other studies evaluated the relationship between structural and functional connectivity and found similar results [35-38]. Even in TBI patients, functional activity was correlated with increased white matter integrity [39]. Altogether, all studies showed a strong positive correlation between increased functional and structural connectivity.

Functional and structural connectivity are largely interrelated. Between regions of strong functional connections there can be intact fiber tracts directly connecting the regions or these regions may be connected via a relay point. The white matter tracts are essentially constant over time, but functional connectivity can be substantially altered and reconfigure around the underlying anatomical skeleton within a few hundred milliseconds [40]. It is helpful to include DTI data alongside fMRI for the following reasons: (a) it provides a complete look at the white matter architecture and gray matter composition of the brain through DTI/fMRI, respectively, to examine the relationship between structure and function, (b) in clinical patients, it aids in guiding neurosurgical and rehabilitation interventions [41], and (c) to determine deficits in white matter pathways may lead to conclusions on the health and integrity of RSNs and vice versa.

4. A diagnostic and prognostic tool for brain injury clinical manifestations: rs-fMRI

Brain injuries frequently result in neurological impairment due to the physical disconnection of brain networks. These structural and functional disruptions can be observed throughout DTI and rs-fMRI. Biswal and colleagues first discovered that functional connectivity could be measured in clinical populations [42]. In a study evaluating RSNs in Tourette's patients, they found that pixel area distribution and average number of activated pixels was greater in patients compared to healthy controls, concluding that abnormal motor function organization can be observed using fMRI. These results further supported the notion that the resting-state and task-active systems are somehow related. Another pioneering study by Dr. Shi-Jiang Li first showed the feasibility to correlate brain functional connectivity to clinical measures in Alzheimer's disease (AD) patients [43]. Over the past two decades, the clinical application of resting state functional connectivity has been extensively studied in more than 30 different disorders, including schizophrenia [44], epilepsy [45], aging [46], and dementia/AD [47, 48]. These studies have identified aberrations in patients' RSNs that are attributed to disease state. Here, we will introduce functional connectivity correlations to clinical manifestations in brain injuries including impaired cognitive, behavioral, motor, and somatosensory function.

Brain injuries affect millions of patients each year and are responsible for a large socio-economic burden on patients and their families. Due to the limited range and efficacy of treatments, many patients are left with a range of debilitating deficits. Rs-

fMRI is a widely used noninvasive modality to acquire information on the status of brain function by evaluating RSNs. Many studies have reported abnormal RSN activity due to injury and shown correlates with poor clinical manifestations [49-51]. For example, a 2016 study found that increased S100b, a commonly used serum biomarker for TBI severity, levels correlated with decreased Glawgow Outcome Scores and functional connectivity in the DMN, fronto-parietal, visual, and motor RSNs [52]. These results support that rs-fMRI can be utilized as a biomarker to predict long-term patient outcome after injury.

The DMN is associated with task-irrelevant activities and switches on/off with task-positive networks such as the sensorimotor network [24]. This coupling between networks can be disrupted after an injury. Observed via rs-fMRI, deficiencies in coupling between the DMN and sensorimotor network are associated with attention impairments [53], while coupling deficiencies between the DMN and salience network are associated with predictable cognitive impairment [54]. Moreover, after a brain injury, overall brain network dynamics are shifted away from the small-world architecture that is optimum for information processing, leading to network dysfunction and manifesting in emotional deficits. Structural connectivity of the salience network can predict DMN efficiency. The salience network is involved in the DMN switch between a task-positive and task-negative activity [55]. After a TBI, patients reported abnormal DMN activity associated with less deactivation after a task-positive activity started [56]. This disconnection within DMN function frequently manifests in attention deficits [57]. DMN connectivity aberrations have also been found to be linked to aggression after mild TBI [58]. The intrinsic functional network disruptions that manifested in emotional aggression were

observed utilizing fMRI, indicating that rs-fMRI may be used as a potential biomarker of many clinical manifestations following TBI, including post-concussive aggression. Furthermore, the associations reported between the efficiency of the DMN to decouple correlated to global white matter integrity (measured by fractional anisotropy) [39]. In stroke patients, spatial neglect, an attentional deficit when responding to stimuli in the contralateral environment, has been reported to be correlated with network dysfunction, notably in the dorsal and ventral attention networks [59]. Network dysfunction is frequently associated with a variety of emotional manifestations after brain injury. Many patients report a decreased attention span and increased aggressive tendencies. Employing rs-fMRI as a biomarker can provide clinicians with the tools to properly diagnose and treat these emotional states.

Rs-fMRI can be used to predict physical manifestations as well as patients' recovery after brain injury. Consequent symptoms following TBI, including post-traumatic headache, frequently occur in TBI patients and greatly affect the quality-of-life post-injury. Functional connectivity differences were able to predict the occurrence of post-traumatic headaches in patients with mild TBI [60-63]. Functional connectivity abnormalities in resting-state connectivity were reported in twelve separate networks in mild TBI patients [64]. These abnormalities also correlated with post-concussive symptom severity where brain network connectivity was modulated by the reported post-concussive symptoms checklist from TBI patients. Additional RSN aberrations have also been reported involving sensory networks. While it is difficult to capture full-body motor deficits within the bore of the scanner, small motor tasks can be implemented to observe potential sensory network discrepancies. After a unilateral finger-thumb opposition task

was performed on patients who had sustained a TBI, Kasahara and colleagues reported reduced interhemispheric interactions between the contralateral primary motor cortex, ipsilateral cerebellum, and bilateral supplementary motor area [65]. These results indicate a functional reorganization of the motor brain networks following TBI. Additionally, this reduced interhemispheric interactions manifested as slower motor reaction that could be attributed to delayed cognitive planning of motor function, in this case, finger movements. In fact, abnormal motor preparation is often reported following brain injury [66]. On the contrary, increased functional connectivity between the primary motor and dorsal premotor cortices has been reported in stroke patients one week after undergoing motor learning and dual transcranial direct current stimulation, indicating that rs-fMRI can also be used to evaluate and predict functional recovery [67]. In addition to motor impairment associated sensorimotor network dysfunction, somatosensory impairments are also observed following brain injuries. An observational study on stroke patients found higher functional network connectivity within the ipsilateral network and between hemispheric network hubs were related to improved somatosensory function of the upper extremities [68]. Many physical manifestations, such as impaired motor control and pain, become apparent after injury due to dysfunction of brain networks.

Unlike psychiatric diseases, brain injuries typically develop a physical disruption, such as tissue atrophy or lesion, in brain regions which then have a secondary effect on overall brain function. Many of these functional deficit manifestations are due to the lesion itself residing in a brain structure responsible for a specific function. Due to this infarct and possible coup-contrecoup effects, the entire brain network is altered, but could function be restored? This warrants further investigation to determine if compensatory

measures can be applied to the injured brain network to restore functionality. Capitalizing on the capabilities of rs-fMRI, a deeper understanding of the structural and functional origins of cognitive and behavioral dysfunction after a brain injury can be brought to light. Rs-fMRI can be employed to monitor recovery and disease progression as well as predict long-term outcomes in network function following brain injuries.

5. Brain injuries impact functionally linked brain regions: resting-state networks

Each individual network is comprised of unique brain structures responsible for various functional tasks. When culminated together, these brain regions communicate in harmony providing the basis of brain function and life itself. After an injury, the balance within these networks can be disrupted and can manifest in a plethora of ways. Overall interference with these intrinsic networks have been described as resulting in cognitive impairments associated with internal focus of attention, outward attention, memory, inhibition, social cognition, emotion, and language [69]. Here, we discuss a few of the major RSNs in the brain, the major nodes that comprise them, and how they have been reported to be affected in clinical populations.

- Basal ganglia network

Regions specifically implicated in this network are the striatum (caudate nucleus and putamen), globus pallidus, substantia nigra, subthalamic nucleus, and ventral striatum [6], with some studies reporting motor cortices involvement as well after independent component analysis decomposition [70]. This is likely due to the basal ganglia being

responsible for motor coordination. The basal ganglia network is also involved in emotional and cognitive control [71]. A large percentage of stroke patients have lesions that reside within basal ganglia structures [72]. In a clinical study of basal ganglia stroke patients, researchers found that the focal lesion resulted in profound functional connectivity dysfunction within the basal ganglia network and these patients performed significantly different from healthy volunteers in a lateralization index [73].

- Default mode network

The default mode network is an extensively studied brain network, arguably the most studied RSN. It is known to be associated with task-negative mental processes such as day-dreaming [74]. The DMN is said to be the source of one's sense of self or ego and is also associated with remembering personal events in one's life [75]. Raichle and colleagues first discovered the DMN when reviewing a pattern of blood flow, glucose metabolism, and oxygen consumption in the resting-state [24, 76]. The DMN is comprised of the posterior cingulate cortex, medial prefrontal cortex, inferior parietal lobule, lateral, medial, and inferior temporal cortex, inferior frontal gyrus, and parahippocampal cortex [16, 77-80]. After an injury, the DMN is reported to be responsible for many attention deficits that are associated with TBI symptoms due to the inability to efficiently uncouple, as described above. It has been shown that hyperactivity persists in the DMN regions when a task-positive network is active, such as the executive control network, indicating overall DMN dysfunction [81]. Other studies have reported decreases in DMN functional connectivity following mild TBI [70, 82]. Finally, increases and decreases can be associated within individual structures of each network and Zhou et

al reported reduced connectivity in the posterior cingulate and parietal cortices together with an increase in functional connectivity in the medial prefrontal cortex [83].

- Executive control network

This higher-order cognitive network becomes active when a task involves working memory and cognitive control, including control of intellectual activities [84]. The executive control network comprises the following brain structures: medial and superior frontal gyrus, anterior cingulate cortex, paracingulate gyri, ventrolateral prefrontal cortex, and subcortical regions of the thalamus [6]. After TBI, it was reported that executive control network function was decreased compared to healthy controls [70]. These results were associated with poorer attention, executive, and memory performance. In children who have sustained a TBI, damage to the developing brain has been reported to manifest in long-term executive control network functional deficits in problem solving, mental flexibility, and behavioral control [85-88].

- Frontoparietal network

The frontoparietal network has been reported to be associated with self-awareness, activated during tasks that engage executive function and attention, and engaged in the control of information flow in the brain [89, 90]. The frontoparietal network facilitates switching between the DMN and the dorsal attention network and has been referred to as a “flexible hub for cognitive control” [91, 92]. The core structures of this network are the superior-middle frontal gyrus, frontal pole, paracingulate gyrus, superior parietal cortex, lateral occipital cortex, cingulate gyrus, temporal gyrus, and cerebellum [70]. Palacios

and coworkers, in accordance with Shumskaya et al's findings, found reduced connectivity in the frontoparietal network following a TBI [70, 93]. These results suggest that subsequent changes to the brain architecture and networks following a TBI encourage cognitive deficits and TBI symptoms associated with frontoparietal network responsibilities.

- Salience network

The salience network mediates the dynamic balance between the frontoparietal network and DMN [94] and consists of the anterior insular cortex, dorsal anterior cingulate cortex, inferior parietal cortex, right temporal parietal junction, lateral prefrontal cortex, and many subcortical structures including the substantia nigra/ventral tegmental area, periaqueductal grey, central nucleus of the amygdala, hypothalamus, parabrachial nucleus, and basal ventromedial nucleus of the thalamus [80, 84, 95-98]. This network is known to be responsible for focusing and redirecting attention on important tasks, most notably between the DMN and other task-positive networks [99]. In a study investigating salience network function in TBI patients by the Stop Signal Task which evaluates response inhibition, it was determined that the degree of salience network tract damage was negatively correlated with functional connectivity between the DMN and salience network [55]. These results indicate that damage within the salience network impairs the dynamic and vital DMN function to control attention and cognition. As we discussed earlier, damage within the white matter tracts of the salience network can predict DMN function.

- Sensorimotor network

As we introduced the origins of rs-fMRI earlier with the work of Dr. Bharat Biswal, the sensorimotor was the first RSN studied [13, 25]. This sensory network is composed of the primary motor and somatosensory cortices, including the supplementary motor and premotor areas [80]. The sensorimotor network comprises both sensory and motor function and is frequently studied in relation to physical outcomes associated with TBI recovery. Adolescents with TBI have been reported to show significantly reduced functional connectivity between the motor network and left caudate and these reduced functional connections correlated with poorer task performance in simple motor activities [100]. Further, stroke patients with deep brain lesions within the basal ganglia and pontine reported that both groups of patients exhibited reductions in functional connectivity within the sensorimotor network. In the acute phase following stroke, reduction in interhemispheric connectivity between the sensorimotor network areas was reported to predict decreased motor performance including visual neglect and upper extremity impairment [101, 102]. Sensorimotor deficits after brain injury commonly lead to global brain network dysfunction [103].

- Visual network

Within the occipital lobe, the visual resting state network operates. The visual cortices and a major nucleus within the thalamus, the lateral geniculate nucleus, make up the visual network [80]. The lateral geniculate nucleus of the thalamus serves as a relay point for the visual information received through the retina to the visual cortex [104].

Following suit with the previously reported RSNs, the visual network has been reported to be linked to less connectivity within the network following a TBI as well as linked to greater post-concussive-type symptoms [64]. On the contrary, this sensory network has also been reported to result in increased functional connectivity in patients following TBI [70]. The authors posit that this increase may be interpreted as compensation for injury, although more research is needed to confirm this theory.

While this section has reported many of these RSNs individually, they all work in harmony within the brain. Patients with a brain injury frequently present with deficits in higher order cognitive functions that require coordination between multiple brain networks. For this reason, as the field progresses, the necessity to investigate brain networks simultaneously becomes more and more apparent.

6. Preclinical applications of rs-fMRI: stroke and TBI animal models of functional connectivity

There is rich literature evaluating preclinical models of stroke and TBI with the end goal of developing state of the art tools to evaluate injury severity and to direct and inform patient rehabilitation plans. In order to truly understand these disease states, preclinical controlled injury models are employed to evaluate minute changes in response to injury or treatment and fMRI holds great potential to noninvasively observe these phenomena. It has been proven that animals including rodents [105], pigs [106], and monkeys [107-109] have similar RSNs to humans. TBI and stroke animal models provide

reproducible means to investigate network disruptions, reorganization, and recovery following injury.

Rodents are a lissencephalic species, while their brain composition is different to the human brain, that are frequently used in preclinical studies to gather more information on the inner workings of the brain. The first study to demonstrate that fMRI can be used to monitor functional impairments and recovery following experimental TBI in rodents found that 40% of animals showed spontaneous recovery of BOLD response at 56 days post-TBI compared to their 7 days post-TBI MRI [110]. In response to a bilateral electrical forepaw stimulation to activate the primary somatosensory cortices, at 7 days post-TBI, the ipsilateral primary somatosensory cortex activity was completely or partially lost in 80% of rats with TBI. The strength of the BOLD response was significantly reduced in all TBI animals when compared to baseline. Interestingly, histological analysis from this study revealed rats with a persistently reduced BOLD signal had a significantly reduced myelin density of 18% lower than rats that exhibited spontaneous BOLD recovery, and 28% lower than sham animals, supporting the correlation between structural and functional brain networks. Another rat fMRI study investigated whether reduced resting-state BOLD fluctuations connected to the lesioned cortex were associated with functional impairments, particularly epilepsy, following an experimental lateral fluid-percussion TBI [111]. They determined that reductions in BOLD signals indicating impaired functional connectivity were predictive of epileptogenesis and could also contribute to other post-TBI comorbidities. More recently, a rodent functional connectomic analysis was completed to monitor resting-state functional connectivity in the rat brain [112]. In a widespread axonal injury model

induced by controlled cortical impact, rs-fMRI was acquired at 7, 14, and 28 days post-TBI. They found that functional connectivity disruptions could be predicted by structural deficits within and outside of the primary injury site. These functional and structural deficits persisted chronically. They hypothesized that deficits within functional brain networks would become apparent in known structurally damaged regions and found correlations between functional and structural connectivity, as well as correlations between global network parameters, such as shortest path length, clustering coefficient, and modularity, and injury severity. After injury, areas of hyper-connectivity surfaced, and weakened over time. Overall, more local connectivity was observed especially after a more severe injury, indicating more random connectivity throughout the brain following TBI.

Similar to clinical patients, preclinical rs-fMRI studies in rodents have reported the reduction of interhemispheric connectivity within RSNs following stroke to be a key correlate of stroke severity and functional recovery [113, 114]. In 2001, Dijkhuizen and colleagues were unable to detect statistically significant correlations between the degree of ischemic damage, neurologic impairments, and the profile of brain activation in a permanent rat stroke model [115]. However, in a follow-on study using a transient ischemic rat model, the same group determined that functional recovery was mainly associated with preserved or restored activation in the ipsilateral hemisphere [116]. Furthermore, as injury severity increased, they found that the activation balance shifted to the contralateral hemisphere, which appeared to be strongest early after stroke onset in patients and animal models [117, 118]. This reorganization away from the ipsilateral injury site may be due to the discovery, unmasking, or strengthening of existing and/or

new network connections [119]. Overall, changes in activation patterns were directly linked to ischemic injury severity, and reinstatement of BOLD activation was also correlated with reinstatement of electrical responsiveness and improved neurologic status [116, 120].

To demonstrate an example of rs-fMRI being utilized to confirm therapeutic efficacy, stem cell grafts were implanted into an ischemic mouse brain and fMRI was evaluated between treated and nontreated animals [121, 122]. In mice that received the intracerebral neural stem cell stem cell graft, functional networks were stabilized early on, indicating a paracrine effect that fMRI modalities were able to observe by strengthened connections in the treated animals between the sensorimotor network regions. Rs-fMRI was also able to observe the decrease in those early strengthened networks when the vitality of the stem cell graft was lost over time. Connections between network dynamics can be noninvasively and longitudinally monitored utilizing rs-fMRI technology.

Rodent studies are valuable in biomedical research because of their small size, ease of maintenance, low cost, and ability to include larger sample sizes, but the translatability to clinical applications is limited. These limitations are manifested in the lack of translation of successful therapeutics in rodent preclinical trails to human stroke and TBI clinical trials. Gyrencephalic species share many more similarities to the human brain than rodents [123]. Especially when it comes to brain injury, the cerebral architecture of the brain is important to consider when evaluating therapeutic options. For example, in a TBI, the injury repercussions ripple through the brain in a much different pattern in a brain with gyri and sulci as compared to a smooth cortex with less surface area.

To date, there are no reported studies evaluating resting-state functional connectivity disruptions following stroke in a gyrencephalic model. However, the TBI literature is quickly growing. In 2006, Duhaime and colleagues demonstrated that functional deficits and recovery over time can be observed through fMRI in a porcine model of TBI [124]. They found a robust cluster of activation apparent across animals in the location of the left rostral gyrus, or primary somatosensory cortex, in response to right snout stimulation. While this study did not compare BOLD responses to a functional outcome parameter, they did prove that the fMRI technique can be measured over time in the developing gyrencephalic brain. In a similar porcine model of TBI, functional disruptions were found within the sensorimotor, executive control, and visual resting state networks when compared to healthy controls [125]. These aberrations within RSNs can be attributed to functional deficits previously reported in this controlled cortical impact pig model of TBI including demonstrated reduction in cognitive flexibility and problem-solving capabilities (executive control network dysfunction) when evaluated in a T-maze test where the TBI group took significantly longer to make correct choices compared to control animals [126]. Further, motor abnormalities have been reported in this preclinical model following TBI including reduced velocity, cadence, and stride length [127, 128]. The authors suggest that deficits seen within the sensorimotor network could be responsible for these physical manifestations. This field of preclinical fMRI in large animal models holds great potential for effectively evaluating therapeutic safety and efficacy in relation to brain function and recovery in a brain that closely resembles the human brain.

Many concerns have been raised about the validity of BOLD fluctuations in anesthetized animals. Since the majority of preclinical animal MRI research is conducted

under general anesthesia, we wanted to address this point. Vincent et al conducted a study on anesthetized monkeys to evaluate if the intrinsic network is still active [107]. Under 0.90% and 1.25% isoflurane, cortical patterns of coherent spontaneous BOLD signals were still considered authentic resting-state signal after comparing the anesthetized findings to a map of BOLD responses evoked during task performance in awake monkeys. They found similar BOLD fluctuations in animals that were awake and under anesthesia. These findings support the perspective that spontaneous low-level fluctuations or BOLD signals are not derived from consciously directed mental activity but persist as a more fundamental property of the brain's functional network governed largely by internal dynamics [2, 129-132]. It is postulated that RSNs likely reflect an evolutionary instinct to conserve functional brain organization throughout all levels of consciousness. Therefore, even in an anesthetized state, temporally coherent BOLD fluctuations should still be observed through fMRI.

While the field is making large strides, further information is warranted on how changes in functional connectivity relate to network reorganization following injury. Preclinical models allow for more invasive answers to be drawn from observed fMRI changes such as post-mortem histological analysis, whereas in clinical populations, conclusions must be drawn only from noninvasive techniques.

7. Conclusion

Our brain is a complex network of structural and functional connections between regions. Rs-fMRI signals emerge from anatomical brain areas that are separated spatially, linked functionally, and communicate continuously within a network [133]. The

subsequent symptoms resulting from brain injuries are not fully understood, but advanced neuroimaging techniques, such as rs-fMRI and DTI, have provided novel insights on functional and structural connectivity of brain networks in both healthy and clinical populations. However, specific functions of individual structures and networks are well-known, and this connectome approach to evaluating brain function and recovery after an injury can allow treatment regimens to be better predicted and more personalized to the heterogenous nature of brain injury. This review presented pioneering and recent empirical findings involving functional and structural connectivity regarding brain injuries. The noninvasive modality of rs-fMRI holds great potential for determining the optimal timing and type of therapeutics and interventions that can be used following a brain injury that will result in the best overall outcome for the patient.

References

1. Raichle, M.E. and M.A. Mintun, *Brain work and brain imaging.* Annu Rev Neurosci, 2006. **29**: p. 449-76.
2. Raichle, M.E., *Neuroscience. The brain's dark energy.* Science, 2006. **314**(5803): p. 1249-50.
3. Ogawa, S., et al., *Intrinsic signal changes accompanying sensory stimulation: functional brain mapping with magnetic resonance imaging.* Proc Natl Acad Sci U S A, 1992. **89**(13): p. 5951-5.
4. Kwong, K.K., et al., *Dynamic magnetic resonance imaging of human brain activity during primary sensory stimulation.* Proc Natl Acad Sci U S A, 1992. **89**(12): p. 5675-9.
5. Bandettini, P.A., et al., *Time course EPI of human brain function during task activation.* Magn Reson Med, 1992. **25**(2): p. 390-7.
6. Smitha, K.A., et al., *Resting state fMRI: A review on methods in resting state connectivity analysis and resting state networks.* Neuroradiol J, 2017. **30**(4): p. 305-317.
7. Ogawa, S., et al., *On the characteristics of functional magnetic resonance imaging of the brain.* Annu Rev Biophys Biomol Struct, 1998. **27**: p. 447-74.
8. Lowe, M.J., et al., *Correlations in low-frequency BOLD fluctuations reflect cortico-cortical connections.* Neuroimage, 2000. **12**(5): p. 582-7.
9. Lowe, M.J., B.J. Mock, and J.A. Sorenson, *Functional connectivity in single and multislice echoplanar imaging using resting-state fluctuations.* Neuroimage, 1998. **7**(2): p. 119-32.
10. Aertsen, A.M., et al., *Dynamics of neuronal firing correlation: modulation of "effective connectivity".* J Neurophysiol, 1989. **61**(5): p. 900-17.
11. Friston, K.J., et al., *Functional connectivity: the principal-component analysis of large (PET) data sets.* J Cereb Blood Flow Metab, 1993. **13**(1): p. 5-14.
12. Haider, B., et al., *Neocortical network activity in vivo is generated through a dynamic balance of excitation and inhibition.* J Neurosci, 2006. **26**(17): p. 4535-45.
13. Biswal, B., et al., *Functional connectivity in the motor cortex of resting human brain using echo-planar MRI.* Magn Reson Med, 1995. **34**(4): p. 537-41.
14. Biswal, B.B., J. Van Kylen, and J.S. Hyde, *Simultaneous assessment of flow and BOLD signals in resting-state functional connectivity maps.* NMR Biomed, 1997. **10**(4-5): p. 165-70.

15. Cordes, D., et al., *Mapping functionally related regions of brain with functional connectivity MR imaging.* AJNR Am J Neuroradiol, 2000. **21**(9): p. 1636-44.

16. Greicius, M.D., et al., *Functional connectivity in the resting brain: a network analysis of the default mode hypothesis.* Proc Natl Acad Sci U S A, 2003. **100**(1): p. 253-8.

17. Cordes, D., et al., *Hierarchical clustering to measure connectivity in fMRI resting-state data.* Magn Reson Imaging, 2002. **20**(4): p. 305-17.

18. Damoiseaux, J.S., et al., *Consistent resting-state networks across healthy subjects.* Proc Natl Acad Sci U S A, 2006. **103**(37): p. 13848-53.

19. van den Heuvel, M., R. Mandl, and H. Hulshoff Pol, *Normalized cut group clustering of resting-state FMRI data.* PLoS One, 2008. **3**(4): p. e2001.

20. Xiong, J., et al., *Interregional connectivity to primary motor cortex revealed using MRI resting state images.* Hum Brain Mapp, 1999. **8**(2-3): p. 151-6.

21. Vincent, J.L., et al., *Coherent spontaneous activity identifies a hippocampal-parietal memory network.* J Neurophysiol, 2006. **96**(6): p. 3517-31.

22. Hampson, M., et al., *Changes in functional connectivity of human MT/V5 with visual motion input.* Neuroreport, 2004. **15**(8): p. 1315-9.

23. Hampson, M., et al., *Detection of functional connectivity using temporal correlations in MR images.* Hum Brain Mapp, 2002. **15**(4): p. 247-62.

24. Raichle, M.E., et al., *A default mode of brain function.* Proc Natl Acad Sci U S A, 2001. **98**(2): p. 676-82.

25. Biswal, B.B., *Resting state fMRI: a personal history.* Neuroimage, 2012. **62**(2): p. 938-44.

26. De Luca, M., et al., *Blood oxygenation level dependent contrast resting state networks are relevant to functional activity in the neocortical sensorimotor system.* Exp Brain Res, 2005. **167**(4): p. 587-94.

27. Kiviniemi, V., et al., *Slow vasomotor fluctuation in fMRI of anesthetized child brain.* Magn Reson Med, 2000. **44**(3): p. 373-8.

28. Mitra, P.P., et al., *The nature of spatiotemporal changes in cerebral hemodynamics as manifested in functional magnetic resonance imaging.* Magn Reson Med, 1997. **37**(4): p. 511-8.

29. Fox, M.D. and M.E. Raichle, *Spontaneous fluctuations in brain activity observed with functional magnetic resonance imaging.* Nat Rev Neurosci, 2007. **8**(9): p. 700-11.

30. Attwell, D. and C. Iadecola, *The neural basis of functional brain imaging signals.* Trends Neurosci, 2002. **25**(12): p. 621-5.

31. Richter, W., et al., *Time-resolved fMRI of mental rotation.* Neuroreport, 1997. **8**(17): p. 3697-702.

32. Damoiseaux, J.S. and M.D. Greicius, *Greater than the sum of its parts: a review of studies combining structural connectivity and resting-state functional connectivity.* Brain Struct Funct, 2009. **213**(6): p. 525-33.

33. Koch, M.A., D.G. Norris, and M. Hund-Georgiadis, *An investigation of functional and anatomical connectivity using magnetic resonance imaging.* Neuroimage, 2002. **16**(1): p. 241-50.

34. Greicius, M.D., et al., *Resting-state functional connectivity reflects structural connectivity in the default mode network.* Cereb Cortex, 2009. **19**(1): p. 72-8.

35. Skudlarski, P., et al., *Measuring brain connectivity: diffusion tensor imaging validates resting state temporal correlations.* Neuroimage, 2008. **43**(3): p. 554-61.

36. Honey, C.J., et al., *Predicting human resting-state functional connectivity from structural connectivity.* Proc Natl Acad Sci U S A, 2009. **106**(6): p. 2035-40.

37. Hagmann, P., et al., *Mapping the structural core of human cerebral cortex.* PLoS Biol, 2008. **6**(7): p. e159.

38. Honey, C.J., et al., *Network structure of cerebral cortex shapes functional connectivity on multiple time scales.* Proc Natl Acad Sci U S A, 2007. **104**(24): p. 10240-5.

39. Palacios, E.M., et al., *White matter integrity related to functional working memory networks in traumatic brain injury.* Neurology, 2012. **78**(12): p. 852-60.

40. Bassett, D.S., et al., *Adaptive reconfiguration of fractal small-world human brain functional networks.* Proc Natl Acad Sci U S A, 2006. **103**(51): p. 19518-23.

41. Rykhlevskaia, E., G. Gratton, and M. Fabiani, *Combining structural and functional neuroimaging data for studying brain connectivity: a review.* Psychophysiology, 2008. **45**(2): p. 173-87.

42. Biswal, B., et al., *Abnormal cerebral activation associated with a motor task in Tourette syndrome.* AJNR Am J Neuroradiol, 1998. **19**(8): p. 1509-12.

43. Li, S.J., et al., *Alzheimer Disease: evaluation of a functional MR imaging index as a marker.* Radiology, 2002. **225**(1): p. 253-9.

44. Jafri, M.J., et al., *A method for functional network connectivity among spatially independent resting-state components in schizophrenia.* Neuroimage, 2008. **39**(4): p. 1666-81.

45. Laufs, H., et al., *Temporal lobe interictal epileptic discharges affect cerebral activity in "default mode" brain regions.* Hum Brain Mapp, 2007. **28**(10): p. 1023-32.

46. Andrews-Hanna, J.R., et al., *Disruption of large-scale brain systems in advanced aging.* Neuron, 2007. **56**(5): p. 924-35.

47. Sorg, C., et al., *Selective changes of resting-state networks in individuals at risk for Alzheimer's disease.* Proc Natl Acad Sci U S A, 2007. **104**(47): p. 18760-5.

48. Rombouts, S.A., et al., *Whole brain analysis of T2* weighted baseline FMRI signal in dementia.* Hum Brain Mapp, 2007. **28**(12): p. 1313-7.

49. Tang, L., et al., *Thalamic resting-state functional networks: disruption in patients with mild traumatic brain injury.* Radiology, 2011. **260**(3): p. 831-40.

50. Messe, A., et al., *Specific and evolving resting-state network alterations in post-concussion syndrome following mild traumatic brain injury.* PLoS One, 2013. **8**(6): p. e65470.

51. Caeyenberghs, K., et al., *Functional Connectivity Density and Balance in Young Patients with Traumatic Axonal Injury.* Brain Connect, 2015. **5**(7): p. 423-32.

52. Thompson, W.H., et al., *Functional resting-state fMRI connectivity correlates with serum levels of the S100B protein in the acute phase of traumatic brain injury.* Neuroimage Clin, 2016. **12**: p. 1004-1012.

53. Shumskaya, E., et al., *Abnormal connectivity in the sensorimotor network predicts attention deficits in traumatic brain injury.* Exp Brain Res, 2017. **235**(3): p. 799-807.

54. Sharp, D.J., G. Scott, and R. Leech, *Network dysfunction after traumatic brain injury.* Nat Rev Neurol, 2014. **10**(3): p. 156-66.

55. Jilka, S.R., et al., *Damage to the Salience Network and interactions with the Default Mode Network.* J Neurosci, 2014. **34**(33): p. 10798-807.

56. Bonnelle, V., et al., *Salience network integrity predicts default mode network function after traumatic brain injury.* Proc Natl Acad Sci U S A, 2012. **109**(12): p. 4690-5.

57. Bonnelle, V., et al., *Default mode network connectivity predicts sustained attention deficits after traumatic brain injury.* J Neurosci, 2011. **31**(38): p. 13442-51.

58. Dailey, N.S., et al., *Resting-state functional connectivity as a biomarker of aggression in mild traumatic brain injury.* Neuroreport, 2018. **29**(16): p. 1413-1417.

59. He, B.J., et al., *Breakdown of functional connectivity in frontoparietal networks underlies behavioral deficits in spatial neglect.* Neuron, 2007. **53**(6): p. 905-18.

60. Niu, X., et al., *Disruption of periaqueductal grey-default mode network functional connectivity predicts persistent post-traumatic headache in mild traumatic brain injury.* J Neurol Neurosurg Psychiatry, 2019. **90**(3): p. 326-332.

61. Lu, L., et al., *Altered hypothalamic functional connectivity in post-traumatic headache after mild traumatic brain injury.* J Headache Pain, 2020. **21**(1): p. 93.

62. Dumkrieger, G., et al., *Static and dynamic functional connectivity differences between migraine and persistent post-traumatic headache: A resting-state magnetic resonance imaging study.* Cephalalgia, 2019. **39**(11): p. 1366-1381.

63. Schwedt, T.J., *Structural and Functional Brain Alterations in Post-traumatic Headache Attributed to Mild Traumatic Brain Injury: A Narrative Review.* Front Neurol, 2019. **10**: p. 615.

64. Stevens, M.C., et al., *Multiple resting state network functional connectivity abnormalities in mild traumatic brain injury.* Brain Imaging Behav, 2012. **6**(2): p. 293-318.

65. Kasahara, M., et al., *Altered functional connectivity in the motor network after traumatic brain injury.* Neurology, 2010. **75**(2): p. 168-76.

66. Di Russo, F., et al., *Abnormal motor preparation in severe traumatic brain injury with good recovery.* J Neurotrauma, 2005. **22**(2): p. 297-312.

67. Lefebvre, S., et al., *Increased functional connectivity one week after motor learning and tDCS in stroke patients.* Neuroscience, 2017. **340**: p. 424-435.

68. De Bruyn, N., et al., *Functional network connectivity is altered in patients with upper limb somatosensory impairments in the acute phase post stroke: A cross-sectional study.* PLoS One, 2018. **13**(10): p. e0205693.

69. Laird, A.R., et al., *Behavioral interpretations of intrinsic connectivity networks.* J Cogn Neurosci, 2011. **23**(12): p. 4022-37.

70. Palacios, E.M., et al., *Resting-State Functional Connectivity Alterations Associated with Six-Month Outcomes in Mild Traumatic Brain Injury.* J Neurotrauma, 2017. **34**(8): p. 1546-1557.

71. Afifi, A.K., *The basal ganglia: a neural network with more than motor function.* Semin Pediatr Neurol, 2003. **10**(1): p. 3-10.

72. Su, C.Y., et al., *Neuropsychological impairment after hemorrhagic stroke in basal ganglia.* Arch Clin Neuropsychol, 2007. **22**(4): p. 465-74.

73. Li, Q.G., et al., *Dynamic Neural Network Changes Revealed by Voxel-Based Functional Connectivity Strength in Left Basal Ganglia Ischemic Stroke.* Front Neurosci, 2020. **14**: p. 526645.

74. Konrad, K. and S.B. Eickhoff, *Is the ADHD brain wired differently? A review on structural and functional connectivity in attention deficit hyperactivity disorder.* Hum Brain Mapp, 2010. **31**(6): p. 904-16.

75. Carhart-Harris, R.L. and K.J. Friston, *The default-mode, ego-functions and free-energy: a neurobiological account of Freudian ideas.* Brain, 2010. **133**(Pt 4): p. 1265-83.

76. Gusnard, D.A., et al., *Medial prefrontal cortex and self-referential mental activity: relation to a default mode of brain function.* Proc Natl Acad Sci U S A, 2001. **98**(7): p. 4259-64.

77. Schilbach, L., et al., *Minds at rest? Social cognition as the default mode of cognizing and its putative relationship to the "default system" of the brain.* Conscious Cogn, 2008. **17**(2): p. 457-67.

78. Buckner, R.L., J.R. Andrews-Hanna, and D.L. Schacter, *The brain's default network: anatomy, function, and relevance to disease.* Ann N Y Acad Sci, 2008. **1124**: p. 1-38.

79. Fransson, P. and G. Marrelec, *The precuneus/posterior cingulate cortex plays a pivotal role in the default mode network: Evidence from a partial correlation network analysis.* Neuroimage, 2008. **42**(3): p. 1178-84.

80. Uddin, L.Q., B.T.T. Yeo, and R.N. Spreng, *Towards a Universal Taxonomy of Macro-scale Functional Human Brain Networks.* Brain Topogr, 2019. **32**(6): p. 926-942.

81. Mayer, A.R., et al., *Functional connectivity in mild traumatic brain injury.* Hum Brain Mapp, 2011. **32**(11): p. 1825-35.

82. Johnson, B., et al., *Alteration of brain default network in subacute phase of injury in concussed individuals: resting-state fMRI study.* Neuroimage, 2012. **59**(1): p. 511-8.

83. Zhou, Y., et al., *Default-mode network disruption in mild traumatic brain injury.* Radiology, 2012. **265**(3): p. 882-92.

84. Seeley, W.W., et al., *Dissociable intrinsic connectivity networks for salience processing and executive control.* J Neurosci, 2007. **27**(9): p. 2349-56.

85. Lindsey, H.M., et al., *Longitudinal Neuroimaging in Pediatric Traumatic Brain Injury: Current State and Consideration of Factors That Influence Recovery.* Front Neurol, 2019. **10**: p. 1296.

86. Scheibel, R.S., *Functional Magnetic Resonance Imaging of Cognitive Control following Traumatic Brain Injury.* Front Neurol, 2017. **8**: p. 352.

87. D'Souza, A., et al., *Measuring Change Over Time: A Systematic Review of Evaluative Measures of Cognitive Functioning in Traumatic Brain Injury.* Front Neurol, 2019. **10**: p. 353.

88. Jenkins, P.O., M.A. Mehta, and D.J. Sharp, *Catecholamines and cognition after traumatic brain injury.* Brain, 2016. **139**(Pt 9): p. 2345-71.

89. Vincent, J.L., et al., *Evidence for a frontoparietal control system revealed by intrinsic functional connectivity.* J Neurophysiol, 2008. **100**(6): p. 3328-42.

90. Ham, T.E., et al., *The neural basis of impaired self-awareness after traumatic brain injury.* Brain, 2014. **137**(Pt 2): p. 586-97.

91. Spreng, R.N., et al., *Intrinsic architecture underlying the relations among the default, dorsal attention, and frontoparietal control networks of the human brain.* J Cogn Neurosci, 2013. **25**(1): p. 74-86.

92. Marek, S. and N.U.F. Dosenbach, *The frontoparietal network: function, electrophysiology, and importance of individual precision mapping.* Dialogues Clin Neurosci, 2018. **20**(2): p. 133-140.

93. Shumskaya, E., et al., *Abnormal whole-brain functional networks in homogeneous acute mild traumatic brain injury.* Neurology, 2012. **79**(2): p. 175-82.

94. Menon, V., *Large-scale brain networks and psychopathology: a unifying triple network model.* Trends Cogn Sci, 2011. **15**(10): p. 483-506.

95. Yeo, B.T., et al., *The organization of the human cerebral cortex estimated by intrinsic functional connectivity.* J Neurophysiol, 2011. **106**(3): p. 1125-65.

96. Corbetta, M. and G.L. Shulman, *Control of goal-directed and stimulus-driven attention in the brain.* Nat Rev Neurosci, 2002. **3**(3): p. 201-15.

97. Gordon, E.M., et al., *Precision Functional Mapping of Individual Human Brains.* Neuron, 2017. **95**(4): p. 791-807 e7.

98. Uddin, L.Q., *Salience processing and insular cortical function and dysfunction.* Nat Rev Neurosci, 2015. **16**(1): p. 55-61.

99. Goulden, N., et al., *The salience network is responsible for switching between the default mode network and the central executive network: replication from DCM.* Neuroimage, 2014. **99**: p. 180-90.

100. Stephens, J.A., et al., *Response Inhibition Deficits and Altered Motor Network Connectivity in the Chronic Phase of Pediatric Traumatic Brain Injury.* J Neurotrauma, 2017. **34**(22): p. 3117-3123.

101. Xu, H., et al., *Contribution of the resting-state functional connectivity of the contralesional primary sensorimotor cortex to motor recovery after subcortical stroke.* PLoS One, 2014. **9**(1): p. e84729.

102. Carter, A.R., et al., *Resting interhemispheric functional magnetic resonance imaging connectivity predicts performance after stroke.* Ann Neurol, 2010. **67**(3): p. 365-75.

103. Favre, I., et al., *Upper limb recovery after stroke is associated with ipsilesional primary motor cortical activity: a meta-analysis.* Stroke, 2014. **45**(4): p. 1077-83.

104. Cudeiro, J. and A.M. Sillito, *Looking back: corticothalamic feedback and early visual processing.* Trends Neurosci, 2006. **29**(6): p. 298-306.

105. Pawela, C.P., et al., *Resting-state functional connectivity of the rat brain.* Magn Reson Med, 2008. **59**(5): p. 1021-9.

106. Simchick, G., et al., *Pig Brains Have Homologous Resting-State Networks with Human Brains.* Brain Connect, 2019. **9**(7): p. 566-579.

107. Vincent, J.L., et al., *Intrinsic functional architecture in the anaesthetized monkey brain.* Nature, 2007. **447**(7140): p. 83-6.

108. Hayashi, T., et al., *Short communication: mapping of somatosensory cortices with functional magnetic resonance imaging in anaesthetized macaque monkeys.* Eur J Neurosci, 1999. **11**(12): p. 4451-6.

109. Leopold, D.A., H.K. Plettenberg, and N.K. Logothetis, *Visual processing in the ketamine-anesthetized monkey. Optokinetic and blood oxygenation level-dependent responses.* Exp Brain Res, 2002. **143**(3): p. 359-72.

110. Niskanen, J.P., et al., *Monitoring functional impairment and recovery after traumatic brain injury in rats by FMRI.* J Neurotrauma, 2013. **30**(7): p. 546-56.

111. Mishra, A.M., et al., *Decreased resting functional connectivity after traumatic brain injury in the rat.* PLoS One, 2014. **9**(4): p. e95280.

112. Harris, N.G., et al., *Disconnection and hyper-connectivity underlie reorganization after TBI: A rodent functional connectomic analysis.* Exp Neurol, 2016. **277**: p. 124-138.

113. van Meer, M.P., et al., *Extent of bilateral neuronal network reorganization and functional recovery in relation to stroke severity.* J Neurosci, 2012. **32**(13): p. 4495-507.

114. van Meer, M.P., et al., *Correspondence between altered functional and structural connectivity in the contralesional sensorimotor cortex after unilateral stroke in rats: a combined resting-state functional MRI and manganese-enhanced MRI study.* J Cereb Blood Flow Metab, 2010. **30**(10): p. 1707-11.

115. Dijkhuizen, R.M., et al., *Functional magnetic resonance imaging of reorganization in rat brain after stroke.* Proc Natl Acad Sci U S A, 2001. **98**(22): p. 12766-71.

116. Dijkhuizen, R.M., et al., *Correlation between brain reorganization, ischemic damage, and neurologic status after transient focal cerebral ischemia in rats: a functional magnetic resonance imaging study.* J Neurosci, 2003. **23**(2): p. 510-7.

117. Cuadrado, M.L., et al., *Bihemispheric contribution to motor recovery after stroke: A longitudinal study with transcranial doppler ultrasonography.* Cerebrovasc Dis, 1999. **9**(6): p. 337-44.

118. Marshall, R.S., et al., *Evolution of cortical activation during recovery from corticospinal tract infarction.* Stroke, 2000. **31**(3): p. 656-61.

119. Dancause, N., *Vicarious function of remote cortex following stroke: recent evidence from human and animal studies.* Neuroscientist, 2006. **12**(6): p. 489-99.

120. Weber, R., et al., *Early prediction of functional recovery after experimental stroke: functional magnetic resonance imaging, electrophysiology, and behavioral testing in rats.* J Neurosci, 2008. **28**(5): p. 1022-9.

121. Green, C., et al., *Sensorimotor Functional and Structural Networks after Intracerebral Stem Cell Grafts in the Ischemic Mouse Brain.* J Neurosci, 2018. **38**(7): p. 1648-1661.

122. Green, C., et al., *Persistent Quantitative Vitality of Stem Cell Graft Is Necessary for Stabilization of Functional Brain Networks After Stroke.* Front Neurol, 2019. **10**: p. 335.

123. Kinder, H.A., E.W. Baker, and F.D. West, *The pig as a preclinical traumatic brain injury model: current models, functional outcome measures, and translational detection strategies.* Neural Regen Res, 2019. **14**(3): p. 413-424.

124. Duhaime, A.C., et al., *Functional magnetic resonance imaging of the primary somatosensory cortex in piglets.* J Neurosurg, 2006. **104**(4 Suppl): p. 259-64.

125. Simchick, G., et al., *Detecting functional connectivity disruptions in a translational pediatric traumatic brain injury porcine model using resting-state and task-based fMRI.* In Review. , 2021.

126. Kinder, H.A., et al., *Controlled Cortical Impact Leads to Cognitive and Motor Function Deficits that Correspond to Cellular Pathology in a Piglet Traumatic Brain Injury Model.* J Neurotrauma, 2019. **36**(19): p. 2810-2826.

127. Kinder, H.A., et al., *Traumatic Brain Injury Results in Dynamic Brain Structure Changes Leading to Acute and Chronic Motor Function Deficits in a Pediatric Piglet Model.* J Neurotrauma, 2019. **36**(20): p. 2930-2942.

128. Baker, E.W., et al., *Controlled cortical impact severity results in graded cellular, tissue, and functional responses in a piglet traumatic brain injury model.* Journal of neurotrauma, 2019. **36**(1): p. 61-73.

129. MacLean, J.N., et al., *Internal dynamics determine the cortical response to thalamic stimulation.* Neuron, 2005. **48**(5): p. 811-23.

130. Buzsaki, G. and A. Draguhn, *Neuronal oscillations in cortical networks.* Science, 2004. **304**(5679): p. 1926-9.

131. Kenet, T., et al., *Spontaneously emerging cortical representations of visual attributes.* Nature, 2003. **425**(6961): p. 954-6.

132. Fiser, J., C. Chiu, and M. Weliky, *Small modulation of ongoing cortical dynamics by sensory input during natural vision.* Nature, 2004. **431**(7008): p. 573-8.

133. van den Heuvel, M.P. and H.E. Hulshoff Pol, *Exploring the brain network: a review on resting-state fMRI functional connectivity.* Eur Neuropsychopharmacol, 2010. **20**(8): p. 519-34.

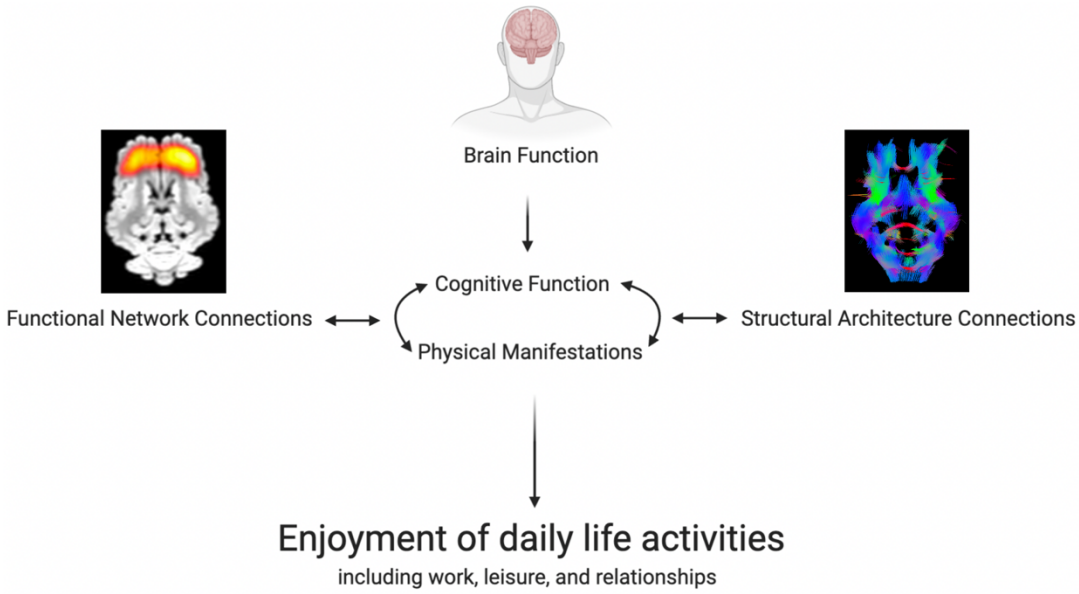

Figure 2.1: Functional and structural networks are interrelated. Brain function is dictated by the relationship between cognitive function and physical manifestations. Functional network connections and structural architecture connections comprise the overall support system whereas if there is a disruption in the functional network or structural architecture connections of the brain, this can have a direct effect on cognitive function and physical manifestations, and therefore overall brain function and enjoyment of daily life activities.

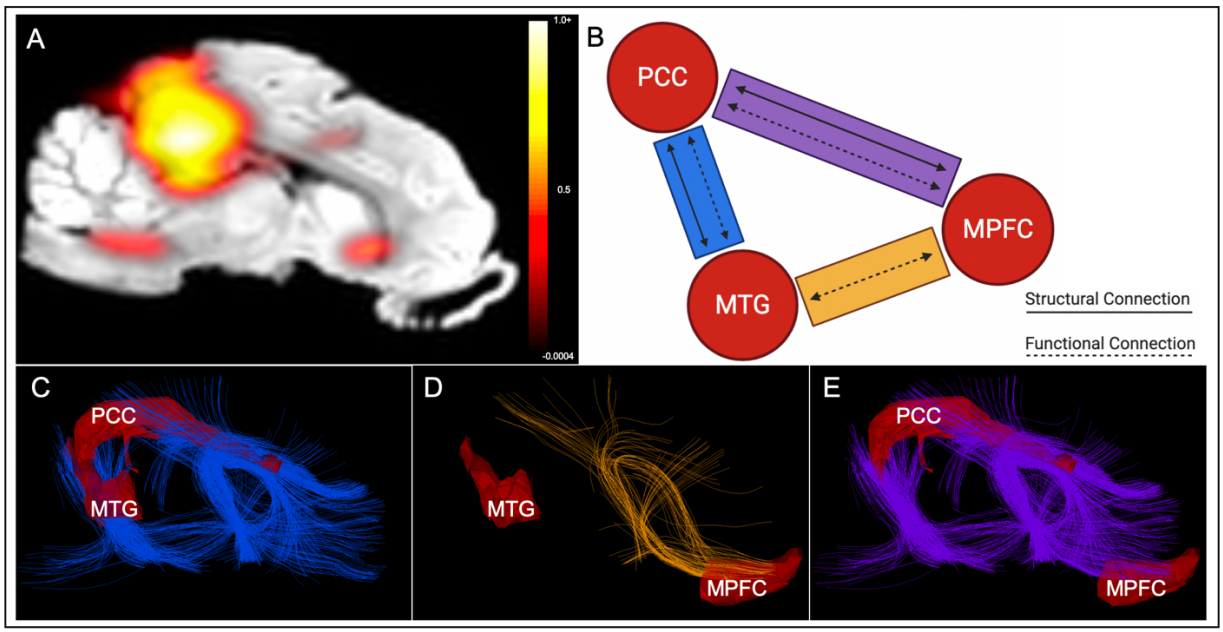

Figure 2.2: Functional and structural networks are interrelated. An activation map of functional connectivity in the default mode network (DMN) in a group of seven healthy porcine subjects (**A**). Schematic representation of the structural and functional connections between the three nodes of the DMN- posterior cingulate cortex (PCC), the middle temporal gyrus (MTG), and medial prefrontal cortex (MPFC) (**B**). DTI tractography of healthy porcine subjects demonstrating the presence of structural connections between the PCC and MTG (blue fibers) (**C**), the absence of structural connections between the MTG and the MPFC (orange fibers) (**D**), and the presence of structural connections between the PCC and the MPFC (purple fibers) (**E**).

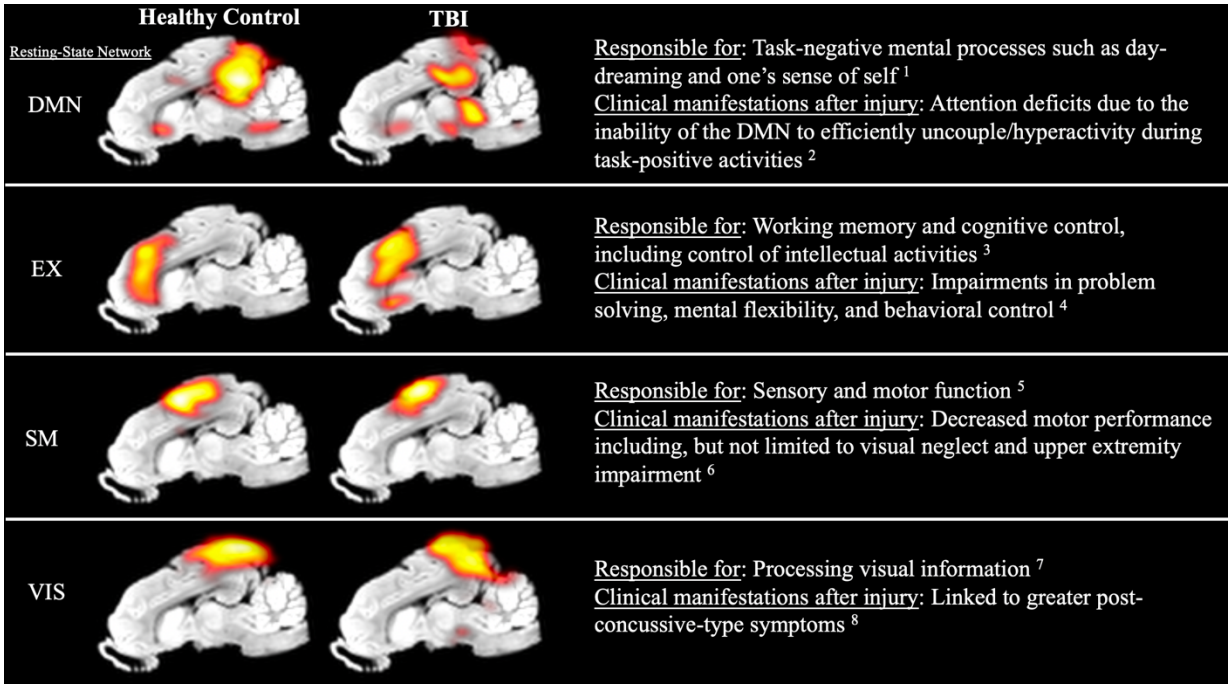

Figure 2.3: Functional network impairments following clinical TBI. The table describes each resting-state network's major function and the clinical manifestations after injury for the default mode network (DMN), executive control network (EX), sensorimotor network (SM), and visual network (VIS). The activation maps are derived from healthy control (left) and TBI (right) pigs during a resting-state functional magnetic resonance imaging (rs-fMRI) scan.

[1] Konrad et al. Hum Brain Mapp. 2010; Carhart-Harris et al. Brain. 2010.
[2] Mayer et al. Hum Brain Mapp. 2011; Palacios et al. J Neurotrauma. 2017; Johnson et al. Neuroimage. 2012.
[3] Seeley et al. J Neurosci. 2007.
[4] Lindsey et al. Front Neurol. 2019; Scheibel et al. Front Neurol. 2017; D'Souza et al. Front Neurol. 2019; Jenkins et al. Brain. 2016.
[5] Biswal et al. Magn Reson Med. 1995; Biswal, B.B., Neuroimage. 2012.
[6] Stephens et al. J Neurotrauma. 2017; Xu et al. PLoS One. 2014; Carter at al. Ann Neurol. 2010.
[7] Cuderiro and Sillito. Trends Neurosci. 2006.
[8] Stevens et al. Brain Imaging Behav. 2012.

CHAPTER 3

EXPLORING THE PREDICTIVE VALUE OF LESION TOPOLOGY ON MOTOR FUNCTION OUTCOMES IN A PORCINE ISCHEMIC STROKE MODEL[1]

---

[1]**Kelly M. Scheulin**†, Brian J. Jurgielewicz†, Samanatha E. Spellicy, Elizabeth S. Waters, Emily W. Baker, Holly A. Kinder, Gregory A. Simchick, Sydney E. Sneed, Janet A. Grimes, Qun Zhao, Steven L. Stice, Franklin D. West. 2021. *Scientific Reports*. 10.1038/s41598-021-83432-5. Reprinted here with permission of the publisher.

† these authors equally contributed to this work

Abstract

Harnessing the maximum diagnostic potential of magnetic resonance imaging (MRI) by including stroke lesion location in relation to specific structures that are associated with particular functions will likely increase the potential to predict functional deficit type, severity, and recovery in stroke patients. This exploratory study aims to identify key structures lesioned by a middle cerebral artery occlusion (MCAO) that impact stroke recovery and to strengthen the predictive capacity of neuroimaging techniques that characterize stroke outcomes in a translational porcine model. Clinically relevant MRI measures showed significant lesion volumes, midline shifts, and decreased white matter integrity post-MCAO. Using a pig brain atlas, damaged brain structures included the insular cortex, somatosensory cortices, temporal gyri, claustrum, and visual cortices, among others. MCAO resulted in severely impaired spatiotemporal gait parameters, decreased voluntary movement in open field testing, and higher modified Rankin Scale (mRS) scores at acute timepoints. Pearson correlation analyses at acute timepoints between standard MRI metrics (e.g., lesion volume) and functional outcomes displayed moderate R values to functional gait outcomes. Moreover, Pearson correlation analyses showed higher R values between functional gait deficits and increased lesioning of structures associated with motor function, such as the putamen, globus pallidus, and primary somatosensory cortex. This correlation analysis approach helped identify neuroanatomical structures predictive of stroke outcomes and may lead to the translation of this topological analysis approach from preclinical stroke assessment to a clinical biomarker.

Keywords: ischemic stroke, permanent middle cerebral artery occlusion, lesion topology, magnetic resonance imaging, porcine stroke model

Introduction

Middle cerebral artery occlusion (MCAO) is the most common cause of ischemic stroke and one of the leading causes of mortality and long-term disability worldwide [1]. Nearly half of survivors with large territory middle cerebral artery (MCA) strokes have permanent deficits and fail to regain functional independence [2]. Magnetic resonance imaging (MRI) is commonly used in clinical practice to evaluate stroke pathology, determine injury severity, and predict patient outcomes. However, standard MRI measures, such as lesion volume and midline shift, alone have limited prognostic value with respect to functional deficit type, severity, and recovery [3-8]. Including stroke lesion location in relation to specific structures that coordinate with functional tasks (e.g., a lesioned primary somatosensory cortex leads to loss of limb coordination in walking) is likely to increase the predictive power of acute MRI metrics as biomarkers of stroke outcomes [9].

The prognostic value of lesion volume, the most commonly used biomarker to assess stroke severity and predict patient outcomes, is only moderate for motor impairments [5]. The correlation between lesion volume and quality of life measurements, such as modified Rankin Scale (mRS), have also proven to be limited [3,4]. To ultimately strengthen the prognostic value of MRI, lesion location has been assessed using topographic maps and resulted in increased predictive power [6,10-18]. Using a voxel-based lesion mapping technique, infarcts in the corona radiata, internal capsule, and insula were associated with worse mRS scores in patients with an MCAO ischemic stroke [6]. Lesions in the insular ribbon, lentiform nuclei, and middle corona radiata resulted in poor recovery based on the National Institutes of Health Stroke Scale (NIHSS) scoring [18].

Additionally, regionalized infarction in the left basal ganglia and frontal lobe were negatively correlated with functional independence scores [1]. Overall, these findings indicate that lesion location is a key metric to determine an accurate prognosis of functional recovery post-stroke. Since discrepancies regarding lesion size and location in clinical stroke recovery exist as well as a void in viable translational models, the current study aims to characterize structures lesioned by an MCAO and evaluate their impact on stroke outcomes.

The Stroke Therapy Academic Industry Roundtable (STAIR) recommends using permanent occlusion gyrencephalic preclinical models, such as a porcine permanent MCAO model, and considering clinically relevant biomarkers, such as MRI detected lesion volume and location, to assess new treatments [19,20]. The pig model serves as a valuable large animal system to study the effects of MCAO on specific structures due to the comparable brain size and similar cerebral composition (e.g., gray to white matter ratio) between pigs and humans [21,22], and the ability to utilize a standardized porcine MRI brain atlas [23]. Critical brain structures present in the human and pig brain such as the hippocampus, caudate, and putamen are found in different locations, orientations, or absent in the rodent brain, the most commonly used stroke animal model [21,24-26]. For example, in the human and pig, the striatum is separated into two individual structures, the caudate nucleus and putamen, while the caudate nucleus and putamen are indistinguishable from each other in the rodent [27,28]. These unique differences in critical structures in the mouse brain relative to the human and pig brain are likely to have a profound effect on stroke outcomes. Our research group has developed a more translational porcine MCAO model that displays stroke pathophysiology comparable to

humans including lesioning, cytotoxic and vasogenic edema, and white matter damage as determined by MRI [29-33]. In addition, we have demonstrated that the porcine MCAO model displays behavioral and motor function deficits similar to human patients [34-37]. Building upon the unique strengths of the porcine MCAO model and initial advancements utilizing basic acute MRI measures to predict functional outcomes, we assessed the potential of lesion topology as an important MRI variable to advance functional prognostication.

In this exploratory study, we utilized MRI to evaluate acute clinical pathologies, including lesion volume and midline shift, and lesioning of individual brain structures to determine their potential in predicting chronic motor function outcomes in a porcine model of ischemic stroke. These findings suggest that including regional damage information in acute clinical evaluations of stroke patients is beneficial in determining acute motor deficits.

Results

MCAO resulted in lesioning, hemispheric swelling/atrophy, and decreased white matter integrity

To assess the dynamic pathophysiological response of an MCAO ischemic stroke, T2Weighted (T2W) MRI sequences were evaluated. Visual assessments of pre-MCAO pig brains showed no observable damage **(Figure 1a)**. At 1 day (d) post-MCAO, the MCAO group displayed substantial lesioning (hyperintense region, white arrows), a midline shift towards the unaffected contralateral hemisphere, and decreased ventricle size due to cerebral swelling **(Figure 1b)**. By 28d post-MCAO, animals showed a decrease in lesion size, a midline shift towards the ipsilateral hemisphere, and increased ventricle size due to tissue atrophy **(Figure 1c)**. Quantitative lesion volume analysis showed significant brain lesioning 1d post-MCAO with an average volume of 11.39±4.91 cm^3 and by 28d post-stroke, lesion volume size (4.22±2.12 cm^3) was significantly ($p=0.0010$) reduced **(Figure 1d)**. To account for potential animal variability, lesion volume was evaluated as a percent of the ipsilateral hemisphere. At 1d post-MCAO, the lesion occupied 32.64±12.99% of the ipsilateral hemisphere and by 28d post-MCAO, the lesion occupied 14.54±7.66% ($p=0.0004$) **(Figure 1e)**. In MCAO pigs, the ipsilateral hemisphere showed 1.57±0.83 mm midline shift towards the contralateral hemisphere at 1d post-MCAO, indicating hemispheric swelling and was different from normal ($p=0.0024$). At 28d post-MCAO, the ipsilateral hemisphere showed a midline shift of -1.99±1.00 mm away from the contralateral hemisphere (1d vs 28d post-MCAO, $p=0.0003$), indicating hemispheric atrophy and was different from normal ($p=0.0019$) **(Figure 1f)**. At 1d post-MCAO, animals showed hemispheric swelling with a

15.17±7.89% increase in ipsilateral hemisphere volume and was different from normal ($p=0.0022$). Cerebral atrophy was observed at 28d post-MCAO with a 10.41±3.63% decrease in ipsilateral hemisphere volume from 1d post-MCAO ($p<0.0001$) **(Figure 1g)** and was different from normal ($p<0.0001$).

Axial diffusion tensor imaging (DTI) images in pre-MCAO animals depict major white matter tracts from a medial slice of the pig brain and showed an intact ipsilateral (right side, white arrow) and contralateral (left) CC with fractional anisotropy (FA) values of 0.42±0.10 and 0.45±0.13, respectively ($p>0.05$) **(Supplementary Figure 2a, d)**. At 1d post-MCAO, the ipsilateral CC was disrupted and showed a significant ($p=0.0347$) decrease in FA (0.33±0.04) compared to the contralateral CC (0.47±0.12) **(Supplementary Figure 2b, e)**. The ipsilateral CC had recovered FA by 28d post-MCAO with ipsilateral FA of 0.39±0.10 and contralateral FA of 0.41±0.05 ($p>0.05$) (**Supplementary Figure 2c, f**). The corpus callosum (CC) is responsible for interhemispheric communications and, due to the location of the ischemic lesion, we found the CC to be impacted. The structural integrity of the CC after stroke has been shown to be repeatedly associated with motor deficits [38,39]. Overall, standard MRI analyses showed significant lesioning along with hemispheric swelling, subsequent atrophy, and decreased white matter integrity post-MCAO.

Ischemic lesioning spanned the thalamic nuclei, striatum, limbic system, and multiple Brodmann's areas

The ischemic lesion affected multiple major brain regions including the thalamic nuclei, striatum, limbic system, and various Brodmann's areas. A regional pixel analysis

was completed to calculate the percentage of each structure lesioned. The structures with the highest percentage of infarction (percent of structure, PoS) at 1d post-MCAO included the claustrum (65.91±29.68%), inferior temporal gyrus (62.15±27.67%), superior temporal gyrus (58.91±36.32%), insular cortex (54.45±31.35%), middle temporal gyrus (44.43±24.49%), putamen (44.00±22.23%), somatosensory association cortex (43.05±27.06%), secondary visual cortex (40.57±28.62%), globus pallidus (34.52±28.61%), and primary somatosensory cortex (33.48±23.73%) **(Figure 2a)**. At 28d post-MCAO, the structures with the highest level of lesioning included the middle temporal gyrus (39.84±31.80%), superior temporal gyrus (31.14±17.55%), inferior temporal gyrus (18.19±13.55%), somatosensory association cortex (16.78±11.46%), insular cortex (15.95±9.28%), associative visual cortex (10.02±14.48%), primary somatosensory cortex (8.44±8.92%), prepiriform area (7.84±5.85%), fusiform gyrus (6.82±10.44%), and secondary visual cortex (5.83±6.30%) **(Figure 2b)**. The percent of the identified lesion (PoL) in each structure was quantified to represent the percent of the lesion that affected specific brain structures and characterized stroke location. At 1d post-MCAO, the structures that occupied the lesion included the insular cortex (8.45±5.09%), primary somatosensory cortex (6.33±4.82%), secondary visual cortex (6.02±4.34%), inferior temporal gyrus (5.16±4.65%), somatosensory association cortex (4.98±2.87%), putamen (3.22±1.58%), middle temporal gyrus (2.59±2.97%), superior temporal gyrus (2.36±1.68%), parahippocampal cortex (2.06±3.00%), claustrum (1.94±0.71%), prepiriform area (1.44±0.61%), amygdala (1.23±1.95%), and primary visual cortex (1.08±1.36%) **(Supplementary Figure 3a)**. By 28d post-MCAO, PoL structures that

occupied the lesion included the insular cortex (7.95±6.02%), primary somatosensory cortex (5.64±6.36%), somatosensory association cortex (5.41±3.59%), middle temporal gyrus (4.23±3.01%), inferior temporal gyrus (3.27±2.72%), superior temporal gyrus (3.15±1.87%), secondary visual cortex (2.07±1.93%), parahippocampal cortex (1.42±2.34%), and prepiriform area (1.30±1.06%) **(Supplementary Figure 3b)**. A complete list of lesioned structures (PoS and PoL) (Mean ± standard deviation (SD)) are detailed in **Supplementary Table 1**. Notably, 100% of pigs had lesioning in the claustrum, putamen, insular cortex, secondary visual cortex, inferior temporal gyrus, superior temporal gyrus, parahippocampal cortex, and prepiriform area **(Table 1)**.

MCAO induced functional gait deficits

To assess changes in motor function, gait analysis was performed on all animals pre-MCAO to establish a baseline and collected over a 27-day period following MCAO. Compiled functional outcome (gait and behavior) parameters definitions that were analyzed in this study can be found in **Supplementary Table 2**. The MCAO group showed significant decreases in the left front (LF) limb (contralateral to MCAO) at 2d post-MCAO in velocity (**Figure 3a**; Pre: 198.78±13.24 cm/s vs. Day 2: 71.49±44.22 cm/s, p=0.0048) and cadence (**Figure 3a**; Pre: 133.01±8.23 stride/min vs. Day 2: 69.78±24.61 stride/min, p=0.0081) as compared to pre-MCAO. In addition, there were significant decreases at 2d post-MCAO in the LF limb in stride length (**Figure 3b**; Pre: 89.01±3.42 cm vs. Day 2: 57.98±10.96 cm, p=0.0042), step length (**Figure 3b**; Pre: 44.36±2.05 cm vs. Day 2: 29.65±5.00 cm, p=0.0031), and swing percent (**Figure 3c**; Pre:

51.93±2.47% vs. Day 2: 31.45±6.14%, p=0.0034), along with an increase in stance percent (**Figure 3c**; Pre: 48.06±2.49% vs. Day 2: 68.55±6.12%, p=0.0034) relative to pre-MCAO. Velocity (**Figure 3a**; Day 8: 114.77±48.21 cm/s, p=0.0168), cadence (**Figure 3a**; Day 8: 90.03±27.37 stride/min, p=0.0247), stride length (**Figure 3b**; Day 8: 73.29±10.29 cm, p=0.0289), step length (**Figure 3b**; Day 8: 36.96±5.39 cm, p=0.0324), swing percent (**Figure 3c**; Day 8: 38.98±5.53%, p=0.0104), and stance percent (**Figure 3c**; Day 8: 61.03±5.52%, p=0.0104) continued to display deficits at 8d post-MCAO. No significant ($p>0.05$) differences between the MCAO and non-stroked groups were measured pre-MCAO. Non-stroked pigs did not have any significant differences at any measured timepoints (**Figure 3**). Stroked animals exhibited signs of recovery after 8d post-MCAO, showing no significant changes in measured parameters to non-stroked animals or pre-stroke values ($p>0.05$). Gait parameters for the other three limbs, right front (RF), left hind (LH), and right hind (RH), are detailed in **Supplementary Figure 4**.

MCAO induced contralateral limb weakness

Changes in weight distribution in all four limbs due to stroke was evaluated by assessing deviations in total pressure index for each individual limb. Total pressure index is the sum of peak pressure values recorded from each activated sensor by a hoof during contact and is representative of weight distribution. The MCAO group showed a significant decrease in total pressure index at 2d post-MCAO in the LF limb (**Supplementary Figure 5a**; Pre: 28.99±1.66 vs. Day 2: 26.87±2.07, p=0.0224) with a corresponding increase in pressure in the RF limb (**Supplementary Figure 5b**; Pre:

29.57±1.95 vs. Day 2: 31.87±2.30, p=0.0413). By 8d post-MCAO, total pressure index showed no significant changes in measured parameters compared to pre-MCAO in the LF limb (**Supplementary Figure 5a**; Pre: 28.99±1.66 vs. Day 8: 27.96±1.45, p=0.1076) and the RF limb (**Supplementary Figure 5b**; Pre: 29.57±1.95 vs. Day 8: 29.65±1.78, p=0.9999). LH and RH limb total pressure indices did not change significantly compared to pre-MCAO (**Supplementary Figure 5c-d;** p>0.05). However, these results were expected in the pig model, as the forelimbs carried 60% of the body weight and, thus, are more susceptible to disruptions in weight distribution. Collectively, gait analysis provided quantifiable parameters showing functional gait deficits in weight distribution induced by MCAO.

MCAO pigs showed deficits in voluntary movement and behavioral scores

Open field testing was performed to assess behavioral changes post-stroke. Representative tracking images displayed decreased voluntary movement at 2d post-MCAO **(Figure 4a)**. At 2d post-MCAO, the MCAO group showed a significant decrease in distance traveled (**Figure 4b**; Non-stroked: 75.70±23.86 m vs. MCAO: 27.83±13.80 m, p=0.0346), movement duration (**Figure 4c**; Non-stroked: 230.55±38.87 s vs. MCAO: 85.87±49.84 s, p=0.0022), and velocity (**Figure 4d**; Non-stroked: 0.13±0.04 m/s vs. MCAO: 0.05±0.02 m/s, p=0.0350) compared to the non-stroked group. By 8d post-MCAO, there were no significant differences between groups (p>0.05).

A pig mRS assessment was used to evaluate the degree of disability pre- and post-MCAO with 0 being no residual stroke symptoms and 6 being death **(Supplementary**

Figure 6). At all timepoints non-stroked animals had an mRS score of 0. At 4 hours (h) to 3d post-MCAO, stroked animals had mean mRS scores above 3 (ranging from 2-5) and were significantly impaired relative to non-stroked animals (4h post-MCAO: 4.86±0.38, $p<0.0001$; 8h post-MCAO: 4.57±0.79, $p<0.0001$; 12h post-MCAO: 3.71±0.76, $p=0.0002$; 16h post-MCAO: 3.71±0.95, $p=0.0007$; 20h post-MCAO: 3.57±0.98, $p=0.001$; 24h post-MCAO: 3.57±0.79, $p=0.0003$; 2d post-MCAO: 3.43±0.98, $p=0.0013$; 3d post-MCAO: 3.29±0.76, $p=0.0004$). At 4d (2.57±1.13, $p=0.0144$), 6d (1.71±0.95, $p=0.0455$) and 8d (1.57±0.79, $p=0.0275$) post-MCAO, stroked animals still had a significantly greater mRS score than non-stroked controls suggesting persistent deficits. After 8d post-MCAO, scores trended between 0-2 and displayed no significant differences from normal animals ($p>0.05$) suggesting overall recovery.

Location of stroke lesion in structures associated with motor coordination had prognostic value when evaluating motor functional outcomes

Development of an accurate prognosis method by identification of acute parameters is vital to assess efficacy of novel treatments in preclinical models. Thus, correlation analyses were performed to determine unique relationships between individual lesioned brain structures at 1d post-MCAO and functional gait outcomes at 2d and 8d post-MCAO. Lesioned structures ranked by PoS (y-axis) and top gait outcomes (x-axis) were evaluated by Pearson correlations for 2d post-MCAO (**Figure 5a**) and 8d post-MCAO (**Figure 5b**). R values were reported with cell color indicating correlation direction and strength. FDR p-values corrected for multiple comparisons can be found in

Supplementary Table 3. In general, structures associated with motor coordination and function had higher R values when using PoS as the quantitative indicator. This suggests that identification of lesion topology, specifically the percentage of structure with an ischemic lesion, can be used as a predictive biomarker for functional outcomes.

Further, commonly used MRI parameters including lesion volume, midline shift, and hemispheric swelling were evaluated for their potential to predict 6 gait functional outcomes **(Figure 5)**. Pearson correlation analyses were also conducted at 2d and 8d post-MCAO between canonical MRI metrics and functional gait outcomes. For 1d post-MCAO MRI parameters (y-axis) and top gait outcomes (x-axis) were evaluated by Pearson correlations for 2d post-MCAO (**Figure 5c**) and 8d post-MCAO (**Figure 5d**). R values were reported with cell color indicating correlation direction and strength. FDR p-values corrected for multiple comparisons can be found in **Supplementary Table 3**. Traditional MRI diagnostic parameters showed moderate prognostic value in this preclinical model. However, the inclusion of lesion topology may further advance the relationship between individual structures and functional outcomes.

Discussion

MRI assessment of stroke severity and injury characteristics has significant clinical potential to better predict functional outcomes. However, standard clinical practice typically relies on basic injury metrics such as lesion volume and midline shift and does not account for injury location [6,14,40-42]. Since brain functions such as motor and executive control are highly regionalized to specific brain structures, it is logical that consideration of injury location would have a profound effect on clinical prognoses [6]. In this exploratory study, we demonstrated that the canonical MRI metrics (e.g., lesion volume, lesion percent, midline shift, and hemispheric swelling) were predictive of functional deficits. However, we showed that specific lesioned brain structures responsible for motor coordination and function (e.g., putamen, globus pallidus, and primary somatosensory cortex) demonstrated higher R values (R= |0.58| to |0.81|) to motor function deficits than canonical MRI metrics (R= |0.30 to |0.69|). The results from this exploratory study showed that lesion topology analysis may be a stronger predictor of functional outcomes at acute timepoints after ischemic stroke when the structures lesioned involve motor coordination and function. However, additional studies are needed with increased animal numbers to confirm this finding. In recent studies, our team has shown the pig MCAO model displays significant similarities to human stroke patients with respect to functional deficits [29-32,34,37,43]. For the first time in a neural injury porcine model, we have adapted an MRI pig atlas [23] to account for stroke induced structural changes and demonstrated that the effected MCA territory and brain structures are also comparable to humans, which likely explains the similarities in functional outcomes [44,45]. These results further support the pig as a translational large animal model for the study of

ischemic stroke pathophysiology, development of prognostic biomarkers, and therapeutic interventions.

The MCA is one of the largest arteries in the brain with the highest incidence of occlusion causing ischemic stroke in humans [1,44]. Anatomically, the MCA provides vascular support to a large territory including the lateral inferior frontal lobe, superior temporal gyrus, primary motor and somatosensory cortices, basal ganglia structures, internal capsule, and insular cortex, among others [1,2,44]. Thus, the blockage of this artery by an embolus or thrombus leading to an ischemic stroke can be particularly detrimental causing behavioral and gait deficits [18]. Clinically, an MCAO stroke lesion typically spans parts of the frontal, temporal, and parietal lobes, including the insular cortex, as well as deep brain structures such as the amygdala, caudate nucleus, putamen, globus pallidus, and thalamic nuclei [6,14-18,45-47]. In pigs, we found MCAO resulted in the highest percent of lesion in the insular cortex, somatosensory cortices, temporal gyri, and visual cortices. In a thromboembolic MCAO cynomolgus monkey model, infarction was similarly observed in the basal ganglion, internal capsule, temporal cortex, and insular cortex and it was noted that contralateral hemiparesis in their model was likely caused by ischemia in the temporal cortex and internal capsule [48]. Although the MCA stroke territory depends on the individual differences of MCA branching, our model showed a high level of reproducibility with respect to infarct location. 100% of the pigs showed lesioning in the claustrum, inferior temporal gyrus, insular cortex, parahippocampal cortex, putamen, prepiriform area, secondary visual cortex, and superior temporal gyrus. Thus, we have identified consistent and reproducible lesion locations that can aid in the understanding of

the pathophysiology of stroke progression and provide a framework for assessing the importance of lesion location on functional outcomes.

Gait and behavior analyses have been used as clinical biomarkers to quantify stroke severity, functional deficits, and subsequent recovery potential. Consistent with human manifestations where patients have decreased cadence and walk six times slower than aged matched pairs [35], the porcine MCAO group showed similar deficits in cadence and velocity [35,36]. Humans display other spatiotemporal abnormalities including a decreased stride length, increased cycle time, and increased stance time [49], which have consistently manifested in the porcine model [30,32,37]. Asymmetrical hemiplegic gait is commonly induced by stroke and results in a shifting of weight between limbs and subsequent decreased propulsion, where the contralateral limb assumes significantly less weight and decreased pressure [36]. Here, stroked pigs showed asymmetrical hemiplegic gait with a decreased total pressure index in the contralateral limb. As seen in the open field test and mRS scoring, MCAO pigs displayed deficits similar to those of stroke patients, including decreased voluntary movement and velocity, with overall behavioral deficits [50,51]. These impairments are typically a result of infarction to the motor and somatosensory cortices, and subcortical structures [50], similar to the regions injured in our pig model. Manifestation of clinically relevant gait deficits in the porcine model suggests that this model may be useful in understanding post-stroke functional deficits and recovery patterns.

Recent clinical retrospective analyses assessing the prognostic capacity of early MRI stroke injury parameters indicate lesion location can be highly predictive of functional outcomes, whereas lesion volume alone is only moderately predictive [4,12-

[14,17,52]. In fact, a voxel-based lesion mapping approach showed location, independent of lesion volume, is predictive of higher NIHSS scores at admission and discharge [18]. Here, regional lesion location showed higher R values to acute functional outcomes in brain regions responsible for motor function, including the putamen, globus pallidus, and primary somatosensory cortex, at 2d post-MCAO compared to brain regions that are not responsible for motor coordination but still highly effected by the stroke lesion, including the claustrum, superior and middle temporal gyri, and secondary visual cortex. The structures impacted that presented higher correlations to gait outcomes are directly involved with motor and executive control and therefore it is expected that they would influence gait deficits 2d post-MCAO [53-55]. For example, effected structures, such as the globus pallidus (a critical regulatory structure of voluntary movement [56]), were predictive of early functional outcomes such as velocity with an R value of -0.76 at 2d post-MCAO, whereas lesion volume only had an R value of -0.37. In addition, the insular cortex, which is sensitive to hypoperfusion [47], has a high likelihood of infarct growth [10], and is associated with functional deficits [46], was affected in 100% of pigs at 1d post-MCAO and was the largest PoL structure effected. The insular cortex also displayed moderate correlation relationships between PoS and gait impairments (R=|0.37| to |0.56|). In a large clinical study, MCA strokes resulted in higher disability with the lowest functional independence measure (FIM), a functional assessment that consists of 13 motor and 5 cognitive metrics, compared to other territory strokes [57]. These findings support strong correlations between MCA territory lesioning of structures involved in motor coordination and motor deficits. Many clinical studies often examine the correlation between MRI based structural changes and one or two functional scales, such as mRS or

NIHSS scores [7,18,57-59], while our study evaluated the relationship between multiple major gait parameters acquired on the sensitive GAITFour mat and the highly lesioned structures in our porcine model. Here, we found that ischemic infarcts in the putamen, globus pallidus, and primary somatosensory cortex were associated with higher R values to motor functional deficits (R>|0.5|). A voxel-based lesion symptom mapping approach in humans determined infarcts within the area leading from the corticospinal tract to cortical motor areas, including fibers from the primary somatosensory cortex and other secondary motor regions, were critical for maintaining proper hand motor performance after a stroke [60]. We were encouraged to discover similar relationships between major structures responsible for motor function and functional gait outcomes in our pig model.

However, a number of limitations were associated with this exploratory study including the lack of significance in our correlation analyses, although it is likely a function of small sample size (**Supplementary Table 3**). Additionally, correlations between MRI and motor function at 8d post-MCAO were reduced relative to 2d post-MCAO. This may be a result of spontaneous recovery observed in functional outcomes 8d post-MCAO, even though significant differences still remained between stroked and non-stroked animals. A general shortcoming of the topological analysis approach is each structure should be considered individually based on its function and associated outcomes. This adds an increased level of complexity with the evaluator needing to be well versed in the function of each structure and making it less practical as a clinical prognostic tool. A benefit of the traditional MRI analysis approaches (e.g., lesion volume, midline shift, and swelling) is the ease of clinical use with no neuroanatomical key of functional information. Furthermore, in both animal stroke models and clinical patients,

MRI image registration to neuroanatomical atlases are often imperfect due to hemispheric swelling and atrophy. In our pig model, registration of larger structures demonstrated an acceptable level of atlas registration fidelity, while there was decreased accuracy in the registration of smaller structures such as the contralateral ventricle and small white matter structures. These potential inconsistencies represent an unmet need in the preclinical and clinical settings to improve atlas registration techniques accounting for swelling, midline shifts, and other commonly observed stroke pathologies. The rodent community has made strides to account for registration errors including the development of an enhanced mathematical framework to correct for edema in evaluating lesion size leading to improved image analysis [61]. Future studies utilizing the pig stroke model should build upon these advances to improve registration. Despite these limitations, the topological approach utilized in this study has helped identify lesioned structures involved in motor function related to stroke outcomes and supports the clinical use of this methodology. Further in-depth studies with larger cohorts are warranted to generate more conclusive preclinical data.

In this exploratory study utilizing the Yucatan pig MCAO model, we demonstrated that evaluating lesioning in specific brain structures demonstrated moderate-to-strong relationships with motor function impairments as compared to lesion volume and other commonly assessed clinical MRI stroke metrics at acute timepoints. The lesioned MCAO territory in the pig model was anatomically similar to human ischemic stroke patients and resulted in comparable functional outcomes, supporting the pig as a robust ischemic stroke model. It is important to note that other key elements such as functional and structural connectivity may also be critical components in predicting

functional outcomes and should be further explored in future studies [62-64]. Nevertheless, using stroke location to improve outcome prediction is rapidly evolving in clinical practice. Currently, the use of stroke location to predict functional outcomes is under assessed in animal models that tend to report traditional metrics such as lesion volumes and midline shifts. Increased frequency of the identification of stroke lesion topology correlated to functional outcomes in preclinical animal models may lead to greater clinical translatability. Improving the accuracy and precision of clinical prognoses is critically important in evidence-based clinical decision-making after stroke to improve acute patient care, develop long-term treatment plans (e.g., rehabilitation programs), and determine required living assistance needs. The findings of this study support the premise of including a structural injury component in acute MRI assessment to improve clinical prognostication.

Materials and Methods

Study design

All work involving the use of animals in this study were performed in accordance with the National Institutes of Health (NIH) Guidelines for the Care and Use of Laboratory Animals and was reviewed and approved by the University of Georgia (UGA) Institutional Animal Care and Use Committee (IACUC; Protocol Number A2018 01-029-Y1-A5). Inclusion criteria established a priori indicated that all castrated/ovariectomized, healthy animals with no lameness would be included. Researchers would exclude an animal if any signs of illness or lameness presented. All animals were included in the study and the experiments have been reported following/in compliance with the Animal Research: Reporting in Vivo Experiments (ARRIVE) guidelines. Biomedical Yucatan miniature pigs were acquired from Exemplar Genetics (Sioux Center, IA) and individually housed. Sexually mature castrated male and ovariectomized (OVX) female Yucatan miniature pigs between 68-98 kg and between 1-2 years of age were randomly assigned to either stroke (MCAO, n = 7) or non-stroked normal control (non-stroked, n = 5) groups. Sex hormones (e.g., testosterone and estrogen) have a confounding effect as they are neuroprotective [65-67]. This challenge is compounded in female animals where phases of the reproductive cycle increase and decrease estrogen levels, thus leading to constantly changing neuroprotective levels in animals. Additionally, strokes typically occur in older women, post-menopause [68]. For uniformity, males were castrated, and females were OVX. All functional analysis was performed blinded with animal

identifiers removed. The sample size for this study was determined by a power calculation based on our previous porcine MCAO studies [29,32].

Middle cerebral artery occlusion

One day prior to surgery, pigs were administered antibiotics (Ceftiofur crystalline free acid; 5mg/kg intramuscular (IM); Zoetis). A right sided permanent MCAO was performed on all stroke animals as described in Platt, et al. [69]. Pre-induction analgesia and sedation was achieved using xylazine (4 mg/kg IM; VetOne), midazolam (0.3 mg/kg IM; Heritage), methadone (0.2 mg/kg IM; Henry Schein Animal Health). Anesthesia was induced with propofol (to effect, intravenous (IV); Zoetis) and prophylactic lidocaine (1.0 mL 2% lidocaine; VetOne) was applied to the laryngeal folds to facilitate intubation. Anesthesia was maintained with isoflurane (1.0 – 2.0%; Abbott Laboratories) in oxygen.

Briefly, the middle cerebral artery (MCA) was accessed by performing a frontotemporal craniectomy with orbital rim ostectomy, zygomatic arch resection, and temporal fascia and muscle incision. The MCA was permanently occluded utilizing bipolar electrocautery forceps at the location distal to the origin of the Circle of Willis, resulting in ischemic infarction. The exposed brain was covered with a sterile oxidized cellulose hemostatic agent (VetSpon). Following occlusion, the temporalis muscle and epidermis were routinely re-apposed. After surgery, anesthesia was discontinued, pigs were returned to their pens and underwent standard monitoring and pain management. To treat and manage post-operative inflammation and pain, MCAO pigs received banamine (2.2 mg/kg IM or IV; Merck) during MCAO surgery and every 12 hours for 24 hours and every 24 hours for 3 days following surgery and methadone (0.2 mg/kg IM or IV) every 6

hours for 24 hours following surgery. Non-stroked normal animals did not undergo surgery.

Magnetic resonance imaging data acquisition

MRI was acquired on a GE Signa HDx 3.0 Tesla scanner using an 8-channel torso coil at 1d and 28d post-MCAO. Under general anesthesia, MRI of the brain was performed with the animal positioned in supine recumbency. The multiplanar MRI protocol included five sequences: 1) 3D Fast SPoiled GRadient echo (FSPGR) T1-Weighted (T1W), 2) Fast Spin Echo (FSE) T2W, 3) T2-Weighted Fluid Attenuated Inversion Recovery (T2FLAIR), 4) Spin Echo (SE) Diffusion Weighted Imaging (DWI), and 5) SE DTI.

Ischemic stroke was confirmed 1d post-MCAO by comparing the hyperintense infarction in T2FLAIR and DWI to the corresponding hypointense region in apparent diffusion coefficient (ADC) maps, indicating cytotoxic edema (data not shown). Axial 3D FSPGR sequences were acquired with the following parameters: inversion time (TI) = 450 ms, flip angle = 20°, slice thickness = 1.0 mm, field of view (FOV) = 19.8 cm^3, and matrix size (frequency x phase) = 198 x 198. Axial and coronal FSE T2W images were acquired with the following parameters: repetition time (TR) = 6260 ms, echo time (TE) = 124 ms, slice thickness = 3.0 mm, FOV = 18-20 cm^2, and matrix size (frequency x phase) = 384 x 288. Axial T2FLAIR images were acquired with the following parameters: TR = 9070 ms, TE =120 ms, TI = 2587 ms, slice thickness = 3.0 mm, FOV = 20 mm^2, and matrix size (frequency x phase) = 320 x 224. Axial DWI was acquired with the following parameters: b = 0 and 1000, TR = 6000 ms, number of excitation (NEX) =

4, slice thickness = 3.0 mm, FOV = 26.6 cm^2, matrix size (frequency x phase) = 256 x 256 with 3 diffusion directions. In order to obtain information on white matter integrity, DTI was acquired in the axial plane with the following parameters: TR = 10,000 ms, isotropic voxel = 2.0 mm x 2.0mm x 2.0mm, with 30 diffusion encoding directions; fractional anisotropy (FA) maps were generated from DTI images as described below. During DTI acquisition, an error occurred when acquiring the DTI sequence of one MCAO animal, therefore, this animal was excluded from FA analysis.

Magnetic resonance imaging data preprocessing

DICOM images of the T1W and T2W volumetric series were converted into NIfTI (Neuroimaging Informatics Technology Initiative) format using the "dcm2niix" tool [70]. Brain masks were obtained by separating brain tissue from the skull and other surrounding tissues using the FSL brain extraction tool (BET) and then manually refining slice-by-slice the generated FSL-BET masks in 3D Slicer version 4 (slicer.org, [71]). Lesion masks were manually drawn in 3D Slicer using the axial T2W images to identify the hyperintense region associated with the lesion after applying an inversion filter to remove bias in lesion identification **(Supplementary Figure 1)**.

The porcine brain atlas [23] was then spatially normalized to each stroked pig's masked T1W image (note that each stroked pig's T2W image is in the same space as its T1W image). First, a spatial transformation was calculated between the pig brain atlas' associated T1W anatomical image, which is in the same space as the atlas, and each pig's masked T1W image using the Old Normalize Statistical Parametric Mapping algorithm (SPM12, Institute of Neurology, University College London) [72]. Then the calculated

spatial transformation was applied to the atlas. Spatial transformations consisted of a 12-parameter affine transformation, followed by a nonlinear deformation transformation in stereotaxic coordinates [73,74].

Magnetic resonance imaging data analysis

Lesion and hemispheric volumes were analyzed using OsiriX software (Version 10.0.5, Pixmeo SARL, Bernex, Switzerland) at default thresholds from T2W sequences. Hemisphere and lateral ventricle volumes were calculated for each slice using manual segmentation of the ipsilateral and contralateral hemispheres to find the area and multiplying by the slice thickness (3.0 mm). The lateral ventricle volumes were subtracted from each hemisphere to eliminate non-brain tissue. The cerebellum was not included in hemispheric volume analysis.

The percentage of the ipsilateral hemisphere that the lesion occupied was calculated as a sum of the lesion volume per slice (multiplied by slice thickness, 3.0 mm) divided by the total ipsilateral hemispheric volume.

Hemispheric swelling and atrophy were calculated using the total ipsilateral hemisphere volume divided by the contralateral hemisphere volume, which is reported as a percentage change.

Midline shift analysis was also analyzed using OsiriX according to a previous publication [34]. Briefly, three linear measurements were utilized to determine the midline after stroke at 1d and 28d post-stroke using the axial T2W images for each pig. The first line was drawn at the septum pellucidum in between the lateral ventricles. The next line drawn was the ideal midline using boney structures and non-brain anatomy to determine

the natural midline (red lines in **Figure 1**). The midline shift was determined by drawing and measuring a third perpendicular line between the ideal midline and septum pellucidum.

DTI was used to evaluate white matter integrity in the corpus callosum (CC) through FA analysis. FA maps were generated using the FMRIB's Diffusion Toolbox (FDT) (FSL, University of Oxford, UK) [75-77], and FA values of the CC were measured using ImageJ, FIJI [78,79] to manually segment each major white matter tract in the ipsilateral and contralateral hemispheres. To account for hemispheric swelling and atrophy, the ipsilateral ROI was manipulated to encompass as much of the remaining visible structure possible without changing the area of the ROI.

Using the co-registered lesion masks and porcine brain atlas [23], percentage of structure (PoS) and percentage of lesion (PoL) were calculated using MatLab (R2018b, The Mathworks, Inc.) to determine the percentage of each individual structure affected by the lesion and the percentage of the lesion that overlaps with individual brain atlas structures, respectively.

$$\text{PoS} = \frac{Number\ of\ pixels\ in\ the\ identified\ lesion\ that\ overlap\ with\ structure\ X}{Total\ number\ of\ pixels\ within\ structure\ X}$$

$$\text{PoL} = \frac{Number\ of\ pixels\ in\ the\ identified\ lesion\ that\ overlap\ with\ structure\ X}{Total\ number\ of\ pixels\ within\ the\ lesion}$$

T1W images were used to generate figures. The pig brain atlas contained 178 individual cerebral structures, including 42 paired and 9 single deep brain structures, 5 ventricular system areas, 6 paired deep cerebellar nuclei, 12 cerebellar lobules, and 28 cortical areas per hemisphere [23].

Gait data collection

Gait analysis was performed utilizing the GAITFour walkway system as previously described [32] and assessed using GAITFour software (Version 4.9 x 5, CIR Systems, Franklin, NJ) . Pre-MCAO gait data was collected on 3 separate days (d) for each pig. After stroke surgery, gait analysis was performed on 2d, 8d, 15d, and 27d post-MCAO. Gait collection occurred for a maximum of 15 minutes at each collection time point for each pig. Five recordings of the pig traversing the track at a consistent trotting gait was used for analysis.

Behavior data collection

Open field testing was performed for all pigs pre-MCAO and on 2d, 8d, 15d, and 27d post-MCAO. Behavior tests were recorded using EthoVision XT software (Version 11.5, Noldus Systems, Wageningen, Netherlands) as described previously [32]. Briefly, individual pigs were placed in a 2.7 x 2.7 m open field arena for 10 minutes and allowed to voluntarily explore. EthoVision was used to track movement duration, velocity, and distance traveled and also to preform data analysis.

Modified Rankin Scale scoring

Neurological disability was assessed post-MCAO using a pig-adapted Modified Rankin Scale (mRS) as previous published [34]. All pigs were assessed 1 day prior to MCAO surgery and 4 hours (h), 8h, 12h, 16h, 20h, 24h, 2d, 3d, 4d, 5d, 6d, 8d, 15d, and 27d post-MCAO surgery. Possible scores ranged from 0 (no residual stroke symptoms) to 6 (death due to stroke).

Statistical analysis

GraphPad Prism 8 (Version 8.4.0; San Diego, CA) was utilized to calculate the statistics. Statistical differences in MRI parameters were evaluated using paired t tests between 1d and 28d post-MCAO. White matter integrity was evaluated between the left and right CC with paired t tests at pre-MCAO, 1d and 28d post-MCAO. To determine if MLS and hemispheric swelling/atrophy were statistically different from normal at each timepoint, one-sample t tests were performed with a hypothetical value of 0 for MLS and 100 for hemispheric changes, statistical significance was indicated by $. For longitudinal analyses of gait and behavior, 2-way repeated measures ANOVA were conducted with Sidak's multiple comparisons test when appropriate. All error bars represented SD. Pearson correlations were evaluated at 2d and 8d post-MCAO for the 6 gait parameters reported in the manuscript to determine the association between percent of lesioned structure (top reported PoS) and canonical MRI metrics (lesion volume, lesion percent, midline shift, and hemispheric swelling) to motor impairments. A minimum of three pigs had to have a lesion within the individual structure to conduct each correlation analysis. From here, R values were reported in a heat map and the False Discovery Rate (FDR) corrected p-values were reported in **Supplementary Table 3**. QQ plots of the residuals were generated to assess normality. Data are shown as mean±SD. Statistical significance was indicated where * (or # or $) signified $p<0.05$; ** (or ## or $$) signified $p<0.01$; *** (### or $$$) signified $p<0.001$; and **** (or #### or $$$$) signified $p<0.0001$.

References

1 Lin, C., Chatterjee, N., Lee, J., Harvey, R. & Prabhakaran, S. Predictive value of the combination of lesion location and volume of ischemic infarction with rehabilitation outcomes. *Neuroradiology* **61**, 1131-1136, doi:10.1007/s00234-019-02234-9 (2019).

2 Walcott, B. P. *et al.* Outcomes in severe middle cerebral artery ischemic stroke. *Neurocrit Care* **21**, 20-26, doi:10.1007/s12028-013-9838-x (2014).

3 Lovblad, K. O. *et al.* Ischemic lesion volumes in acute stroke by diffusion-weighted magnetic resonance imaging correlate with clinical outcome. *Ann Neurol* **42**, 164-170, doi:10.1002/ana.410420206 (1997).

4 Schiemanck, S. K. *et al.* Ischemic lesion volume correlates with long-term functional outcome and quality of life of middle cerebral artery stroke survivors. *Restor Neurol Neurosci* **23**, 257-263 (2005).

5 Schiemanck, S. K., Post, M. W., Witkamp, T. D., Kappelle, L. J. & Prevo, A. J. Relationship between ischemic lesion volume and functional status in the 2nd week after middle cerebral artery stroke. *Neurorehabil Neural Repair* **19**, 133-138, doi:10.1177/154596830501900207 (2005).

6 Cheng, B. *et al.* Influence of stroke infarct location on functional outcome measured by the modified rankin scale. *Stroke* **45**, 1695-1702, doi:10.1161/STROKEAHA.114.005152 (2014).

7 Ernst, M. *et al.* Association of Computed Tomography Ischemic Lesion Location With Functional Outcome in Acute Large Vessel Occlusion Ischemic Stroke. *Stroke* **48**, 2426-2433, doi:10.1161/STROKEAHA.117.017513 (2017).

8 Vora, N. A. *et al.* A 5-item scale to predict stroke outcome after cortical middle cerebral artery territory infarction: validation from results of the Diffusion and Perfusion Imaging Evaluation for Understanding Stroke Evolution (DEFUSE) Study. *Stroke* **42**, 645-649, doi:10.1161/STROKEAHA.110.596312 (2011).

9 Borich, M. R., Brodie, S. M., Gray, W. A., Ionta, S. & Boyd, L. A. Understanding the role of the primary somatosensory cortex: Opportunities for rehabilitation. *Neuropsychologia* **79**, 246-255, doi:10.1016/j.neuropsychologia.2015.07.007 (2015).

10 Cheng, B. *et al.* Dynamics of regional distribution of ischemic lesions in middle cerebral artery trunk occlusion relates to collateral circulation. *J Cereb Blood Flow Metab* **31**, 36-40, doi:10.1038/jcbfm.2010.185 (2011).

11 Phan, T. G., Fong, A. C., Donnan, G. A., Srikanth, V. & Reutens, D. C. Digital probabilistic atlas of the border region between the middle and posterior cerebral arteries. *Cerebrovasc Dis* **27**, 529-536, doi:10.1159/000214215 (2009).

12 Menezes, N. M. *et al.* The real estate factor: quantifying the impact of infarct location on stroke severity. *Stroke* **38**, 194-197, doi:10.1161/01.STR.0000251792.76080.45 (2007).

13 Munsch, F. *et al.* Stroke Location Is an Independent Predictor of Cognitive Outcome. *Stroke* **47**, 66-73, doi:10.1161/STROKEAHA.115.011242 (2016).

14 Wu, O. *et al.* Role of Acute Lesion Topography in Initial Ischemic Stroke Severity and Long-Term Functional Outcomes. *Stroke* **46**, 2438-2444, doi:10.1161/STROKEAHA.115.009643 (2015).

15 Phan, T. G. *et al.* Proof of concept study: relating infarct location to stroke disability in the NINDS rt-PA trial. *Cerebrovasc Dis* **35**, 560-565, doi:10.1159/000351147 (2013).

16 Laredo, C. *et al.* Prognostic Significance of Infarct Size and Location: The Case of Insular Stroke. *Sci Rep* **8**, 9498, doi:10.1038/s41598-018-27883-3 (2018).

17 Timpone, V. M. *et al.* Percentage insula ribbon infarction of >50% identifies patients likely to have poor clinical outcome despite small DWI infarct volume. *AJNR Am J Neuroradiol* **36**, 40-45, doi:10.3174/ajnr.A4091 (2015).

18 Payabvash, S., Taleb, S., Benson, J. C. & McKinney, A. M. Acute Ischemic Stroke Infarct Topology: Association with Lesion Volume and Severity of Symptoms at Admission and Discharge. *AJNR Am J Neuroradiol* **38**, 58-63, doi:10.3174/ajnr.A4970 (2017).

19 Fisher, M. *et al.* Update of the stroke therapy academic industry roundtable preclinical recommendations. *Stroke* **40**, 2244-2250, doi:10.1161/STROKEAHA.108.541128 (2009).

20 McBride, D. W. & Zhang, J. H. Precision Stroke Animal Models: the Permanent MCAO Model Should Be the Primary Model, Not Transient MCAO. *Transl Stroke Res*, doi:10.1007/s12975-017-0554-2 (2017).

21 Lind, N. M. *et al.* The use of pigs in neuroscience: modeling brain disorders. *Neurosci Biobehav Rev* **31**, 728-751, doi:10.1016/j.neubiorev.2007.02.003 (2007).

22 Gieling, E. T., Schuurman, T., Nordquist, R. E. & van der Staay, F. J. The pig as a model animal for studying cognition and neurobehavioral disorders. *Curr Top Behav Neurosci* **7**, 359-383, doi:10.1007/7854_2010_112 (2011).

23 Saikali, S. *et al.* A three-dimensional digital segmented and deformable brain atlas of the domestic pig. *J Neurosci Methods* **192**, 102-109, doi:10.1016/j.jneumeth.2010.07.041 (2010).

24 Ulyanova, A. V. *et al.* Electrophysiological Signature Reveals Laminar Structure of the Porcine Hippocampus. *eNeuro* **5**, doi:10.1523/ENEURO.0102-18.2018 (2018).

25 Holm, I. E. & West, M. J. Hippocampus of the domestic pig: a stereological study of subdivisional volumes and neuron numbers. *Hippocampus* **4**, 115-125, doi:10.1002/hipo.450040112 (1994).

26 Matsas, R., Kenny, A. J. & Turner, A. J. An immunohistochemical study of endopeptidase-24.11 ("enkephalinase") in the pig nervous system. *Neuroscience* **18**, 991-1012, doi:10.1016/0306-4522(86)90113-2 (1986).

27 Hof PR, Y. W., Bloom FE, Belichenko PV, Celio MR. (Elsevier, Amsterdam, 2000).

28 A, P. Vol. Ninth Edition (Williams and Wilkins, Baltimore, 1996).

29 Baker, E. W. *et al.* Induced Pluripotent Stem Cell-Derived Neural Stem Cell Therapy Enhances Recovery in an Ischemic Stroke Pig Model. *Sci Rep* **7**, 10075, doi:10.1038/s41598-017-10406-x (2017).

30 Kaiser, E. E. *et al.* Characterization of tissue and functional deficits in a clinically translational pig model of acute ischemic stroke. *Brain Res* **1736**, 146778, doi:10.1016/j.brainres.2020.146778 (2020).

31 Platt, S. R. *et al.* Development and characterization of a Yucatan miniature biomedical pig permanent middle cerebral artery occlusion stroke model. *Exp Transl Stroke Med* **6**, 5, doi:10.1186/2040-7378-6-5 (2014).

32 Webb, R. L. *et al.* Human Neural Stem Cell Extracellular Vesicles Improve Recovery in a Porcine Model of Ischemic Stroke. *Stroke* **49**, 1248-1256, doi:10.1161/STROKEAHA.117.020353 (2018).

33 Kaiser, E. E. & West, F. D. Large animal ischemic stroke models: replicating human stroke pathophysiology. *Neural Regen Res* **15**, 1377-1387, doi:10.4103/1673-5374.274324 (2020).

34 Spellicy, S. E. *et al.* Neural Stem Cell Extracellular Vesicles Disrupt Midline Shift Predictive Outcomes in Porcine Ischemic Stroke Model. *Transl Stroke Res*, doi:10.1007/s12975-019-00753-4 (2019).

35 Beyaert, C., Vasa, R. & Frykberg, G. E. Gait post-stroke: Pathophysiology and rehabilitation strategies. *Neurophysiol Clin* **45**, 335-355, doi:10.1016/j.neucli.2015.09.005 (2015).

36 Balaban, B. & Tok, F. Gait disturbances in patients with stroke. *PM R* **6**, 635-642, doi:10.1016/j.pmrj.2013.12.017 (2014).

37 Duberstein, K. J. *et al.* Gait analysis in a pre- and post-ischemic stroke biomedical pig model. *Physiol Behav* **125**, 8-16, doi:10.1016/j.physbeh.2013.11.004 (2014).

38 Stewart, J. C. *et al.* Role of corpus callosum integrity in arm function differs based on motor severity after stroke. *Neuroimage Clin* **14**, 641-647, doi:10.1016/j.nicl.2017.02.023 (2017).

39 Wang, L. E. *et al.* Degeneration of corpus callosum and recovery of motor function after stroke: a multimodal magnetic resonance imaging study. *Hum Brain Mapp* **33**, 2941-2956, doi:10.1002/hbm.21417 (2012).

40 Kim, B. J. *et al.* Magnetic resonance imaging in acute ischemic stroke treatment. *J Stroke* **16**, 131-145, doi:10.5853/jos.2014.16.3.131 (2014).

41 Thijs, V. N. *et al.* Is early ischemic lesion volume on diffusion-weighted imaging an independent predictor of stroke outcome? A multivariable analysis. *Stroke* **31**, 2597-2602, doi:10.1161/01.str.31.11.2597 (2000).

42 Saver, J. L. *et al.* Infarct volume as a surrogate or auxiliary outcome measure in ischemic stroke clinical trials. The RANTTAS Investigators. *Stroke* **30**, 293-298, doi:10.1161/01.str.30.2.293 (1999).

43 Lau, V. W., Platt, S. R., Grace, H. E., Baker, E. W. & West, F. D. Human iNPC therapy leads to improvement in functional neurologic outcomes in a pig ischemic stroke model. *Brain Behav* **8**, e00972, doi:10.1002/brb3.972 (2018).

44 Navarro-Orozco, D. & Sanchez-Manso, J. C. in *StatPearls* (2020).

45 Nogles, T. E. & Galuska, M. A. in *StatPearls* (2020).

46 Payabvash, S. *et al.* Location-weighted CTP analysis predicts early motor improvement in stroke: a preliminary study. *Neurology* **78**, 1853-1859, doi:10.1212/WNL.0b013e318258f799 (2012).

47 Payabvash, S. *et al.* Regional ischemic vulnerability of the brain to hypoperfusion: the need for location specific computed tomography perfusion thresholds in acute stroke patients. *Stroke* **42**, 1255-1260, doi:10.1161/STROKEAHA.110.600940 (2011).

48 Kito, G. *et al.* Experimental thromboembolic stroke in cynomolgus monkey. *J Neurosci Methods* **105**, 45-53, doi:10.1016/s0165-0270(00)00351-4 (2001).

49 Titianova, E. B., Pitkanen, K., Paakkonen, A., Sivenius, J. & Tarkka, I. M. Gait characteristics and functional ambulation profile in patients with chronic unilateral stroke. *Am J Phys Med Rehabil* **82**, 778-786; quiz 787-779, 823, doi:10.1097/01.PHM.0000087490.74582.E0 (2003).

50 Lang, C. E., Bland, M. D., Bailey, R. R., Schaefer, S. Y. & Birkenmeier, R. L. Assessment of upper extremity impairment, function, and activity after stroke: foundations for clinical decision making. *J Hand Ther* **26**, 104-114;quiz 115, doi:10.1016/j.jht.2012.06.005 (2013).

51 Langhorne, P., Coupar, F. & Pollock, A. Motor recovery after stroke: a systematic review. *Lancet Neurol* **8**, 741-754, doi:10.1016/S1474-4422(09)70150-4 (2009).

52 Riley, J. D. *et al.* Anatomy of stroke injury predicts gains from therapy. *Stroke* **42**, 421-426, doi:10.1161/STROKEAHA.110.599340 (2011).

53 Saga, Y., Hoshi, E. & Tremblay, L. Roles of Multiple Globus Pallidus Territories of Monkeys and Humans in Motivation, Cognition and Action: An Anatomical, Physiological and Pathophysiological Review. *Front Neuroanat* **11**, 30, doi:10.3389/fnana.2017.00030 (2017).

54 Blair, C. Educating executive function. *Wiley Interdiscip Rev Cogn Sci* **8**, doi:10.1002/wcs.1403 (2017).

55 Sherman, S. M. Functioning of Circuits Connecting Thalamus and Cortex. *Compr Physiol* **7**, 713-739, doi:10.1002/cphy.c160032 (2017).

56 Gillies, M. J. *et al.* The Cognitive Role of the Globus Pallidus interna; Insights from Disease States. *Exp Brain Res* **235**, 1455-1465, doi:10.1007/s00221-017-4905-8 (2017).

57 Ng, Y. S., Stein, J., Ning, M. & Black-Schaffer, R. M. Comparison of clinical characteristics and functional outcomes of ischemic stroke in different vascular territories. *Stroke* **38**, 2309-2314, doi:10.1161/STROKEAHA.106.475483 (2007).

58 Furlanis, G. *et al.* Ischemic Volume and Neurological Deficit: Correlation of Computed Tomography Perfusion with the National Institutes of Health Stroke Scale Score in Acute Ischemic Stroke. *J Stroke Cerebrovasc Dis* **27**, 2200-2207, doi:10.1016/j.jstrokecerebrovasdis.2018.04.003 (2018).

59 Ernst, M. *et al.* Impact of Ischemic Lesion Location on the mRS Score in Patients with Ischemic Stroke: A Voxel-Based Approach. *AJNR Am J Neuroradiol* **39**, 1989-1994, doi:10.3174/ajnr.A5821 (2018).

60 Lo, R., Gitelman, D., Levy, R., Hulvershorn, J. & Parrish, T. Identification of critical areas for motor function recovery in chronic stroke subjects using voxel-based lesion symptom mapping. *Neuroimage* **49**, 9-18, doi:10.1016/j.neuroimage.2009.08.044 (2010).

61 Koch, S. *et al.* Atlas registration for edema-corrected MRI lesion volume in mouse stroke models. *J Cereb Blood Flow Metab* **39**, 313-323, doi:10.1177/0271678X17726635 (2019).

62 Ktena, S. I. *et al.* Brain Connectivity Measures Improve Modeling of Functional Outcome After Acute Ischemic Stroke. *Stroke* **50**, 2761-2767, doi:10.1161/STROKEAHA.119.025738 (2019).

63 Etherton, M. R. *et al.* White Matter Integrity and Early Outcomes After Acute Ischemic Stroke. *Transl Stroke Res* **10**, 630-638, doi:10.1007/s12975-019-0689-4 (2019).

64 Zhang, J. *et al.* Disrupted structural and functional connectivity networks in ischemic stroke patients. *Neuroscience* **364**, 212-225, doi:10.1016/j.neuroscience.2017.09.009 (2017).

65 Vannucci, S. J. & Hurn, P. D. Gender differences in pediatric stroke: is elevated testosterone a risk factor for boys? *Ann Neurol* **66**, 713-714, doi:10.1002/ana.21925 (2009).

66 Hawk, T., Zhang, Y. Q., Rajakumar, G., Day, A. L. & Simpkins, J. W. Testosterone increases and estradiol decreases middle cerebral artery occlusion lesion size in male rats. *Brain Res* **796**, 296-298, doi:10.1016/s0006-8993(98)00327-8 (1998).

67 Manwani, B. & McCullough, L. D. Sexual dimorphism in ischemic stroke: lessons from the laboratory. *Womens Health (Lond)* **7**, 319-339, doi:10.2217/whe.11.22 (2011).

68 Lisabeth, L. & Bushnell, C. Stroke risk in women: the role of menopause and hormone therapy. *Lancet Neurol* **11**, 82-91, doi:10.1016/S1474-4422(11)70269-1 (2012).

69 Platt, S. R. *et al.* Development and characterization of a Yucatan miniature biomedical pig permanent middle cerebral artery occlusion stroke model. *Experimental & translational stroke medicine* **6**, 5-5, doi:10.1186/2040-7378-6-5 (2014).

70 Li, X., Morgan, P. S., Ashburner, J., Smith, J. & Rorden, C. The first step for neuroimaging data analysis: DICOM to NIfTI conversion. *J Neurosci Methods* **264**, 47-56, doi:10.1016/j.jneumeth.2016.03.001 (2016).

71 Fedorov, A. *et al.* 3D Slicer as an image computing platform for the Quantitative Imaging Network. *Magn Reson Imaging* **30**, 1323-1341, doi:10.1016/j.mri.2012.05.001 (2012).

72 Ashburner, J. *et al.* SPM12 manual. *URL: http://www. fil. ion. ucl. ac. uk/spm/doc/spm12 manual. pdf* (2016).

73 Ashburner, J. & Friston, K. Multimodal image coregistration and partitioning--a unified framework. *Neuroimage* **6**, 209-217, doi:10.1006/nimg.1997.0290 (1997).

74 Ashburner, J. & Friston, K. J. Nonlinear spatial normalization using basis functions. *Hum Brain Mapp* **7**, 254-266 (1999).

75 Jenkinson, M., Beckmann, C. F., Behrens, T. E., Woolrich, M. W. & Smith, S. M. Fsl. *Neuroimage* **62**, 782-790, doi:10.1016/j.neuroimage.2011.09.015 (2012).

76 Smith, S. M. *et al.* Advances in functional and structural MR image analysis and implementation as FSL. *Neuroimage* **23 Suppl 1**, S208-219, doi:10.1016/j.neuroimage.2004.07.051 (2004).

77 Woolrich, M. W. *et al.* Bayesian analysis of neuroimaging data in FSL. *Neuroimage* **45**, S173-186, doi:10.1016/j.neuroimage.2008.10.055 (2009).

78 Rueden, C. T. *et al.* ImageJ2: ImageJ for the next generation of scientific image data. *BMC Bioinformatics* **18**, 529, doi:10.1186/s12859-017-1934-z (2017).

79 Schindelin, J. *et al.* Fiji: an open-source platform for biological-image analysis. *Nat Methods* **9**, 676-682, doi:10.1038/nmeth.2019 (2012).

Acknowledgements

We would like to thank Dr. E. Kaiser, Dr. G. Kim, Dr. J. Mumaw, Dr. E. Howerth, X. Fang, J. Jeon, E. Karstedt, K. McClanahan, L. Reno, and M. Wendzik for assistance with pig care, K. Mason for MRI technical assistance, Dr. S. Platt for performing stroke surgeries, and T. Ellison and C. Temple for assistance with data analysis. We would also like to thank our team of undergraduate researchers: M. Alcalde-Santa Ana, W. Anand, J. Bourbo, T. Burnette, A. Cieszewski, L. Francis, Z. Jones, J. Johnston, Z. Oberholzer, L. Parker, S. Patel, S. Radhakrishnan, H. Rasheed, S. Shin, A. Simmons, E. Smith, M. Snyder, H. Stavas, C. Temple, B. Winkler, and J. Winkler, we could not have done this research without your help. Research reported in this publication was supported by the National Institutes of Health under award number **1R43NS103596-01**.

Authors' contribution statement

KMS, BJJ, SLS, and FDW wrote and edited the manuscript. KMS, BJJ, SESp, EWB, HAK, SLS, and FDW participated in study design. KMS, BJJ, and ESW performed pig work. JAG performed ovariectomy surgeries on female pigs. KMS, GAS, SESn, and QZ performed MRI analysis. KMS and BJJ performed statistical tests. All authors reviewed the manuscript.

Competing interests statement

SLS is a stockholder in Aruna Bio Inc and was a part-time employee of Aruna Bio Inc during the study. EWB was a full-time employee of Aruna Bio Inc during the study. All other authors declare no competing interests.

Data availability statement

Data and MatLab code is available at https://zenodo.org/. [10.5281/zenodo.4339189]

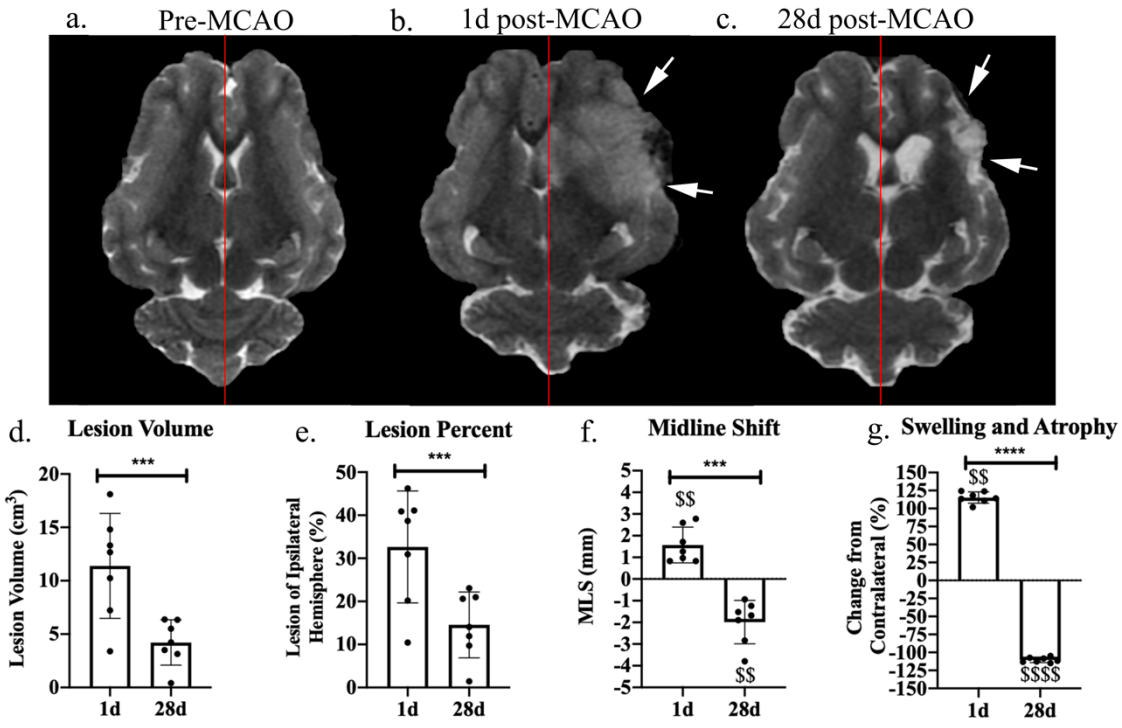

Figure 3.1: Canonical MRI measurements of MCAO induced ischemic stroke at 1d and 28d post-MCAO. T2W images prior to MCAO reveal homology between the hemispheres (**a**). At 1d (**b**) and 28d (**c**) post-MCAO, T2W images exhibited territorial hyperintense lesions indicated by white arrows and a shift from the natural midline (red lines indicate natural midline). Lesion volume (**d**), lesion volume as a percent of the ipsilateral hemisphere (**e**), midline shift (MLS) (**f**), and hemispheric changes (**g**) were quantified at 1d and 28d post-MCAO. *** and **** indicated statistically different between timepoints. $$ and $$$$ indicated statistically different from hypothetical normal.

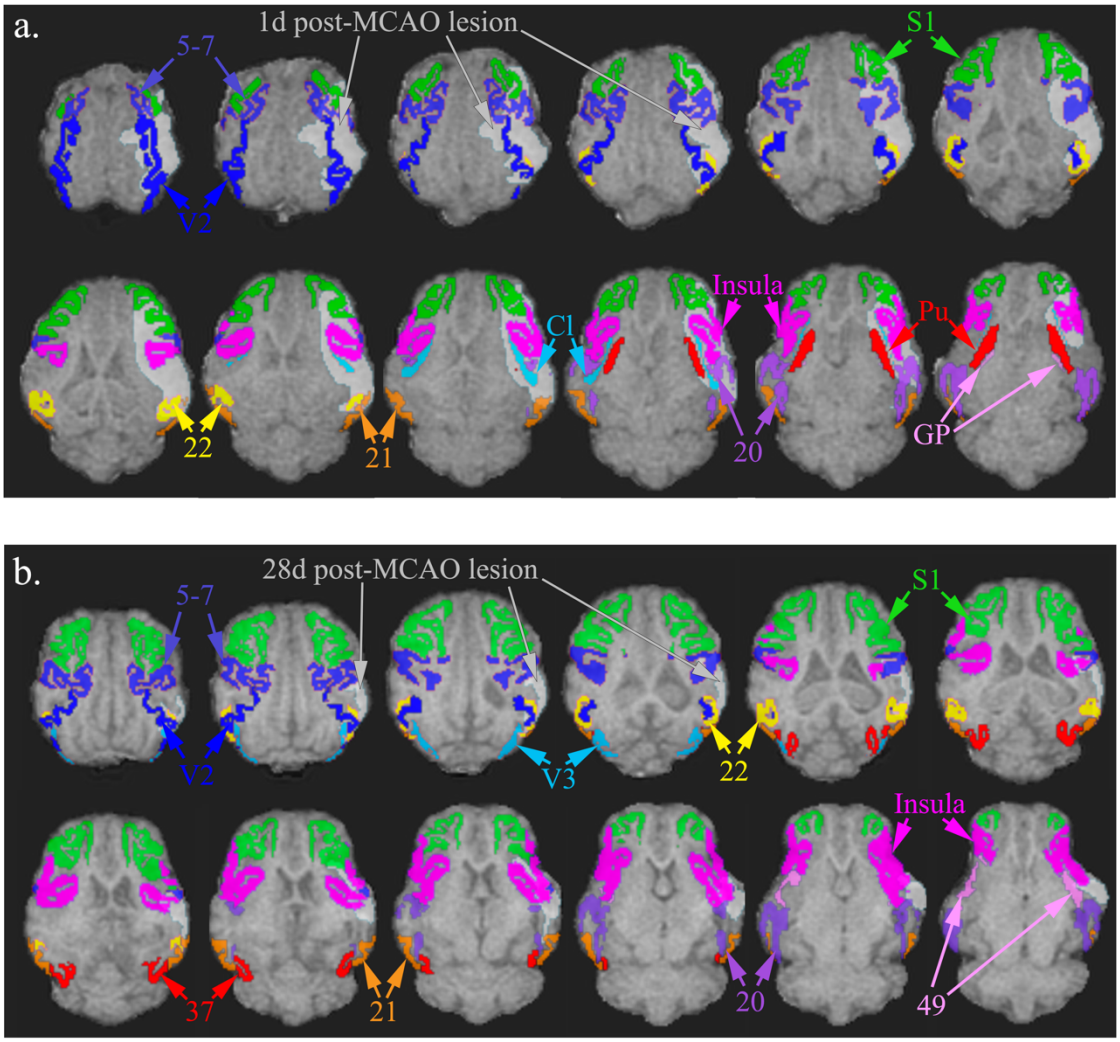

Figure 3.2: Structures most highly lesioned by MCAO in a porcine ischemic stroke model. Images depict axial T1 brain overlay with entire bilateral structures most affected by the lesion. The structures with the highest percentage of infarction (percent of structure, PoS) at 1d post-MCAO in descending order include the claustrum (*Cl*), inferior temporal gyrus (*Brodmann's Area 20*), superior temporal gyrus (*Brodmann's Area 22*), insular cortex (*Insula*), middle temporal gyrus (*Brodmann's Area 21*), putamen (*Pu*), somatosensory association cortex (*Brodmann's Area 5-7*), secondary visual cortex (*V2*),

globus pallidus (*GP*), and primary somatosensory cortex (*S1*) (**a**). At 28d post-MCAO, the structures with the highest level of lesioning included the middle temporal gyrus (*Brodmann's Area 21*), superior temporal gyrus (*Brodmann's Area 22*), inferior temporal gyrus (*Brodmann's Area 20*), somatosensory association cortex (*Brodmann's Area 5-7*), insular cortex (*Insula*), associative visual cortex (*V3*), primary somatosensory cortex (*S1*), prepiriform area (*Brodmann's Area 49*), fusiform gyrus (*Brodmann's Area 37*), and secondary visual cortex (*V2*) (**b**).

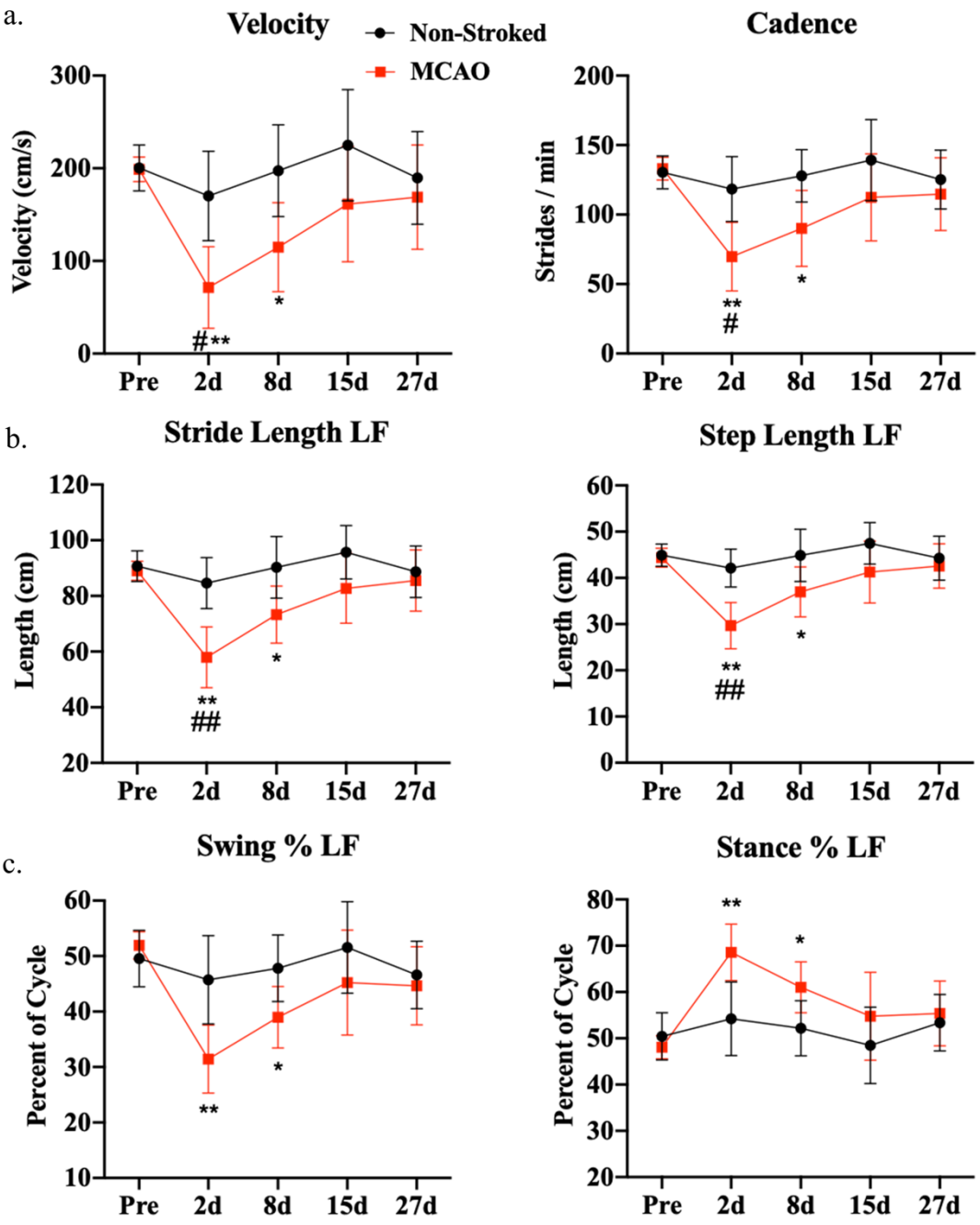

Figure 3.3: MCAO resulted in acute functional gait deficits. At 2d and 8d post-MCAO, MCAO pigs exhibited significant decreases in velocity (**a**), cadence (**a**), stride length (**b**), step length (**b**), swing percent (**c**), and an increase in stance percent (**c**) relative

to pre-MCAO values. At 15d and 27d post-MCAO, there were no significant differences compared to pre-stroke, which was indicative of functional recovery ($p>0.05$). At 2d post-MCAO, MCAO pigs exhibited significantly different velocity (**a**), cadence (**a**), stride length (**b**), and step length (**b**) relative to non-stroked controls. Non-stroked controls had no significant changes over the course of the study ($p>0.05$). * and ** indicated statistical difference from pre-MCAO values. # and ## indicated statistically different between groups.

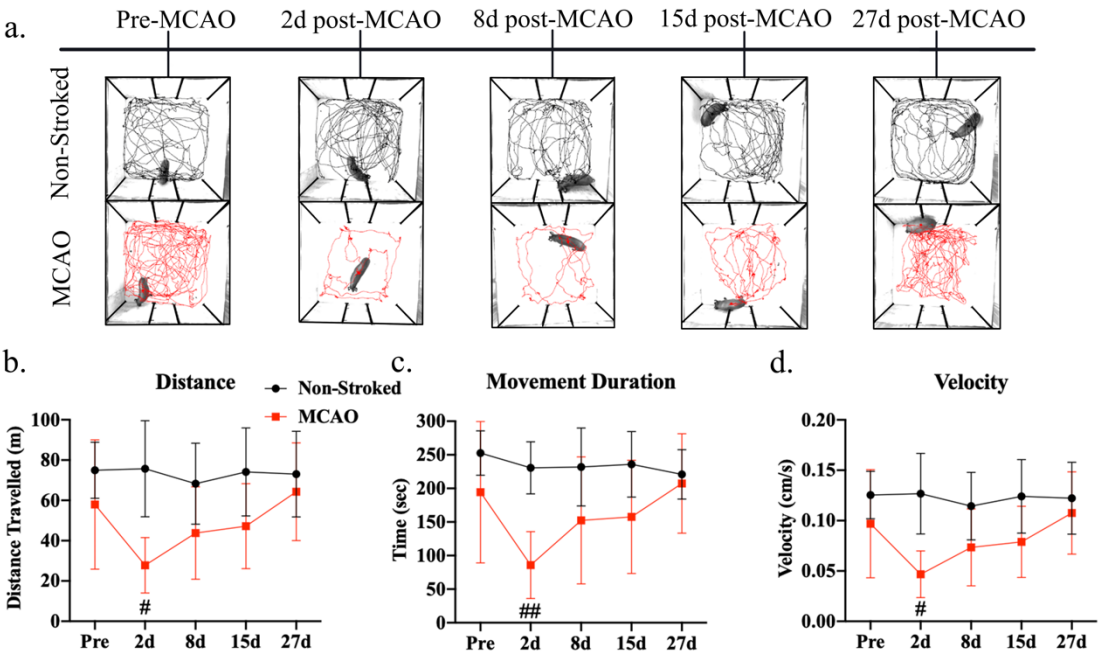

Figure 3.4: Stroke decreased acute voluntary movement in open field behavioral test. Representative 10-min movement tracings shown for non-stroked (black) and MCAO (red) pigs across all time points (**a**). At 2d post-MCAO, MCAO pigs had decreased distance traveled (**b**), movement duration (**c**), and average velocity (**d**) compared to non-stroked pigs. No significant differences were observed at 8d, 15d, and

27d post-MCAO in both groups (p>0.05). # and ## indicated statistically different between groups.

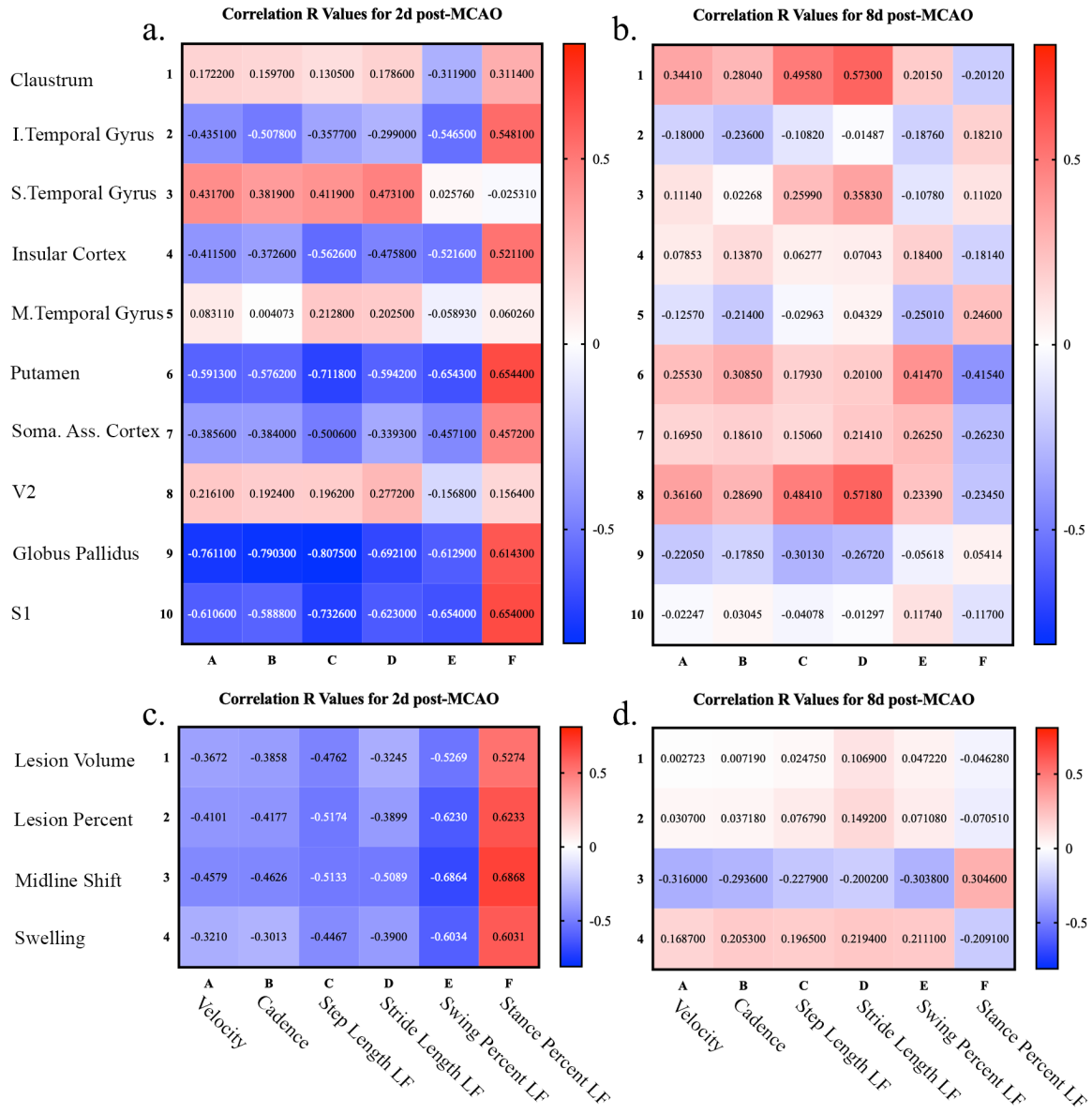

Figure 3.5: Location of stroke lesion in structures associated with motor coordination had prognostic value when evaluating motor functional outcomes.

Pearson correlations between top PoS structures impacted by the lesion (y-axis) to gait functional outcomes (x-axis) were evaluated at 2d post-MCAO (**a**) and 8d post-MCAO (**b**). Pearson correlations between canonical MRI parameters (y-axis), including lesion volume, lesion percent of ipsilateral hemisphere, midline shift, and hemispheric swelling, and gait functional outcomes (x-axis) were evaluated at 2d post-MCAO (**c**) and 8d post-MCAO (**d**). R values were reported with cell color indicating correlation direction and strength. FDR p-values corrected for multiple comparisons can be found in **Supplementary Table 3**.

Table 3.1: Percentage of pigs effected with lesion in each structure. Identified structures were separated into regions including the thalamus, striate system, limbic system, and Brodmann's Areas. Activated pixels in each structure signified positive lesion. Lesion locations were identified at 1d and 28d post-MCAO. 100% signifies that all pigs (n=7) had lesion in structure.

Region	Structure	Pigs Effected at 1d Post-MCAO (%)	Pigs Effected at 28d Post-MCAO (%)
Thalamus	Pulvinar Nuclei	42.9	--
	Reticular Thalamic Nucleus	42.9	--
	Ventral Anterior Thalamic Nucleus	14.3	--
	Ventral Posterior Thalamic Nucleus	42.9	--
Striate System	Caudate Nucleus	71.4	--
	Claustrum	100	28.6
	Globus Pallidus	71.4	--
	Putamen	100	14.3
Limbic System	Fornix	85.7	28.6
	Hippocampus	85.7	14.3
	Subiculum	42.9	--
	Amygdala	71.4	28.6
Brodmann's Area	Primary Somatosensory Cortex	71.4	71.4
	Primary Motor Cortex	28.6	--
	Somatosensory Association Cortex	85.7	100
	Dorsolateral Prefrontal Cortex	42.9	14.3
	Anterior Prefrontal Cortex	28.6	--
	Orbitofrontal Cortex	14.3	--
	Insular Cortex	100	85.7
	Primary Visual Cortex	71.4	28.6
	Secondary Visual Cortex	100	85.7
	Associative Visual Cortex	85.7	57.1
	Inferior Temporal Gyrus	100	100
	Middle Temporal Gyrus	85.7	100
	Superior Temporal Gyrus	100	85.7
	Dorsal Anterior Cingulate Cortex	14.3	--
	Anterior Entorhinal Cortex	85.7	14.3
	Parahippocampal Cortex	100	71.4
	Fusiform Gyrus	71.4	42.9

	Prepiriform Area	100	100

Supplementary Information

Supplementary Table 3.1: Percent of structure signifies the percent of individual anatomical structure with a lesion. Percent of structure (PoS) was calculated by the total number of activated pixels (lesion) in structure divided by the total number of pixels in structure. Percent of lesion (PoL) signifies the percent of each structure in the identified lesion. PoL was calculated by dividing number of activated pixels per structure by the total number of pixels of the lesion.

	Percent of Structure 1d post-MCAO		**Percent of Structure 28d post-MCAO**		**Percent of Lesion 1d post-MCAO**		**Percent of Lesion 28d post-MCAO**	
Structure	**Mean**	**SD**	**Mean**	**SD**	**Mean**	**SD**	**Mean**	**SD**
Amygdala	24.13	27.18	4.31	8.25	1.23	1.95	0.60	1.03
Anterior Commissure	0.97	2.55	0	0	0.004	0.01	0	0
Anterior Entorhinal Cortex	9.95	9.29	0.16	0.43	0.93	1.66	0.06	0.15
Anterior Prefrontal Cortex	2.43	4.40	0	0	0.19	0.36	0	0
Associative Visual Cortex	15.49	13.95	10.02	14.48	0.54	0.51	0.85	1.03
Caudate Nucleus	7.20	8.73	0	0	0.45	0.62	0	0
Claustrum	65.91	29.68	0.96	2.45	1.94	0.71	0.07	0.17
Corpus Callosum	0.22	0.56	0	0	0.03	0.07	0	0
Dorsal Anterior Cingulate Cortex	0.19	0.51	0	0	0.008	0.02	0	0
Dorsolateral Prefrontal Cortex	1.23	2.05	0.01	0.03	0.07	0.12	0.002	0.006
Fornix	2.93	2.82	0.25	0.53	0.18	0.18	0.08	0.18
Fusiform Gyrus	10.43	12.06	6.82	10.44	0.72	1.31	0.59	0.77
Geniculate Nucleus	0.04	0.12	0	0	0.0004	0.001	0	0
Globus Pallidus	34.52	28.61	0	0	0.59	0.69	0	0
Hippocampus	4.46	3.66	0.46	1.23	0.48	0.68	0.21	0.54

Inferior Temporal Gyrus	62.15	27.67	18.19	13.55	5.16	4.65	3.27	2.72
Insular Cortex	54.45	31.35	15.95	9.28	8.45	5.09	7.95	6.02
Middle Temporal Gyrus	44.43	24.49	39.84	31.80	2.59	2.97	4.23	3.01
Parahippocampal Cortex	12.98	10.99	3.11	3.51	2.06	3.00	1.42	2.34
Piriform Cortex	0	0	0.21	0.54	0	0	0	0
Prepiriform Area	23.76	15.86	7.84	5.85	1.44	1.31	1.30	1.06
Primary Motor Cortex	0.18	0.32	0	0	0.007	0.01	0	0
Primary Somatosensory Cortex	33.48	23.73	8.44	8.92	6.33	4.82	5.65	6.36
Primary Visual Cortex	4.90	6.86	0.02	0.03	1.08	1.36	0.009	0.02
Pulvinar Nuclei	0.53	0.98	0	0	0.008	0.02	0	0
Putamen	44.00	22.23	0.27	0.72	3.22	1.58	0.04	0.11
Reticular Thalamic Nucleus	7.61	9.74	0	0	0.09	0.13	0	0
Orbitofrontal Cortex	0.41	1.08	0	0	0.002	0.004	0	0
Secondary Visual Cortex	40.57	28.62	5.83	6.30	6.02	4.34	2.07	1.93
Somatosensory Association Cortex	43.05	27.06	16.78	11.46	4.98	2.87	5.41	3.59
Subiculum	2.23	3.56	0	0	0.02	0.03	0	0
Superior Temporal Gyrus	58.91	36.32	31.14	17.55	2.36	1.68	3.15	1.87
Ventral Anterior Thalamic Nucleus	0.02	0.06	0	0	0.001	0.002	0	0
Ventral Posterior Thalamic Nucleus	0.29	0.40	0	0	0.004	0.006	0	0

Supplementary Table 3.2: Functional outcomes evaluated. Compiled list of functional outputs with corresponding definitions.

	Gait or Behavior Parameter Measured
Spatial Gait Parameters	▪ Step Length (cm) LF, RF, LH, RH (*Measured between the heel center of the current hoof print to the heel center of the previous hoof print on the opposite foot*) ▪ Stride Length (cm) LF, RF, LH, RH (*Distance between consecutive hoof prints of the same hoof)*
Temporal Gait Parameters	▪ Velocity (*Distance traveled (cm)/sec*) ▪ Cadence (S*trides/min*) ▪ Swing Percent (%) LF, RF, LH, RH *(The percent of 1 full gait cycle in which the limb was in the non-contact phase*) ▪ Stance Percent (%) LF, RF, LH, RH *(The percent of 1 full gait cycle in which the limb was in the contact phase*)
Pressure Gait Parameters	▪ Total Pressure Index LF, RF, LH, RH (*TSP expressed as a percentage of all four limbs. This shows % of weight distribution across all four hoofs*)
Open Field Mobility Behavior Parameters	▪ Distance (m) (*Distance traveled by the pig within the open field arena)* ▪ Velocity (*Distance traveled (cm)/sec*) ▪ Movement Moving Duration (*Elapsed time the running average velocity exceeds the start velocity*)
Modified Rankin Scale Score	Observational behavior assessment modified for a pig. 0 (no residual stroke symptoms) to 6 (death due to stroke). *See Spellicy et al.[1] for further information on the scale.*

Supplementary Table 3.3: FDR Corrected P-Values. False discovery rate analysis was completed on original p-values to correct for multiple comparisons.

	2d post-MCAO					
	Velocity	**Cadence**	**Step Length LF**	**Stride Length LF**	**Swing % LF**	**Stance % LF**
Claustrum	0.8134	0.8134	0.8134	0.8134	0.8134	0.8134
Inferior Temporal Gyrus	0.5704	0.5704	0.5704	0.5704	0.5704	0.5704
Superior Temporal Gyrus	0.6893	0.6893	0.6893	0.6893	0.9716	0.9716
Insular Cortex	0.4716	0.4716	0.4716	0.4716	0.4716	0.4716
Middle Temporal Gyrus	1	1	1	1	1	1
Putamen	0.2336	0.2336	0.2336	0.2336	0.2336	0.2336
Somatosensory Association Cortex	0.5156	0.5156	0.5156	0.5156	0.5156	0.5156
Secondary Visual Cortex	0.775	0.775	0.775	0.775	0.775	0.775
Globus Pallidus	0.1592	0.1592	0.1592	0.1933	0.1978	0.1978
Primary Somatosensory Cortex	0.2211	0.2211	0.2211	0.2211	0.2211	0.2211

	8d post-MCAO					
	Velocity	**Cadence**	**Step Length LF**	**Stride Length LF**	**Swing % LF**	**Stance % LF**
Claustrum	0.6721	0.6721	0.6721	0.6721	0.6721	0.6721
Inferior Temporal Gyrus	0.9846	0.9846	0.9846	0.9846	0.9846	0.9846

Superior Temporal Gyrus	0.9712	0.9712	0.9712	0.9712	0.9712	0.9712
Insular Cortex	0.9026	0.9026	0.9026	0.9026	0.9026	0.9026
Middle Temporal Gyrus	0.9592	0.9592	0.9592	0.9592	0.9592	0.9592
Putamen	0.7074	0.7074	0.7074	0.7074	0.7074	0.7074
Somatosensory Association Cortex	0.7547	0.7547	0.7547	0.7547	0.7547	0.7547
Secondary Visual Cortex	0.6198	0.6198	0.6198	0.6198	0.6198	0.6198
Globus Pallidus	0.9173	0.9173	0.9173	0.9173	0.9173	0.9173
Primary Somatosensory Cortex	0.9879	0.9879	0.9879	0.9879	0.9879	0.9879

	2d post-MCAO					
	Velocity	**Cadence**	**Step Length LF**	**Stride Length LF**	**Swing % LF**	**Stance % LF**
Lesion Volume	0.5356	0.5356	0.5356	0.5356	0.5356	0.5356
Lesion Percent	0.4492	0.4492	0.4492	0.4492	0.4492	0.4492
Midline Shift	0.3648	0.3648	0.3648	0.3648	0.3648	0.3648
Swelling	0.5673	0.5673	0.5673	0.5673	0.5673	0.5673

	8d post-MCAO					
	Velocity	**Cadence**	**Step Length LF**	**Stride Length LF**	**Swing % LF**	**Stance % LF**
Lesion Volume	1	1	1	1	1	1
Lesion Percent	0.9574	0.9574	0.9574	0.9574	0.9574	0.9574
Midline Shift	0.6735	0.6735	0.6735	0.6735	0.6735	0.6735
Swelling	0.7248	0.7248	0.7248	0.7248	0.7248	0.7248

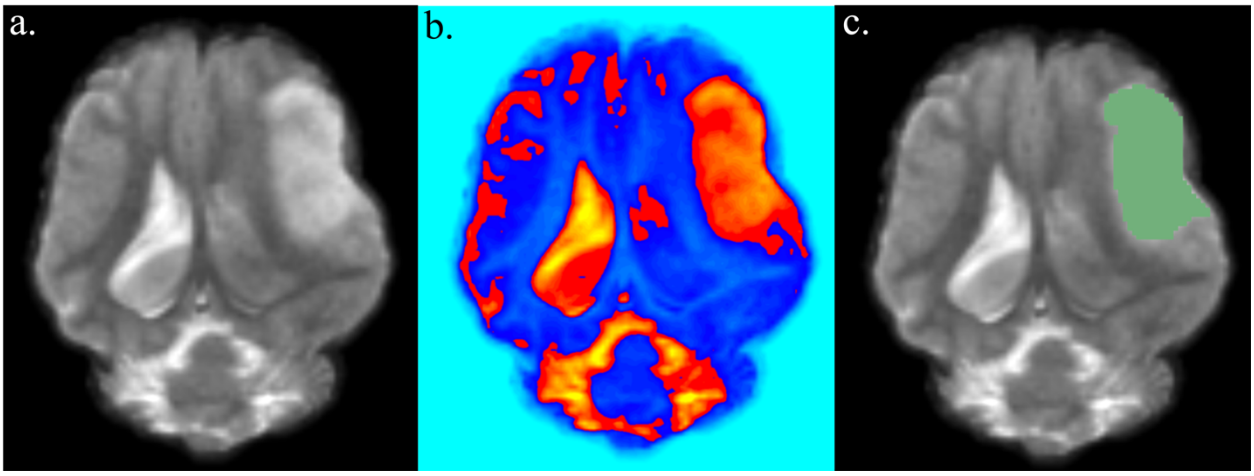

Supplementary Figure 3.1: Method of identifying lesion volume with inversion filter.

T2W image (**a**) with a territorial hyperintense lesion in the ipsilateral hemisphere.

Inversion filter applied (**b**) and lesion manually outlined in each slice (**c**).

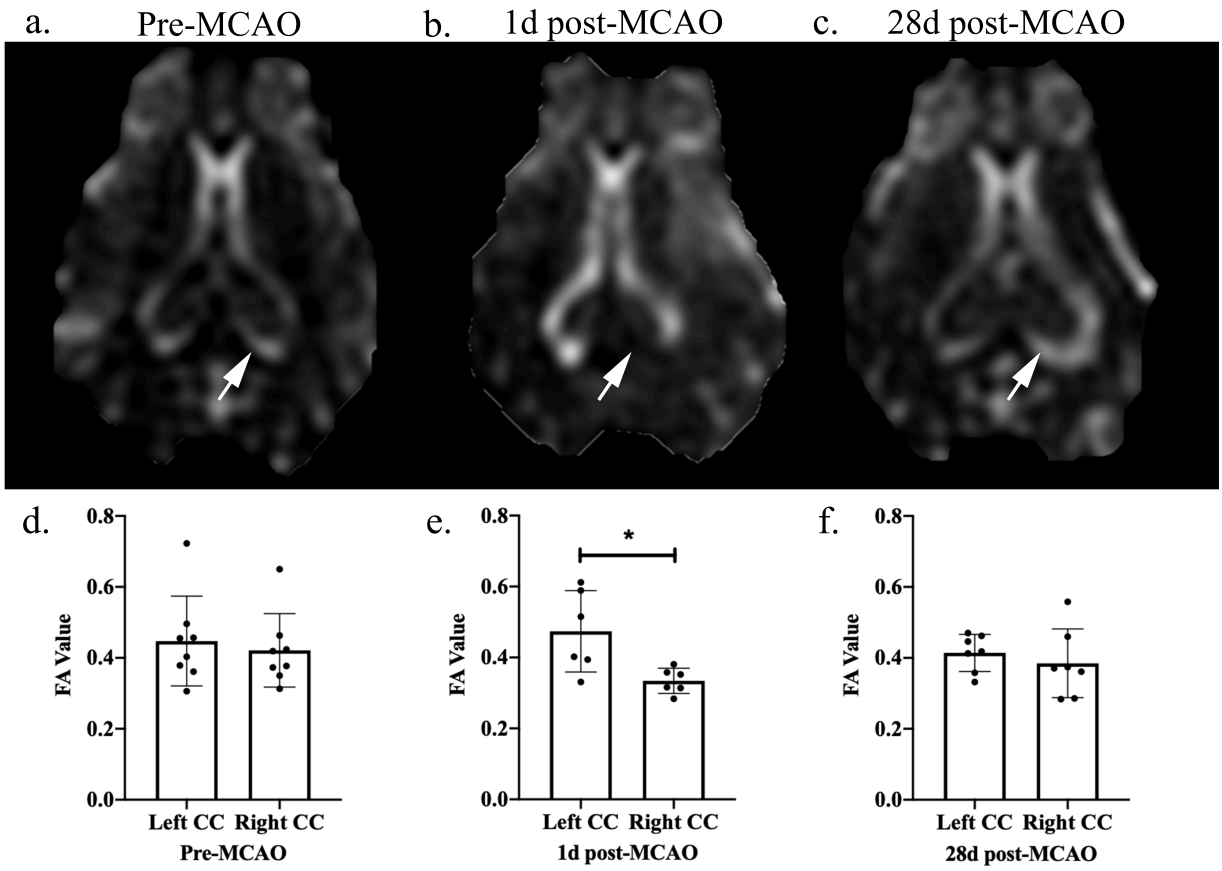

Supplementary Figure 3.2: MCAO results in acute white matter integrity decreases in the corpus callosum. Axial DTI images show an intact corpus callosum (CC) at pre-MCAO (**a**), reduced ipsilateral (right CC) integrity at 1d post-MCAO (**b**), and recovered ipsilateral integrity at 28d post-MCAO (**c**). Pre-MCAO fractional anisotropy (FA) values did not reveal a significant difference between hemispheres (**d**). At 1d post-MCAO, ipsilateral (right) CC FA value was reduced compared to the contralateral (left) CC (**e**). By 28d post-MCAO, FA values had recovered (**f**). * indicated statistical difference between hemispheres.

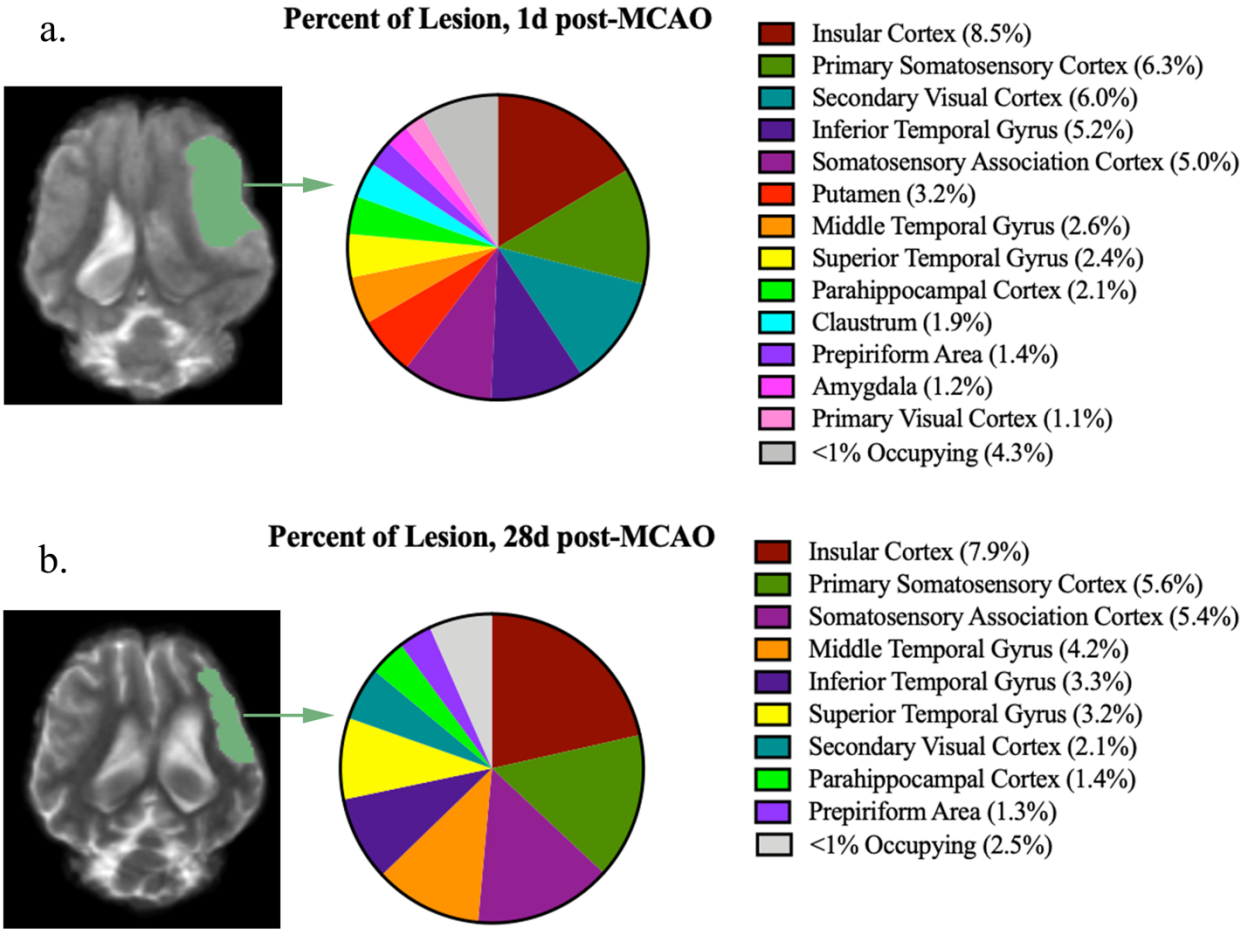

Supplementary Figure 3.3: Percent of identified lesion in effected brain structures. The percent of the identified lesion (PoL) in each structure was quantified to determine the percent of the identified lesion that affected specific brain structures. Summary of the structures occupying the highest percent of lesion measured at 1d post-MCAO (**a**) and at 28d post-MCAO (**b**).

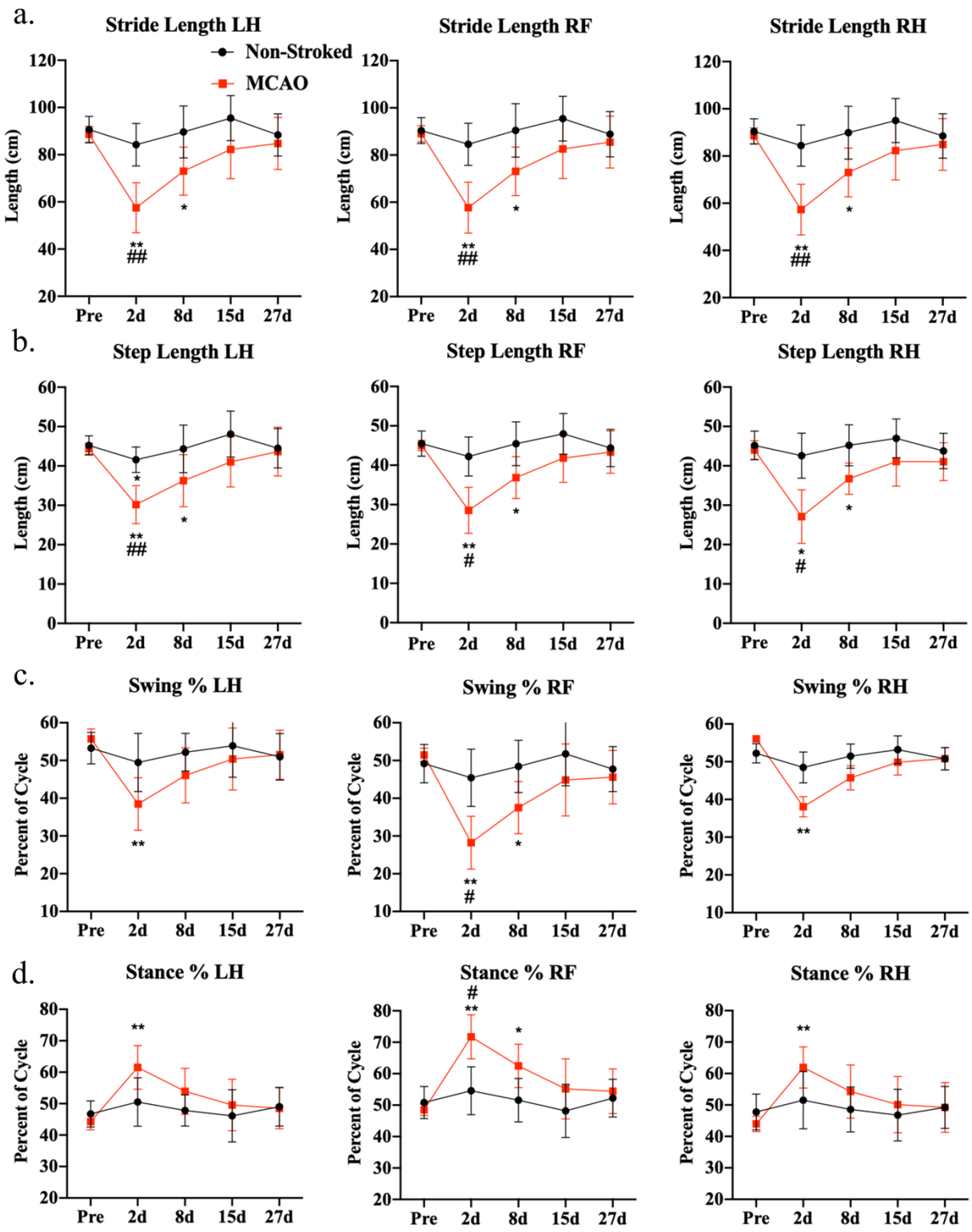
a.
Stride Length LH
Stride Length RF
Stride Length RH
Non-Stroked
MCAO
Length (cm)
b.
Step Length LH
Step Length RF
Step Length RH
Length (cm)
c.
Swing % LH
Swing % RF
Swing % RH
Percent of Cycle
d.
Stance % LH
Stance % RF
Stance % RH
Percent of Cycle
Pre
2d
8d
15d
27d

Supplementary Figure 3.4: MCAO resulted in acute deficits in right front, right hind, and left hind spatiotemporal gait parameters. Stride length of the left hind (LH), right front (RF), and right hind (RH), decreased at 2d (p=0.0038, p=0.0037, and p=0.0040, respectively) and 8d (p=0.0290, p=0.0277, and p=0.0325, respectively) post-MCAO compared to pre-MCAO values (**a**). Stroked animals exhibited a decrease in stride length at 2d post-MCAO compared to non-stroked controls in LH (p=0.0075), RF (p=0.0073), and RH (p=0.0063). Step length of the LH, RF, and RH decreased at 2d (p=0.0017, p=0.0050, and p=0.0104, respectively) and 8d (p=0.0437, p=0.0332, and p=0.0238, respectively) post-MCAO compared to pre-MCAO values (**b**). Stroked animals exhibited a decrease in step length at 2d post-MCAO compared to non-stroked controls in LH (p=0.0067), RF (p=0.0117), and RH (p=0.0135). Swing percent decreased in the LH (p=0.0093), RF (p=0.0033), and RH (p=0.0091) at 2d post-MCAO and in the RF (p=0.0110) at 8d post-MCAO compared to pre-MCAO values (**c**). Stroked animals exhibited a decrease in swing percent at 2d post-MCAO compared to non-stroked controls in RF (p=0.0219). Stance percent increased in the LH (p=0.0093), RF (p=0.0033), and RH (p=0.0091) at 2d post-MCAO and in the RF (p=0.0110) at 8d post-MCAO compared to pre-MCAO values (**d**). Stroked animals exhibited an increase in stance percent at 2d post-MCAO compared to non-stroked controls in RF (p=0.0222). Non-stroked controls had no changes in the measured parameters for the duration of the study (p>0.05), except for step length LH compared to pre-MCAO values at 2d post-MCAO (p=0.0497). * and ** indicated statistical difference from pre-MCAO values. # and ## indicated statistically different between groups.

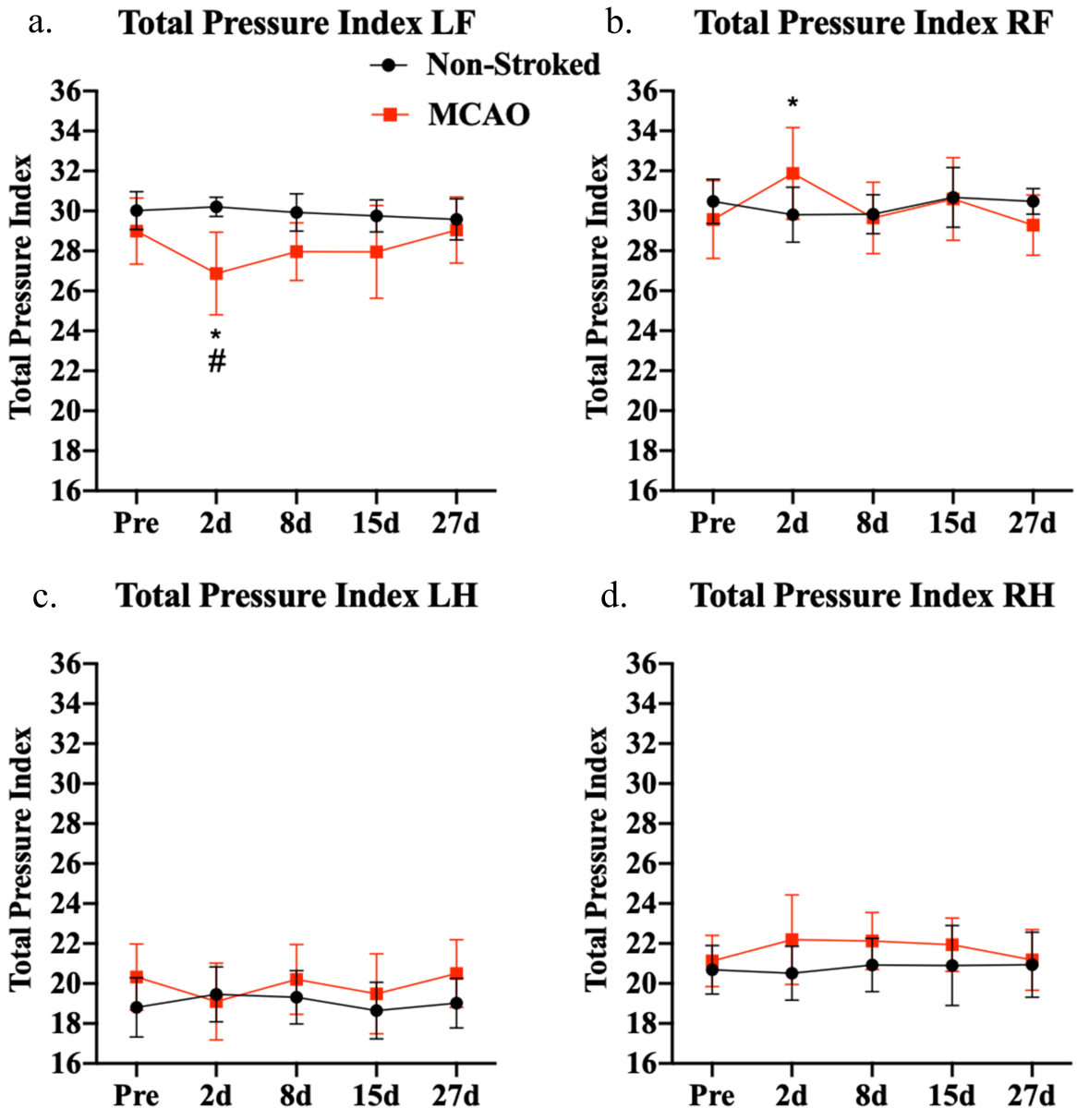

Supplementary Figure 3.5: MCAO induced limb weakness as measured by total pressure index. Total pressure index in the left front (LF) decreased compared to pre-MCAO and was significantly different than non-stroked controls at 2d post-MCAO (**a**). Total pressure index in the right front (RF) correspondingly increased at 2d post-MCAO compared to pre-MCAO (**b**) indicating weight and strength compensation. Hind limbs did

not display any significant observed weight distribution abnormalities (**c**, **d**). * indicated statistical difference from pre-MCAO values. # indicated statistical difference between groups.

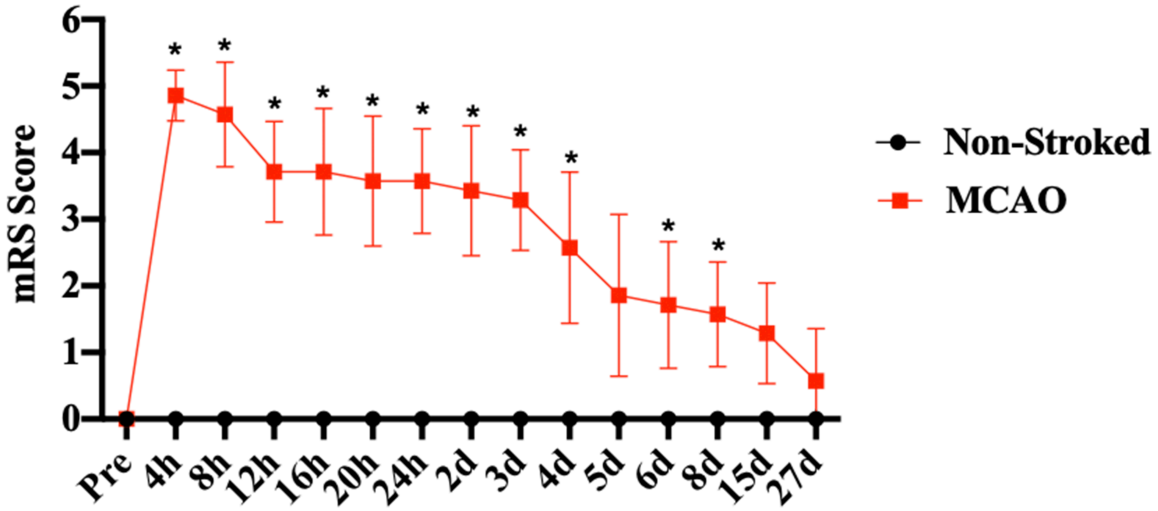

Supplementary Figure 3.6: Modified Rankin Scale score quantified behavioral deficits induced by stroke. Modified Rankin Scale (mRS) score is highest in the acute phase and statistically ($p<0.05$) different than pre-MCAO values through 8d post-MCAO. * indicated statistical difference from pre-MCAO values.

References

1 Spellicy, S. E. *et al.* Neural Stem Cell Extracellular Vesicles Disrupt Midline Shift Predictive Outcomes in Porcine Ischemic Stroke Model. *Transl Stroke Res*, doi:10.1007/s12975-019-00753-4 (2019).

CHAPTER 4

DETECTING FUNCTIONAL CONNECTIVITY DISRUPTIONS IN A TRANSLATIONAL PEDIATRIC TRAUMATIC BRAIN INJURY PORCINE MODEL USING RESTING-STATE AND TASK-BASED FUNCTIONAL MAGNETIC RESONANCE IMAGING [1]

---

[1] **Kelly M. Scheulin†**, Gregory Simchick†, Wenwu Sun, Sydney E. Sneed, Madison M. Fagan, Savannah R. Cheek, Franklin D. West, Qun Zhao. Submitted to *Scientific Reports*, 10/15/2020.

† these authors equally contributed to this work

Abstract

Functional magnetic resonance imaging (fMRI) has significant potential to evaluate changes in brain network activity after traumatic brain injury (TBI) and enable early prognosis of potential functional (e.g., motor, cognitive, behavior) deficits. In this study, resting-state and task-based fMRI (rs- and tb-fMRI) were utilized to examine network changes in a pediatric porcine TBI model that has increased predictive potential in the development of novel therapies. rs- and tb-fMRI were performed one day post-TBI in piglets. Activation maps were generated using group independent component analysis (ICA) and sparse dictionary learning (sDL). Activation maps were compared to pig reference functional connectivity atlases and evaluated using Pearson spatial correlation coefficients and mean ratios. Nonparametric permutation analyses were used to determine significantly different activation areas between the TBI and healthy control groups. Significantly lower Pearson values and mean ratios were observed in the visual, executive control, and sensorimotor networks for TBI piglets compared to controls. Significant differences were also observed within several specific individual anatomical structures within each network. In conclusion, both rs- and tb-fMRI demonstrate the ability to detect functional connectivity disruptions in a translational TBI piglet model, and these disruptions can be traced to specific affected anatomical structures.

Keywords: pig model, traumatic brain injury, functional connectivity, resting-state fMRI, task-based fMRI, independent component analysis, sparse dictionary learning

1. Introduction

Traumatic brain injury (TBI) is a worldwide socio-economic problem that is regularly referred to as a "silent epidemic" with 2.87 million people annually suffering from a TBI in the United States, alone [1]. The largest affected population are children under 14 years of age, which is an early developmental period with increased vulnerability to injury [2,3]. Pediatric TBI can lead to life-long effects on brain structure and function and cause significant cognitive, behavioral and motor function impairments [4]. Due to the substantial effects of TBI, there have been significant efforts to develop better magnetic resonance imaging (MRI) approaches to detect and characterize changes in neural network activity to predict functional outcomes and to generate animal models that are more representative of human TBI responses. These efforts have resulted in highly sensitive resting-state and task-based functional MRI (rs- and tb-fMRI) approaches and a porcine TBI model that has similar brain anatomy, physiology, and TBI pathophysiology to humans [3,5-9]. To date, rs- and tb-fMRI has not been performed in the TBI piglet model; raising questions as to how functional network connectivity changes in the piglet brain after TBI.

fMRI is a powerful tool that can be used to characterize injury severity and recovery in specific functional networks with known functional tasks (e.g., cognition) and can be used to predict potential deficits (e.g., learning, memory, motor) with precision in TBI patients [10-13]. Rs- and tb-fMRI have both been shown to have substantial clinical and pre-clinical potential to assess TBI injury and recovery [5-7]. On one hand, rs-fMRI can easily be conducted with minors, elderly, or mentally challenged populations [14], and the intrinsic connectivity of neural networks mapped by rs-fMRI may be more heritable than

task-elicited activity [15]. On the other hand, network mapping using tb-fMRI are found to be similar to those mapped by rs-fMRI, and tb-fMRI has been used for studies of intrinsic connectivity when rs-fMRI data is not available [16]. Furthermore, tb-fMRI has been found to underline individual differences in network dynamics [17,18]. Recently, a general functional connectivity approach was proposed for leveraging shared features across rs- and tb-fMRI [19], and by doing so, this method was found to improve the reliability of intrinsic connectivity estimates and identify meaningful correlates of individual differences in behavior. Therefore, a combined rs- and tb-fMRI approach is important in monitoring system-level changes within and between brain functional networks after TBI. fMRI also enables assessment of critical network changes, including 1) changes in activation timing, which can enable identification of specifically affected subnetworks, 2) detection of the type of functional alteration (e.g., hypoactivation vs hyperactivation), and 3) potential reorganization of network signaling pathways. Predicting changes in cognition, behavior, and similar long-term outcomes in TBI patients has proven to be imprecise using standard clinical assessments [20]. However, fMRI has shown promise as a prognostic modality, as it has been used to successfully predict patient cognitive deficits even six months after injury [20]. Our research team has recently identified multiple resting-state networks (RSNs) in the piglet brain, including the visual (VIS), executive control (EX), sensorimotor (SM), cerebellar (CERE), and default mode (DMN) networks [9]. However, it has yet to be examined how these RSNs change in response to TBI.

Our research group has developed and characterized a controlled cortical impact (CCI) piglet TBI model with cognitive and motor function deficits [21-23]. The pig was selected as a model species as the pig brain has more comparable anatomy and

physiology to the human brain than the rodent, the most commonly used TBI animal model. Both pig and human brains are gyrencephalic, unlike the lissencephalic rodent brain, which is directly correlated with brain connectivity and complexity [24-26]. In the gyrencephalic brain, TBI mechanical stress is focused near the base of the sulci and is more heterogeneously distributed relative to the lissencephalic brain [27]. In addition, brain size plays a crucial role in TBI. Smaller rodent brains can tolerate greater angular acceleration forces opposed to larger pig and human brains. In the CCI TBI piglet model, deficits associated with the SM network have been observed, including gait changes such as increased stance time, decreased velocity, percent of two limb support, and proprioception [23,28,29]. These changes are commonly observed in human TBI patients with SM damage and are due to a loss of coordination, lack of bilateral arm/leg coupling, and reduced agility and balance [30]. Additionally, TBI piglets displayed impairments in exploratory behaviors and spatial memory formation, which are associated with the EX network [23]. The similarities between pig and human brain anatomy, physiology, brain network activity, cognition, and motor function responses to TBI make the pig an attractive translational model to study functional network changes due to TBI.

In this study, both rs- and tb-fMRI are employed to examine the functional connectivity disruptions caused by TBI using a porcine CCI model. A reference pig functional connectivity atlas was constructed for seven different networks using a previously published pig anatomical atlas [31]. Functional connectivity activation maps for each individual piglet were generated using two methods: a group independent component analysis (ICA) with back reconstruction method and a group sparse dictionary learning (sDL) with dual regression method. The activation maps generated from each

method were compared to each reference atlas using Pearson spatial correlation coefficients and mean ratios to evaluate differences between healthy control and TBI groups. To further locate and evaluate significantly different voxels between the TBI and control groups, a nonparametric permutation test was performed using the activation maps generated by the sDL analysis.

2. Results

2.1 Reference atlas analysis

2.1.1 rs-fMRI detects differences in VIS and EX networks

When examining the activation maps obtained from the rs-fMRI data, significant decreases ($p<0.05$) in the Pearson spatial correlation coefficients and mean ratios for the TBI group in comparison to the control group for the EX network were observed using both ICA and sDL (Table 1a and Figure 1). Significant decreases in individual structures comprising the EX network (the primary somatosensory, dorsolateral prefrontal, and anterior prefrontal cortices) were observed using sDL (Figure 1b), and although not significant, similar decreasing patterns were observed for these structures using ICA (Figure 1a). However, contradictory decreasing and increasing significant differences were observed in the insular and ventral anterior cingulate cortices for ICA and sDL, respectively. No statistical differences were observed for the orbitofrontal or dorsal anterior cingulate cortices using either method.

No statistical differences were observed in the TBI group compared to the control group for the SM or CERE networks (Table 1a and Figure 2). However, within the SM network, a significant decrease in the premotor cortex was observed using ICA (Figure 2a), and a similar decrease was observed using sDL (Figure 2b). A consistent increasing trend for the somatosensory associative cortex was also observed, while no statistical difference was observed for the primary motor cortex.

For the VIS network, a significant decrease was observed using sDL (Table 1a and Figure 3b), and although a significant difference was not observed when using ICA to detect functional networks, a similar decreasing pattern was observed (Figure 3a).

When examining the individual structures comprising the VIS network, the primary and associative visual cortices displayed the same significant decreases as the whole network for sDL, and ICA displayed similar decreasing patterns. No statistical difference was observed for the secondary visual cortex using either sDL or ICA. However, both methods consistently showed decreased activation compared to controls for this anatomical structure.

No statistical differences were observed in the TBI group in comparison to the control group for the DMN, SAL, or BAS networks using either method (Table S1 and Figures S1-3 of the Supplementary Material). Overall, relatively low Pearson values and mean ratios were observed for these networks, even for the control group. Therefore, it's possible that these networks weren't able to be properly detected.

In Figures 1-3, single plane representative images of two-dimensional activation maps are also presented for the control and TBI group. However, it is important to note that these images only show a cross-section of the brain, whereas the Pearson values and mean ratios are calculated based on the entire three-dimensional volume of the brain. Additional cross-sectional images in all three planes for each network and method for the rs-fMRI analysis are provided in Figures S4a,b and S5a,b.

2.1.2 tb-fMRI detects differences in EX and SM networks

When examining the activation maps obtained from the tb-fMRI tactile stimulus data, a significant decrease in the EX network using ICA was observed (Table 1b and Figure 4a), and a similar decreasing trend was observed using sDL (Figure 4b). Within the EX network, the primary somatosensory and insular cortices displayed similar

significant decreases using ICA. sDL also found a significant decrease in the primary somatosensory cortex and displayed a similar decreasing pattern in the insular cortex. An increasing trend in the ventral anterior cingulate cortex was observed using ICA and supported by a similar increasing pattern observed using sDL. No statistical differences were observed for the dorsolateral prefrontal, anterior prefrontal, orbitofrontal, or dorsal anterior cingulate cortices using either method.

A significant decrease in the TBI group in comparison to the control group was also observed for the SM network using ICA to analyze the tb-fMRI tactical stimulus data (Table 1b and Figure 5a), and the sDL results showed a similar decreasing pattern (Figure 5b). Within the SM network, the primary motor and somatosensory associative cortices displayed significant decreases using ICA, and sDL displaying similar decreasing patterns. Although not significant, a consistent decreasing pattern was also observed for the premotor cortex for both methods, and a consistent increase was observed in TBI animals in the CERE network (Table 1b and Figure 5a,b).

When examining the activation maps obtained from the tb-fMRI visual stimulus data, no statistical difference in the Pearson spatial correlation coefficients or mean ratios for the TBI group in comparison to the control group were observed for the VIS network or any of its individual anatomical structures using ICA or sDL (Table 1b and Figure 6). Representative images of two-dimensional activation maps generated using sDL for the tb-fMRI analysis for the VIS, EX, and SM networks are provided in Figure S4c,d.

Single plane representative images of two-dimensional activation maps are also presented for the control and TBI group in Figures 4-6. Again, it is important to note that these images only show a cross-section of the brain, whereas the Pearson values and

mean ratios are calculated based on the entire three-dimensional volume of the brain. Additional cross-sectional images in all three planes for each network and method for the tb-fMRI analysis are provided in Figures S4c,d and S5c,d.

2.2 Permutation analysis

2.2.1 Permutation analysis of rs-fMRI detects disruptions in SM and CERE networks

Since sDL outperformed ICA at detecting the examined networks in the control group, as observed by the higher measured Pearson values and mean ratios (Figures 1-6), permutation analysis was performed using the activation maps generated using the sDL methodology. The percentages of voxels that contained significantly decreasing and increasing activation values for the TBI group in comparison to the control group for each network and individual anatomical structure for the rs- and tb-fMRI data are shown in Figure 7.

When examining the activation maps obtained from the rs-fMRI data using permutation analysis, the EX network, as well as all comprising individual anatomical structures except the insular (EX5) and dorsal anterior cingulate (EX7) cortices, contained higher percentages of significantly decreasing voxels than increasing voxels (>9.0% decreasing in comparison to <3.0% increasing; Figure 7a). This agrees with the trends observed in rs-fMRI reference atlas analysis (Figures 1). However, it was observed that the insular cortex only contained a small percentage of significantly increasing voxels (1.3%), and the dorsal anterior cingulate cortex contained relatively similar percentages of significantly decreasing and increasing voxels (7.4% and 9.0%, respectively).

The SM network as a whole also contained relatively similar percentages of significantly decreasing and significantly increasing voxels (7.2% and 5.5%, respectively), with the primary motor (SM1) and premotor (SM3) cortices showing relatively higher percentages of significantly decreasing voxels (11.5% and 11.1% decreasing in comparison to 1.9% and 0.0% increasing, respectively) and the somatosensory associative cortex (SM2) showing a relatively higher percentage of significantly increasing voxels (9.5% increasing in comparison to 3.6% decreasing; Figure 7a). The CERE network contained a slightly higher percentage of significantly increasing voxels (11.7%) than significantly decreasing voxels (8.5%). Except for the primary motor cortex, these observations also agree with the trends observed in rs-fMRI reference atlas analysis (Figure 2). Although no statistical differences were observed in the Pearson values and mean ratios when examining the SM and CERE networks, relatively large percentages of voxels within these networks are observed to be significantly different using permutation analysis.

The VIS network, as well as all of its comprising individual anatomical structures (primary, secondary, and associative visual cortices), also contained relatively higher percentages of significantly decreasing voxels than increasing voxels (19.2%, 21.5%, 14.0% and 25.2% decreasing in comparison to 5.3%, 4.1%, 8.5% and 0.0% increasing, respectively; Figure 7a). Figure 8a displays representative images of two-dimensional permutation maps generated for the rs-fMRI analysis for the VIS, EX, and SM networks and their corresponding reference atlases overlaid on the template pigs' T1-weighted anatomical images.

2.2.2 Permutation analysis of tb-fMRI detects differences in the VIS network

When using permutation analysis to examine the activation maps obtained from the tb-fMRI tactile stimulus data, both the EX and SM networks contained relatively higher percentages of significantly decreasing voxels than increasing voxels (8.2% and 14.6% decreasing in comparison to 0.6% and 0.0% increasing, respectively; Figure 7b). In the EX network, the primary somatosensory (EX1) and insular (EX5) cortices contained the largest percentages of significantly decreasing voxels (12.2% and 12.8%, respectively), while all other structures contained relatively small percentages of significantly different voxels (<1.0%). In the SM network, all three structures contained relatively high percentages of significantly decreasing voxels (>8.0%). These observations agree with the trends observed in the pig reference atlas analysis (Figures 4-5). The CERE network, which showed a slight increasing trend in the pig reference analysis (Figure 5), contained the same small percentage of significantly decreasing and significantly increasing voxels (1.3% each) for the permutation analysis (Figure 7b).

When using permutation analysis to examine the activation maps obtained from the tb-fMRI visual stimulus data, the VIS network, including the primary (VIS1) and secondary visual (VIS2) cortices, contained higher, although relatively similar, percentages of significantly decreasing voxels than significantly increasing voxels (11.9% in VIS, 13.0% in VIS1, and 11.8% in VIS2 decreasing in comparison to 8.9% in VIS, 10.9% in VIS1, and 7.1% in VIS2 increasing; Figure 7b). The associative visual cortex (VIS3) contained similarly small percentages of significantly decreasing and significantly increasing voxels (2.7% and 2.0%, respectively). Although no statistical difference was observed in the Pearson values and mean ratios when examining the VIS

network using the pig reference atlas analysis (Figure 6), relatively large percentages of voxels within this network and its individual anatomical structures were observed to be significantly different using permutation analysis.

Figure 8b displays representative images of two-dimensional permutation maps generated for the tb-fMRI analysis for the VIS, EX, and SM networks and their corresponding reference atlases overlaid on the template pigs' T1-weighted anatomical image.

3. Discussion

In this study, functional networks were examined using rs- and tb-fMRI in a pediatric porcine model of TBI and healthy age-matched controls to determine changes in functional connectivity after insult. Capitalizing on the advantages of both ICA and sDL, functional connectivity disruptions in the piglet TBI brain were consistently detected in the EX and VIS networks using rs-fMRI, as well as the EX and SM networks using tb-fMRI (Table 1, and Figures 1, 3, 4, and 5). Pearson values and mean ratios showed significant reductions in these networks in the TBI group relative to the control group. The relatively high percentages of significantly decreasing voxels within these networks determined by the permutation analysis also provides additional evidence of these disruptions (Figure 7). Although statistically different Pearson values and mean ratios were not observed for the SM and CERE networks using rs-fMRI (Figure 2) or the VIS network using tb-fMRI (Figure 6), permutation analysis showed indications of abnormal network activity masked by network compensation, as evident by the relatively large and similar percentages of significantly decreasing and increasing voxels observed in these networks (Figure 7). Therefore, this study demonstrates significant changes in clinically relevant functional networks using rs-fMRI and tb-fMRI through ICA, sDL, and permutation analysis approaches in a piglet TBI model.

Children who experience moderate-to-severe TBI often demonstrate functional weakening in brain circuitry and have associated long-term deficits when compared to their peers [32,33]. It has been previously demonstrated that piglets have significant parallels to children in terms of TBI pathophysiology (e.g., intracerebral swelling, white matter damage) and cognitive, behavioral, and motor deficits [8], making the pig a valuable

preclinical model to study the dynamic changes in brain functional networks after TBI. In pediatric TBI patients, damage that occurs to the developing brain often results in abnormal EX network function and long-term functional deficits in cognition, including impaired cognitive flexibility, problem solving, and behavioral control [34-37]. In this study, reduced overall EX network activation was observed using rs-fMRI with ICA and sDL analyses (Table 1 and Figure 1). Specifically, brain activity reductions were observed in the primary somatosensory, dorsolateral, and anterior prefrontal cortices using sDL [38,39]. In a previous study with an identical CCI TBI piglet model [21], T-maze testing showed that TBI animals made significantly more wrong choices and took four days longer to make correct choices as compared to control animals. These results suggest reduced problem-solving ability and cognitive flexibility, which support the findings of reduced EX network activity in this study. In a comparable preclinical study, TBI pigs underwent T-maze testing where they learned that a food reward was in a specific arm of the maze [29]. However, once the reward was reversed to the alternate arm, TBI animals spent significantly more time in the old food location attempting to find the reward in comparison to sham pigs, indicating problems in relearning and executive function after insult. TBI pigs have also shown increased fear and anxiety behaviors, including running and escape behaviors in open field testing [40]. Fear and anxiety are modulated by structures associated with the EX network, such as the dorsal anterior cingulate cortex [41]. The results presented here in this work indicate that the entire EX network is significantly impaired, which accurately models what has been shown in pediatric TBI patients [42] and correlates with previous cognitive and behavioral deficits observed in the piglet TBI model [21].

Moderate-to-severe TBI in children may also give rise to significant gait deficits, including a reduction in velocity, cadence, and stride length [43-45], which are correlated with abnormal connectivity throughout the motor networks [46,47]. fMRI studies in humans have demonstrated that the CERE network is also involved in lower limb proprioception and thus gait [48]. The coordination between the SM and CERE networks is important for basic motor tasks, such as limb movement control and processing of touch [49,50], and TBI leads to aberrant communication between these networks. These gait abnormalities have been characterized in TBI piglets and similarly resulted in decreased velocity, cadence, and stride length [22,23]. In this work, rs-fMRI ICA analysis showed a significant decrease in the premotor cortex activity of the SM network after injury (Table 1 and Figure 2), which is responsible for motor planning [51]. The premotor cortex is a vital node in the SM network for accurate performance of goal-oriented tasks [52]. This reduction in premotor activity in TBI pigs likely explains previously observed deficits in motor control.

Functional changes in the EX network, known to be associated with the sense of touch and pain [16], and the SM network, known to be associated with sensory processing, were examined using tactile stimulus and tb-fMRI. When a tactile stimulus was applied, ICA tb-fMRI analysis revealed the overall EX network (including the primary somatosensory, dorsolateral prefrontal, and insular cortices) and the overall SM network (including the primary motor and somatosensory associative cortices) followed an expected decrease in brain activation after injury (Table 1 and Figures 4-5). Notably, the primary somatosensory cortex is responsible for receiving tactile information from the body and contributes to the integration of sensory and motor signals for skilled movements that involve other impacted structures, including the primary motor cortex [53].

Thus, an external stimulus, such as a tactile pressure, allows for isolated investigation of individual networks.

Additionally, pigs and humans have similar visual acuity, ability to distinguish colors, and maturational and topographic similarities related to visually evoked responses [54]. The visual cortex in the pig brain is especially similar to the corresponding human visual cortex. Here, in a piglet model of TBI, a significant decrease in the VIS network in TBI animals utilizing rs-fMRI data analyzed by sDL was observed (Table 1 and Figure 3). Although statistically different Pearson values and mean ratios were not observed for the VIS network using tb-fMRI (Figure 6), the permutation analysis shows that this network contained relatively high and similar percentages of significantly decreasing and increasing voxels (Figure 7b). This likely indicates that disruptions in this network were present, and certain areas of the network were compensating for the damaged areas. The decreasing voxels correspond to damaged areas where the TBI group showed reduced activation values in comparison to the control group, and the increasing voxels correspond to the compensating areas where the TBI group showed elevated activation values in comparison to the control group. Situations in which similar percentages of significantly decreasing and increasing voxels are also observed for the SM and CERE networks using rs-fMRI (Figure 7a) and for the dorsal anterior cingulate cortex of the EX network. Again, this indicates that the areas showing high percentages of increasing voxels within these networks and region are likely compensating for damaged areas (the areas showing high percentages of decreasing voxels).

In this work, the ICA and sDL methods showed consistent patterns, with both detecting disruptions in six of the same individual anatomical structures (the primary

visual and associative visual cortices of the VIS network, the primary somatosensory, dorsolateral prefrontal, and anterior prefrontal cortices of the EX network, and the premotor cortex of the SM network) using rs-fMRI and five of the same individual anatomical regions (the primary somatosensory, insular, and ventral anterior cingulate cortices of the EX network and the primary motor and somatosensory associative cortices of the SM network) using tb-fMRI (Table 1). However, despite the consistency in similarly detected disrupted structures by both ICA and sDL, some differences were also observed. Both methods detected disruptions in the insular and ventral anterior cingulate cortices of the EX network using rs-fMRI (Table 1 and Figure 1); however, ICA detected a significant decrease in connectivity of the TBI group in comparison to the control group, whereas sDL detected a significant increase. Previous work has shown that the ventral anterior cingulate cortex can be effected by anesthesia [9,55], which may lead to suppressed activations and unreliable measurements in this region. Additionally, some non-significant differing trends between ICA and sDL were also observed within other individual anatomical regions for both rs- and tb-fMRI (regions not denoted by $ in Table 1). However, relatively high consistency was observed across the two methods overall. The tb-fMRI analysis was more consistent with all four networks and 10 out of 13 individual anatomical structures showing similar trends. rs-fMRI analysis was less consistent with only two of the four networks and eight out of 13 individual anatomical regions showing similar trends.

rs-fMRI and tb-fMRI are inherently different. rs-fMRI measures spontaneous synchronized fluctuations in the BOLD signal due to neural firing, whereas tb-fMRI measures fluctuations provoked by performing a specific task or applying a stimulus. Not

only are the signal patterns generated by each of these methods different in humans [56], but recent work suggests that two different neurological processes may govern the underlying mechanisms behind rs- and tb- responses [57]. Other previous works present contradictory results with some suggesting that measured rs- responses are composed of tb- responses and vice versa [15,17-19,58-60]. For example, an earlier study suggested that individual tb- responses are inherent to the individual's brain and can be predicted from rs- measurements [61]. However, several other human studies yielded evidence that tb- activation of cortical networks shape the pattern of correlated rs- activity [58-60]. It was shown that training for a shape discrimination task induced a negative correlation in the rs- response between the visual cortex and fronto-parietal attentional areas [62]. This study demonstrated that rs- activity may be affected by physiological network level neuro-plasticity arising from experience-driven co-activation of cortical circuitries leading to an anti-correlation between the rs- and tb- responses [63]. It is still unclear whether or how rs- and tb- functional connectivity relate to each other; therefore, the two different types of functional connectivity may be affected or disrupted differently by TBI, as well as additional factors such as anesthesia [55,64,65]. This may explain differences between the rs- and tb- results.

The differing neurological processes governing rs- and tb- responses may also explain the differences in sensitivity of ICA and sDL to the two types of fMRI observed in this study. sDL appeared to be more sensitive to changes in rs- activity between the TBI and control groups, as observed by lower p-values and more individual anatomical structures showing significant differences (Table 1), while ICA seemed to be more sensitive to changes in tb- activity. Recent work also showed that sDL was superior to

ICA in detecting healthy RSNs using a pig model [9]. sDL is different from ICA in that it does not assume independent signal components. It allows for the possibility of the signal to contain independent and/or dependent components. As discussed above, it is still unclear whether or how rs- and tb- functional connectivity relate to each other. Therefore, using an independent (ICA) or dependent-allowing (sDL) signal decomposition may be more beneficial depending on whether rs- or tb- data is being evaluated.

This work demonstrates for the first time in a pediatric piglet TBI model that rs- and tb-fMRI can detect functional connectivity disruptions caused by TBI with relatively high consistency in activation trends utilizing ICA and sDL analysis approaches. Significant differences ($p<0.05$) were observed in the VIS, EX, and SM networks between the control and TBI groups, as well as within several individual anatomical structures. Functional disruptions spanning the entire brain, well beyond the primary lesioned cerebral cortex, in TBI pigs were observed, which agrees with clinical studies that found moderate-to-severe TBIs result in whole brain functional connectivity alterations and diminished network dynamics [66,67]. This study opens the door for future research to test the effects of novel therapies that alter brain network connectivity and improve recovery in the piglet TBI model; and thus, hasten the translation of treatments to the clinical patient population.

4. Materials and Methods

4.1 Subjects

Four-week-old castrated male and intact female Landrace-cross piglets (n=12) were used in this study. TBI was induced in five (n=5) pigs using the previously published procedure [23], while the remaining seven (n=7) served as controls (normal, healthy pigs). All experimental procedures were approved by the Institutional Animal Use and Care Committee (IAUCC, University of Georgia; Protocol Number A2019 07-007-Y1) and performed in accordance with the National Institutes of Health (NIH) Guidelines for the Care and Use of Laboratory Animals. Pigs were group housed in a Public Health Service (PHS) and Association for Assessment and Accreditation of Laboratory Animal Care (AAALAC) approved facility at room temperature (approximately 27°C) with a 12-hour light/dark cycle. Pigs encountered daily enrichment through toys and human contact and were fed standard pig starter 1 diets.

4.2 Controlled cortical impact

Pigs were anesthetized, and a periosteal block (0.5% bupivacaine; 2 mg/kg; Pfizer) at the cranium was applied under aseptic technique. A craniectomy was performed, approximately 20mm in diameter, to expose the underlying dura at the left anterior junction of the coronal and sagittal sutures. Each pig was secured in a controlled cortical impactor device (University of Georgia Instrument Design and Fabrication Shop, Athens, GA), and a 15mm impactor tip was positioned over the intact dura to induce injury with the following parameters: velocity of 4m/s, depth of depression of 9mm, and

dwell time of 400ms. These parameters were based on previous studies to generate a moderate TBI [23,68,69].

Pre-operatively, TBI pigs received antibiotics (ceftiofur crystalline free acid; 5mg/kg intramuscular (IM); Zoetis). Pre-induction sedation and analgesia for TBI surgery was achieved using buprenorphine (0.01 mg/kg IM; Covetrus), midazolam (0.2 mg/kg IM; Heritage), and xylazine (2 mg/kg IM; VetOne). Prophylactic lidocaine (0.5 mL 2% lidocaine; VetOne) was topically applied to laryngeal folds, and propofol (to effect, intravenous (IV); Zoetis) was administered to achieve intubation. Anesthesia was maintained with isoflurane (2.0%; Abbott Laboratories) in oxygen. Post-operatively, once vitals returned to normal ranges, they were monitored every four hours for 24 hours and then twice a day. For pain and inflammation maintenance, pigs received buprenorphine (0.01 mg/kg IM; Covetrus) every eight hours for 24 hours and banamine (2.2 mg/kg IM; Merck) every 12 hours for 24 hours, and then every 24 hours for 72 hours post-operatively. TBI pigs displayed contralateral ataxia. Healthy control pigs did not receive pre-operative antibiotics or post-operative medications.

4.3 Data acquisition

One day post-TBI, pigs were initially sedated using xylazine (2 mg/kg IM; VetOne), ketamine (4 mg/kg IM; Henry Schein), and midazolam (0.2 mg/kg IM; Heritage). Then mild anesthesia was maintained with inhalational isoflurane (1.5%; Abbott Laboratories) in oxygen in order to keep the pigs sedated while reducing anesthetic agent interference with pig brain neural activity and neurovascular coupling.

Using a GE 32-channel fixed-site Discovery MR750 3.0 Tesla MRI magnet and 8-channel knee coil, T1-weighted anatomical, rs-fMRI, and tb-fMRI data was acquired using the following two sequences: 1.) 3D fast spoiled gradient echo (FSPGR) sequence (repetition time TR=5.5s, echo time TE=2.1ms, flip angle FA=9°, field-of-view FOV=12.8x12.8x6.4cm, slice thickness=1mm, a reconstruction matrix size of 256x256x112 (resulting in cubic voxels of 0.5mm), axial slice plane, and an acquisition time of 10min 57s), and 2.) gradient echo-planar imaging (EPI) sequence (TR=3s, TE=30ms, FA=80°, FOV=12.8x12.8x6.2cm, a matrix size of 96x96x31, coronal slice plane, 305 total volumes for rs-fMRI (an acquisition time of 15min 15s) and 125 volumes for tb-fMRI (6min 15s)).

The tb-fMRI data was acquired in a block design paradigm with the first 15s being dead time (stimulus off) to allow the magnetization to reach a steady state, followed by six repetitions of 30s stimulus ON and 30s stimulus OFF cycles. The visual stimuli were generated bilaterally using a high-intensity 300W xenon arc lamp (Cermax, Excelitas Technologies, Fermont, CA) and a specially made high-fidelity fiber optic bifurcated cable (Atlas Specialty Lighting). This lamp produced a color rendering index (CRI) of 98, which demonstrated similarity to noon-day sunlight (CRI=100). The pig was in supine position, and the fiber optic cable was positioned to direct light into both the pig's left and right closed eyes. The tactile stimuli were also generated bilaterally by placing MRI-safe plastic hemostats with locking mechanisms on the inguinal region to activate the saphenous nerve that innervates the skin of the inner hind limbs [70].

The rs-fMRI data was acquired for all twelve pigs (n=7 controls and n=5 TBIs), while tb-fMRI data with visual stimuli was acquired for eleven pigs (n=6 controls and

n=5 TBIs) and tb-fMRI data with tactile stimuli was acquired for nine pigs (n=4 controls and n=5 TBIs).

4.4 Data preprocessing

Each fMRI dataset was preprocessed to realign images to correct for motion and perform slice-timing correction using Statistical Parametric Mapping (SPM) software [71]. For motion correction, all acquired rs-fMRI and tb-fMRI volumes for each pig were aligned to that pig's corresponding first acquired rs-fMRI volume. All fMRI datasets and T1-weighted anatomical images were skull stripped by manual slice-by-slice segmentation. The first five volumes of each fMRI dataset were removed to allow the magnetization to reach a steady state; therefore, 300 total volumes were remaining for rs-fMRI data and 120 for tb-fMRI data.

To determine spatial activation maps for each individual pig ($\boldsymbol{\alpha_i}$), functional connectivity analysis was performed using two methods: 1) group independent component analysis (ICA) with back reconstruction and 2) group sparse dictionary learning (sDL) with dual regression. First, group datasets were created and group activation maps were generated using a previously published procedure [9]. In summary, one pig from the control group and one from the TBI group was selected as the template pig based on visual inspection of the fMRI data and the remaining pigs within each group were spatially normalized to the template pig using the first volume of each rs-fMRI dataset to calculate a transformation. The calculated transformation for each pig was then applied to the rest of the prior motion-corrected volumes (including both rs-fMRI and tb-fMRI volumes) of that corresponding pig. Spatial normalization was accomplished using

SPM's Old Normalize algorithm [71]. For the control group and TBI group, separate group datasets for rs-fMRI, tb-fMRI with visual stimuli, and tb-fMRI with tactile stimuli were created by temporally concatenating the corresponding fMRI time series of the spatially normalized pigs at each voxel.

Therefore, a total of six group datasets were created: a rs-fMRI control group dataset with 2100 volumes (7 pigs with 300 volumes each), a rs-fMRI TBI group dataset with 1500 volumes (5 pigs with 300 volumes each), a tb-fMRI with visual stimuli control group dataset with 720 volumes (6 pigs with 120 volumes each), a tb-fMRI with visual stimuli TBI group dataset with 600 volumes (5 pigs with 120 volumes each), a tb-fMRI with tactile stimuli control group dataset with 480 volumes (4 pigs with 120 volumes each), and a tb-fMRI with tactile stimuli TBI group dataset with 600 volumes (5 pigs with 120 volumes each).

4.5 Data analysis

Group ICA with back reconstruction and group sDL with dual regression were performed on each group dataset to generate spatial activation maps for each individual pig ($\boldsymbol{\alpha_i}$).

Spatial group ICA was performed using the Group ICA of fMRI Toolbox's (GIFT) Infomax algorithm [72], which includes dimensionality reduction using principle component analysis (PCA), to produce group activation maps ($\boldsymbol{\alpha_g}$). Back reconstruction was then performed using $\boldsymbol{\alpha_g}$ and the results from the data reduction step to obtain $\boldsymbol{\alpha_i}$ for each individual pig [73]. Both the group and individual datasets were decomposed into 70 independent components, which is a value commonly used throughout the literature.

sDL was performed using the SPArse Modeling Software (SPAMS) toolbox [74] to minimize the equation

$$\min_{\boldsymbol{D}\in C} \lim_{n\to+\infty} \frac{1}{n}\sum_{j=1}^{n}\left(\min_{\alpha^j} \frac{1}{2}\left\|\boldsymbol{s}^j - D\boldsymbol{\alpha}^j\right\|_2^2 + \lambda\left\|\boldsymbol{\alpha}^j\right\|_1\right) \quad (1)$$

where $\boldsymbol{s}$ is the fMRI dataset, $\boldsymbol{D}$ is the dictionary or associated time series, λ is a sparsity parameter, and n is the number of atoms or dictionary elements the fMRI data is decomposed into.

When performing the sDL analysis, $\boldsymbol{\alpha_g}$ was first obtained by minimizing Eq. (1) for each group dataset, and dual regression was then performed to obtain $\boldsymbol{\alpha_i}$ for each individual pig. The first regression used $\boldsymbol{\alpha_g}$ and each pig's individual rs-fMRI data ($\mathbf{s_i}$) to determine an individual dictionary ($\boldsymbol{D_i}$) or associated time series using linear least squares to solve the equation $\mathbf{s_i} = \boldsymbol{D_i}\,\boldsymbol{\alpha_g}$. The second regression then used each pig's $\boldsymbol{D_i}$ and $\mathbf{s_i}$ to determine $\boldsymbol{\alpha_i}$ by minimizing Eq. (1).

Note that the difference between back reconstruction and dual regression is that back reconstruction uses the group result ($\boldsymbol{\alpha_g}$) and the results of the data reduction step to generate $\boldsymbol{\alpha_i}$, whereas dual regression uses the group result ($\boldsymbol{\alpha_g}$) and the original fMRI data ($\mathbf{s_i}$) [75]. When performing sDL, it is not common to perform dimensionality reduction, and the use of a complete or over-complete dictionary is often employed to achieve sparseness [74]. For this study, dictionaries with n=300 and n=120 were used for the rs-fMRI and tb-fMRI datasets, respectively, as these values correspond to the time series length (number of volumes) of the acquired fMRI datasets. A sparsity parameter λ=0.15 was also used when solving for all individual and group activation maps, which was based on a previous optimization procedure [9].

All individual pig activation maps were normalized by the maximum activation value from the corresponding group dataset, thresholded using a Z-score of one, and then spatially normalized to the template pig's anatomical space. Spatial normalization was accomplished using SPM to calculate a spatial transformation between the template pig's first rs-fMRI volume and its corresponding T1-weighted anatomical data. The transformation was then applied to the activation maps for all pigs within the template pig's group. When applying these transformations, voxel size was reshaped to 1mm cubed, opposed to the 0.5mm cubed voxels of anatomical space, in order to reduce the computational size of the activation map datasets.

4.6 Pig reference functional connectivity atlases and activation map analysis

Next, reference pig functional connectivity atlases were created also using the same previously published procedure [9]. First, a standard pig brain atlas [76] was spatially normalized to the T1-weighted anatomical space of each template pig. Spatial normalization was accomplished by calculating a spatial transformation using T1-weighted anatomical data provided in the same space as, and associated with, the standard pig brain atlas and the T1-weighted anatomical data acquired for each template pig. The calculated transformation was then applied to the atlas, and when applying this transformation, voxel size was again reshaped to 1mm cubed. Using the anatomical structures provided in Table 1 and Table S1 of the Supplementary Material, seven reference functional connectivity atlases were created for each pig: visual (VIS), executive control (EX), sensorimotor (SM), cerebellar (CERE), default mode (DMN), salience (SAL), and basal ganglia (BAS) networks.

With the activation maps and reference atlases in the same space, Pearson spatial correlation coefficients and mean ratios (defined as mean activation value within a given atlas divided by the mean activation value outside of the given atlas) were calculated for each activation map and reference atlas. For activation maps generated using the ICA analysis, the map for each fMRI dataset and reference atlas that produced the largest Pearson value was determined. From these maximal maps, Pearson values and mean ratios were then calculated for each individual anatomical structure comprising each corresponding reference atlas, as listed in Tables 1 and S1 under each network. Note that the mean ratio for individual anatomical structures was calculated as the mean activation value within a given anatomical region divided by the mean activation value outside of the full corresponding atlas. For the CERE atlas, the individual lobes were not examined. Instead, the CERE network is discussed as a whole in conjunction with the SM network, as it has been shown that coordination between these networks is necessary for basic motor tasks to occur [48].

Since sDL generates multiple similar activation maps with near maximum Pearson values, the three maps (corresponding to three separate atoms in the learned dictionary) for each fMRI dataset and reference atlas that produced the largest Pearson values were determined and averaged to produce final activation maps. Pearson values and mean ratios were then re-calculated for these final maps and each corresponding reference atlas, as well as for each individual anatomical structure comprising each corresponding reference atlas.

P-values associated with the Pearson values and mean ratios were calculated between the TBI group and the control group for each network as a whole, as well as for

each individual anatomical region, using a two-sample t-test assuming the groups had unequal variances. For each metric, the groups were considered to be significantly different if $p<0.05$, and a network or anatomical structure was only considered significantly different if the p-values for both the Pearson values and mean ratios were below 0.05.

4.7 Permutation analysis

To locate significantly different voxels between the TBI and control groups, permutation tests were performed using the activation maps generated by the sDL analysis [77]. Pigs in the TBI group were registered to the control group using SPM's Old Normalize algorithm [71]. Spatial normalization was accomplished by calculating a spatial transformation between the T1-weighted anatomical datasets of the template pigs for the TBI and control groups. The transformation was then applied to the activation maps for all pigs within the TBI group, which had previously been spatially normalized to the TBI template pig's T1-weighted anatomical space (Section 2.5).

For permutation tests, the null hypothesis stated that no statistical difference existed between the mean activation values of the TBI and control groups [77]. For N_C pigs in the control group and N_T pigs in TBI group, there were $C_{N_C+N_T}^{N_C}$ possible combinations of arranging all pigs into the two groups. For every possible combination, the difference in the mean activation values of the two groups

$$T = mean_C - mean_T \qquad (2)$$

were calculated on a voxel-by-voxel basis. For each voxel, if the true experimental combination of control and TBI groups created a mean difference (T_{actual}) among the largest five percent of all calculated *T* values (α-level of 0.05), the null hypothesis was rejected, and the activation values of the TBI group were considered to be significantly decreased in comparison to the control group. If T_{actual} was among the lowest five percent (negative number), then the activation values of the TBI group were considered to be significantly increased in comparison to the control group. Permutation tests were performed for every voxel throughout the brain, and the percentage of significantly decreasing and increasing voxels within each network's corresponding reference atlas and comprising individual anatomical structures were calculated.

References

1 Peterson, A. B., Xu, L., Daugherty, J., Breiding, M. J. *Surveillance Report of Traumatic Brain Injury-related Emergency Department Visits, Hospitalizations, and Deaths*, 2014).

2 Faul M, X. L., Wald MM, Coronado VG. Traumatic Brain Injury in the United States: Emergency Department Visits, Hospitalizations and Deaths 2002–2006. *Centers for Disease Control and Prevention, National Center for Injury Prevention and Control* (2010).

3 Conrad, M. S., Dilger, R. N. & Johnson, R. W. Brain growth of the domestic pig (Sus scrofa) from 2 to 24 weeks of age: a longitudinal MRI study. *Dev Neurosci* **34**, 291-298, doi:10.1159/000339311 (2012).

4 Maas, A. I., Stocchetti, N. & Bullock, R. Moderate and severe traumatic brain injury in adults. *Lancet Neurol* **7**, 728-741, doi:10.1016/S1474-4422(08)70164-9 (2008).

5 Laatsch, L., Jobe, T., Sychra, J., Lin, Q. & Blend, M. Impact of cognitive rehabilitation therapy on neuropsychological impairments as measured by brain perfusion SPECT: a longitudinal study. *Brain Inj* **11**, 851-863, doi:10.1080/026990597122927 (1997).

6 Laatsch, L., Pavel, D., Jobe, T., Lin, Q. & Quintana, J. C. Incorporation of SPECT imaging in a longitudinal cognitive rehabilitation therapy programme. *Brain Inj* **13**, 555-570, doi:10.1080/026990599121304 (1999).

7 Laatsch, L. K., Thulborn, K. R., Krisky, C. M., Shobat, D. M. & Sweeney, J. A. Investigating the neurobiological basis of cognitive rehabilitation therapy with fMRI. *Brain Inj* **18**, 957-974, doi:10.1080/02699050410001672369 (2004).

8 Kinder, H. A., Baker, E. W. & West, F. D. The pig as a preclinical traumatic brain injury model: current models, functional outcome measures, and translational detection strategies. *Neural regeneration research* **14**, 413 (2019).

9 Simchick, G. *et al.* Pig Brains Have Homologous Resting State Networks with Human Brains. *Brain connectivity* (2019).

10 Studerus-Germann, A. M., Thiran, J. P., Daducci, A. & Gautschi, O. P. Diagnostic approaches to predict persistent post-traumatic symptoms after mild traumatic brain injury - a literature review. *Int J Neurosci* **126**, 289-298, doi:10.3109/00207454.2015.1033620 (2016).

11 Chen, J. K., Johnston, K. M., Collie, A., McCrory, P. & Ptito, A. A validation of the post concussion symptom scale in the assessment of complex concussion using cognitive testing and functional MRI. *J Neurol Neurosurg Psychiatry* **78**, 1231-1238, doi:10.1136/jnnp.2006.110395 (2007).

12 Henry, L. C. *et al.* Metabolic changes in concussed American football players during the acute and chronic post-injury phases. *BMC Neurol* **11**, 105, doi:10.1186/1471-2377-11-105 (2011).

13 Messe, A. *et al.* Specific and evolving resting-state network alterations in post-concussion syndrome following mild traumatic brain injury. *PLoS One* **8**, e65470, doi:10.1371/journal.pone.0065470 (2013).

14 Shehzad, Z. *et al.* The Resting Brain: Unconstrained yet Reliable. *Cerebral Cortex* **19**, 2209-2229, doi:10.1093/cercor/bhn256 (2009).

15 Winkler, A. M. *et al.* Cortical thickness or grey matter volume? The importance of selecting the phenotype for imaging genetics studies. *NeuroImage* **53**, 1135-1146, doi:https://doi.org/10.1016/j.neuroimage.2009.12.028 (2010).

16 Smith, S. M. *et al.* Correspondence of the brain's functional architecture during activation and rest. *Proceedings of the National Academy of Sciences* **106**, 13040-13045, doi:10.1073/pnas.0905267106 (2009).

17 Finn, E. S. *et al.* Can brain state be manipulated to emphasize individual differences in functional connectivity? *NeuroImage* **160**, 140-151, doi:https://doi.org/10.1016/j.neuroimage.2017.03.064 (2017).

18 Greene, A. S., Gao, S., Scheinost, D. & Constable, R. T. Task-induced brain state manipulation improves prediction of individual traits. *Nature Communications* **9**, 2807, doi:10.1038/s41467-018-04920-3 (2018).

19 Elliott, M. L. *et al.* General functional connectivity: Shared features of resting-state and task fMRI drive reliable and heritable individual differences in functional brain networks. *NeuroImage* **189**, 516-532, doi:https://doi.org/10.1016/j.neuroimage.2019.01.068 (2019).

20 Palacios, E. M. *et al.* Resting-State Functional Connectivity Alterations Associated with Six-Month Outcomes in Mild Traumatic Brain Injury. *J Neurotrauma* **34**, 1546-1557, doi:10.1089/neu.2016.4752 (2017).

21 Kinder, H. A., Baker, E. W., Howerth, E. W., Duberstein, K. J. & West, F. D. Controlled Cortical Impact Leads to Cognitive and Motor Function Deficits that Correspond to Cellular Pathology in a Piglet Traumatic Brain Injury Model. *J Neurotrauma* **36**, 2810-2826, doi:10.1089/neu.2019.6405 (2019).

22 Kinder, H. A. *et al.* Traumatic Brain Injury Results in Dynamic Brain Structure Changes Leading to Acute and Chronic Motor Function Deficits in a Pediatric Piglet Model. *J Neurotrauma* **36**, 2930-2942, doi:10.1089/neu.2018.6303 (2019).

23 Baker, E. W. *et al.* Controlled cortical impact severity results in graded cellular, tissue, and functional responses in a piglet traumatic brain injury model. *Journal of neurotrauma* **36**, 61-73 (2019).

24 Nakamura, M. *et al.* Experimental investigation of encephalomyosynangiosis using gyrencephalic brain of the miniature pig: histopathological evaluation of dynamic reconstruction of vessels for functional anastomosis. Laboratory investigation. *J Neurosurg Pediatr* **3**, 488-495, doi:10.3171/2008.6.PEDS0834 [pii]

10.3171/2008.6.PEDS0834 (2009).

25 Kuluz, J. W. *et al.* New pediatric model of ischemic stroke in infant piglets by photothrombosis: acute changes in cerebral blood flow, microvasculature, and early histopathology. *Stroke* **38**, 1932-1937, doi:STROKEAHA.106.475244 [pii]

10.1161/STROKEAHA.106.475244 (2007).

26 Tanaka, Y. *et al.* Experimental model of lacunar infarction in the gyrencephalic brain of the miniature pig: neurological assessment and histological, immunohistochemical, and physiological evaluation of dynamic corticospinal tract deformation. *Stroke* **39**, 205-212, doi:STROKEAHA.107.489906 [pii]

10.1161/STROKEAHA.107.489906 (2008).

27 Vink, R. Large animal models of traumatic brain injury. *J Neurosci Res* **96**, 527-535, doi:10.1002/jnr.24079 (2018).

28 Jaber, S. M., Sullivan, S. & Margulies, S. S. Noninvasive metrics for identification of brain injury deficits in piglets. *Developmental neuropsychology* **40**, 34-39 (2015).

29 Sullivan, S. *et al.* Improved behavior, motor, and cognition assessments in neonatal piglets. *Journal of neurotrauma* **30**, 1770-1779 (2013).

30 Ustinova, K. I., Chernikova, L. A., Dull, A. & Perkins, J. Physical therapy for correcting postural and coordination deficits in patients with mild-to-moderate traumatic brain injury. *Physiotherapy theory and practice* **31**, 1-7 (2015).

31 Saikali, S. *et al.* A three-dimensional digital segmented and deformable brain atlas of the domestic pig. *J Neurosci Methods* **192**, 102-109, doi:10.1016/j.jneumeth.2010.07.041 (2010).

32 Schachar, R., Levin, H. S., Max, J. E., Purvis, K. & Chen, S. Attention deficit hyperactivity disorder symptoms and response inhibition after closed head injury in children: do preinjury behavior and injury severity predict outcome? *Dev Neuropsychol* **25**, 179-198, doi:10.1080/87565641.2004.9651927 (2004).

33 Green, C. *et al.* Sensorimotor Functional and Structural Networks after Intracerebral Stem Cell Grafts in the Ischemic Mouse Brain. *J Neurosci* **38**, 1648-1661, doi:10.1523/JNEUROSCI.2715-17.2018 (2018).

34 Lindsey, H. M., Wilde, E. A., Caeyenberghs, K. & Dennis, E. L. Longitudinal Neuroimaging in Pediatric Traumatic Brain Injury: Current State and

Consideration of Factors That Influence Recovery. *Front Neurol* **10**, 1296, doi:10.3389/fneur.2019.01296 (2019).

35 Scheibel, R. S. Functional Magnetic Resonance Imaging of Cognitive Control following Traumatic Brain Injury. *Front Neurol* **8**, 352, doi:10.3389/fneur.2017.00352 (2017).

36 D'Souza, A. *et al.* Measuring Change Over Time: A Systematic Review of Evaluative Measures of Cognitive Functioning in Traumatic Brain Injury. *Front Neurol* **10**, 353, doi:10.3389/fneur.2019.00353 (2019).

37 Jenkins, P. O., Mehta, M. A. & Sharp, D. J. Catecholamines and cognition after traumatic brain injury. *Brain* **139**, 2345-2371, doi:10.1093/brain/aww128 (2016).

38 Mushiake, H. *et al.* Involvement of the prefrontal cortex in problem solving. *Int Rev Neurobiol* **85**, 1-11, doi:10.1016/S0074-7742(09)85001-0 (2009).

39 Mushiake, H., Saito, N., Sakamoto, K., Itoyama, Y. & Tanji, J. Activity in the lateral prefrontal cortex reflects multiple steps of future events in action plans. *Neuron* **50**, 631-641, doi:10.1016/j.neuron.2006.03.045 (2006).

40 Sullivan, S. *et al.* Behavioral deficits and axonal injury persistence after rotational head injury are direction dependent. *Journal of neurotrauma* **30**, 538-545 (2013).

41 Etkin, A. & Wager, T. D. Functional neuroimaging of anxiety: a meta-analysis of emotional processing in PTSD, social anxiety disorder, and specific phobia. *American Journal of Psychiatry* **164**, 1476-1488 (2007).

42 Max, J. E. Neuropsychiatry of pediatric traumatic brain injury. *Psychiatr Clin North Am* **37**, 125-140, doi:10.1016/j.psc.2013.11.003 (2014).

43 Kuhtz-Buschbeck, J. P. *et al.* Sensorimotor recovery in children after traumatic brain injury: analyses of gait, gross motor, and fine motor skills. *Dev Med Child Neurol* **45**, 821-828, doi:10.1017/s001216220300152x (2003).

44 Katz-Leurer, M., Rotem, H., Lewitus, H., Keren, O. & Meyer, S. Relationship between balance abilities and gait characteristics in children with post-traumatic brain injury. *Brain Inj* **22**, 153-159, doi:10.1080/02699050801895399 (2008).

45 Kuhtz-Buschbeck, J. P., Stolze, H., Golge, M. & Ritz, A. Analyses of gait, reaching, and grasping in children after traumatic brain injury. *Arch Phys Med Rehabil* **84**, 424-430, doi:10.1053/apmr.2003.50017 (2003).

46 Kasahara, M. *et al.* Altered functional connectivity in the motor network after traumatic brain injury. *Neurology* **75**, 168-176, doi:10.1212/WNL.0b013e3181e7ca58 (2010).

47 Walker, W. C. & Pickett, T. C. Motor impairment after severe traumatic brain injury: A longitudinal multicenter study. *J Rehabil Res Dev* **44**, 975-982, doi:10.1682/jrrd.2006.12.0158 (2007).

48 Iandolo, R. *et al.* Neural correlates of lower limbs proprioception: An fMRI study of foot position matching. *Human Brain Mapping* **39**, 1929-1944, doi:doi:10.1002/hbm.23972 (2018).

49 Hua, S. E. & Houk, J. C. Cerebellar guidance of premotor network development and sensorimotor learning. *Learn Mem* **4**, 63-76, doi:10.1101/lm.4.1.63 (1997).

50 Kilteni, K. & Ehrsson, H. H. Functional Connectivity between the Cerebellum and Somatosensory Areas Implements the Attenuation of Self-Generated Touch. *J Neurosci* **40**, 894-906, doi:10.1523/JNEUROSCI.1732-19.2019 (2020).

51 Purves, D., Augustine, G.J., Fitzpatrick, D., et al. *Neuroscience*. Vol. 2nd edition (Sinauer Associates, 2001).

52 Kantak, S. S., Stinear, J. W., Buch, E. R. & Cohen, L. G. Rewiring the brain: potential role of the premotor cortex in motor control, learning, and recovery of function following brain injury. *Neurorehabil Neural Repair* **26**, 282-292, doi:10.1177/1545968311420845 (2012).

53 Borich, M. R., Brodie, S. M., Gray, W. A., Ionta, S. & Boyd, L. A. Understanding the role of the primary somatosensory cortex: Opportunities for rehabilitation. *Neuropsychologia* **79**, 246-255, doi:10.1016/j.neuropsychologia.2015.07.007 (2015).

54 Mattsson, J., Fry, W., Boward, C. & Miller, E. Maturation of the visual evoked response in newborn miniature pigs. *American journal of veterinary research* **39**, 1279-1281 (1978).

55 Yin, T., Gruetter, R. & Jelescu, I. O. Altered bilateral functional connectivity in rat brain under isoflurane and medetomidine anesthesia. *In Proceedings of the 27th Annual Meeting of ISMRM, Montreal, Canada* (2019).

56 Zhang, S. *et al.* Characterizing and differentiating task-based and resting state fMRI signals via two-stage sparse representations. *Brain imaging and behavior* **10**, 21-32 (2016).

57 Parker, D. B. & Razlighi, Q. R. Task-evoked Negative BOLD Response and Functional Connectivity in the Default Mode Network are Representative of Two Overlapping but Separate Neurophysiological Processes. *Scientific reports* **9** (2019).

58 Cole, M. W., Ito, T., Bassett, D. S. & Schultz, D. H. Activity flow over resting-state networks shapes cognitive task activations. *Nature neuroscience* **19**, 1718-1726 (2016).

59 Chan, M. Y., Alhazmi, F. H., Park, D. C., Savalia, N. K. & Wig, G. S. Resting-state network topology differentiates task signals across the adult life span. *Journal of Neuroscience* **37**, 2734-2745 (2017).

60 Kannurpatti, S. S. & Biswal, B. B. Prediction of task-related BOLD fMRI with amplitude signatures of resting-state fMRI. *Frontiers in systems neuroscience* **6**, 7 (2012).

61 Tavor, I. *et al.* Task-free MRI predicts individual differences in brain activity during task performance. *Science* **352**, 216-220, doi:10.1126/science.aad8127 (2016).

62 Lewis, C. M., Baldassarre, A., Committeri, G., Romani, G. L. & Corbetta, M. Learning sculpts the spontaneous activity of the resting human brain. *Proceedings of the National Academy of Sciences* **106**, 17558-17563, doi:10.1073/pnas.0902455106 (2009).

63 Mastrovito, D. Interactions between Resting-State and Task-Evoked Brain Activity Suggest a Different Approach to fMRI Analysis. *The Journal of Neuroscience* **33**, 12912-12914, doi:10.1523/jneurosci.2580-13.2013 (2013).

64 Hamilton, C., Ma, Y. & Zhang, N. Global reduction of information exchange during anesthetic-induced unconsciousness. *Brain Structure and Function* **222**, 3205-3216, doi:10.1007/s00429-017-1396-0 (2017).

65 Liang, Z., King, J. & Zhang, N. Intrinsic Organization of the Anesthetized Brain. *The Journal of Neuroscience* **32**, 10183-10191, doi:10.1523/jneurosci.1020-12.2012 (2012).

66 Imms, P. *et al.* The structural connectome in traumatic brain injury: A meta-analysis of graph metrics. *Neurosci Biobehav Rev* **99**, 128-137, doi:10.1016/j.neubiorev.2019.01.002 (2019).

67 Gilbert, N. *et al.* Diminished neural network dynamics after moderate and severe traumatic brain injury. *PLoS One* **13**, e0197419, doi:10.1371/journal.pone.0197419 (2018).

68 Kinder, H. A. *et al.* Traumatic Brain Injury Results in Dynamic Brain Structure Changes Leading to Acute and Chronic Motor Function Deficits in a Pediatric Piglet Model. *Journal of neurotrauma* (2019).

69 Baker, E. W. *et al.* Scaled traumatic brain injury results in unique metabolomic signatures between gray matter, white matter, and serum in a piglet model. *PloS one* **13** (2018).

70 Lynn, B., Faulstroh, K. & Pierau, F. K. The classification and properties of nociceptive afferent units from the skin of the anaesthetized pig. *European Journal of Neuroscience* **7**, 431-437 (1995).

71 Ashburner, J. *et al.* SPM12 manual. *URL: http://www. fil. ion. ucl. ac. uk/spm/doc/spm12 manual. pdf* (2016).

72 Bell, A. J. & Sejnowski, T. J. An information-maximization approach to blind separation and blind deconvolution. *Neural computation* **7**, 1129-1159 (1995).

73 Calhoun, V. D., Adali, T., Pearlson, G. D. & Pekar, J. J. A method for making group inferences from functional MRI data using independent component analysis. *Human brain mapping* **14**, 140-151 (2001).

74 Mairal, J., Bach, F., Ponce, J. & Sapiro, G. Online learning for matrix factorization and sparse coding. *Journal of Machine Learning Research* **11**, 19-60 (2010).

75 Rachakonda, S., Egolf, E., Correa, N. & Calhoun, V. Group ICA of fMRI toolbox (GIFT) manual. (2020).

76 Saikali, S. *et al.* A three-dimensional digital segmented and deformable brain atlas of the domestic pig. *Journal of Neuroscience Methods* **192**, 102-109, doi:https://doi.org/10.1016/j.jneumeth.2010.07.041 (2010).

77 Nichols, T. E. & Holmes, A. P. Nonparametric permutation tests for functional neuroimaging: A primer with examples. *Human Brain Mapping* **15**, 1-25, doi:10.1002/hbm.1058 (2002).

Acknowledgements

The authors would like to thank Dr. Erin Kaiser, Dr. Holly Kinder, Ethan Karstedt, and Christina Welch for assistance with pig care, Kim Mason for assistance with MRI acquisition, as well as our team of undergraduate researchers: Logan Brown, Sungjae Cho, Kristin Dennard, Luke Frost, Nik Ghayal, Chris Littlejohn, Brendan Mahoney, Mikayla Mashburn, Ashton Pearson, Bridgette Pronesti, Jordyn White, and Anna Zukowski. We would also like to thank Kelly Parham and Rick Utley for their pig expertise. This work was supported by the Franklin Foundation for Neuroimaging and the College of Agricultural and Environmental Sciences, University of Georgia.

Author Contributions

GS, KMS, FDW, and QZ participated in experimental planning. GS and KMS were responsible for MRI acquisition and fMRI stimuli administration. GS, WS, and QZ conducted data analysis. KMS, SES, MMF, SRC, and FDW conducted animal work. GS, KMS, FDW, and QZ wrote and edited the manuscript. GS and WS generated figures.

Authors' Disclosure Statement

No competing or financial interests exist.

Funding Statement

This work was supported by the Franklin Foundation for Neuroimaging and the College of Agricultural and Environmental Sciences, University of Georgia.

Data Availability Statement

Data and MatLab code will be available upon reasonable request.

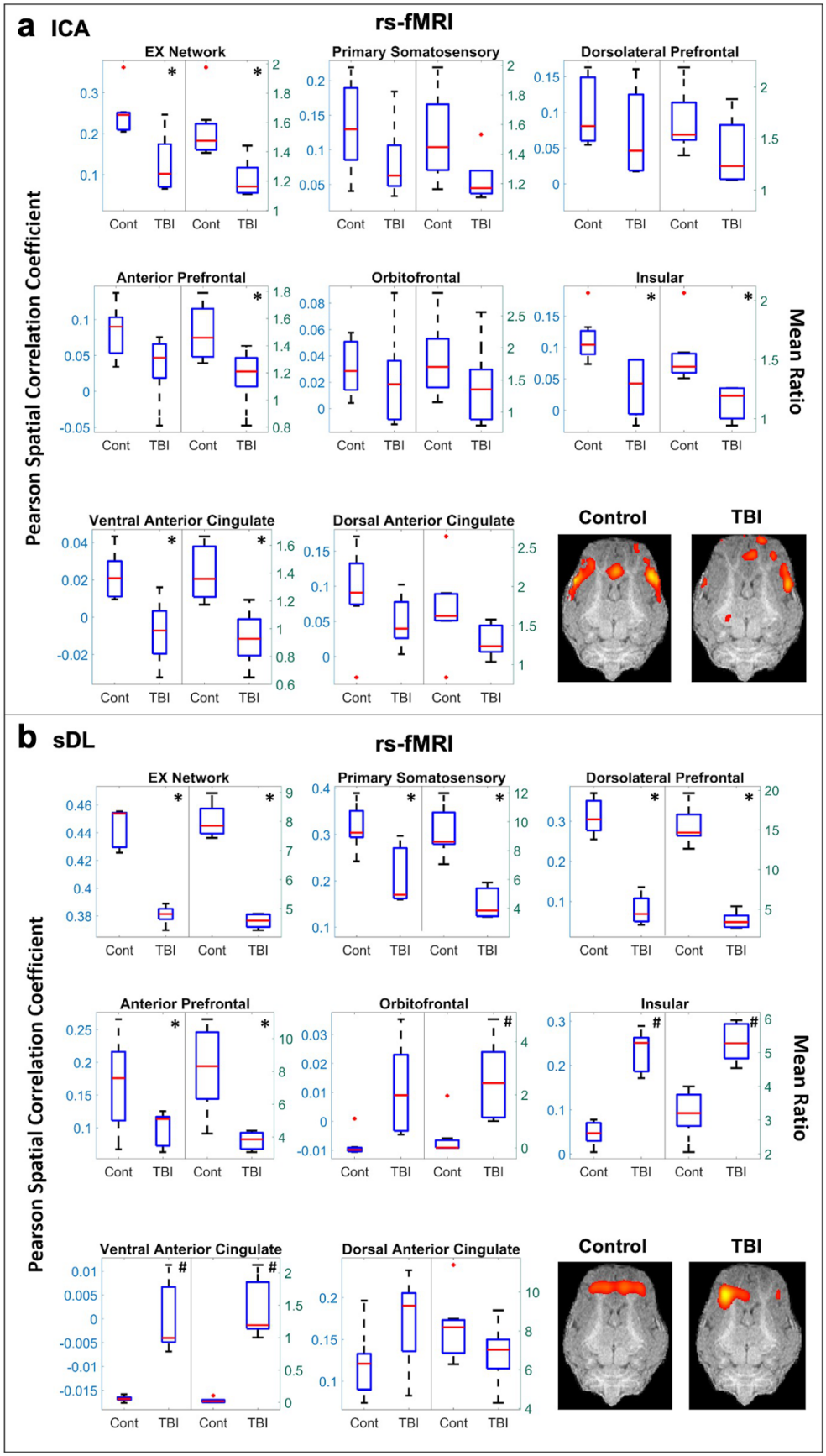
a ICA
rs-fMRI
EX Network
Primary Somatosensory
Dorsolateral Prefrontal
Anterior Prefrontal
Orbitofrontal
Insular
Ventral Anterior Cingulate
Dorsal Anterior Cingulate
Control
TBI
Pearson Spatial Correlation Coefficient
Mean Ratio
Cont
TBI
b sDL
rs-fMRI
EX Network
Primary Somatosensory
Dorsolateral Prefrontal
Anterior Prefrontal
Orbitofrontal
Insular
Ventral Anterior Cingulate
Dorsal Anterior Cingulate
Control
TBI
Pearson Spatial Correlation Coefficient
Mean Ratio
Cont
TBI

Figure 4.1: Resting-state (rs-) analysis of the executive control (EX) network. Boxplots of Pearson spatial correlation coefficients (left) and mean ratios (right) obtained from the rs- analysis for the EX network and its individual anatomical regions obtained using independent component analysis (ICA; **a**) and sparse dictionary learning (sDL; **b**). The red line denotes the median, the blue box denotes the interquartile range, and the lower and upper whiskers denote the min and max, respectively. An asterisk (*) or pound (#) in the upper right-hand corner indicates significant decrease or increase ($p<0.05$), respectively, for the TBI group in comparison to the control group. Representative coronal plane activation maps overlaid on the template pigs' T1-weighted anatomical image are also displayed. Representative maps in the axial and sagittal plane are provided in the Figures S4 and S5.

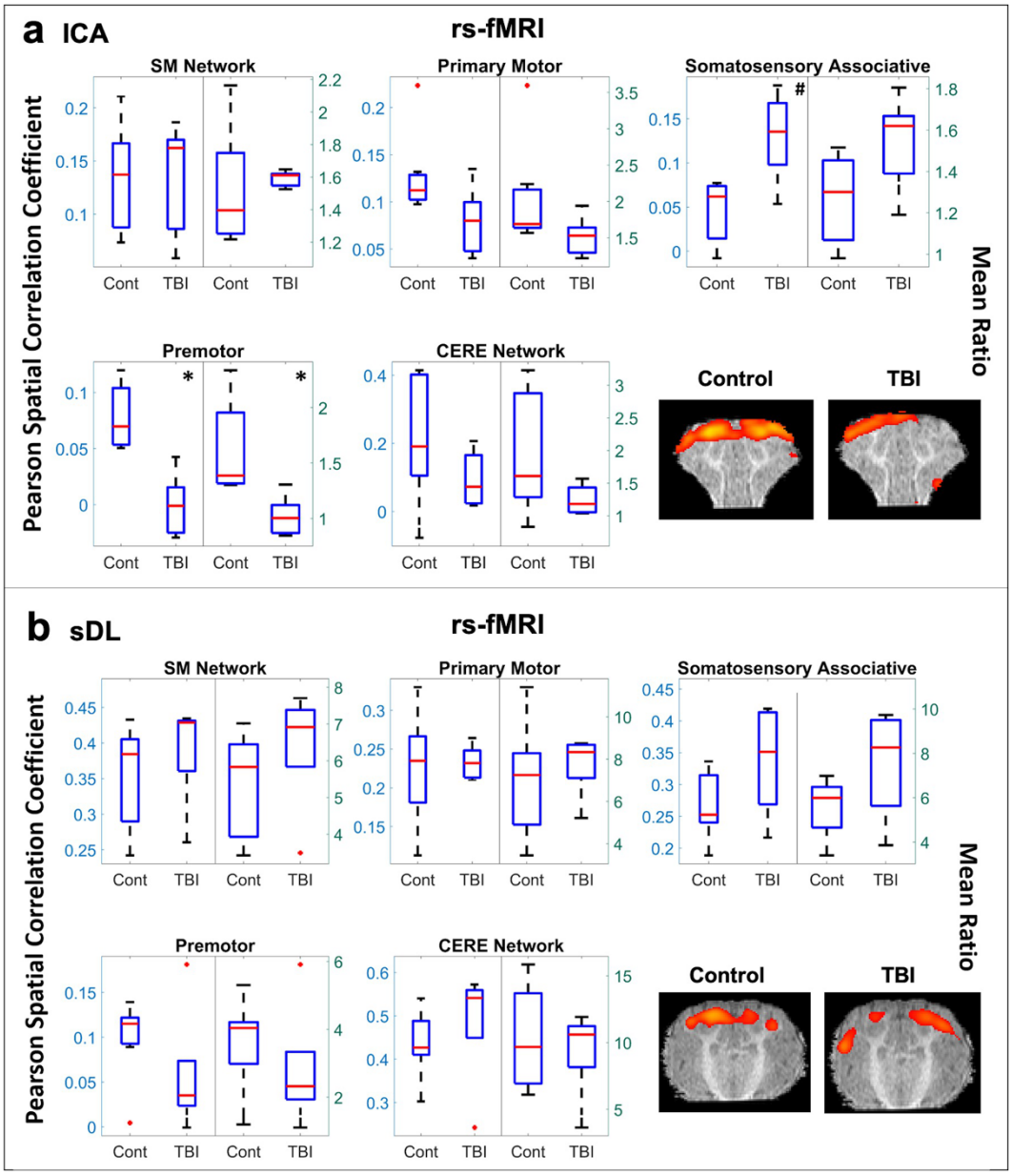

Figure 4.2: Resting-state (rs-) analysis of the sensorimotor (SM) and cerebellar (CERE) networks. Boxplots of Pearson spatial correlation coefficients (left) and mean ratios (right) obtained from the rs- analysis for the SM network and its individual anatomical regions, as well as the CERE network, obtained using independent component analysis (ICA; **a**) and sparse dictionary learning (sDL; **b**). The red line denotes the

median, the blue box denotes the interquartile range, and the lower and upper whiskers denote the min and max, respectively. An asterisk (*) or pound (#) in the upper right-hand corner indicates significant decrease or increase ($p<0.05$), respectively, for the TBI group in comparison to the control group. Representative coronal plane activation maps overlaid on the template pigs' T1-weighted anatomical image are also displayed. Representative maps in the axial and sagittal plane are provided in the Figures S4 and S5.

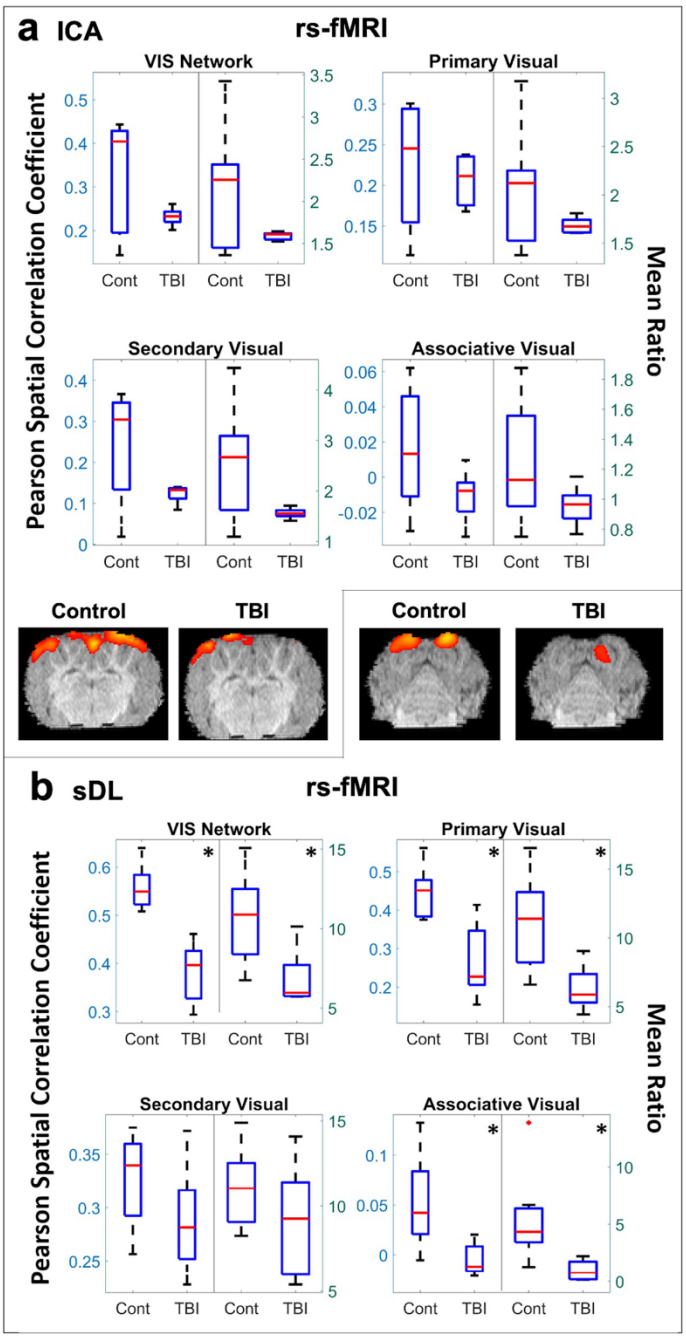

Figure 4.3: Resting-state (rs-) analysis of the visual (VIS) network. Boxplots of Pearson spatial correlation coefficients (left) and mean ratios (right) obtained from rs-analysis for the VIS network and its individual anatomical regions obtained using independent component analysis (ICA; **a**) and sparse dictionary learning (sDL; **b**). The

red line denotes the median, the blue box denotes the interquartile range, and the lower and upper whiskers denote the min and max, respectively. An asterisk (*) or pound (#) in the upper right-hand corner indicates significant decrease or increase ($p<0.05$), respectively, for the TBI group in comparison to the control group. Representative axial plane activation maps overlaid on the template pigs' T1-weighted anatomical image are also displayed. Representative maps in the coronal and sagittal plane are provided in the Figures S4 and S5.

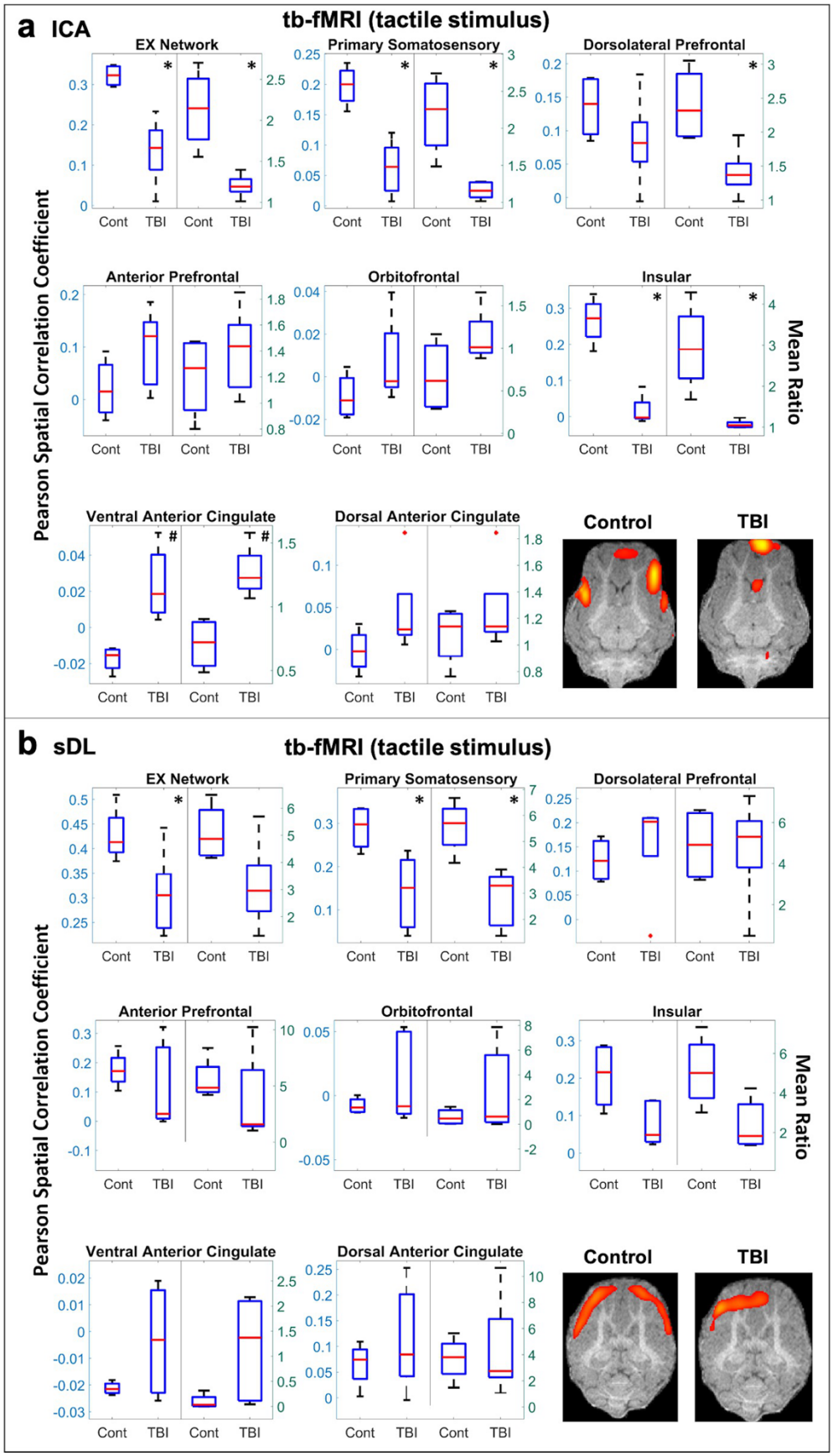
a ICA
tb-fMRI (tactile stimulus)
EX Network
Primary Somatosensory
Dorsolateral Prefrontal
Anterior Prefrontal
Orbitofrontal
Insular
Ventral Anterior Cingulate
Dorsal Anterior Cingulate
Pearson Spatial Correlation Coefficient
Mean Ratio
Cont
TBI
Control
TBI
b sDL
tb-fMRI (tactile stimulus)
EX Network
Primary Somatosensory
Dorsolateral Prefrontal
Anterior Prefrontal
Orbitofrontal
Insular
Ventral Anterior Cingulate
Dorsal Anterior Cingulate
Pearson Spatial Correlation Coefficient
Mean Ratio
Cont
TBI
Control
TBI

Figure 4.4: Task-based (tb-) tactile stimulus analysis of the executive control (EX) network. Boxplots of Pearson spatial correlation coefficients (left) and mean ratios (right) obtained from the tb- analysis for the EX network and its individual anatomical regions obtained using independent component analysis (ICA; **a**) and sparse dictionary learning (sDL; **b**). The red line denotes the median, the blue box denotes the interquartile range, and the lower and upper whiskers denote the min and max, respectively. An asterisk (*) or pound (#) in the upper right-hand corner indicates significant decrease or increase ($p<0.05$), respectively, for the TBI group in comparison to the control group. Representative coronal plane activation maps overlaid on the template pigs' T1-weighted anatomical image are also displayed. Representative maps in the axial and sagittal plane are provided in the Figures S4 and S5.

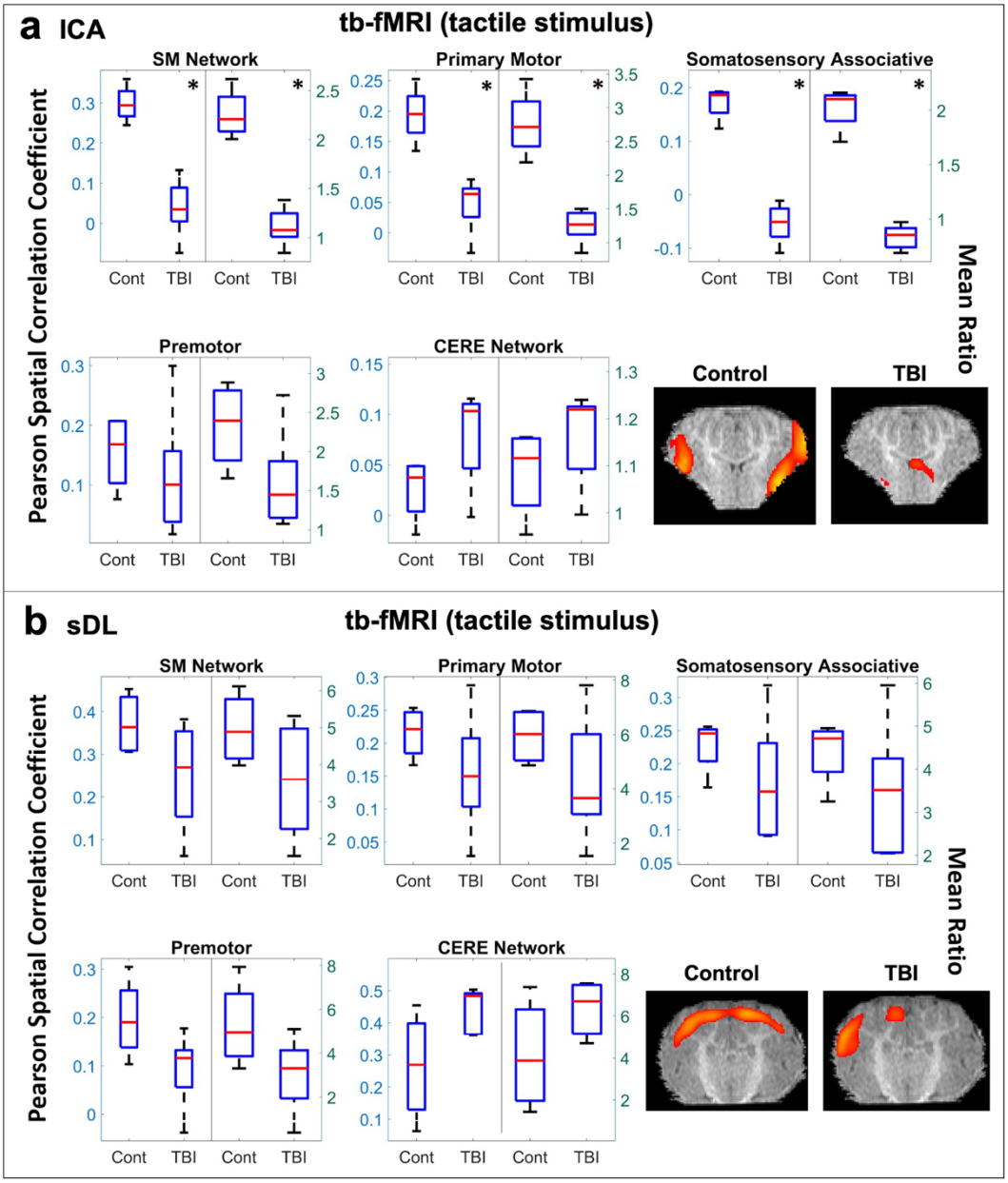

Figure 4.5: Task-based (tb-) tactile stimulus analysis of the sensorimotor (SM) and cerebellar (CERE) networks. Boxplots of Pearson spatial correlation coefficients (left) and mean ratios (right) obtained from the tb- analysis for the SM network and its individual anatomical regions, as well as the CERE network, obtained using independent component analysis (ICA; **a**) and sparse dictionary learning (sDL; **b**). The red line

denotes the median, the blue box denotes the interquartile range, and the lower and upper whiskers denote the min and max, respectively. An asterisk (*) or pound (#) in the upper right-hand corner indicates significant decrease or increase ($p<0.05$), respectively, for the TBI group in comparison to the control group. Representative coronal plane activation maps overlaid on the template pigs' T1-weighted anatomical image are also displayed. Representative maps in the axial and sagittal plane are provided in the Figures S4 and S5.

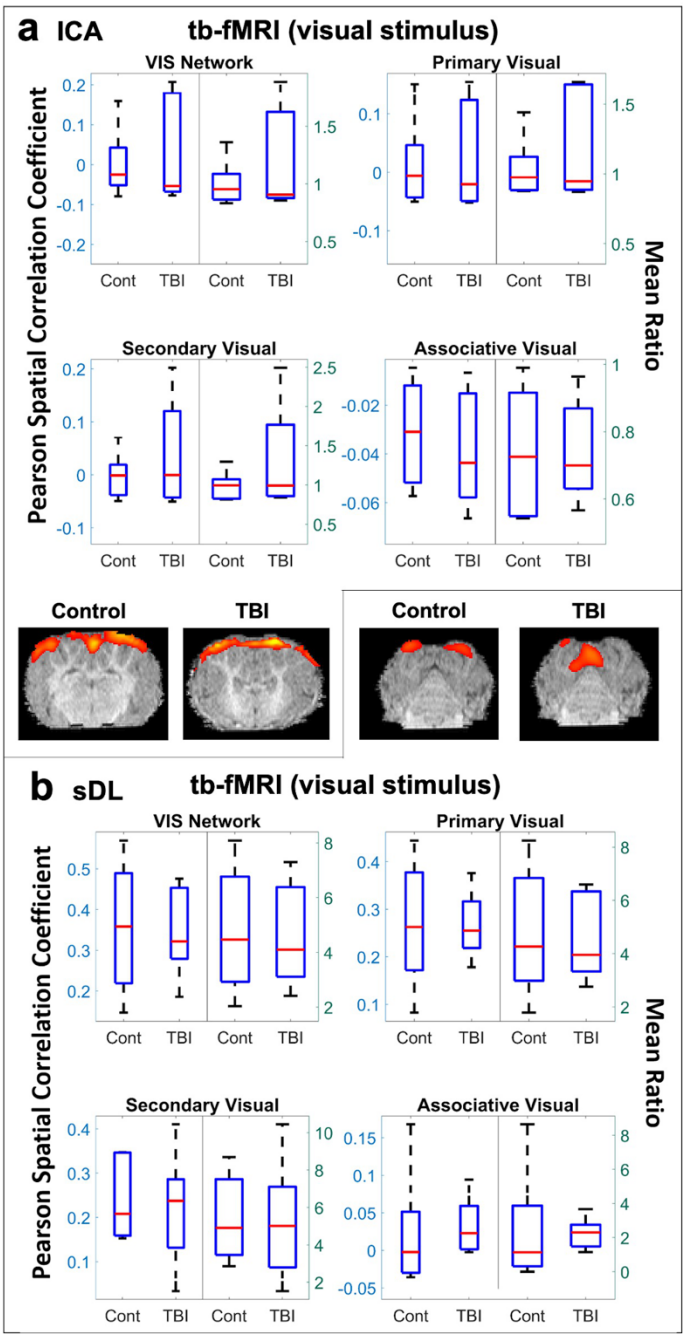

Figure 4.6: Task-based (tb-) visual stimulus analysis of the visual (VIS) network. Boxplots of Pearson spatial correlation coefficients (left) and mean ratios (right) obtained from the tb- analysis for the VIS network and its individual anatomical regions obtained using independent component analysis (ICA; **a**) and sparse dictionary learning (sDL; **b**).

The red line denotes the median, the blue box denotes the interquartile range, and the lower and upper whiskers denote the min and max, respectively. An asterisk (*) or pound (#) in the upper right-hand corner indicates significant decrease or increase ($p<0.05$), respectively, for the TBI group in comparison to the control group. Representative axial plane activation maps overlaid on the template pigs' T1-weighted anatomical image are also displayed. Representative maps in the coronal and sagittal plane are provided in the Figures S4 and S5.

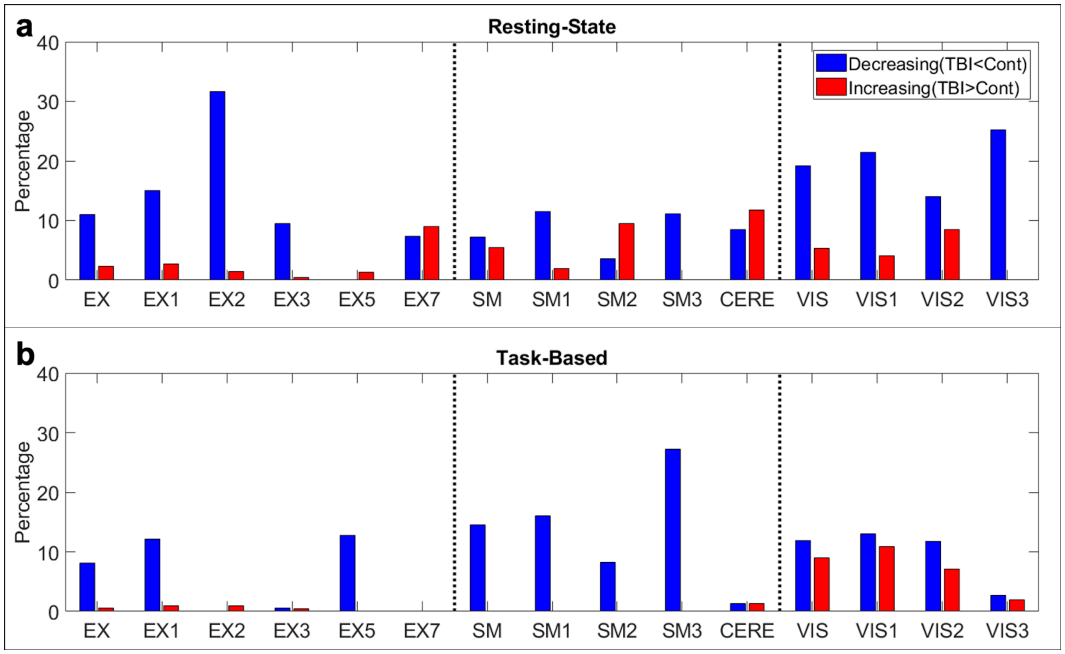

Figure 4.7: Permutation analysis percentages of significantly different voxels. Bar plots of the percentages of significantly decreasing (blue, TBI<Control) and increasing (red, TBI>Control) voxels contained within each network and each individual anatomical region comprising each network for the resting-state (**a**) and task-based (**b**) fMRI permutation analysis. Abbreviations: visual (VIS), executive control (EX), sensorimotor (SM), and cerebellar (CERE). Regions EX4 and EX6, corresponding to the orbitofrontal and ventral anterior cingulate cortices, are not shown, as they did not contain any significantly different voxels for either analysis. For identification of other regions, refer to Table 1.

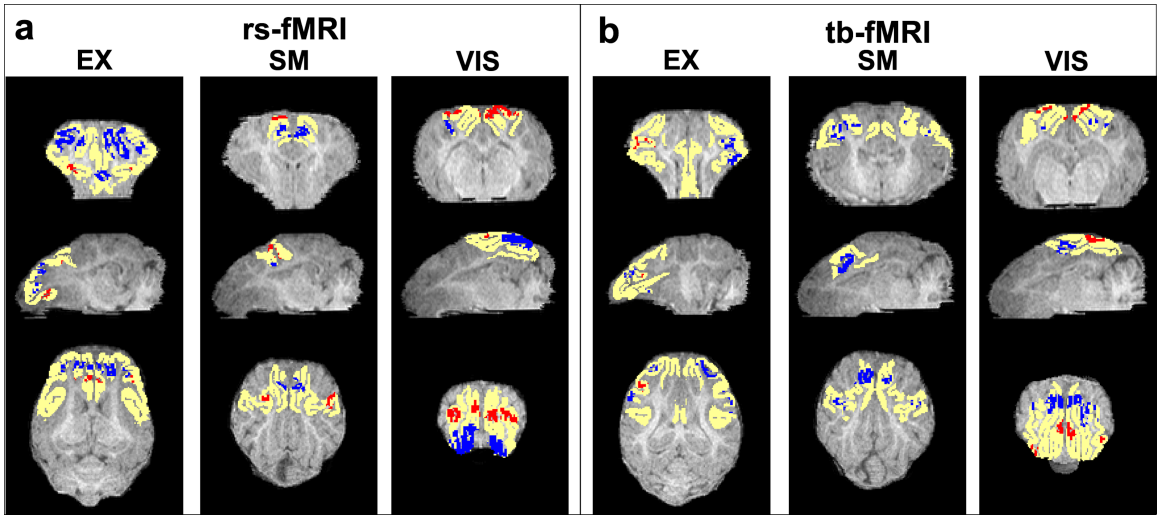

Figure 4.8: Permutation maps generated from sDL analysis. Representative images of two-dimensional permutation maps from the resting-state (rs-; **a**) and task- based (tb-; **b**) fMRI analysis for the visual (VIS), executive control (EX), and sensorimotor (SM) networks and their corresponding reference atlases (yellow) overlaid on the template pigs' T1-weighted anatomical image. The blue indicates voxels with significantly decreased activation values of the TBI group in comparison to the control group, and red indicates significantly increased activation values.

Table 4.1: P-Values Comparing Control vs TBI Group. P-values comparing the Pearson spatial correlation coefficients and mean ratios obtained from the resting-state (rs-) fMRI and task-based (tb-) fMRI analysis for the control group and the TBI group for each network and each individual anatomical region. For each metric, the groups were considered significantly different if $p<0.05$ (denoted by * for a significant decrease in the TBI group in comparison to the control group and $^{\#}$ for a significant increase). However, a network or anatomical region was only considered significantly different if the p-values for both the Pearson values and mean ratios were below 0.05 ('Sig' columns). Networks and regions that showed consistent trends across ICA and sDL are denoted by $^{\$}$.

a. rs-fMRI	**ICA**			**sDL**		
Networks and Anatomical Regions	**Sig**	**Pearson**	**Mean Ratio**	**Sig**	**Pearson**	**Mean Ratio**
Executive Control$^{\$}$	*	0.02*	<0.01*	*	<0.01*	<0.01*
EX1: Primary Somatosensory Cortex$^{\$}$	-	0.19	0.07	*	0.02*	<0.01*
EX2: Dorsolateral Prefrontal Cortex$^{\$}$	-	0.42	0.17	*	<0.01*	<0.01*
EX3: Anterior Prefrontal Cortex$^{\$}$	-	0.10	0.03*	*	0.04*	<0.01*
EX4: Orbitofrontal Cortex	-	0.66	0.31	-	0.06	0.03$^{\#}$
EX5: Insular Cortex	*	0.02*	<0.01*	$^{\#}$	<0.01$^{\#}$	<0.01$^{\#}$
EX6: Ventral Anterior Cingulate Cortex	*	0.02*	<0.01*	$^{\#}$	<0.01$^{\#}$	<0.01$^{\#}$
EX7: Dorsal Anterior Cingulate Cortex	-	0.18	0.11	-	0.14	0.20
Sensorimotor	-	0.92	0.67	-	0.46	0.31
SM1: Primary Motor Cortex	-	0.06	0.11	-	0.75	0.54
SM2: Somatosensory Associative Cortex$^{\$}$	-	0.02$^{\#}$	0.07	-	0.17	0.16
SM3: Premotor Cortex$^{\$}$	*	<0.01*	<0.01*	-	0.29	0.42
Cerebellar	-	0.15	0.09	-	0.09	0.77
Visual$^{\$}$	-	0.11	0.10	*	<0.01*	0.02*
VIS1: Primary Visual Cortex$^{\$}$	-	0.54	0.20	*	0.01*	0.01*
VIS2: Secondary Visual Cortex$^{\$}$	-	0.06	0.06	-	0.22	0.30
VIS3: Associative Visual Cortex$^{\$}$	-	0.10	0.10	*	0.02*	0.02*
b. tb-fMRI	**ICA**			**sDL**		
Networks and Anatomical Regions	**Sig**	**Pearson**	**Mean Ratio**	**Sig**	**Pearson**	**Mean Ratio**
Executive Control (tactile stimulus) $^{\$}$	*	<0.01*	0.03*	-	0.04*	0.07
EX1: Primary Somatosensory Cortex$^{\$}$	*	<0.01*	0.03*	*	0.02*	<0.01*

EX2: Dorsolateral Prefrontal Cortex	-	0.23	0.03*	-	0.57	0.91
EX3: Anterior Prefrontal Cortex	-	0.13	0.41	-	0.46	0.43
EX4: Orbitofrontal Cortex[$]	-	0.15	0.12	-	0.27	0.25
EX5: Insular Cortex[$]	*	<0.01*	0.04*	-	0.06	0.05
EX6: Ventral Anterior Cingulate Cortex[$]	[#]	<0.01[#]	<0.01[#]	-	0.12	0.08
EX7: Dorsal Anterior Cingulate Cortex	-	0.13	0.32	-	0.37	0.68
Sensorimotor (tactile stimulus) [$]	*	<0.01*	<0.01*	-	0.12	0.15
SM1: Primary Motor Cortex[$]	*	<0.01*	<0.01*	-	0.24	0.24
SM2: Somatosensory Associative Cortex [$]	*	<0.01*	<0.01*	-	0.29	0.29
SM3: Premotor Cortex[$]	-	0.51	0.12	-	0.10	0.12
Cerebellar (tactile stimulus) [$]	-	0.10	0.31	-	0.13	0.21
Visual (visual stimulus) [$]	-	0.66	0.41	-	0.92	0.91
VIS1: Primary Visual Cortex[$]	-	0.80	0.48	-	0.99	0.93
VIS2: Secondary Visual Cortex[$]	-	0.46	0.34	-	0.80	0.94
VIS3: Associative Visual Cortex[$]	-	0.65	0.98	-	0.83	0.85

Supplementary Material

Table 4.S1: P-Values Comparing Control vs TBI Group. P-values comparing the Pearson spatial correlation coefficients and mean ratios obtained from the resting-state (rs-) fMRI analysis for the control group and the TBI group for each network and each individual anatomical region. For each metric, the groups were considered significantly different if $p<0.05$ (denoted by * for a significant decrease in the TBI group in comparison to the control group and # for a significant increase). However, a network or anatomical region was only considered significantly different if the p-values for both the Pearson values and mean ratios were below 0.05 ('Sig' columns). Networks and regions that showed consistent trends across ICA and sDL are denoted by $.

rs-fMRI	**ICA**			**sDL**		
Networks and Anatomical Regions	**Sig**	**Pearson**	**Mean Ratio**	**Sig**	**Pearson**	**Mean Ratio**
Default Mode$	-	0.95	0.99	-	0.55	0.98
Hippocampus$	-	0.08	0.11	-	0.10	0.36
Medial Anterior Prefrontal Cortex$	-	0.14	0.13	-	0.45	0.46
Orbitofrontal Cortex$	-	0.43	0.44	-	0.29	0.29
Inferior Temporal Gyrus	*	<0.01*	<0.01*	#	<0.01#	<0.01#
Ventral Posterior Cingulate Cortex	-	0.06	0.07	*	0.01*	<0.01*
Dorsal Posterior Cingulate Cortex	-	0.54	0.68	-	0.10	0.12
Retrosplenial Cingular Cortex	-	0.36	0.35	*	0.04*	0.04*
Anterior Entorhinal Cortex	-	0.70	0.55	-	0.24	0.64
Parahippocampal Cortex	*	0.02*	0.01*	-	0.66	0.56
Salience$	-	0.18	0.54	-	0.35	0.41
Caudate Nucleus	#	0.01#	0.01#	-	0.08	0.21
Globus Pallidus	#	0.02#	0.04#	-	0.58	0.62
Insular Cortex	-	0.97	0.49	-	0.21	0.45
Middle Temporal Gyrus	-	0.04*	0.10	-	0.70	0.34

Ventral Posterior Cingulate Cortex[$]	-	0.61	0.62	-	0.59	0.98
Ventral Anterior Cingulate Cortex[$]	-	0.36	0.39	-	0.27	0.37
Retrosplenial Cingular Cortex[$]	-	0.15	0.17	-	0.12	0.53
Dorsal Posterior Cingulate Cortex	[#]	0.04[#]	0.04[#]	-	0.91	0.82
Dorsal Anterior Cingulate Cortex	*	<0.01*	<0.01*	-	0.21	0.20
Basal Ganglia	-	0.33	0.24	-	0.03[#]	0.06
Thalamus	*	<0.01*	<0.01*	[#]	<0.01[#]	<0.01[#]
Caudate Nucleus	*	0.01*	0.02*	-	0.99	0.87
Putamen	-	0.99	0.96	-	0.14	0.15
Amygdala	-	0.78	0.95	-	0.11	0.13
Primary Motor Cortex[$]	-	0.75	0.81	-	0.58	0.66
Orbitofrontal Cortex	-	0.49	0.48	-	0.68	0.68
Parahippocampal Cortex[$]	-	0.32	0.27	*	<0.01*	<0.01*

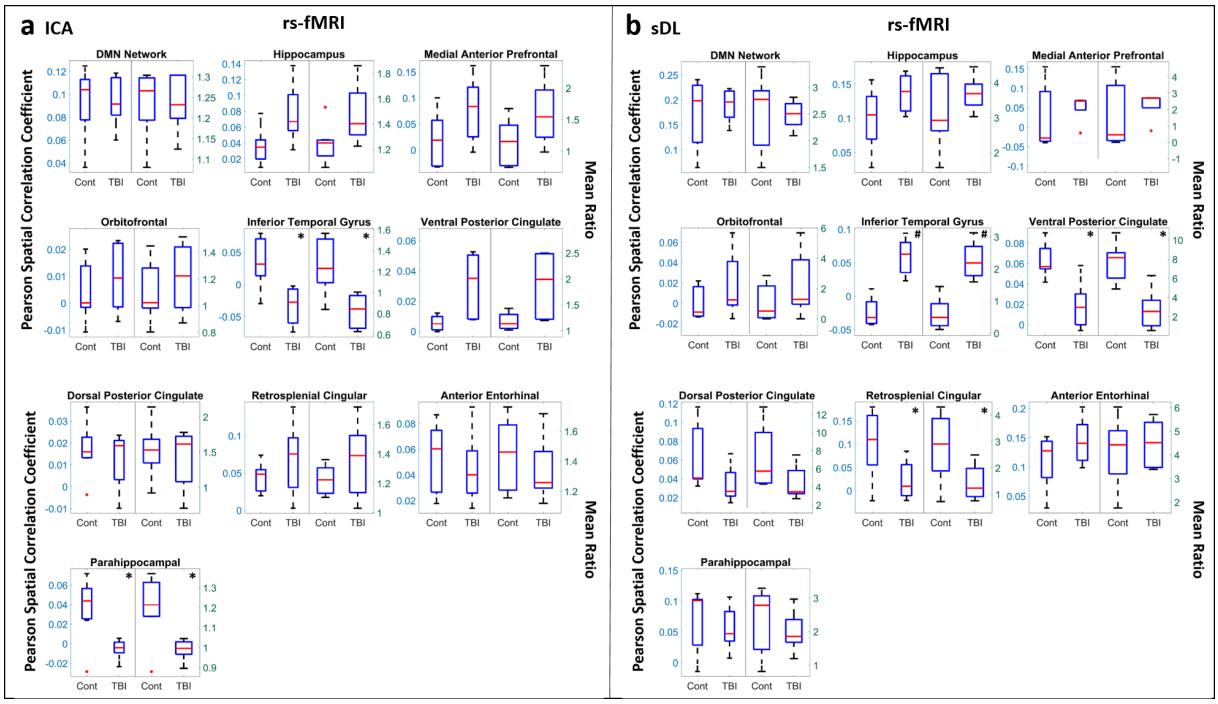

Figure 4.S1: Boxplots of Pearson spatial correlation coefficients (left) and mean ratios (right) obtained from the resting-state (rs-) analysis for the default mode (DMN) network and its individual anatomical regions obtained using independent component analysis (ICA; **a**) and sparse dictionary learning (sDL; **b**). The red line denotes the median, the blue box denotes the interquartile range, and the lower and upper whiskers denote the min and max, respectively. An asterisk (*) or pound ($^{\#}$) in the upper right-hand corner indicates significant decrease or increase ($p<0.05$), respectively, for the TBI group in comparison to the control group.

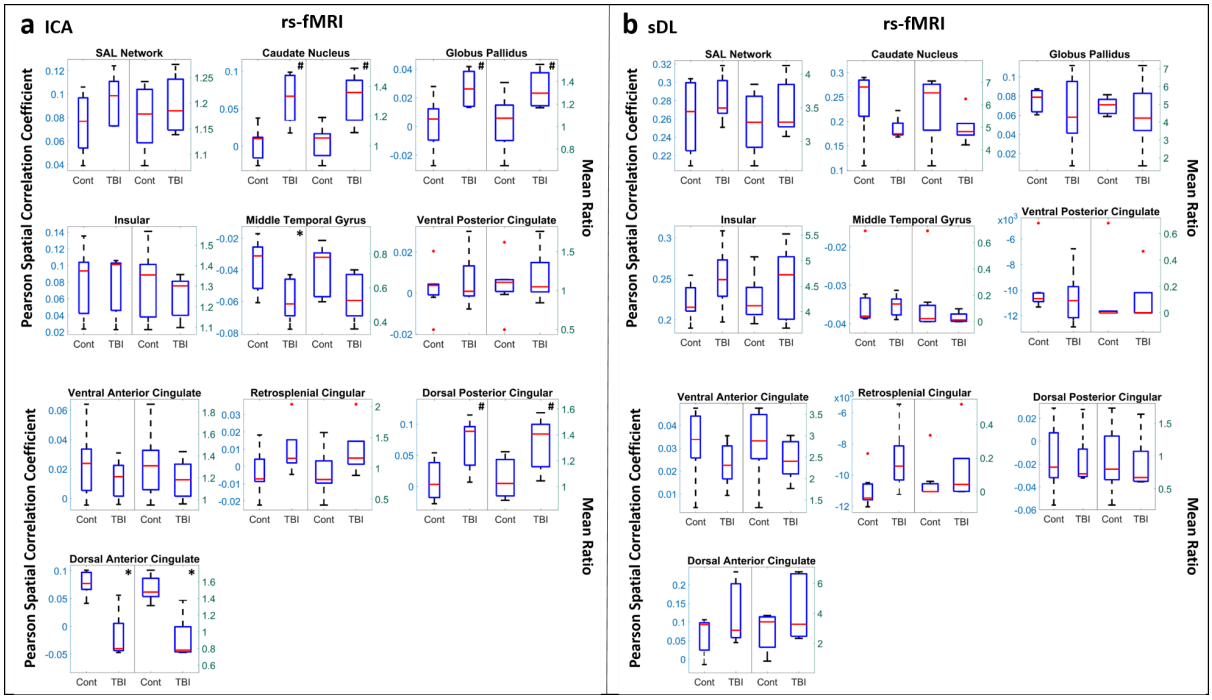

Figure 4.S2: Boxplots of Pearson spatial correlation coefficients (left) and mean ratios (right) obtained from the resting-state (rs-) analysis for the salience (SAL) network and its individual anatomical regions obtained using independent component analysis (ICA; **a**) and sparse dictionary learning (sDL; **b**). The red line denotes the median, the blue box denotes the interquartile range, and the lower and upper whiskers denote the min and max, respectively. An asterisk (*) or pound ($^{\#}$) in the upper right-hand corner indicates significant decrease or increase ($p<0.05$), respectively, for the TBI group in comparison to the control group.

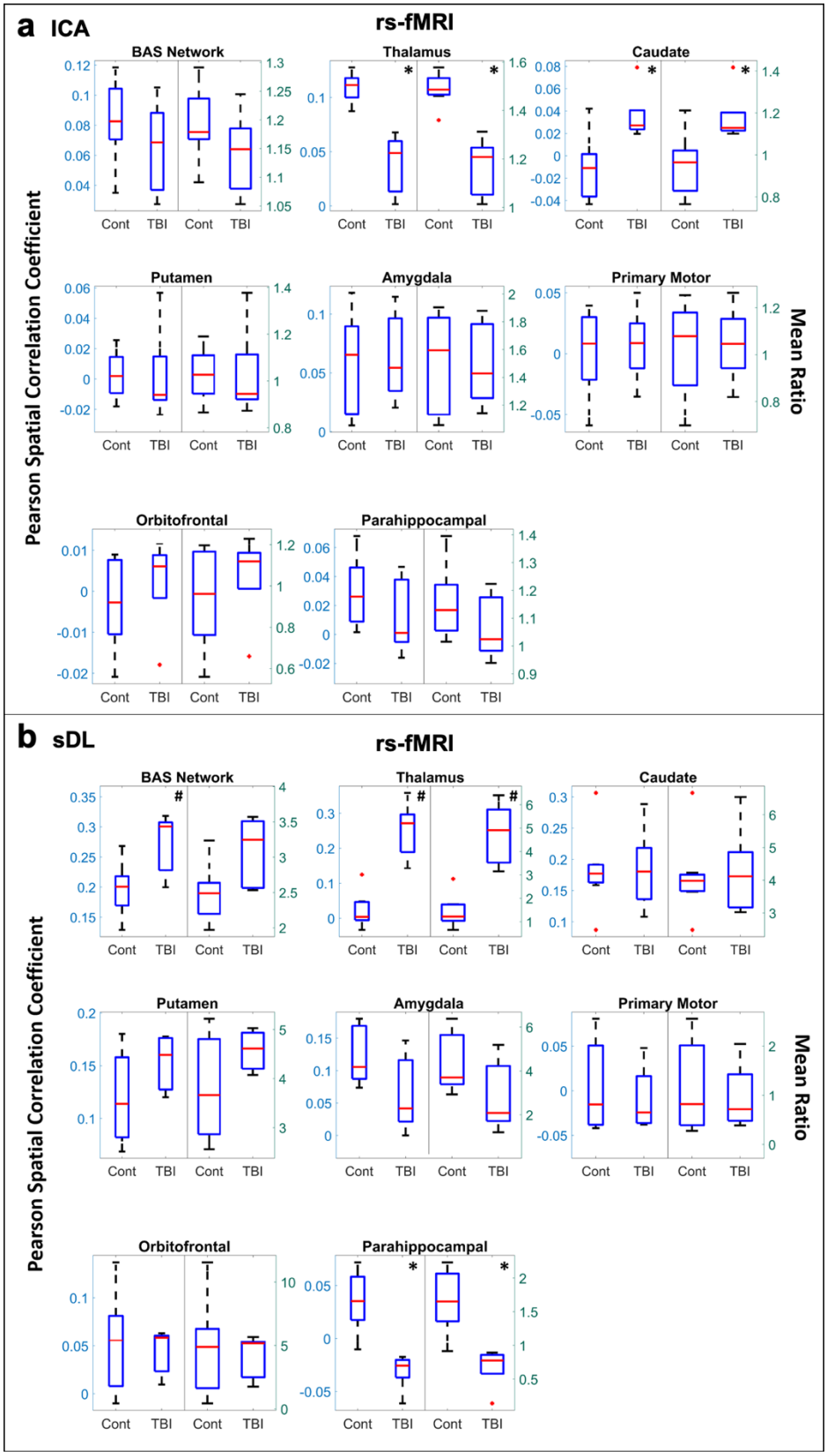
a ICA
rs-fMRI
BAS Network
Thalamus
Caudate
Putamen
Amygdala
Primary Motor
Orbitofrontal
Parahippocampal
Pearson Spatial Correlation Coefficient
Mean Ratio
Cont
TBI
b sDL
rs-fMRI
BAS Network
Thalamus
Caudate
Putamen
Amygdala
Primary Motor
Orbitofrontal
Parahippocampal
Pearson Spatial Correlation Coefficient
Mean Ratio
Cont
TBI

Figure 4.S3: Boxplots of Pearson spatial correlation coefficients (left) and mean ratios (right) obtained from the resting-state (rs-) analysis for the basal ganglia (BAS) network and its individual anatomical regions obtained using independent component analysis (ICA; **a**) and sparse dictionary learning (sDL; **b**). The red line denotes the median, the blue box denotes the interquartile range, and the lower and upper whiskers denote the min and max, respectively. An asterisk (*) or pound ($^{\#}$) in the upper right-hand corner indicates significant decrease or increase ($p<0.05$), respectively, for the TBI group in comparison to the control group.

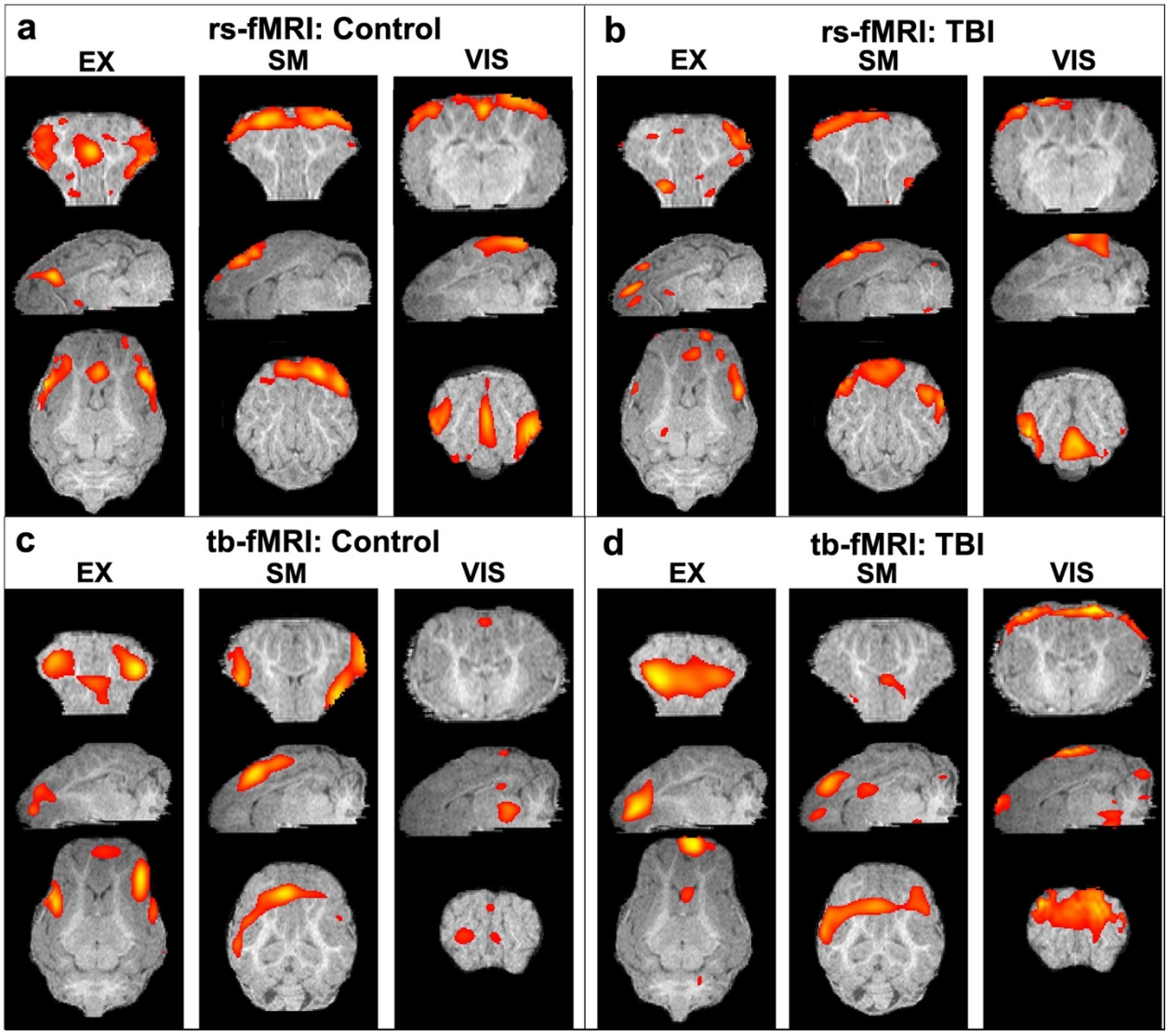

Figure 4.S4: Representative images of two-dimensional activation maps from the resting-state (rs-; a and b) and task-based (tb-; c and d) ICA fMRI analysis for the control (a and c) and TBI (b and d) groups for the executive control (EX), sensorimotor (SM), and visual (VIS) networks overlaid on the template pigs' T1-weighted anatomical images.

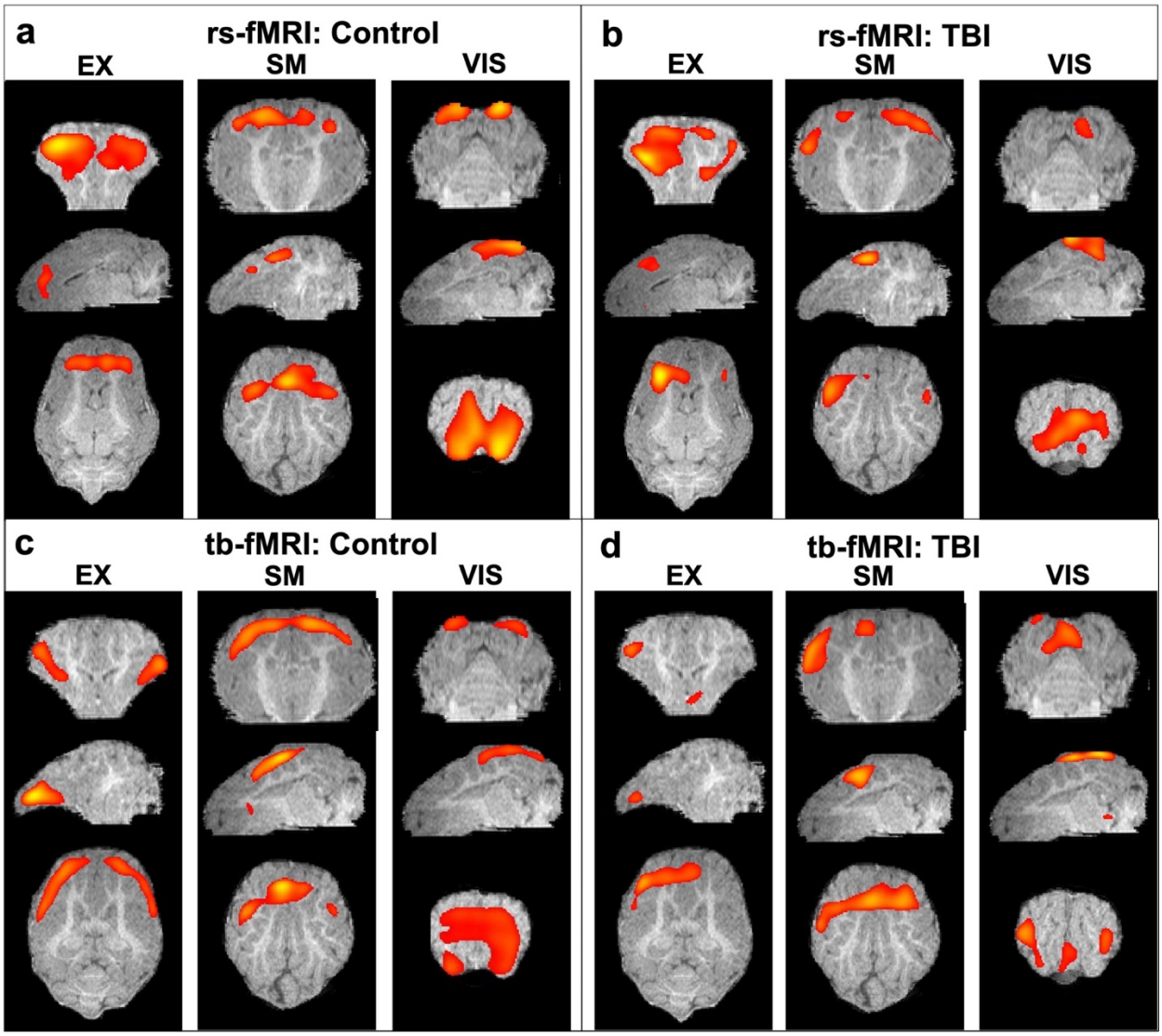

Figure 4.S5: Representative images of two-dimensional activation maps from the resting-state (rs-; a and b) and task-based (tb-; c and d) sDL fMRI analysis for the control (a and c) and TBI (b and d) groups for the executive control (EX), sensorimotor (SM), and visual (VIS) networks overlaid on the template pigs' T1-weighted anatomical images.

CHAPTER 5

SEMI-AUTOMATED CELL AND TISSUE ANALYSES REVEAL REGIONALLY SPECIFIC MORPHOLOGICAL ALTERATIONS OF IMMUNE AND NEURAL CELLS IN A PORCINE MIDDLE CEREBRAL ARTERY OCCLUSION MODEL OF STROKE [1]

---

[1]**Kelly M. Scheulin†**, Samantha E. Spellicy†, Emily W. Baker, Brian J. Jurgielewicz, Holly A. Kinder, Elizabeth S. Waters, Janet A. Grimes, Steven L. Stice, Franklin D. West. 2021. *Frontiers in Cellular Neuroscience Cellular Neuropathology.* 14(489). Reprinted here with permission of the publisher.

† these authors equally contributed to this work

Abstract

Histopathological analysis of cellular changes in the stroked brain provides critical information pertaining to inflammation, cell death, glial scarring, and other dynamic injury and recovery responses. However, commonly used manual approaches are hindered by limitations in speed, accuracy, bias, and the breadth of morphological information that can be obtained. Here, a semi-automated high-content imaging (HCI) and CellProfiler histological analysis method was developed and used in a Yucatan miniature pig permanent middle cerebral artery occlusion (pMCAO) model of ischemic stroke to overcome these limitations. Evaluation of 19 morphological parameters in $IBA1^+$ microglia/macrophages, $GFAP^+$ astrocytes, $NeuN^+$ neuronal, $FactorVIII^+$ vascular endothelial, and DCX^+ neuroblast cell areas was conducted on porcine brain tissue 4 weeks post pMCAO. Out of 19 morphological parameters assessed in the stroke perilesional and ipsilateral hemisphere regions (38 parameters), a significant change in $\frac{38}{38}$ measured $IBA1^+$ parameters, $\frac{34}{38}$ $GFAP^+$ parameters, $\frac{32}{38}$ $NeuN^+$ parameters, $\frac{31}{38}$ $FactorVIII^+$ parameters, and $\frac{28}{38}$ DCX^+ parameters were observed in stroked vs non-stroked animals. Principal component analysis (PCA) and correlation analyses demonstrated that stroke-induced significant and predictable morphological changes that demonstrated strong relationships between $IBA1^+$, $GFAP^+$, and $NeuN^+$ areas. Ultimately, this unbiased, semi-automated HCI and CellProfiler histopathological analysis approach revealed regional and cell specific morphological signatures of immune and neural cells after stroke in a highly translational porcine model. These identified features can provide information of

disease pathogenesis and evolution with high resolution, as well as be used in therapeutic screening applications.

Keywords: Cell morphology, permanent middle cerebral artery occlusion model, porcine, ischemic stroke, high-content imaging

Introduction

Stroke remains a leading cause of death and long-term disability worldwide despite numerous preclinical and clinical trials to develop novel treatments (1). The development of new therapeutic targets and more effective treatments hinge on having a more complete understanding of cellular dynamics after stroke to assess changes in key processes such as the immune response and glial scar formation, which may also serve as biomarkers of injury severity and recovery. Modern histological approaches have led to significant breakthroughs in understanding thrombus etiology (2, 3), patterns of immune cell activation (4, 5), and other important pathological and recovery cellular changes. However, these standard approaches are limited by the number of cellular features that can be assessed, accompanied by decreased spatial information, slow data processing speeds, and subjectivity. Recent advances in imaging and processing power have led to the development of high-content image (HCI) analysis that enables high-throughput assessment of multiple single cell features, reduces time of analysis, and decreases subjectivity (6, 7). Assessment of micro-scale cellular morphological changes, garnered through HCI analysis of stroked tissues, is likely to result in more predictive studies of neural injury and recovery responses- a critical need in the stroke field (8).

HCI individual cell analysis has been utilized to better understand the dynamic changes in cellular morphological features in the injured brain (9, 10). Recent studies have identified distinct morphological changes in microglia in basic shape descriptions, such as surface area and perimeter, skeleton properties of ramified cells, and graph theory parameters in the peri-infarct region after ischemic stroke in rodent models. Additionally, automated analysis has resulted in substantial decreases in time to result acquisition (5

minutes vs. 7 hours) relative to manual approaches, with no compromise of result integrity (9). However, the limited number of *in vivo* HCI stroke studies have focused on either a well-demarcated perilesional region or a specific brain structure (9, 11), rather than global ipsilateral hemisphere changes. While region-specific differences in cellular morphology have been identified, such as in the case of astrocyte morphology (12), analysis of the peri-infarct region as well as the ipsilateral hemisphere should be conducted to determine local and global alterations in cellular morphology. For example, significant differences in cellular morphology of microglia within the infarct and a few millimeters from the infarct region have been previously observed, demonstrating the existence of transitions in morphological populations (9). Examining differences in inflammatory cell morphology changes induced by ischemia, edema, intracerebral hemorrhage, or even in response to therapy, may provide more descriptive information about the pervasiveness of injury throughout the affected issue than solely considering the direct lesioned area alone. To date, most HCI neural analysis studies have focused primarily on individual cell assessments of only a few hundred of the billions of brain cells with an emphasis typically on one specific cell type such as microglia/macrophages (9, 13), neurons (14), or astrocytes (12, 15). While these studies provide significant detail into the changes of single cell-type features, they neglect other key cell types and relationships between these cells that contribute to normal and injured brain activity. For example, morphological changes of $IBA1^+$ microglia/macrophages and $GFAP^+$ astrocytes following activation has been documented in many studies of neuroinflammation (16, 17) and stroke specifically (18). Activation of $IBA1^+$ microglia/macrophages is associated with a transition from ramified, extended cells with a large perimeter to area ratio, to cells

that are more ameboid, compact, and have a smaller perimeter phenotype (19, 20). Additionally, activation of $GFAP^+$ astrocytes proximal to the lesion site exhibit a stellate, hypertrophied appearance with processes extending toward the ischemic core at acute timepoints during glial scar formation (21). However, the relationship between the morphological changes in each of these cell types to each other has yet to be quantitatively characterized. The improved understanding of these relationships between cell types is likely to be important in investigating novel cell interaction in the stroke environment and discovering new therapeutic targets and mechanisms.

Utilizing animal models with similar neural cellular composition and organization as humans in preclinical stroke research is becoming increasingly important to improve the potential of successful clinical translation (8). In this study, the porcine brain is utilized for HCI cellular histological analysis following pMCAO due to similar white matter content, size, and hierarchical organization to the human brain (22). White matter is exceedingly vulnerable to ischemic damage relative to gray matter due to the lack of sufficient collateral circulation, excitotoxicity susceptibility, and destruction of damaged oligodendrocytes by microglia and infiltrating macrophages (23). Therefore, for translational purposes, it is imperative to quantify morphological changes of inflammatory and neural cells in large animal brains that show greater similarity to the human stroke condition.

To comprehensively investigate quantitative cellular morphological changes after stroke, a custom, semi-automated HCI and CellProfiler analysis pipeline (24) was used to capture 19 morphological features of 5 different cell types in a pMCAO porcine model of ischemic stroke. While the methodology and analysis pipeline presented here are

generalizable to small animal stroke models, it is especially useful in the quantification of cells and associated aspects in large animal models that have sizable brain mass, which historically has made detailed quantitative analysis of discrete segments challenging. This study demonstrated significant differences in the morphology of microglia/macrophages, astrocytes, neurons, neuronal precursors, and vasculature cells in the stroked porcine brain. Additionally, significant correlations were observed between morphological changes in these cell types following stroke, suggesting that this HCI histological analysis approach can lead to new information on the dynamic interplay between cytoarchitectural and inflammatory cell types in the post-stroke brain.

Materials and Methods

Study design

All work involving the use of animals or animal tissue in this study was performed in accordance with the National Institutes of Health (NIH) Guidelines for Care and Use of Laboratory Animals and was reviewed and approved by the University of Georgia (UGA) Institutional Animal Care and Use Committee (IACUC; Animal Use Protocol (AUP) Number A2018 01-029-Y1-A5). Pigs were acquired from Lonestar Laboratory Swine (Sioux Center, IA) and individually housed in a Public Health Service (PHS) and Association for Assessment and Accreditation of Laboratory Animal Care (AAALAC) approved facility. Animal rooms were maintained at temperature of approximately 27°C with a 12-hour light/dark cycle. Pigs were fed standard UGA grower 1 diet with daily enrichment through toys and human contact. Predefined exclusion criteria included instances that would prevent the animal from reaching the 4-week timepoint such as death or euthanasia due to severe self- inflicted injuries, inability to thermoregulate, uncontrolled seizure activity, respiratory distress, and/or confounding infections at the incision. No pigs reached the aforementioned exclusion criteria, and therefore all animals were included in the analysis.

Porcine ischemic stroke surgery

In this single-blinded study, sexually mature [>1 year] male and ovariectomized (OVX) female Yucatan miniature pigs weighing between 68-98 kg were randomly assigned to either non-stroke (NS, n=3 females, n=2 males) or stroke (S, n=3 females, n=4 males) groups. Due to the global effect of the ischemic injury on the entire brain,

normal healthy animals were selected to be used as the control group rather than the contralateral hemisphere. The day prior to surgery, pigs were administered antibiotics (Ceftiofur crystalline free acid; 5mg/ kg intramuscular (IM); Zoetis) to prevent infection as required by institutional guidelines. A right sided pMCAO procedure was performed on all stroked animals by a trained veterinary neurosurgeon as described in Platt et. al (22). Briefly, pre-induction analgesia and sedation was achieved using xylazine (4 mg/kg IM; Vet-One), midazolam (0.3 mg/kg IM; Heritage), and methadone (0.2 mg/kg IM; Henry Schein Animal Health). Anesthesia was induced with propofol (to effect; intravenous (IV); Zoetis) and prophylactic lidocaine (1.0 mL 2% lidocaine; VetOne) was applied to the laryngeal folds to facilitate intubation. Anesthesia was maintained with isoflurane (1.0 - 2.0%; Abbot Laboratories) in oxygen. Pigs were determined to be at an adequate anesthetic depth when animals displayed complete muscle relaxation and no longer responded to a toe pinch or ear stimulation per AUP. For anesthetic depth monitoring during anesthesia events, heart rate and blood pressure were monitored using a stethoscope and/or Doppler Probe every 5 minutes, respiration rate was regulated using a ventilator every 5 minutes, and temperature was monitored using a thermometer every 15 minutes. Following a frontotemporal craniectomy with orbital rim ostectomy and zygomatic arch resection, the temporal fascia and muscle were elevated, and the local dura mater was exposed. The middle cerebral artery (MCA) and collaterals were then identified just distal to the Circle of Willis. Permanent occlusion of the distal MCA and associated branches was achieved by bipolar electrocauterization resulting in territorial ischemia. The exposed brain was then covered with a sterile oxidized cellulose hemostatic agent (VetSpon). Following occlusion, the temporalis muscle and epidermis

were routinely re-apposed. Once the incision was closed, anesthesia was discontinued, pigs were returned to their pens, and extubated. Temperature, respiration, and heart rate were monitored every 15 minutes until vitals returned to a normal range. Additionally, vitals were observed every 4 hours for 24 hours and then pigs received health checks twice daily until completion of the study. To control for postoperative pain, acute inflammation, and fever management, banamine (2.2 mg/kg IM or IV; Merck) was administered every 12 hours for 24 hours and every 24 hours for 3 days following surgery and methadone (0.2 mg/kg IM or IV; Henry Schein Animal Health) was administered every 6 hours for 24 hours following surgery.

Porcine magnetic resonance imaging

Pigs underwent magnetic resonance imaging (MRI) at 1-day post-pMCAO to confirm ischemic stroke and determine brain infarct volume and patterning. MRI was acquired on a GE Signa HDx 3.0 Tesla scanner using an 8-channel large torso coil with the pig positioned in supine recumbency under general anesthesia described during stroke surgery. Fast Spin Echo (FSE) T2-Weighted (T2W) and Spin Echo (SE) Diffusion Weighted Imaging (DWI) were acquired in the multiplanar MRI protocol. Apparent diffusion coefficient (ADC) maps were generated from DWI sequences. Using OsiriX software (Version 10.0.5, Pixmeo SARL, Bernex, Switzerland), hemisphere volumes were calculated utilizing T2W sequences and ischemic lesion volumes were calculated utilizing ADC maps, as previously described (25). To control for edema in the brain due to the stroke, DWI corrected lesion volumes were calculated according to the following formula modified from Loubinoux et al (26, 27). $LV^c = HV_c+HV_i-(HV_c+HV_i-$

LV^u)*($\frac{HVc+HVi}{2HVc}$) where lesion volume corrected (LV^c), lesion volume uncorrected (LV^u), contralateral hemisphere volume (HVc), and ipsilateral hemisphere volume (HVi). A representative MRI image of the ischemic lesion patterning is demonstrated in **Supplementary Figure 9A**.

Porcine histology

Four weeks after pMCAO, NS and S pigs were euthanized by IV pentobarbital (1 mL/4.5kg) injection. Brains from both groups were removed and immersed in 10% buffered formalin (Millipore Sigma). Next, brains were sectioned coronally using a pig brain slicer (Zivic Instruments, Pittsburgh, PA). Right (ipsilateral to pMCAO) hemisphere sections were formalin-fixed, embedded in paraffin, and sectioned for immunohistochemistry (Leica RM2255, Germany). Following an enzyme block in 3% H_2O_2 for 5 minutes and Power Block (BioGenex) for 5 minutes, 4 μM thick sections were incubated with primary antibodies for 1 hour on a Biocare Medical Nemesis 7200 Autostainer. Primary antibodies used were GFAP (mouse 1:4000, Biogenex MU020-UC, Clone GA-5), IBA1 (rabbit 1:8000, Wako, 019-19741), NeuN (guinea pig 1:3000, Millipore Sigma, ABN90), FactorVIII (rabbit, Cell Marque, 250A-18), and DCX (rabbit, 1:4000, Abcam, ab18723). Secondary antibodies used were Biotinylated goat anti-rabbit 1:100, Vector Labs, BA-1000 for IBA1, Biotinylated horse anti-mouse 1:100, Vector Labs, BA-2001 for GFAP, Biotinylated goat anti-guinea pig 1:100, Vector Labs, BA-7000 for NeuN, Biotinylated goat anti-rabbit 1:100, Vector Labs, BA-1000 for FactorVIII, and Biotinylated goat anti-rabbit 1:100, Vector Labs, BA-1000 for DCX. The

substrate is DAB + Chromogen (12 minutes) from Biocare and all were counterstained with hematoxylin.

Morphological profiling

Each stained ipsilateral hemisphere slide was imaged using a Cytation 5 Imaging Multi-mode reader (BioTek, Vermont) in a 12 x 19-30 grid. This acquisition resulted in between 209-330 images per section, each representing a separate region of interest (ROI) per ipsilateral section. Individual images from each ipsilateral hemisphere were analyzed through a custom CellProfiler pipeline for individual stains **(Figure 1A)**. The pipeline was run on a Dell 5820 Tower Workstation using a Windows 10 Pro operating system and powered by a Xenon W-2133 3.6 Gigahertz processor with 32 gigabytes (GB) of memory and 256 GB of solid-state drive (SSD). CellProfiler detailed 19 parameters including area occupied, count, perimeter, shape area, compactness, eccentricity, Euler number, extent, form factor, major axis length, max ferret diameter, area shape maximum radius, area shape mean radius, area shape median radius, min ferret diameter, area shape minor axis length, orientation, area shape perimeter, and solidity per positive area or cell. All units represented are either in pixels or are unitless. Definitions and equations for each parameter are defined in **Supplementary Table 1** and examples are provided in **Figure 1B** and **Figure 1C**.

The values of each parameters for each positive area were averaged for a given ROI. ROI averages were used for statistical comparisons between NS and S groups. All

ROIs per section were used for ipsilateral hemispheric section comparisons (~300 ROIs per animal), and only ROIs from the perilesional area were used for perilesional comparisons (~60 ROIs per animal). In NS animals, an equal number of ROIs from the corresponding neuroanatomical locations of S animals were used for perilesional histological analysis. Principal component analysis (PCA) was conducted including all of the morphological features previously described. Each dot in the plot represents 1 ROI from 1 animal.

Whole processed and stitched images from each animal for IBA1 (**Supplementary Figure 4**), GFAP (**Supplementary Figure 5**), NeuN (**Supplementary Figure 6**), FactorVIII (**Supplementary Figure 7**), and DCX (**Supplementary Figure 8**) are displayed in Supplementary Materials.

Statistical Analysis

Morphological parameters from each positive area were recorded and quantified. Per cell or per area analysis was then averaged in each ROI captured. Average of each ROI (ranging from 100s to 10000s, depending on stain and location) was compared. A normality test was conducted for each parameter and a Mann-Whitney test was utilized for nonparametric data (GraphPad Prism 8). For heatmap generation and correlation analysis, all ROIs were averaged to a per-pig level to allow for comparison of cell type-specific morphological variation within each pig. All 10 parameters of each treatment group were compared utilizing PCA and Welch's unpaired t-test to determine significant

differences between principal components of NS and S animals. Simple linear regression analysis was conducted between each pig's lesion volume and area of each stain per whole section (GraphPad Prism 8).

Results

IBA1$^+$ areas transitioned to a more ameboid and swollen morphology after stroke

Qualitatively, positive area outlines generated through CellProfiler analysis revealed a visual difference in the size of IBA1$^+$ areas throughout the ipsilateral sections and perilesional regions in S animals compared to NS animals (**Figure 2A-B**). In addition, morphological changes of individual IBA1$^+$ cells in NS animals presented a more extended, ramified appearance compared to S animals, which presented a more rounded, ameboid appearance. Quantification of morphological parameters of IBA1$^+$ area in the ipsilateral hemispheric section revealed significant differences between S (n=1,860 ROIs) and NS (n=1,362 ROIs) animals. A significant increase in IBA1$^+$ area occupied (**Figure 2C**; Median NS=72,843px, S=96,963px, $p<0.0001$), IBA1$^+$ area shape perimeter (**Figure 2D**; Median NS=35.42px, S=38.99px, $p<0.0001$), major axis length (**Figure 2E**; Median NS=12.19px, S=12.93px, $p<0.0001$), solidity (**Figure 2F**; Median NS=0.7781px, S=0.7833px, $p=0.0008$), and mean radius (**Figure 2G**; Median NS=1.254px, S=1.331px, $p<0.0001$) in S compared to NS animals. Additionally, there was a significant decrease in ipsilateral hemispheric section IBA1$^+$ area eccentricity (**Figure 2H**; Median NS=0.8382px, S=0.8122px, $p<0.0001$) in S animals compared to NS animals. Collectively, this analysis revealed an overall increase in IBA1$^+$ area and transition to a larger (increase in area occupied and major axis length) and more amoeboid/rounded morphology (increases in solidity and decreases in eccentricity) in the ipsilateral hemisphere section of S animals compared to NS animals. Additional significant differences of IBA1$^+$ areas between S and NS animals, as well as all other quantified

stains, are detailed in the supplemental (**Supplementary Table 1**). PCA (**Figure 2I-L**) revealed a significant increase in ipsilateral section PC1-3 in S animals compared to NS animals ($p<0.0001$).

Quantification of morphological parameters of $IBA1^+$ area in the ipsilateral perilesional ROIs (S; n=453 ROIs and NS; n=304 ROIs) showed similar findings to ipsilateral hemispheric section analysis. A significant increase in $IBA1^+$ area occupied (**Figure 3A**; Median NS=67,697px, S=125,584px, $p<0.0001$), $IBA1^+$ area shape perimeter (**Figure 3B**; Median NS=34.76px, S=44.94px, $p<0.0001$), major axis length (**Figure 3C**; Median NS=12.12px, S=14.22px, $p<0.0001$), and mean radius (Median NS=1.255px, S=1.347px, $p<0.0001$) as well as a significant decrease in solidity (**Figure 3D**; Mean NS=0.7838, S=0.7759, $p<0.0001$) and eccentricity (**Figure 3F**; Mean NS=0.8406, S=0.8106 $p<0.0001$) were shown in S compared to NS animals. $IBA1^+$ area increased and transitioned to a more ameboid/rounded (decrease in eccentricity), larger (increase in major axis length, area occupied, and mean radius), morphology in the perilesional region of S animals compared to NS animals. There were additional significant differences between S and NS animals (**Supplementary Table 2**). PCA (**Figure 3G-J**) revealed a significant increase in perilesional PC1-3 between S and NS animals.

GFAP$^+$ areas transitioned to more sprawled and extended morphology after stroke

Positive area outlines revealed global visual differences between S and NS animals with regard to the density of GFAP$^+$ areas in ipsilateral hemispheric sections (**Figure 4A-B**). Additionally, qualitative morphological evaluations revealed smaller, more rounded cells in NS animals and larger, more extended cells in S animals. These qualitative observations are supported by quantification of morphological parameters of GFAP$^+$ in the ipsilateral hemisphere section, which showed significant differences between S (n=1,848 ROIs) and NS (n=1,668 ROIs) animals. A significant increase in GFAP$^+$ area shape perimeter (**Figure 4D**; Median NS=15.29px, S=17.59px, p<0.0001), major axis length (**Figure 4E**; Median NS=5.492px, S=6.236px, p<0.0001), mean radius (**Figure 4G**; Median NS=1.067px, S=1.085px, p<0.0001) and a significant decrease in solidity (**Figure 4F**; Median NS=1.041px, S=1.005px, p<0.0001) were discovered in S compared to NS animals. Significant differences were not seen in ipsilateral section GFAP$^+$ area occupied (**Figure 4C**; Median NS=77,435px, S=px, p76,282, p=0.5642) and eccentricity (**Figure 4H**; Median NS=0.8009px, S=px, p<0.8040, p<0.0001) in S animals compared to NS animals. Collectively, GFAP$^+$ area increased in S animals compared to NS animals (evidenced by an increase in perimeter, major axis length, and radius), and a transition to a less rounded and more ramified A1-like reactive astrocyte in S compared to NS animals (decrease in solidity) was observed. PC1-3 for GFAP$^+$ areas significantly increased in ipsilateral hemispheric sections (p<0.0001) in S animals compared to NS animals (**Figure 4I-L**).

Quantification of morphological parameters of GFAP$^+$ area in the perilesional region revealed a major difference from ipsilateral section ROI showing an increase in area occupied by GFAP$^+$ area in S (n=461 ROIs) relative to NS (n=324 ROIs) animals (**Figure 5A**; Median NS=116,517px, S=168,980px, p<0.0001). Similar to hemispheric section analysis, there was also a significant increase in compactness (**Figure 5C**; Median NS=1.412px, S=1.507x, p<0.0001) and major axis length (**Figure 5E**; Median NS=5.911px, S=7.770px, p<0.0001) and a significant decrease in form factor (**Figure 5B**; Median NS=0.7143px, S=0.6570px, p<0.0001), solidity (**Figure 5D**; Median NS=1.032px, S=0.9710px, p<0.0001), and orientation (**Figure 5F**; Median NS=15.32px, S=13.55px, p=0.0002) suggesting a transition of GFAP$^+$ areas to a more A1-like reactive astrocyte morphology in the perilesional region, as well as a greater area occupied by GFAP$^+$ in S compared to NS animals. A significant increase in perilesional PC1 (p<0.0001) and PC3 (p=0.0162), but no significant differences in PC2 of GFAP$^+$ ROIs was observed in perilesional tissue between S and NS animals (**Figure 5G-J**).

NeuN$^+$ cells transitioned to a stressed phenotype after stroke

While neuron loss is observed and expected at early time points following stroke, ongoing inflammation perpetuates a stressed/apoptotic state altering residual neuronal health. The nuclear morphology of these residual cells undergoing inflammatory stress even at chronic timepoints can indicate overall neuronal health, evidenced by a quantifiable transition to more apoptotic, stressed, morphology ($\frac{nuclear\ circumference}{form\ factor}$) (28), or nuclear pyknosis and fragmentation (29) following stroke (30, 31). A qualitative

loss of NeuN$^+$ area was observed in perilesional regions in S compared to NS animals (**Figure 6A-B**). The ipsilateral section sections of S (n=2,230 ROIs) were significantly decreased when compared to NS (n=1,476 ROIs) in areas occupied by NeuN$^+$ (**Figure 6C**; Median NS=57,883px, S=38,475px, p<0.0001), NeuN$^+$ area shape perimeter (**Figure 6D**; Median NS=76.18px, S=71.00px, p<0.0001), major axis length (**Figure 6E**; Median NS=24.78px, S=22.65px, p<0.0001), and eccentricity (**Figure 6H**; Median NS=0.8065px, S=0.7872px, p<0.0001). A significant increase in solidity (**Figure 6F**; Median NS=0.7841px, S=0.7936px, p<0.0001) was observed in S animals compared to NS animals. No significant difference was seen in mean radius (**Figure 6G**; Median NS=1.980px, S=1.955px, p=0.3949). Collectively, there was an overall decrease in NeuN$^+$ areas in S animals compared to NS animals and a transition to smaller, more compact and oblong cells (evidenced by a decrease in perimeter, major axis length, compactness, and eccentricity) as is associated with nuclear morphological apoptosis. PCA (**Figure 6I-L**) revealed a significant (p<0.0001) increase in ipsilateral section PC1 and a significant decrease in PC3 of NeuN$^+$ areas in S compared to NS animals.

Quantification of morphological parameters of NeuN$^+$ cells in the perilesional region of S (n=452 ROIs) and NS (n=304 ROIs) animals demonstrated differences from ipsilateral section ROI quantification. While there was a significant decrease in area occupied by NeuN$^+$ cells (**Figure 7A**; Median NS=70,417px, S=54,171px, p<0.0001), as observed in hemisphere section analysis, there was an increase in NeuN$^+$ perimeter (**Figure 7B**; Median NS=67.52px, S=85.73px, p<0.0001), and eccentricity (**Figure 7F**; Median NS=0.7921px, S=0.8260px, p<0.0001) contrary to directions seen in ipsilateral

hemisphere analysis. There was also a decrease in NeuN$^+$ solidity (**Figure 7D**; Median NS=0.8184px, S=0.6950px, p<0.0001), and mean radius (**Figure 7E**; Median NS=2.067px, S=1.771px, p<0.0001) which was opposite in direction to ipsilateral hemisphere analysis as well. PCA (**Figure 7G-J**) revealed a significant (p<0.0001) increase in perilesional PC1 and a significant decrease in PC3 of S animals compared to NS animals.

Disoriented FactorVIII$^+$ areas increased in coverage but decreased in size after stroke

FactorVIII has previously been utilized to identify vasculature in tissues and organs (32-34). In this study, qualitative evaluation of FactorVIII$^+$ areas depict distribution and morphological differences in S animals compared to NS animals (**Figure 8A-B**). FactorVIII$^+$ areas in perilesional regions in S animals displayed a dense distribution and unique morphological changes compared to NS animals. Quantification of morphological parameters of FactorVIII$^+$ in the ipsilateral section sections revealed a significant increase in area occupied (**Figure 8C**; Median NS=13,185px, S=21,425px, p<0.0001), solidity (**Figure 8F**; Median NS=0.6806px, S=0.6884px, p<0.0001) and mean radius (**Figure 8G**; Median NS=1.407px, S=1.419px, p<0.0001) between S (n=1,584 ROIs) and NS (n=1,128 ROIs) animals. Additionally, a significant decrease in area shape perimeter (**Figure 8D**; Median NS=76.68px, S=72.86px, p<0.0001), major axis length (**Figure 8E**; Median NS=23.98px, S=23.30px, p<0.0001), and orientation (**Figure 8H**; Median NS=8.728px, S=-4.177px, p<0.0001) were observed in S animal compared to NS

animals. Collectively, this analysis showed an overall increase in smaller, more circular FactorVIII$^+$ areas as well as a significant change in orientation in S animals. PCA (**Figure 8I-L**) revealed a significant ($p<0.0001$) decrease in PC2 and a significant increase in PC3 of FactorVIII$^+$ area in ipsilateral section ROIs of S animals compared to NS animals.

Quantification of morphological parameters of FactorVIII$^+$ area in the perilesional ROIs in NS (n=240 ROIs) and S (n=334 ROIs) animals showed similar findings to ipsilateral section ROI quantification. While in perilesional regions there was a significant increase in area occupied by FactorVIII$^+$ (**Figure 9A**; Median NS=5,667px, S=16,598px, $p<0.0001$) and a decrease in major axis length (**Figure 9C**; Median NS=26.60px, S=23.38px, $p<0.0001$) and eccentricity (**Figure 9F**; Median NS=0.8917px, S=0.8637px, $p<0.0001$) in S animals compared to NS animals similar to ipsilateral section analysis, there was a contrasting decrease in solidity (**Figure 9D**; Median NS=0.7550px, S=0.7086px, $p<0.0001$). No significant differences were seen in area shape perimeter (**Figure 9B**; Median NS=75.01px, S=70.62px, $p=0.0869$) and mean radius (**Figure 9E**; Median NS=1.466px, S=1.459px, $p=0.6348$). PCA (**Figure 9G-J**) resulted in a significant ($p<0.0001$) decrease in PC2 and increase in PC3 of S animals compared to NS animals in perilesional region analysis, similar to ipsilateral section analysis.

Smaller rounded DCX$^+$ areas increased after pMCAO

There were no stark visual differences of DCX$^+$ areas in the ipsilateral hemisphere section between S and NS animals (**Supplementary Figure 1A-B**). Quantification of morphological DCX$^+$ parameters, however, did show a significant increase in area occupied (**Supplementary Figure 1C**; Median NS=1,878px, S=2,528px, $p<0.0001$) and solidity (**Supplementary Figure 1F**; Median NS=0.9328px, S=0.9393px, $p<0.0001$) of S (n=2,004 ROIs) compared to NS (n=1,241 ROIs). Additionally, a significant decrease in area shape perimeter (**Supplementary Figure 1D**; Median NS=18.98px, S=18.40px, $p<0.0001$), and major axis length (**Supplementary Figure 1E**; Median NS=6.994px, S=6.921px, $p=0.0029$), and mean radius (**Supplementary Figure 1G**; Median NS=1.179px, S=1.165px, $p<0.0002$). There were no significant differences in orientation (**Supplementary Figure 1H**; Median NS=0.1663px, S=0.3648px, $p=0.6869$). Collectively, ipsilateral section ROI analysis showed a significant increase in DCX$^+$ area occupied with a transition to smaller (decrease in perimeter) rounder cells (increase in solidity) in S animals compared to NS animals. PCA (**Supplementary Figure 1I-L**) revealed a significant increase in PC1 ($p<0.0001$) and PC2 ($p<0.0001$) in DCX$^+$ areas of ipsilateral section ROIs of S animals compared to NS animals.

Quantification of morphological parameters of DCX$^+$ area in the ipsilateral perilesional ROIs of NS (n=93 ROIs) and S (n=128 ROIs) revealed differences from ipsilateral section ROI quantification. While in perilesional regions there was a significant increase in solidity (**Supplementary Figure 2D**; Median NS=0.9348px, S=0.9477px, $p<0.0001$) and eccentricity (**Supplementary Figure 2F**; Median

NS=0.7673px, S=0.7851px, p=0.0008) and a decrease in perimeter (**Supplementary Figure 2B**; Median NS=18.95px, S=18.19px, p<0.0001) of S compared to NS animals, as seen in ipsilateral section quantification, there was also a significant decrease in major axis length (**Supplementary Figure 2C**; Median NS=6.875px, S=6.528px, p<0.0001), and mean radius (**Supplementary Figure 2E**; Median NS=1.192px, S=1.142px, p<0.0001). There were no significant differences in area occupied by DCX^+ (**Supplementary Figure 2A**; Mean NS=3,162px S=3,461px, p=0.3344) of S compared to NS animals. PCA (**Supplementary Figure 2G-J**) revealed a significant decrease in PC1 (p<0.0001) and PC2 (p=0.0246) in S animals compared to NS animals in perilesional region analysis.

In addition to ipsilateral section and perilesional ROI quantification, DCX^+ area in the subventricular zone (SVZ) was also quantified as the SVZ is a recognized neural stem cell niche in NS (**Supplementary Figure 3A**) and S (**Supplementary Figure 3B**) animals. DCX^+ cells were also identified in the choroid plexus and included in the SVZ ROI quantification in NS (**Supplementary Figure 3A**) and S (**Supplementary Figure 3B**) animals. There was a significant difference of DCX^+ morphology identified between S (n=93 ROIs) and NS (n=128 ROIs). There was a significant increase in area occupied by DCX^+ (**Supplementary Figure 3C**; Median NS=2,060px, S=3,461px, p<0.0001), major axis length (**Supplementary Figure 3E**; Median NS=6.528x, S=7.003px, p<0.0001), solidity (**Supplementary Figure 3F**; Median NS=0.9348px, S=0.9477px, p<0.0001), and eccentricity (**Supplementary Figure 3H**; Median NS=0.7704px, S=0.7836px, p=0.0015). There was also a significant decrease in area shape perimeter

(**Supplementary Figure 3D**; Median NS=18.90px, S=17.24px, p<0.0001) and mean radius (**Supplementary Figure 3G**; Median NS=1.192px, S=1.142px, p<0.0001). PCA (**Supplementary Figure 3I-L**) revealed a significant increase in PC2 (p=0.0310) in S animals compared to NS animals in SVZ analysis.

Relationships of morphological parameters across cell types altered in stroked Yucatan brain

PCA was conducted on NS and S ROIs labeled by DCX^+ (red), $FactorVIII^+$ (light green), $GFAP^+$ (dark blue), $IBA1^+$ (tan), and $NeuN^+$ (dark green). While ellipses of NS animals for each stain are well delineated (**Figure 10A**), PCA ellipses of S ROIs were not (**Figure 10B**).

The regional and inflammatory state-specific morphology of $IBA1^+$, $GFAP^+$, and $NeuN^+$ cell types have been documented, making them excellent candidates to examine morphological correlations between these cell types using this novel HCI analysis approach. Heatmaps of each parameter measured (1-19) were generated for $IBA1^+$ vs. $GFAP^+$ (**Figure 10C**), $IBA1^+$ vs. $NeuN^+$ (**Figure 10D**), and $NeuN^+$ vs. $GFAP^+$ (**Figure 10E**) for hemispheric section and perilesional regions of S and NS groups. Multiple correlations of cell type to cell type S animal parameter comparisons (**Figure 10C-E**) were significantly divergent, often switching direction of correlation from NS animals regardless of location. In S animals, there were $\frac{26}{361}$ significant correlations of ipsilateral section and $\frac{49}{361}$ in perilesional tissue of $IBA1^+$ morphology to $GFAP^+$ morphology

compared to only $\frac{6}{361}$ and $\frac{9}{361}$ respectively in NS animals. In correlations of IBA1$^+$ morphology to NeuN$^+$ morphology in S animals, there were $\frac{21}{361}$ in ipsilateral section and $\frac{16}{361}$ in perilesional analysis compared to only $\frac{14}{361}$ and $\frac{2}{361}$ in NS animals respectively. Lastly, in S animals there were $\frac{45}{361}$ significant ipsilateral section and $\frac{64}{361}$ perilesional correlations of GFAP$^+$ morphology to NeuN$^+$ morphology, compared to only $\frac{7}{361}$ and $\frac{1}{361}$ in S animals. Ultimately in comparisons of all stains and locations, there were $\frac{221}{2166}$ significant correlations in S animals compared to $\frac{39}{2166}$ in NS animals.

Linear correlations, representative of one square of each heatmap, were evaluated to determine more specific relationships between morphological changes in stained areas (**Figure 10F-H**). While linear correlations between IBA1$^+$ extent and GFAP$^+$ mean radius are not significant between NS and S animals in ipsilateral section comparison, it is significant for S animals in perilesional comparisons (p=0.0220) but not NS animals (p=0.6779) (**Figure 10F**). In hemisphere section analysis, there was a significant linear correlation between IBA1$^+$ major axis length and GFAP$^+$ cell area in S animals (p=0.0289), but not in NS animals (p=0.6402). While there was no significant linear correlation between these parameters in either group in perilesional analysis, the x-intercepts of each group line were significantly different (p=0.0119) (**Figure 10G**). There was a significant linear correlation in hemispheric section GFAP$^+$ eccentricity and IBA1$^+$ solidity in NS animals (p=0.0311), but not S animals (p=0.3103). In perilesional analysis, this was reversed and there was a significant linear correlation in GFAP$^+$ eccentricity and

IBA1$^+$ solidity in S animals (p=0.0011), but not NS animals (p=0.7858) (**Figure 10H).** Quantified significant correlations between stains and treatment groups can be found in **Supplementary Figure 10.** These representative examples show some of the ways these correlations between cell types are regionally and injury dependent.

MRI analysis showed MCA territorial lesions with an average volume of 5.36±3.68cm^3 in stroked animals (**Supplementary Figure 9A, B**). Simple linear regression revealed a significantly negative correlation between lesion volume and NeuN$^+$ areas (**Supplementary Figure 9E**, p=0.0126) and a significantly positive correlation between lesion volume and DCX$^+$ areas (**Supplementary Figure 9G**, p=0.083) in whole hemispheric analysis.

Discussion

Standard histological analysis of cell morphology in most stroke studies have typically only examined a small subset of cellular features and relied on manual counting and analysis in a limited number of directly affected brain regions. Leveraging the advantages of HCI in a translational pig stroke model, semi-automated analysis of cell morphology was used to significantly increase the number of morphological features examined, eliminate the potential of user-bias, decrease processing time, and altogether increase histological analysis efficiency. Building from previous HCI studies, which detail computationally ascertained morphological changes in a single cell-type (9, 10, 35-39), this study revealed significant post-stroke morphological changes in 19 different cellular parameters in $IBA1^+$, $GFAP^+$, $NeuN^+$, $FactorVIII^+$, and DCX^+ areas post-pMCAO. From all quantified parameters in both regions, perilesional and ipsilateral hemisphere section (19 parameters per region), a significant change in $\frac{38}{38}$ measured $IBA1^+$ parameters, $\frac{34}{38}$ $GFAP^+$ parameters, $\frac{32}{38}$ $NeuN^+$ parameters, $\frac{31}{38}$ $FactorVIII^+$ parameters, and $\frac{28}{38}$ DCX^+ parameters were observed in injured animals. While the p-values for many of these parameters indicated a strong significant difference between stroked and non-stroked animals, it is important to note that the large sample sizes utilized in this analysis may result in statistically significant results that may not be biologically significant. In light of this, analysis was not only directed at identifying individual parameter differences but also collective over-arching differences between respective cells in non-stroked and stroked animals through PCA. PCA demonstrated that these stroke-induced morphological changes were highly significant and suggested a

stroke cell morphological fingerprint. Morphological analysis also revealed significant relationships between IBA1$^+$, GFAP$^+$, and NeuN$^+$ areas with 1.8% of examined morphologies between these areas correlating pre-stroke and 10.2% correlating post-stroke. These correlative morphological changes suggest coordinated interactions associated with stroke pathological (e.g., immune and inflammatory responses) and recovery (e.g., neural reorganization) responses. However, additional studies modulating key cell signaling and molecular events are needed to further confirm the interplay between these cell types. The adapted HCI cellular morphological analysis approach showed that the stroke environmental effects led to comprehensive changes in cell morphology. This approach can be used as a platform technology to study unique cellular alterations due to injury or therapeutic intervention even in challenging systems such as the pig stroke model.

Identification of morphological correlations and relationships will enable the connection of cell specific interactions previously unknown. For example, here a positive correlation was observed between IBA1$^+$ solidity (more round) and GFAP$^+$ eccentricity (less round) in perilesional tissue in S animals, but not NS animals. While the morphological changes of activated astrocytes and microglia/macrophages have been described previously, in many studies these morphological changes are not directly quantified as in this study but rely on more qualitative observation (40-44). The analysis utilized here not only quantifies activation-specific morphological changes through individual parameters, but also utilizes data reduction techniques to provide an overall value indicative of cellular change following stroke. This unbiased high throughput technique can be utilized to better quantify and demarcate discrete zones of activation

stemming away from the focal area of ischemia. Furthermore, while the presence of DCX^+ cells in the choroid plexus was unexpected in this study, it is not without precedence. Previously, neuroblasts co-labeled with DCX^+ and $BrdU^+$ were found to be present in the choroid plexus in chick embryos (45). Additionally, Nestin and MAP2 expression has been shown to increase in rodent choroid plexus epithelial cells following exposure to traumatic human CSF, demonstrating the potential for neural blast cells to be located in this region following pro-inflammatory exposure (46). Moreover, this multi-cellular morphological analysis approach allowed for unique correlation analysis between post-stroke morphological changes in different cell types. While there was a small number of morphological correlations between cell types in the NS brain, there was a substantial increase in the number of significant correlations between cell types following stroke, indicating a strong relationship between the changing morphologies of immune and cytoarchitectural cells. In addition to understanding basic cell interactions in the stroke environment, the enhanced understanding of cell-to-cell morphological correlations may serve as biomarkers for key stroke molecular and cellular events or for therapeutic responses. Future studies utilizing this high content analysis platform are needed to more closely examine statistically significant changes in morphology for biological relevance.

As part of this work, we developed a generalizable morphological profiling pipeline that could serve as a platform for future histological stroke studies. When using manual processing approaches, stroke studies are often limited to a select range of features such as the number of positive cells (47, 48), cell body size (49, 50), and number of extensions or processes (51, 52). Previous semi-automated systems, such as Sholl

concentric circle analysis used to identify cellular processes, ramification, and length of post-stroke GFAP$^+$ astrocytes, did provide additional morphology-specific information, but lacked informative measures of ellipticity and other measures often associated with ischemia-induced immune cell alterations (12). These additional measures provide further insight into the continuous spectrum of cellular activation states outside of the previous bimodal classifications (53). Additionally, previous GFAP$^+$ cell analyses also only provided information on 3 unique features, which is less relative to standard HCI studies (54, 55). Traditional methods often rely on trained users to either manually count or trace cell outlines using image-based software, which can lead to bias in these measurements. In addition to an increase in bias, manual methods are more time consuming than more robust computational or semi-automated methods. In previous studies, automated processing of post-stroke microglia was shown to decrease an average manual counting time of 4-5 minutes per cell for a trained investigator to 5 minutes for the entire data-set of all cells (9). Here, each individual pig (300 images per section, with 100s to 1000s of cells per image) took approximately 1 hour to analyze 1 stain spanning the ipsilateral hemisphere for 19 features. In contrast, the traditional manual quantification approach required up to 3.5 hours per pig to analyze 1 stain in just the lesion border for a single feature (e.g., positive cells). Ultimately, when totaling the multiple stains per animal (5 stains) and multiple regions (2 regions) analyzed, semi-automation allowed for processing of approximately 160 million cells in 160 hours for 16 animals, whereas analyzing the perilesional region alone for 5 stains would take approximately 280 hours of manual counting. While this analysis was completed utilizing a standard desktop computer, the use of servers with faster processing speeds could drastically improve the

efficiency of this semi-automated method. Current limitations of this study include the use of two-dimensional image analysis, whereas in the future, thicker sections can be utilized to capture more three-dimensional data. Given that the porcine brain is approximately 87x larger than a mouse brain, similar automated methods could increase the feasibility and efficiency of large animal studies or even be useful in histology-based clinical studies. As the large animal model is becoming increasingly valuable in the stroke field (56), the presented approach, which decreases bias by removing the element of human error and increasing regional sample size, is particularly valued for complex large animal experiments that have been historically prone to bias. The approaches shown herein can reduce bias which will improve translatability and allow the benefits of the large animal model to be used to its full potential. Further reduction of bias is vital to the success of large animal studies, including reports of lesion size variability, inclusion/exclusion criteria, randomization, and blinded assessment of outcome (57).

Efficiencies afforded through this semi-automated analysis approach allowed for more robust quantification, interpretation, and elucidation of detailed biologically relevant cellular features. In this study, we evaluated 19 unique morphological features and determined significant morphological differences between $IBA1^+$ areas in S and NS animals that demonstrated an increase in area occupied, perimeter, and major axis length that indicate a greater immune response in the perilesional area of S animals at 4 weeks post-pMCAO. While lesion volume may peak in early timepoints post-MCAO, rodent studies have demonstrated increases in inflammatory cells and cytokines in the post-acute stroke environment. For example, increases in neurotoxic factors and neuronal cell death persist from 7-25 days in young and aged rodent models of stroke (58). In regard to

chronic inflammation, rodent studies have shown that resident immune cells are persistently or sequentially activated at chronic time points with M1 microglia peaking at around 21 days post ischemic stroke (59). Additionally, infiltrating cells such as $CD4^+$ and $CD8^+$ T-cells were found in the peri-infarct region of rodents 1 month after stroke in a transient occlusion model (60). While there is a growing body of evidence in rodent literature, there is a lack of data surrounding post-MCAO inflammation at later timepoints in the porcine literature. For these reasons, this later time point was chosen. For $GFAP^+$ perilesional areas, we observed an opposite trend in the S animals compared to $IBA1^+$, which aligns with an activated immune response morphology (e.g., sprawled and extended vs. rounded and ameboid, respectively) (40). This data also supports that analyzing multiple cell types in the post-stroke brain is informative because of unique interactions between cell types. For example, microglia are highly sensitive responders to central nervous system injuries with a relatively low activation threshold. Microglia release cytokines that influence the activation of $GFAP^+$ cells resulting in glial scar formation and are critical for neuron-glial communication after ischemia (41-43, 61). While these interactions between microglia, astrocytes (44), neurons, and key factors in the stroke environment (e.g., cytokines) (62-64) have been characterized in the post-stroke brain, ischemia-induced morphological correlations between cells have not.

Ultimately, this study demonstrated for the first time dynamic morphological changes in microglia/macrophages, neurons, astrocytes, and vasculature after ischemic stroke and simultaneously found significant relationships between these morphological changes in these cell types in a preclinical gyrencephalic pig model. Understanding these morphological changes in specific cell populations in the stroke environment is critically

important as it may provide insight into key cellular functions and biological responses. Future studies warrant further investigation into the dynamic morphological relationships between these cell types and specific signaling factors (e.g., inflammatory or neurodegenerative signaling) to better understand the interplay and organization of important injury and recovery processes and to ensure observed changes are not only statistically significant but biologically significant. Directly correlating more easily obtainable clinical data such as lesion volume from MRI to post-mortem histology findings offers significant contributions to further understanding the disease state at the cellular level (65). Here, we found a significant relationship between lesion volume and whole hemisphere section area occupied for both $NeuN^+$ and DCX^+ cells, indicating that an increase in DCX expression (neurogenesis) and a simultaneous decrease in NeuN expression (neuronal death) is correlated with overall stroke severity. Furthermore, correlating these histological findings to advanced MRI findings, such as functional MRI to observe neural reorganization, or to behavioral phenotyping would strengthen HCI data conclusions. The semi-automated HCI cellular morphology pipeline developed in this study is an unbiased tool that offers increased efficiency when evaluating cellular interactions in the stroke environment and offers a unique opportunity for therapeutic and biomarker discovery.

Conflict of Interest

SLS is a stockholder in Aruna Bio Inc and was a part-time employee of Aruna Bio Inc during the study. EWB was a full-time employee of Aruna Bio Inc during the study. SES, KMS, BJJ, HAK, ESW, JAG, and FDW declare that the research was conducted in the absence of any commercial or financial relationships that could be construed as a potential conflict of interest.

Author Contributions

SES constructed CellProfiler pipelines and conducted histological imaging, processing, stitching, histopathological analysis, and generated figures. SES, KMS, BJJ, and ESW conducted animal work. SES, KMS, FDW, and SLS wrote and edited the paper. SES, KMS, EWB, BJJ, HAK, SLS and FDW participated in experimental planning. JAG performed OVX surgeries. HAK and EWB processed brains for histological submission.

Funding

This was funded by the National Science Foundation (Science and Technology Center grant CBET-0939511) and the National Institutes of Health (Small Business Innovation Research Grant 1R43NS103596-01).

Acknowledgments

The authors would like to acknowledge Dr. S. Platt, Dr. E. Howerth, Dr. G. Kim, Dr. J. Mumaw, E. Karstedt, and M. Wendzik for assistance with pig care and surgeries. We would also like to thank our team of undergraduate researchers. N. Alcalde-Santa Ana,

W. Anand, J. Bourbo, M. Bowler, T. Burnette, A. Cieszewski, L. Francis, Z. Jones, J. Johnston, Z. Oberholzer, L. Parker, S. Patel, S. Radhakrishnan, H. Rasheed, S. Shin, A. Simmons, E. Smith, M. Snyder, H. Stavas, C. Temple, B. Winkler, and J. Winkler.

Ethics Statement

All applicable international, national, and/or institutional guidelines for the care and use of animals were followed. All work involving the use of animals in this study were performed in accordance with the National Institutes of Health Guidelines for the Care and Use of Laboratory Animals and was reviewed and approved by the University of Georgia Institutional Animal Care and Use Committee (Protocol Number A2018 01-029-Y1-A5). This article does not contain any studies with human participants performed by any of the authors.

Data Availability Statement

The datasets and CellProfiler code generated for this study will be made available by the authors, without undue reservation.

References

1. Virani Salim S, Alonso A, Benjamin Emelia J, Bittencourt Marcio S, Callaway Clifton W, Carson April P, et al. Heart Disease and Stroke Statistics—2020 Update: A Report From the American Heart Association. Circulation. 2020;141(9):e139-e596.

2. Sporns Peter B, Hanning U, Schwindt W, Velasco A, Minnerup J, Zoubi T, et al. Ischemic Stroke. Stroke. 2017;48(8):2206-10.

3. Heo JH, Nam HS, Kim YD, Choi JK, Kim BM, Kim DJ, et al. Pathophysiologic and Therapeutic Perspectives Based on Thrombus Histology in Stroke. Journal of stroke. 2020;22(1):64-75.

4. Rayasam A, Hsu M, Kijak JA, Kissel L, Hernandez G, Sandor M, et al. Immune responses in stroke: how the immune system contributes to damage and healing after stroke and how this knowledge could be translated to better cures? Immunology. 2018;154(3):363-76.

5. Savchenko ES, Pevzner IB, Zorova LD, Silachev DN, Babenko VA, Manskikh VN, et al. Changes in number of neurons, astrocytes and microglia in brain after ischemic stroke assessed by immunohistochemistry and immunoblotting. Cell and Tissue Biology. 2016;10(6):445-52.

6. Riordan DP, Varma S, West RB, Brown PO. Automated Analysis and Classification of Histological Tissue Features by Multi-Dimensional Microscopic Molecular Profiling. PloS one. 2015;10(7):e0128975-e.

7. Chen S, Zhao M, Wu G, Yao C, Zhang J. Recent advances in morphological cell image analysis. Comput Math Methods Med. 2012;2012:101536-.

8. Kaiser EE, West FD. Large animal ischemic stroke models: replicating human stroke pathophysiology. Neural Regen Res. 2020;15(8):1377-87.

9. Heindl S, Gesierich B, Benakis C, Llovera G, Duering M, Liesz A. Automated Morphological Analysis of Microglia After Stroke. Frontiers in cellular neuroscience. 2018;12:106-.

10. Morrison HW, Filosa JA. A quantitative spatiotemporal analysis of microglia morphology during ischemic stroke and reperfusion. Journal of neuroinflammation. 2013;10:4-.

11. Brown Craig E, Wong C, Murphy Timothy H. Rapid Morphologic Plasticity of Peri-Infarct Dendritic Spines After Focal Ischemic Stroke. Stroke. 2008;39(4):1286-91.

12. Mestriner RG, Saur L, Bagatini PB, Baptista PPA, Vaz SP, Ferreira K, et al. Astrocyte morphology after ischemic and hemorrhagic experimental stroke has no influence on the different recovery patterns. Behavioural Brain Research. 2015;278:257-61.

13. Thored P, Heldmann U, Gomes-Leal W, Gisler R, Darsalia V, Taneera J, et al. Long-term accumulation of microglia with proneurogenic phenotype concomitant with persistent neurogenesis in adult subventricular zone after stroke. Glia. 2009;57(8):835-49.

14. Gonzalez CLR, Kolb B. A comparison of different models of stroke on behaviour and brain morphology. European Journal of Neuroscience. 2003;18(7):1950-62.

15. Wilhelmsson U, Bushong EA, Price DL, Smarr BL, Phung V, Terada M, et al. Redefining the concept of reactive astrocytes as cells that remain within their unique domains upon reaction to injury. Proceedings of the National Academy of Sciences. 2006;103(46):17513.

16. Karperien A, Ahammer H, Jelinek HF. Quantitating the subtleties of microglial morphology with fractal analysis. Frontiers in cellular neuroscience. 2013;7:3-.

17. Hovens I, Nyakas C, Schoemaker R. A novel method for evaluating microglial activation using ionized calcium-binding adaptor protein-1 staining: Cell body to cell size ratio. Neuroimmunology and Neuroinflammation. 2014;1:82-8.

18. Heindl S, Gesierich B, Benakis C, Llovera G, Duering M, Liesz A. Automated Morphological Analysis of Microglia After Stroke. Frontiers in Cellular Neuroscience. 2018;12(106).

19. Avignone E, Lepleux M, Angibaud J, Nägerl UV. Altered morphological dynamics of activated microglia after induction of status epilepticus. Journal of neuroinflammation. 2015;12:202-.

20. Davis BM, Salinas-Navarro M, Cordeiro MF, Moons L, De Groef L. Characterizing microglia activation: a spatial statistics approach to maximize information extraction. Scientific Reports. 2017;7(1):1576.

21. Ding S. Dynamic reactive astrocytes after focal ischemia. Neural Regen Res. 2014;9(23):2048-52.

22. Platt SR, Holmes SP, Howerth EW, Duberstein KJJ, Dove CR, Kinder HA, et al. Development and characterization of a Yucatan miniature biomedical pig permanent middle cerebral artery occlusion stroke model. Experimental & translational stroke medicine. 2014;6(1):5-.

23. Moxon-Emre I, Schlichter LC. Evolution of Inflammation and White Matter Injury in a Model of Transient Focal Ischemia. Journal of Neuropathology & Experimental Neurology. 2010;69(1):1-15.

24. Jones TR, Carpenter AE, Lamprecht MR, Moffat J, Silver SJ, Grenier JK, et al. Scoring diverse cellular morphologies in image-based screens with iterative feedback and machine learning. Proc Natl Acad Sci U S A. 2009;106(6):1826-31.

25. Gerriets T, Stolz E, Walberer M, Muller C, Kluge A, Bachmann A, et al. Noninvasive quantification of brain edema and the space-occupying effect in rat stroke models using magnetic resonance imaging. Stroke. 2004;35(2):566-71.

26. Loubinoux I, Volk A, Borredon J, Guirimand S, Tiffon B, Seylaz J, et al. Spreading of vasogenic edema and cytotoxic edema assessed by quantitative diffusion and T2 magnetic resonance imaging. Stroke. 1997;28(2):419-26; discussion 26-7.

27. Webb RL, Kaiser EE, Jurgielewicz BJ, Spellicy S, Scoville SL, Thompson TA, et al. Human Neural Stem Cell Extracellular Vesicles Improve Recovery in a Porcine Model of Ischemic Stroke. Stroke. 2018;49(5):1248-56.

28. Eidet JR, Pasovic L, Maria R, Jackson CJ, Utheim TP. Objective assessment of changes in nuclear morphology and cell distribution following induction of apoptosis. Diagn Pathol. 2014;9:92-.

29. Zille M, Farr TD, Przesdzing I, Müller J, Sommer C, Dirnagl U, et al. Visualizing cell death in experimental focal cerebral ischemia: promises, problems, and perspectives. Journal of cerebral blood flow and metabolism : official journal of the International Society of Cerebral Blood Flow and Metabolism. 2012;32(2):213-31.

30. Sairanen T, Karjalainen-Lindsberg M-L, Paetau A, Ijäs P, Lindsberg PJ. Apoptosis dominant in the periinfarct area of human ischaemic stroke—a possible target of antiapoptotic treatments. Brain. 2005;129(1):189-99.

31. Paltsyn A, Komissarova S, Dubrovin I, Kubatiev A. Increased cell fusion in cerebral cortex may contribute to poststroke regeneration. Stroke research and treatment. 2013;2013:869327-.

32. Liang Y, Besch-Williford C, Brekken RA, Hyder SM. Progestin-dependent progression of human breast tumor xenografts: a novel model for evaluating antitumor therapeutics. Cancer Res. 2007;67(20):9929-36.

33. Birner P, Obermair A, Schindl M, Kowalski H, Breitenecker G, Oberhuber G. Selective immunohistochemical staining of blood and lymphatic vessels reveals independent prognostic influence of blood and lymphatic vessel invasion in early-stage cervical cancer. Clin Cancer Res. 2001;7(1):93-7.

34. Nag S, Manias J, Eubanks JH, Stewart DJ. Increased Expression of Vascular Endothelial Growth Factor-D Following Brain Injury. Int J Mol Sci. 2019;20(7).

35. York EM, LeDue JM, Bernier L-P, MacVicar BA. 3DMorph Automatic Analysis of Microglial Morphology in Three Dimensions from Ex Vivo and In Vivo Imaging. eneuro. 2018;5(6):ENEURO.0266-18.2018.

36. Otxoa-de-Amezaga A, Miró-Mur F, Pedragosa J, Gallizioli M, Justicia C, Gaja-Capdevila N, et al. Microglial cell loss after ischemic stroke favors brain neutrophil accumulation. Acta Neuropathologica. 2019;137(2):321-41.

37. Verdonk F, Roux P, Flamant P, Fiette L, Bozza FA, Simard S, et al. Phenotypic clustering: a novel method for microglial morphology analysis. Journal of Neuroinflammation. 2016;13(1):153.

38. Morrison H, Young K, Qureshi M, Rowe RK, Lifshitz J. Quantitative microglia analyses reveal diverse morphologic responses in the rat cortex after diffuse brain injury. Scientific Reports. 2017;7(1):13211.

39. Fernández-Arjona MdM, Grondona JM, Granados-Durán P, Fernández-Llebrez P, López-Ávalos MD. Microglia Morphological Categorization in a Rat Model of Neuroinflammation by Hierarchical Cluster and Principal Components Analysis. Frontiers in Cellular Neuroscience. 2017;11(235).

40. Wang Y, Zhang JH, Sheng J, Shao A. Immunoreactive Cells After Cerebral Ischemia. Front Immunol. 2019;10:2781.

41. Zhou W, Liesz A, Bauer H, Sommer C, Lahrmann B, Valous N, et al. Postischemic brain infiltration of leukocyte subpopulations differs among murine permanent and transient focal cerebral ischemia models. Brain Pathol. 2013;23(1):34-44.

42. Huang L, Wu ZB, Zhuge Q, Zheng W, Shao B, Wang B, et al. Glial scar formation occurs in the human brain after ischemic stroke. Int J Med Sci. 2014;11(4):344-8.

43. Price CJ, Wang D, Menon DK, Guadagno JV, Cleij M, Fryer T, et al. Intrinsic activated microglia map to the peri-infarct zone in the subacute phase of ischemic stroke. Stroke. 2006;37(7):1749-53.

44. Hersh J, Yang S-H. Glia-immune interactions post-ischemic stroke and potential therapies. Exp Biol Med (Maywood). 2018;243(17-18):1302-12.

45. Prasongchean W, Vernay B, Asgarian Z, Jannatul N, Ferretti P. The neural milieu of the developing choroid plexus: neural stem cells, neurons and innervation. Frontiers in neuroscience. 2015;9:103-.

46. Hashemi E, Sadeghi Y, Aliaghaei A, Seddighi A, Piryaei A, Broujeni M, et al. Neural differentiation of choroid plexus epithelial cells: role of human traumatic cerebrospinal fluid. Neural Regen Res. 2017;12(1):84-9.

47. Hamzei Taj S, Kho W, Aswendt M, Collmann FM, Green C, Adamczak J, et al. Dynamic Modulation of Microglia/Macrophage Polarization by miR-124 after Focal Cerebral Ischemia. Journal of Neuroimmune Pharmacology. 2016;11(4):733-48.

48. Ito D, Tanaka K, Suzuki S, Dembo T, Fukuuchi Y. Enhanced Expression of Iba1, Ionized Calcium-Binding Adapter Molecule 1, After Transient Focal Cerebral Ischemia In Rat Brain. Stroke. 2001;32(5):1208-15.

49. Zhan X, Kim C, Sharp FR. Very brief focal ischemia simulating transient ischemic attacks (TIAs) can injure brain and induce Hsp70 protein. Brain Research. 2008;1234:183-97.

50. Fumagalli S, Perego C, Ortolano F, De Simoni M-G. CX3CR1 deficiency induces an early protective inflammatory environment in ischemic mice. Glia. 2013;61(6):827-42.

51. Masuda T, Croom D, Hida H, Kirov SA. Capillary blood flow around microglial somata determines dynamics of microglial processes in ischemic conditions. Glia. 2011;59(11):1744-53.

52. Go V, Bowley BGE, Pessina MA, Zhang ZG, Chopp M, Finklestein SP, et al. Extracellular vesicles from mesenchymal stem cells reduce microglial-mediated

neuroinflammation after cortical injury in aged Rhesus monkeys. Geroscience. 2020;42(1):1-17.

53. Hamby ME, Sofroniew MV. Reactive astrocytes as therapeutic targets for CNS disorders. Neurotherapeutics : the journal of the American Society for Experimental NeuroTherapeutics. 2010;7(4):494-506.

54. Caicedo JC, Cooper S, Heigwer F, Warchal S, Qiu P, Molnar C, et al. Data-analysis strategies for image-based cell profiling. Nat Methods. 2017;14(9):849-63.

55. Carpenter AE, Jones TR, Lamprecht MR, Clarke C, Kang IH, Friman O, et al. CellProfiler: image analysis software for identifying and quantifying cell phenotypes. Genome Biol. 2006;7(10):R100.

56. Herrmann AM, Meckel S, Gounis MJ, Kringe L, Motschall E, Mulling C, et al. Large animals in neurointerventional research: A systematic review on models, techniques and their application in endovascular procedures for stroke, aneurysms and vascular malformations. J Cereb Blood Flow Metab. 2019;39(3):375-94.

57. Kringe L, Sena ES, Motschall E, Bahor Z, Wang Q, Herrmann AM, et al. Quality and validity of large animal experiments in stroke: A systematic review. J Cereb Blood Flow Metab. 2020;40(11):2152-64.

58. Aurel P-W, Stanley Thomas C, Zaal K, Christof K, Lary CW. The Response of the Aged Brain to Stroke: Too Much, Too Soon? Current Neurovascular Research. 2007;4(3):216-27.

59. Jiang CT, Wu WF, Deng YH, Ge JW. Modulators of microglia activation and polarization in ischemic stroke (Review). Mol Med Rep. 2020;21(5):2006-18.

60. Xie L, Li W, Hersh J, Liu R, Yang S-H. Experimental ischemic stroke induces long-term T cell activation in the brain. Journal of Cerebral Blood Flow & Metabolism. 2019;39(11):2268-76.

61. Yang T, Dai Y, Chen G, Cui S. Dissecting the Dual Role of the Glial Scar and Scar-Forming Astrocytes in Spinal Cord Injury. Front Cell Neurosci. 2020;14:78.

62. Becerra-Calixto A, Cardona-Gómez GP. The Role of Astrocytes in Neuroprotection after Brain Stroke: Potential in Cell Therapy. Front Mol Neurosci. 2017;10:88-.

63. Li L-Z, Huang Y-Y, Yang Z-H, Zhang S-J, Han Z-P, Luo Y-M. Potential microglia-based interventions for stroke. CNS Neurosci Ther. 2020;26(3):288-96.

64. Barreto G, White RE, Ouyang Y, Xu L, Giffard RG. Astrocytes: targets for neuroprotection in stroke. Cent Nerv Syst Agents Med Chem. 2011;11(2):164-73.

65. Annese J. The importance of combining MRI and large-scale digital histology in neuroimaging studies of brain connectivity and disease. Front Neuroinform. 2012;6:13.

66. Mittelbrunn M, Gutiérrez-Vázquez C, Villarroya-Beltri C, González S, Sánchez-Cabo F, González MÁ, et al. Unidirectional transfer of microRNA-loaded exosomes from T cells to antigen-presenting cells. Nature communications. 2011;2:282-.

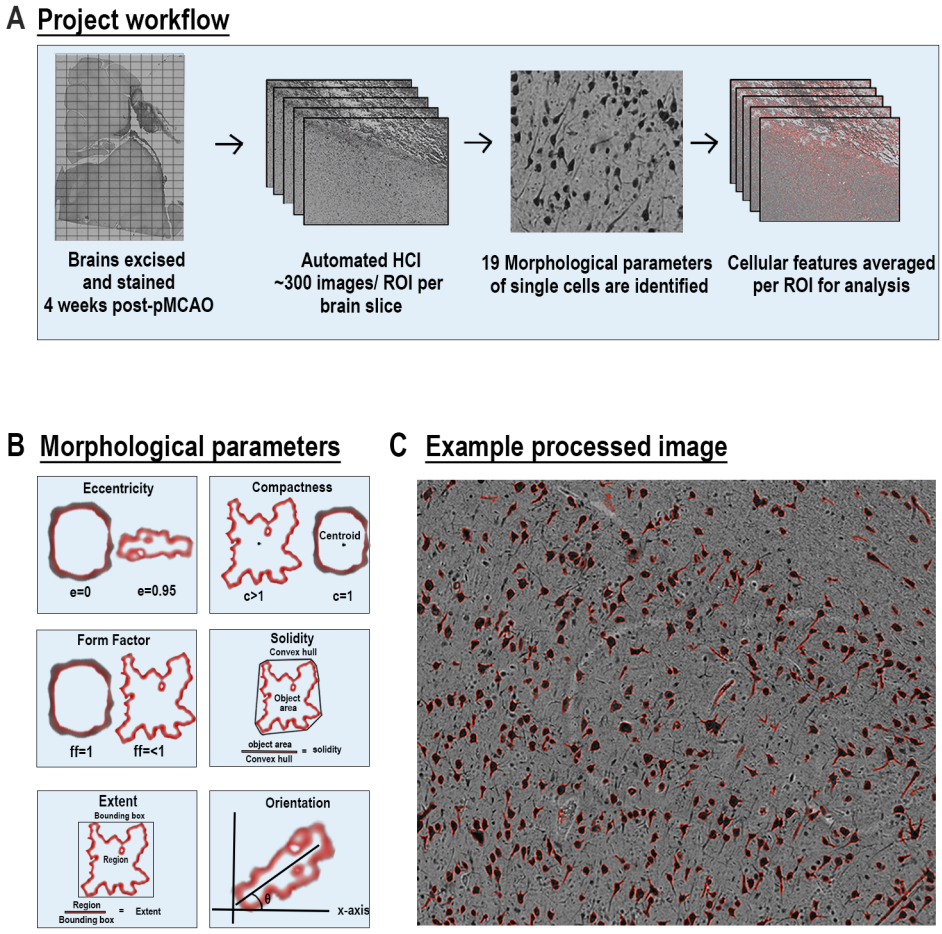

Figure 5.1. Automated high-content image processing pipeline and morphological parameters. Diagram of multiparametric HCI processing pipeline of cellular features from S and NS animals (**A**). Explanation of 6 of the 19 morphological parameters measured for each cell per ROI (**B**). Representative NeuN stained ROI after processing with outlines (red) of each positve cell area (**C**).

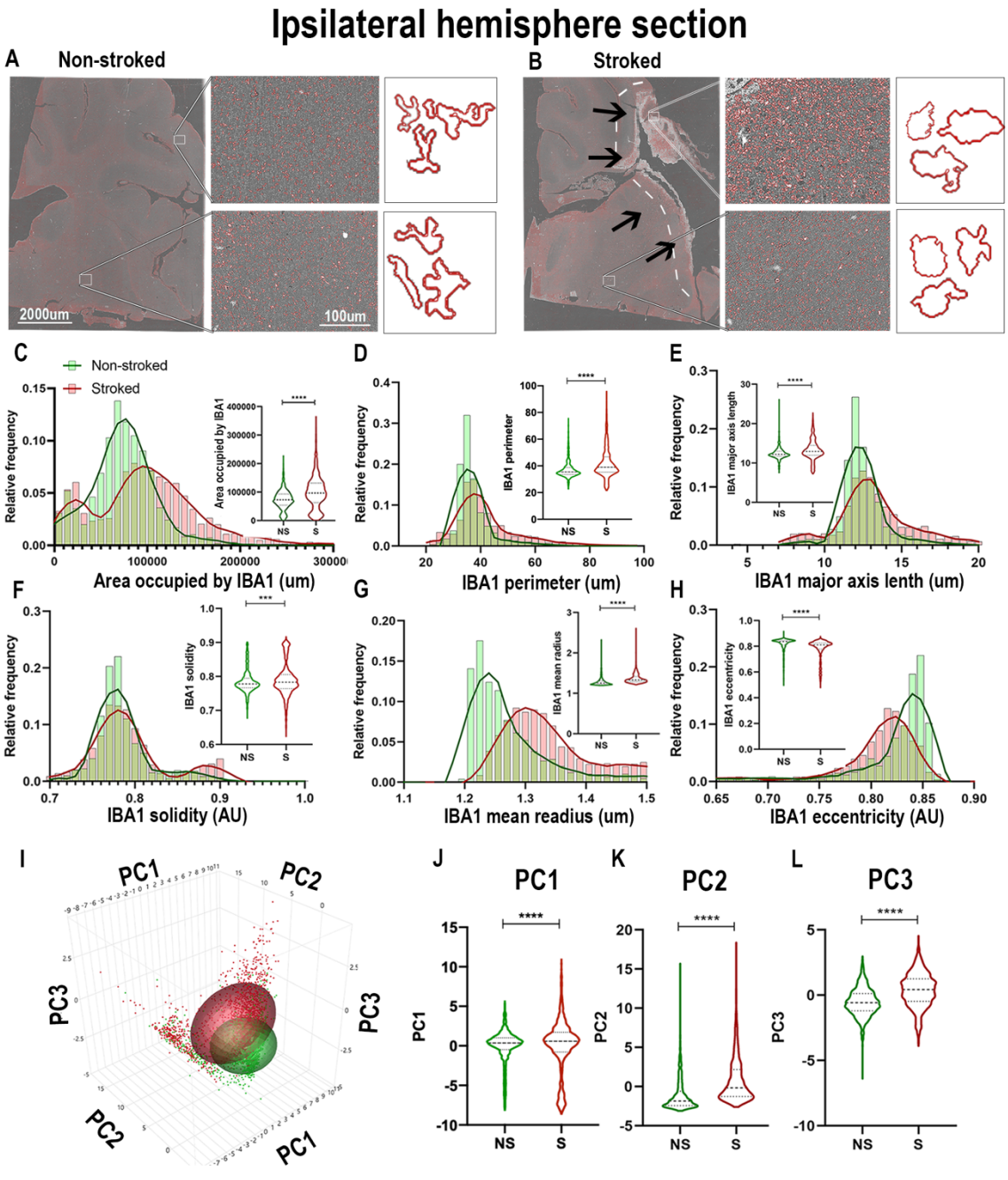

Figure 5.2. IBA1$^+$ areas transitioned to a more ameboid and swollen morphology after stroke in the ipsilateral hemisphere. Visual differences in density and morphological changes of IBA1$^+$ areas were observed between NS and S animals (**A-B**). Arrows indicate location of stroke lesion (**B**). Significant ($p<0.0001$) increases in IBA1+

area occupied (**C**), perimeter (**D**), major axis length (**E**), solidity (**F**; p=0.0008), and mean radius (**G**) were observed in hemisphere section of S (n=1,860 ROIs) compared NS (n=1,362 ROIs). There was a significant (p<0.0001) decrease observed in eccentricity (**H**) of $IBA1^+$ ROIs in hemisphere section analysis in S animals compared to NS animals. PCA (**I**) analysis showed significant (p<0.0001) increases in PC1 - PC3 (**I-L**) in S compared to NS animals.

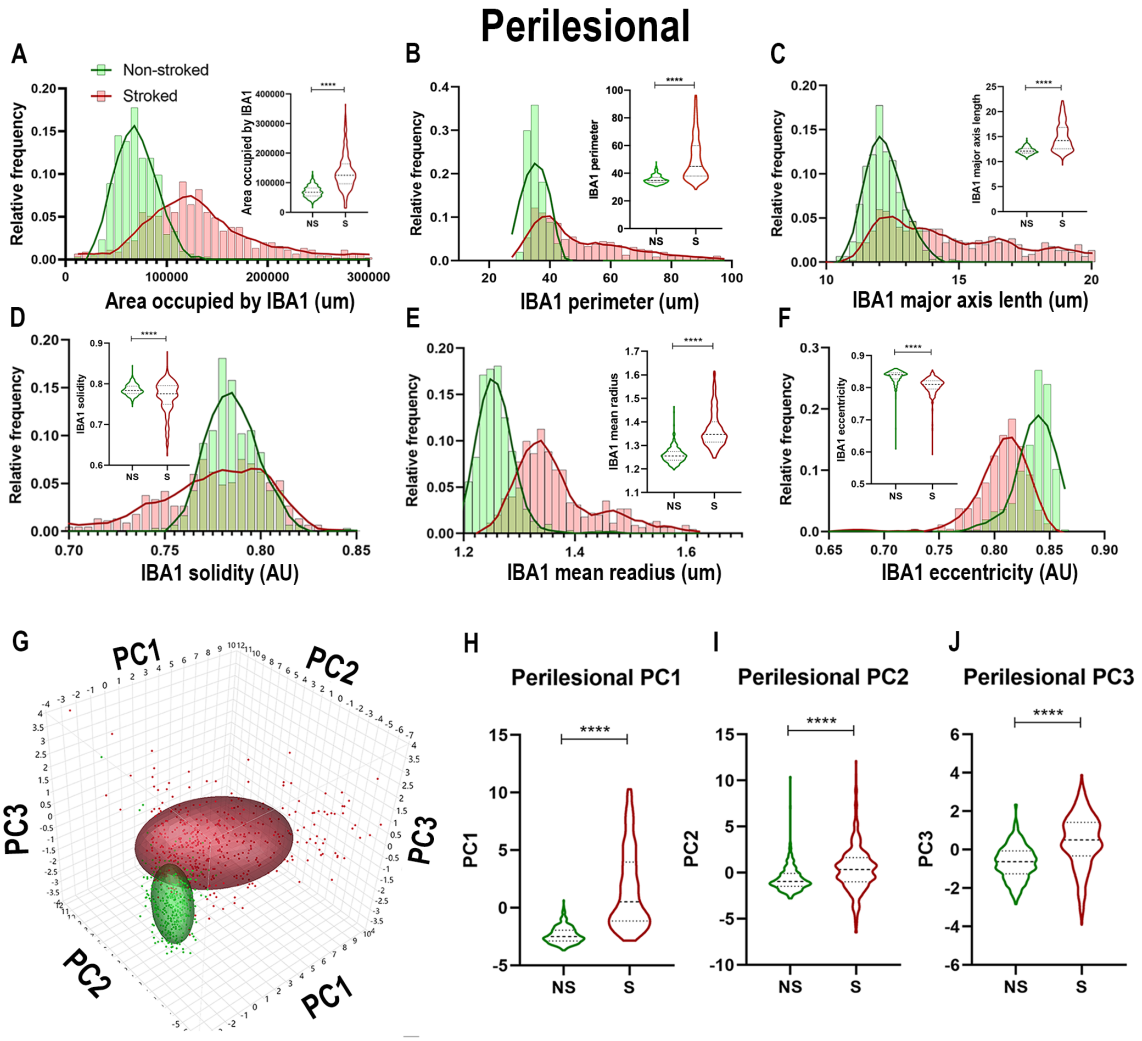

Figure 5.3. Stroke resulted in an amoeboid morphological transition of IBA1^{+} areas in perilesional tissue. Significant ($p<0.0001$) increases in IBA1+ area occupied (**A**), perimeter (**B**), major axis length (**C**), and mean radius (**E**) were observed in perilesional ROIs of S (n=452 ROIs) animals compared NS (n=304 ROIs) animals. There was a significant ($p<0.0001$) decrease in solidity (**D**), and eccentricity (**F**) of IBA1+ perilesional ROIs in S animals compared to NS animals. PCA (**G**) analysis showed a significant ($p<0.0001$) increase in PC1-3 (**H-J**) in S compared to NS animals.

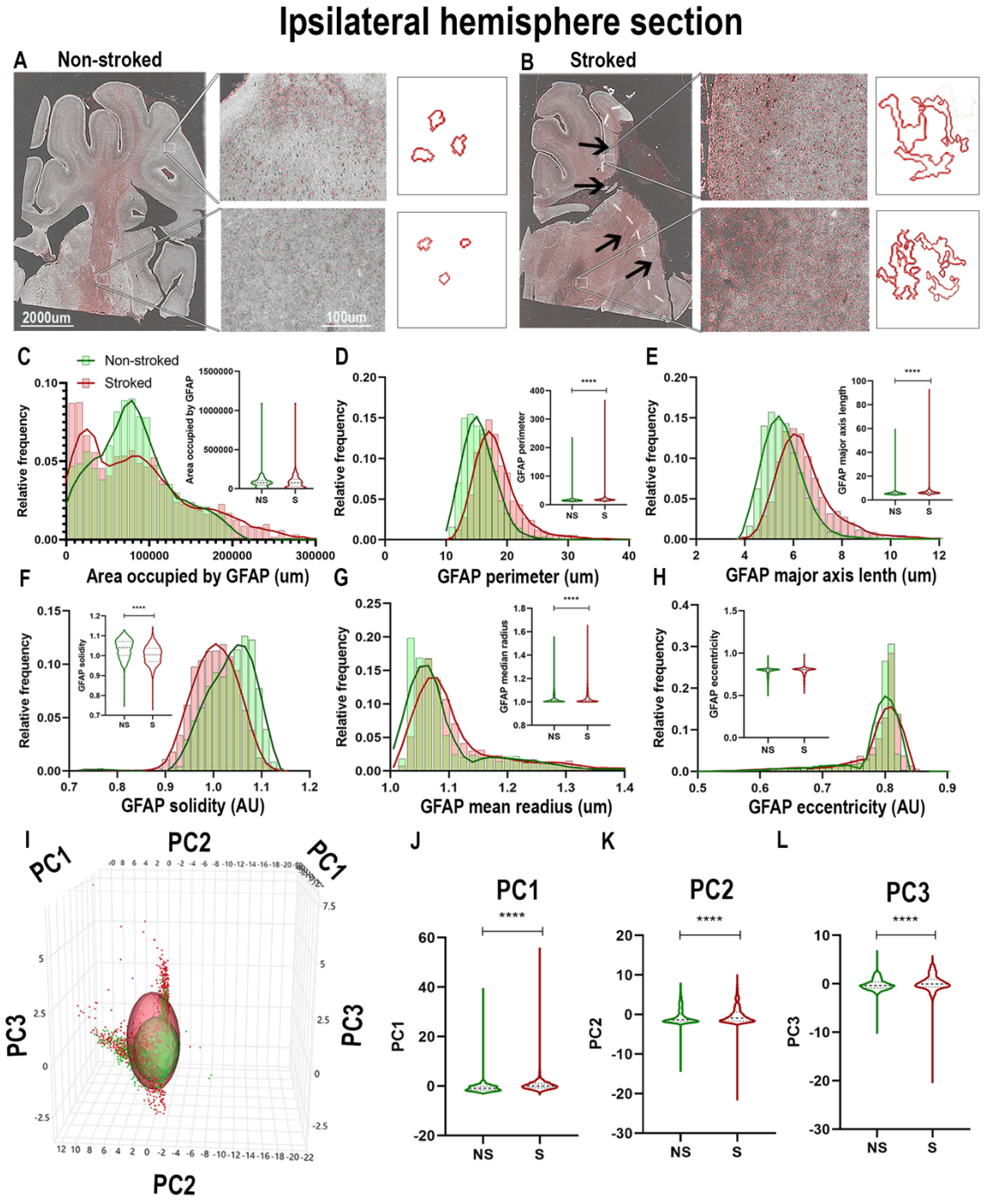

Figure 5.4. GFAP$^+$ areas transitioned to more sprawled and extended morphology after stroke in ipsilateral tissue. Visual differences in density and location of GFAP$^+$ areas were observed in ipsilateral sections, between S and NS animals (**A-B**). Arrows

indicate location of stroke lesion (**B**). Significant ($p<0.0001$) increases in perimeter (**D**), major axis length (**E**), solidity (**F**; $p=0.0003$), and mean radius (**G**) were observed in hemispheric section ROIs of S (n=1,848 ROIs) animals relative to NS (n=1,668 ROIs) animals. There was a significant ($p<0.0001$) decrease observed in $GFAP^+$ area occupied (**C**) and solidity (**F**) of $IBA1^+$ ROIs of in S animals compared to NS animals. No significant difference was seen in eccentricity (**H**). PCA (**I**) analysis revealed a significant ($p<0.0001$) difference in PC1-3 (**J-L**) in S animals compared to NS animals.

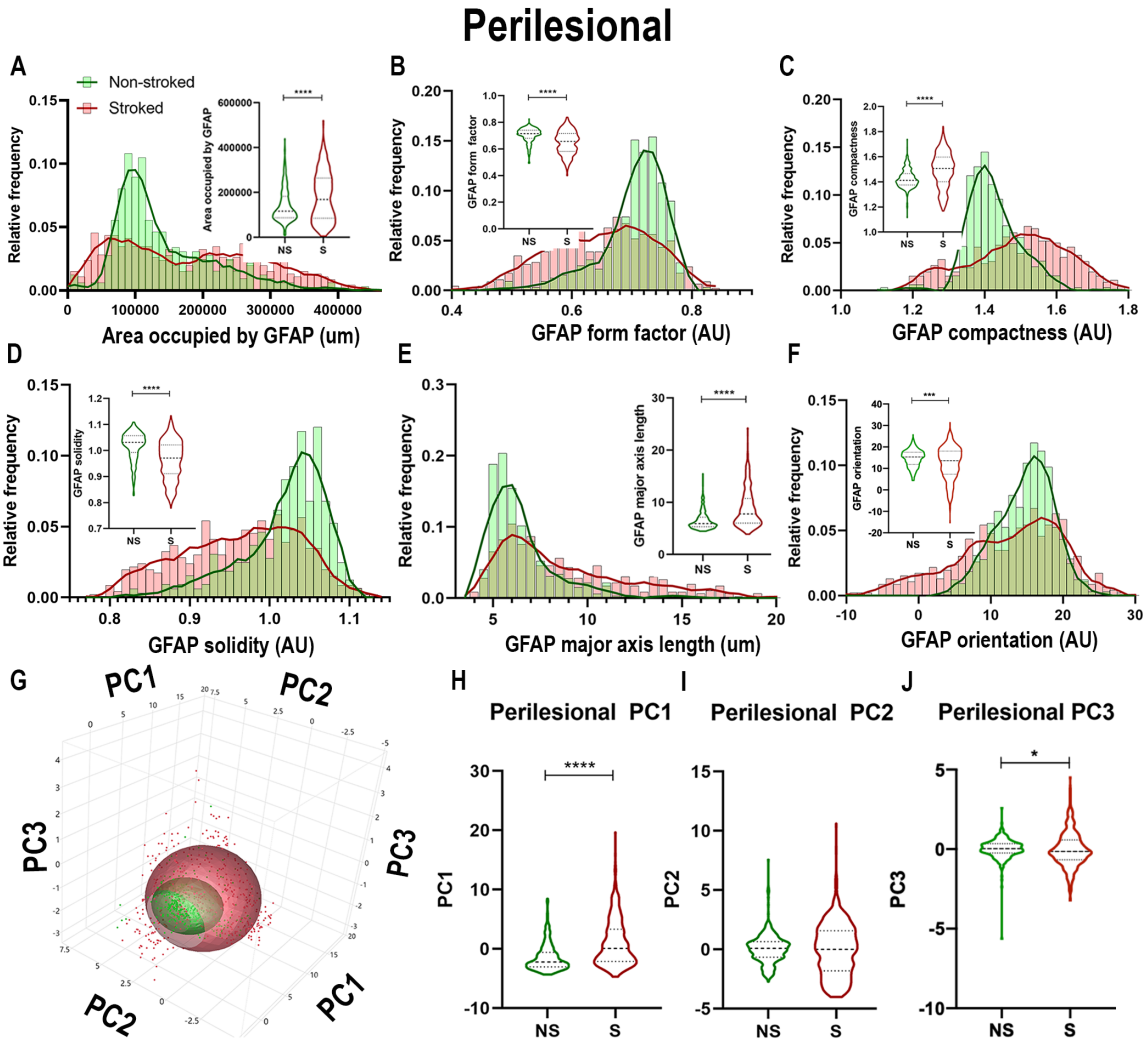

Figure 5.5. Stroke resulted in larger A1-like morphological changes of GFAP$^+$ areas in perilesional tissue. Significant ($p<0.0001$) increases in GFAP$^+$ area occupied (**A**), compactness (**C**), and major axis length (**E**) were observed in ROIs of S (n=461 ROIs) animals compared NS (n=324 ROIs) animals. There was a significant decrease in form factor (**B**; $p<0.0001$), solidity (**D**; $p<0.0001$) and orientation (**F**; $p=0.0002$) of IBA1$^+$ ROIs in the perilesional region of S animals compared to NS animals. Upon PCA (**G**) analysis,

a significant increase was observed in PC1 (**H**; $p<0.0001$) and PC3 (**J**; $p=0.0162$), but no significant difference was observed in PC2 (**I**).

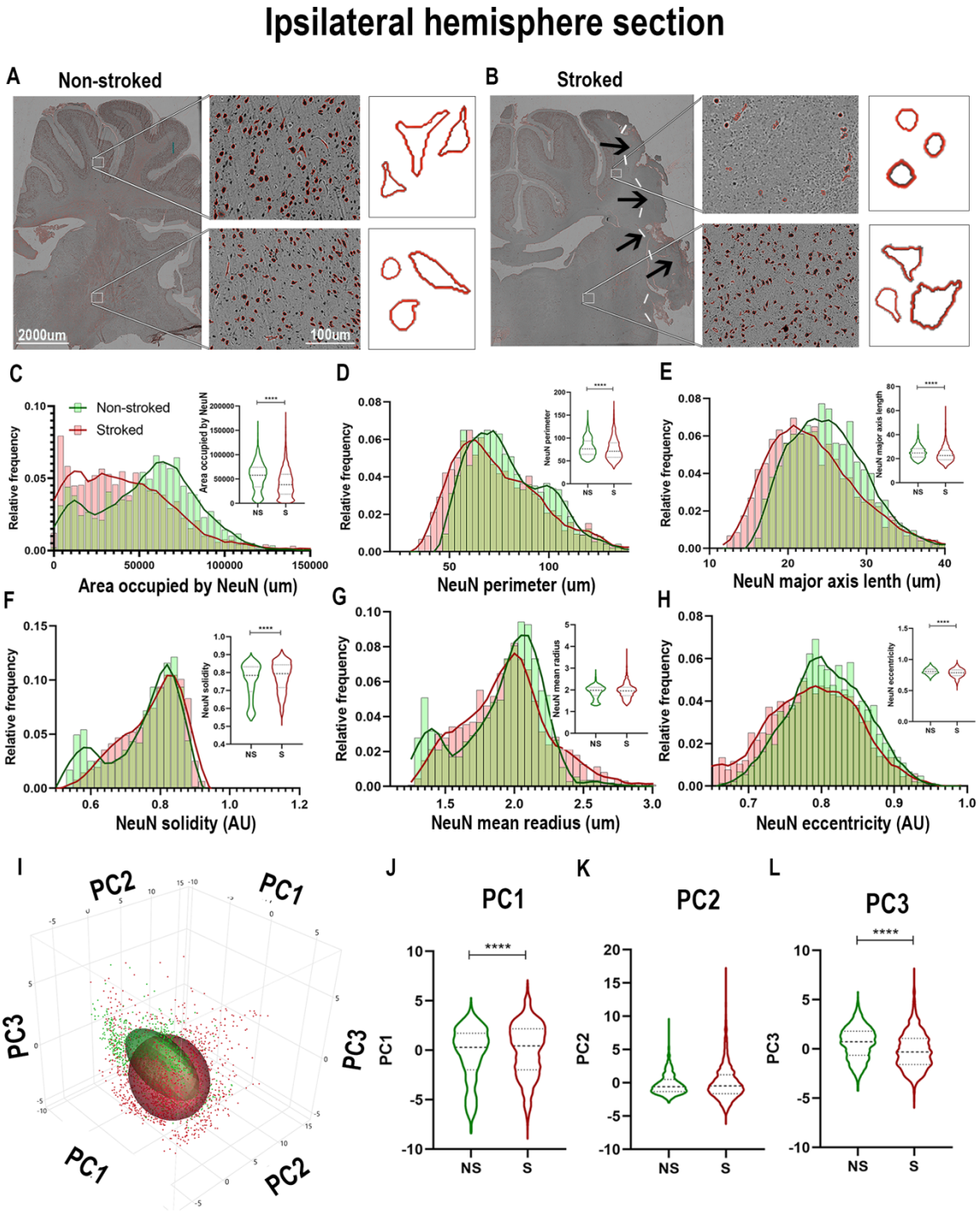

Figure 5.6. NeuN$^+$ cells transitioned to a stressed phenotype after stroke in the ipsilateral hemisphere. Visual differences in density and location of NeuN$^+$ areas in

ipsilateral hemispheric sections were observed between NS and S animals (**A-B**). Arrows indicate location of stroke lesion (**b**). Significant ($p<0.0001$) decreases in area occupied (**C**), perimeter (**D**), major axis length (**E**), and eccentricity (**H**) were observed between ROIs of S (n=2,230 ROIs) compared to NS (n=1,476 ROIs) animals. There was a significant ($p<0.0001$) increase observed in solidity (**F**) between NS and S animals. No significant difference was seen in mean radius (**G**). PCA (**I**) analysis demonstrated a significant ($p<0.0001$) increase in PC1 (**J**) and decrease in PC3 (**L**) of $NeuN^+$ cells in S animals compared to NS animals, but no significant difference was observed in PC2 (**K**).

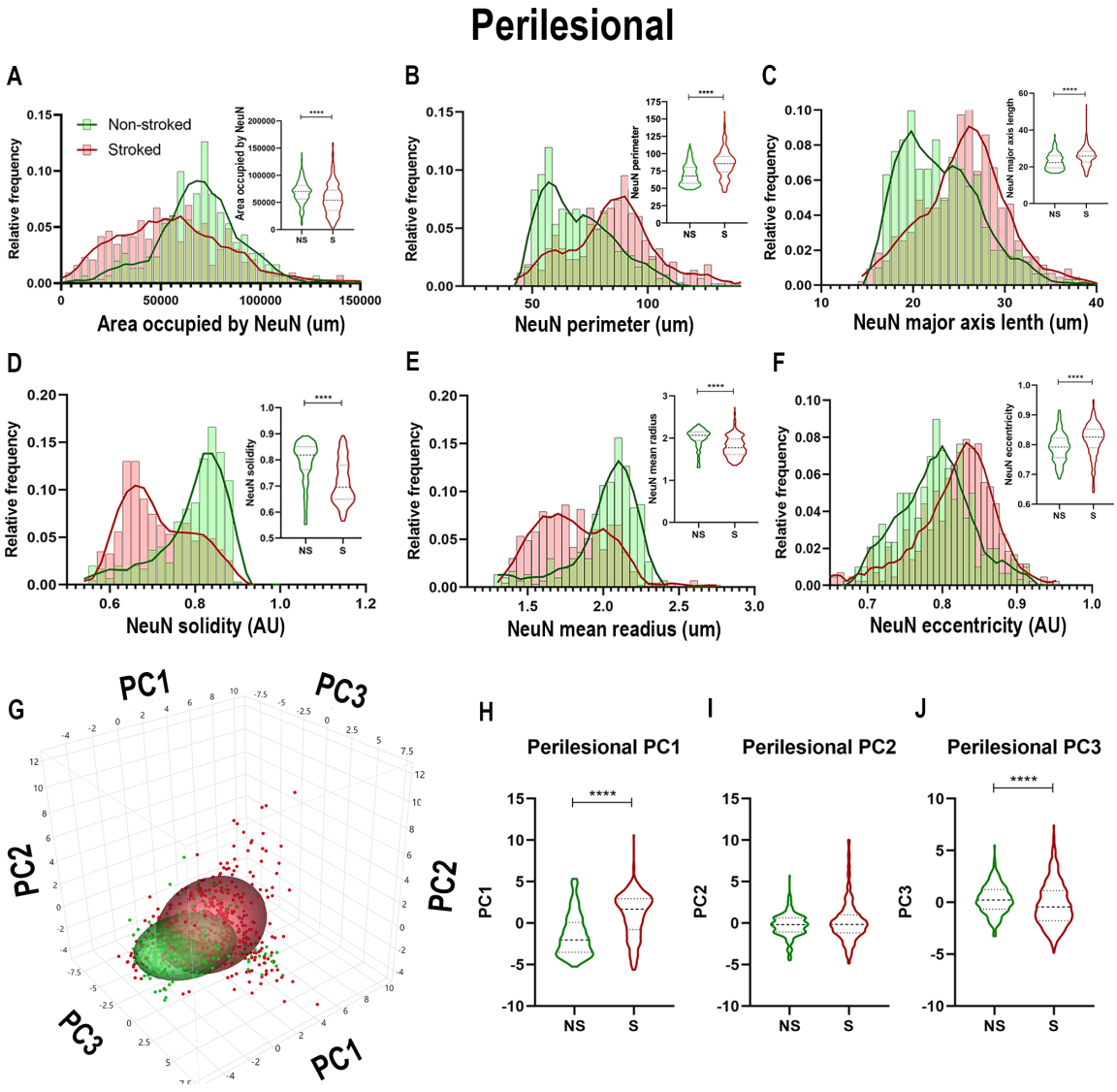

Figure 5.7. NeuN$^+$ morphological changes in perilesional tissues differed from those in the larger ipsilateral hemisphere. Significant ($p<0.0001$) decreases in NeuN$^+$ area occupied (**A**), perimeter (**B**), solidity (**D**), and mean radius (**E**) were observed in ROIs of S (n=452 ROIs) animals compared NS (n=354 ROIs) animals. Significant (**$p<0.0001$**) increases in major axis length (**C**) and eccentricity (**F**) were observed in S animals compared to NS animals. PCA (**G**) analysis showed a significant ($p<0.0001$) increase in

PC1 (**H**) and decrease in PC3 (**J**; $p<0.0001$) between S and NS animals, but no significant difference was observed in PC2 (**I**).

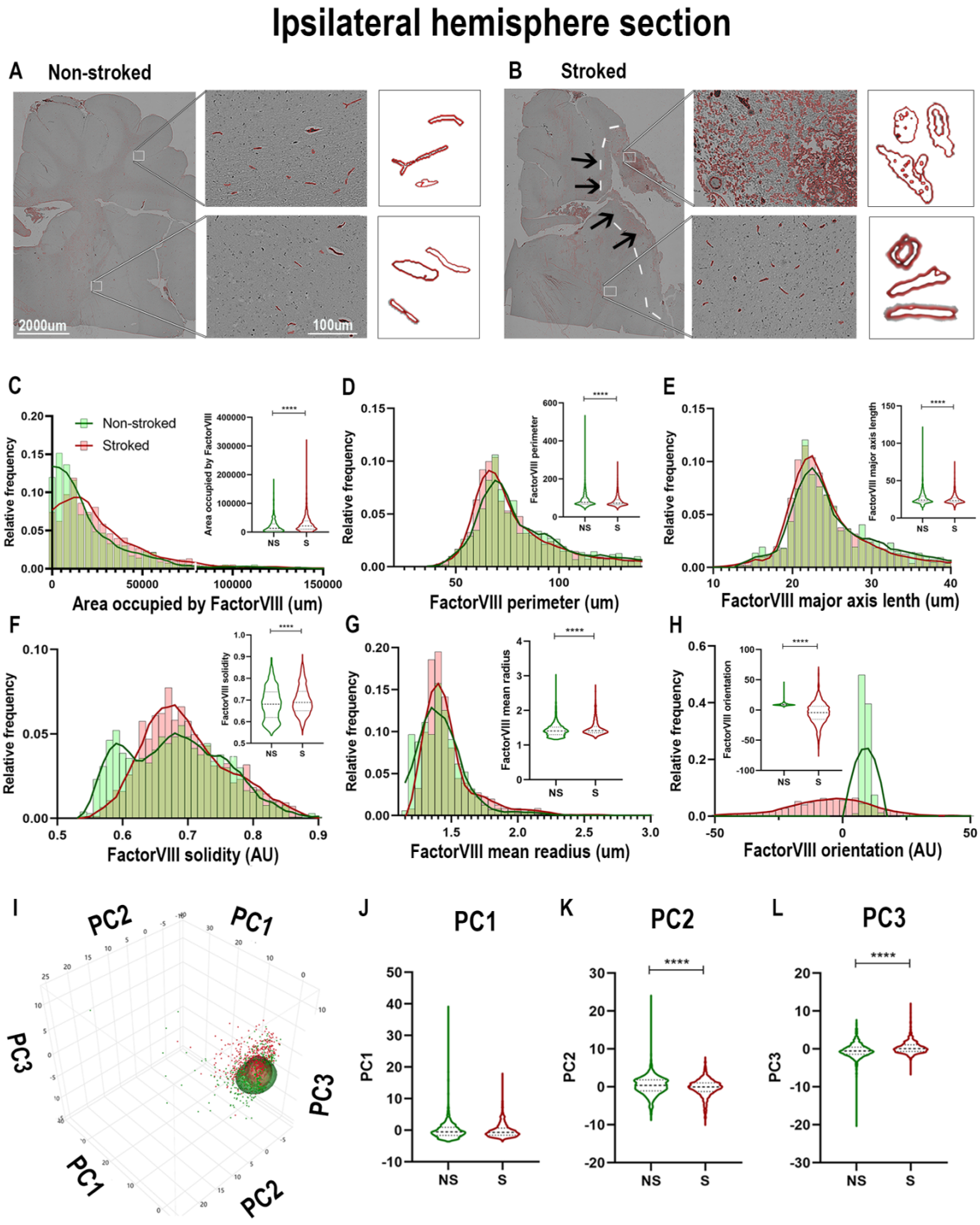

Figure 5.8. FactorVIII$^+$ areas showed altered orientations and decreased size in the ipsilateral hemisphere following stroke. Visual differences in density and location of

FactorVIII^{+} areas in ipsilateral hemispheric sections were observed between NS and S animals (**A-B**) (66) (64). Arrows indicate location of stroke lesion (**B**). Significant ($p<0.0001$) increases in area occupied (**C**), solidity (**F**), and mean radius (**G**) were observed between ROIs of S (n=1,228 ROIs) compared to NS (n=1,584 ROIs) animals. There were also significant (**$p<0.0001$)** decreases in perimeter (**D**), major axis length (**E**), and orientation (**H**) observed in between NS and S animals. PCA (**I**) analysis showed no difference in PC1 (**J**), but a significant ($p<0.0001$) decrease in PC2 (**K**) and increase in PC3 (**L**) of FactorVIII^{+} cells in S animals compared to NS animals.

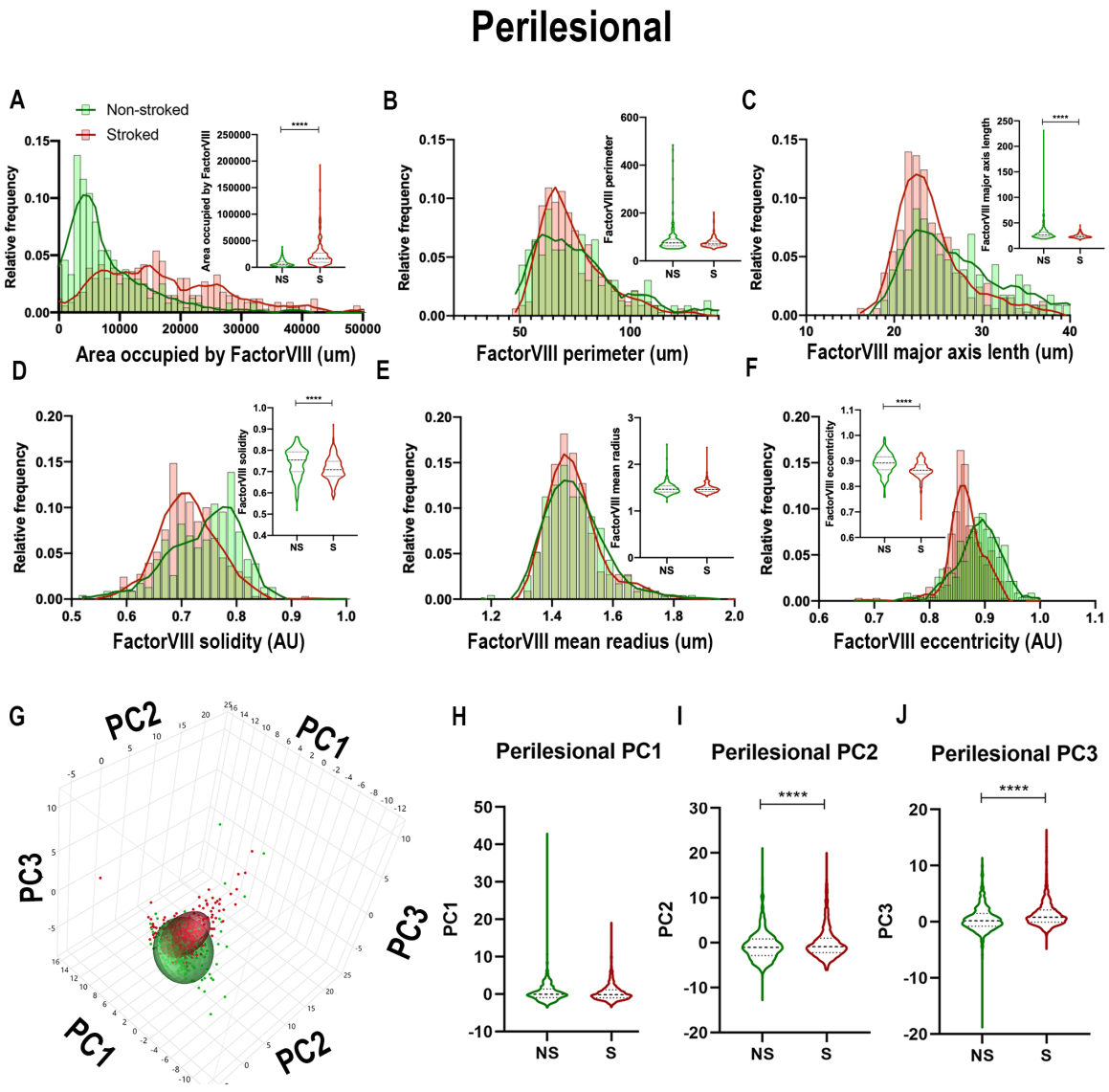

Figure 5.9. Stroke resulted in a decrease in size and solidity of FactorVIII$^+$ areas in perilesional tissue. Significant ($p<0.0001$) increase in NeuN$^+$ area occupied (**A**), and decreases in major axis length (**C**), solidity (**D**), and eccentricity (**F**) were observed in S (n=334 ROIs) animals compared to NS (n=240 ROIs) animals. No significant differences were seen in perimeter (**B**) and mean radius (**E**). PCA (**G**) analysis showed no difference

in PC1 (**H**), but a significant ($p<0.0001$) decrease in PC2 **(I)** and increase in PC3 (**J**) observed between S and NS animals.

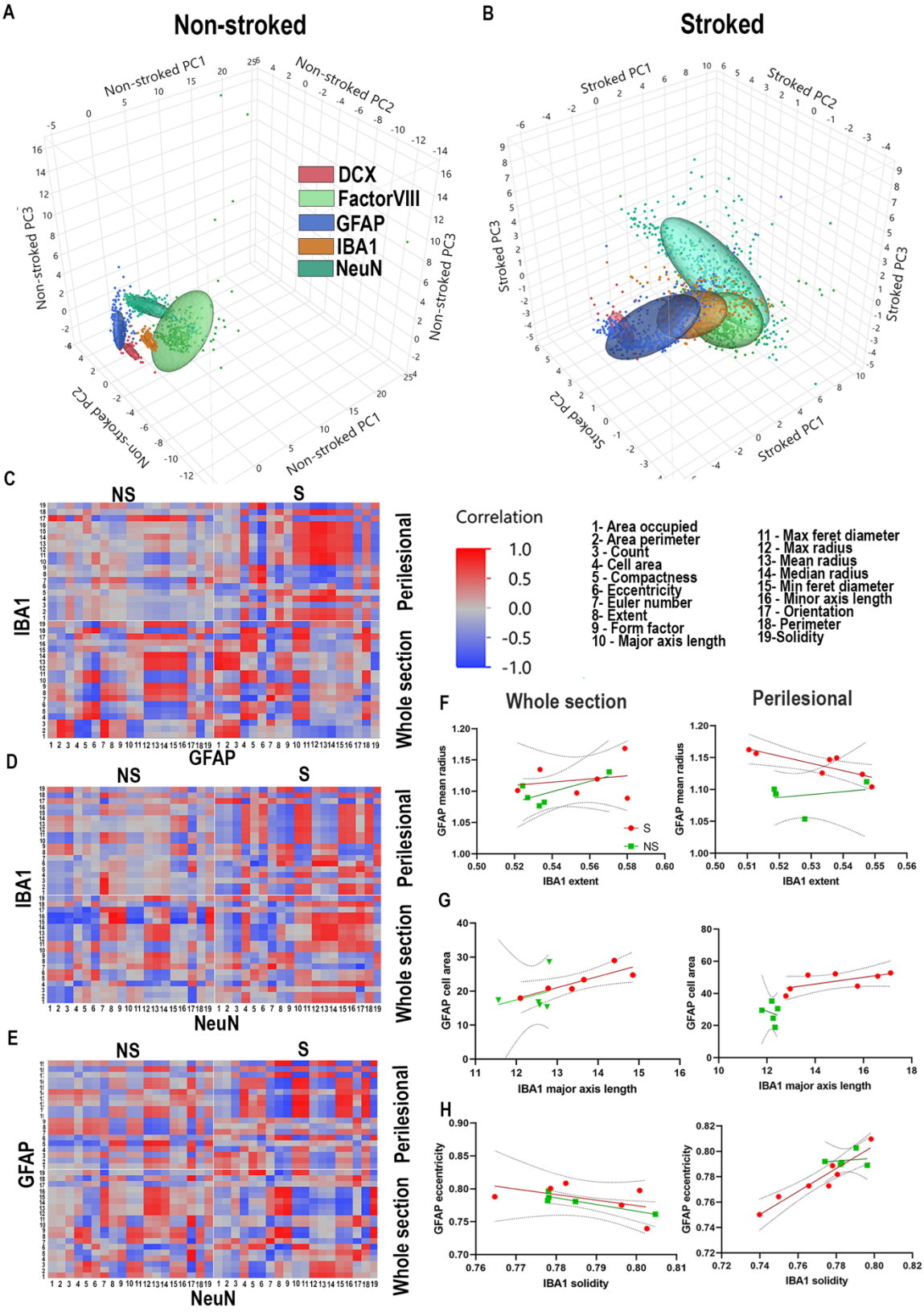
A
Non-stroked
Non-stroked PC1
Non-stroked PC2
Non-stroked PC3
DCX
FactorVIII
GFAP
IBA1
NeuN
B
Stroked
Stroked PC1
Stroked PC2
Stroked PC3
C
NS
S
IBA1
GFAP
Perilesional
Whole section
D
NeuN
E
Correlation
1.0
0.5
0.0
-0.5
-1.0
1- Area occupied
2- Area perimeter
3 - Count
4- Cell area
5 - Compactness
6- Eccentricity
7- Euler number
8- Extent
9 - Form factor
10 - Major axis length
11 - Max feret diameter
12 - Max radius
13- Mean radius
14- Median radius
15- Min feret diameter
16 - Minor axis length
17 - Orientation
18- Perimeter
19-Solidity
F
Whole section
Perilesional
GFAP mean radius
IBA1 extent
S
NS
G
GFAP cell area
IBA1 major axis length
H
GFAP eccentricity
IBA1 solidity

Figure 5.10. Stroke alters relationship of morphological parameters across cell types. PCA of NS and S ROIs labeled by DCX (red), FactorVIII (light green), GFAP (dark blue), IBA1 (tan), and NeuN (dark green). PCA ellipses for each stain are well delineated in NS animals (**A**), but not in S animals (**B**). Heatmaps of each parameter measured 1-19 were generated for GFAP vs. IBA1 (**C**), IBA1 vs. NeuN (**D**), and NeuN vs. GFAP (**E**) for each treatment group (S and NS) as well as each ROI location (perilesional or hemispheric section). NS animals generally showed an increase in strength of correlations, positively or negatively, when comparing heatmaps of perilesional areas and hemispheric section areas. In S animals, there often was a complete reversal of correlation directionality between perilesional and hemispheric sections (**C-E**). Linear correlations, representative of one square of the heatmap showed significant correlations of perilesional IBA1 extent and GFAP mean radius in S ($p=0.0220$) but not NS animals ($p=0.6779$) (**F**); in hemispheric section IBA1 major axis length and GFAP cell area in S animals ($p=0.0289$), but not NS animals ($p=0.6402$); in hemispheric section ROIs of GFAP eccentricity and IBA1 solidity in NS animals ($p=0.0311$), but not S animals ($p=0.3103$) (**G**); and in perilesional GFAP eccentricity and IBA1 solidity in S animals ($p=0.0011$), but not NS animals ($p=0.7858$) (**H**).

Supplementary Material

Supplementary Table 5.1. Definitions of all parameters measured. The 19 parameters measured for each cell are defined in the table. Equations for parameter calculations are also included where applicable.

	Parameter	Definition	Equation
1	Area occupied	The number of positive pixels in a defined ROI	
2	Area shape area	The number of positive pixels in an object	
3	Compactness	The mean squared distance of the object's pixels from the centroid divided by the area	$\frac{\mu^2\ distance\ of\ objects\ pixels\ from\ centroid}{area}$ A perfect circle will have a compactness = 1 Irregular or objects with holes having values >1
4	Count	The number of positive objects in a specific ROI	
5	Eccentricity	The ratio of the distance between the foci of the ellipse and it's major axis length	$\frac{distance\ between\ the\ foci\ of\ the\ ellipse}{major\ axis\ length}$ A perfect circle = 0, whereas a line =1
6	Euler number	The number of objects in the region subtracted from the number of holes in those objects	
7	Extent	The proportion of positive pixels in the bounding box that are also in the region	$\frac{area}{volume\ of\ the\ bounding\ box}$
8	Form factor	Measure of circularity of object. Equal 1 for perfectly circular object	$\frac{4\pi Area}{Perimeter^2}$
9	Major axis length	The length of the major axis of the positive ellipses that has the same normalized second central moments as the region	
10	Maximum radius	The maximum distance of any pixel in the object to the closest pixel outside of the object	
11	Maximum ferret diameter	The largest distance between 2 parallel lines tangent on either side of the object	

12	Mean radius	The mean distance of any pixel in the object to the closest pixel outside of the object	
13	Median radius	The median distance of any pixel in the object to the closest pixel outside of the object	
14	Min ferret diameter	The smallest distance between 2 parallel lines tangent on either side of the object	
15	Minor axis length	The length in pixels of the minor axis of the ellipse that has the same normalized second central movements as the region	
16	Orientation	The angle between the x-axis and the major axis of the ellipse that has the same second-moments as the region between -90 and +90	
17	Perimeter	The additive number of pixels around the boundary of positive areas total for each ROI	
18	Perimeter shape area	The number of pixels around the boundary of each positive area	
19	Solidity	The proportion of positive pixels in the convex hull which are also in the object	$\frac{ObjectArea}{ConvexHullArea}$

Supplementary Table 5.2. Morphological parameters for each stain by location. All parameter means for NS and S groups, and p-values not included in figures are included in the table here. P-values < 0.0001 are bold and italicized and values <0.05 are bolded.

Parameter	Location	IBA1			GFAP			NeuN			FactorVIII			DCX		
		NS median	S median	p-value	NS median	S median	p-value	NS median	S median	p-value	NS median	S median	p-value	NS median	S mean	p-value
Count	Hemisphere section	1704	1826	***0.0017***	6891	4996	0.1638	381.0	262.0	***<0.001***	100.0	171.5	***<0.001***	86.00	114.0	***<0.001***
	Perilesional	1597	2010	***<0.001***	6370	5031	***<0.001***	466.0	343.0	***<0.001***	46.00	145.5	***<0.001***	135.00	172.0	***0.0044***
Compactness	Hemisphere section	1.848	1.749	***<0.001***	1.376	1.443	***<0.001***	1.964	1.818	***<0.001***	2.920	2.654	***<0.001***	1.350	1.351	0.7441
	Perilesional	1.833	1.747	***<0.001***	1.412	1.507	***<0.001***	1.700	2.164	***<0.001***	3.061	2.564	***<0.001***	1.301	1.344	**0.0218**
Perimeter of area occupied (pixels)	Hemisphere section	49,421	60,676	***<0.001***	57,863	54,608	***<0.001***	24,219	15,708	***<0.001***	7,383	11,332	***<0.001***	1,269	1,596	***<0.001***
	Perilesional	45,904	76,312	***<0.001***	75,272	103,089	***<0.001***	26,861	23,605	***<0.001***	3,200	9,213	***<0.001***	2,123	2,311	**0.0399**
Area of positive shape areas (pixels)	Hemisphere section	42.91	52.81	***<0.001***	13.68	17.27	***0.0011***	157.5	151.1	**<0.0001**	111.1	111.0	0.0741	20.731	19.73	***0.0025***
	Perilesional	42.39	64.85	***<0.001***	18.42	27.22	***<0.001***	151.72	151.1	0.1678	117.6	111.8	0.2436	21.19	17.661	***<0.001***
Euler number	Hemisphere section	0.9571	0.9228	***<0.001***	0.9845	0.9762	0.5282	1.000	1.000	0.7072	0.6042	0.6579	***0.0026***	0.9873	0.9930	***<0.001***
	Perilesional	0.9638	0.8427	***<0.001***	0.9503	0.9181	***<0.001***	1.000	1.000	0.71887	0.7388	0.7222	0.2290	0.9885	0.9950	***<0.001***
Extent	Hemisphere section	0.51719	0.5333	***<0.001***	0.6661	0.6509	***<0.001***	0.5355	0.55511	***<0.001***	0.4112	0.4291	***<0.001***	0.6616	0.6656	**0.0124**
	Perilesional	0.5265	0.5313	**0.0181**	0.6460	0.6259	***<0.001***	0.5640	0.4572	**<0.0001**	0.4223	0.4519	***<0.001***	0.6783	0.6767	0.4927
Form Factor	Hemisphere section	0.4734	0.4893	**<0.0001**	0.7454	0.7107	***<0.001***	0.4820	0.4779	**0.00005**	0.2837	0.3060	***<0.001***	0.6943	0.7006	**0.0007**
	Perilesional	0.4821	0.4793	***0.0034***	0.7413	0.6570	***<0.001***	0.5582	0.3342	**<0.0001**	0.4282	0.4449	***<0.001***	0.7522	0.7155	0.7522
Max ferret diameter (pixels)	Hemisphere section	10.90	11.72	***<0.001***	4.395	5.149	***<0.001***	23.91	21.814	***<0.001***	22.00	21.33	***0.0002***	6.068	5.951	**0.011**
	Perilesional	10.77	13.09	***<0.001***	4.814	6.714	***<0.001***	21.82	24.53	***<0.001***	24.333	21.41	***<0.001***	5.975	5.541	***<0.001***

Maximum Radius (pixels)	Hemisphere section	2.251	2.510	***<0.001***	1.364	1.4589	***<0.001***	4.571	4.469	0.8092	2.853	2.893	***<0.001***	1.861	1.810	***0.0002***
	Perilesional	2.249	2.568	***<0.001***	1.411	1.600	***<0.001***	4.782	4.085	***<0.001***	2.952	2.983	0.2068	1.890	1.724	***<0.001***
Median radius (pixels)	Hemisphere section	1.033	1.081	***<0.001***	1.010	1.013	***<0.001***	1.758	1.735	0.5548	1.159	1.228	***<0.001***	1.040	1.033	0.2247
	Perilesional	1.033	1.092	***<0.001***	1.015	1.020	***=0.001***	1.843	1.518	***<0.001***	1.215	1.201	**0.0311**	1.049	1.024	**0.0005**
Min ferret diameter (pixels)	Hemisphere section	5.259	5.922	***<0.001***	1.987	2.361	***<0.001***	10.93	10.64	**<0.001**	8.586	8.736	0.2778	2.992	2.869	***0.0002***
	Perilesional	5.198	6.655	***<0.001***	2.262	3.151	***<0.001***	10.81	11.25	***<0.001***	7.607	8.613	***<0.001***	3.059	2.664	***<0.001***
Minor axis length (pixels)	Hemisphere section	5.703	6.382	***<0.001***	2.612	2.974	***<0.001***	11.01	11.74	***<0.001***	8.728	8.853	0.3636	3.756	3.618	***<0.001***
	Perilesional	5.623	7.020	***<0.001***	2.869	3.680	***<0.001***	10.81	11.25	***<0.001***	7.750	8.812	***<0.001***	3.809	3.431	***<0.001***
Orientation	Hemisphere section	-2.274	-1.1443	***0.0006***	16.29	13.45	***<0.001***	-6.822	-2.410	***<0.001***	8.728	-4.177	***<0.001***	0.1663	0.3648	0.6869
	Perilesional	-2.216	-0.3821	***<0.001***	15.32	13.55	***0.0002***	-9.170	1.289	***<0.001***	-5.192	3.260	***<0.001***	0.5714	3.543	***0.0015***
Total significant	Hemisphere section Perilesional			*12 out of 12 12 out of 12*			*10 out of 12 12 out of 12*			*9 out of 12 10 out of 12*			*9 out of 12 9 out of 12*			*10 out of 12 10 out of 12*

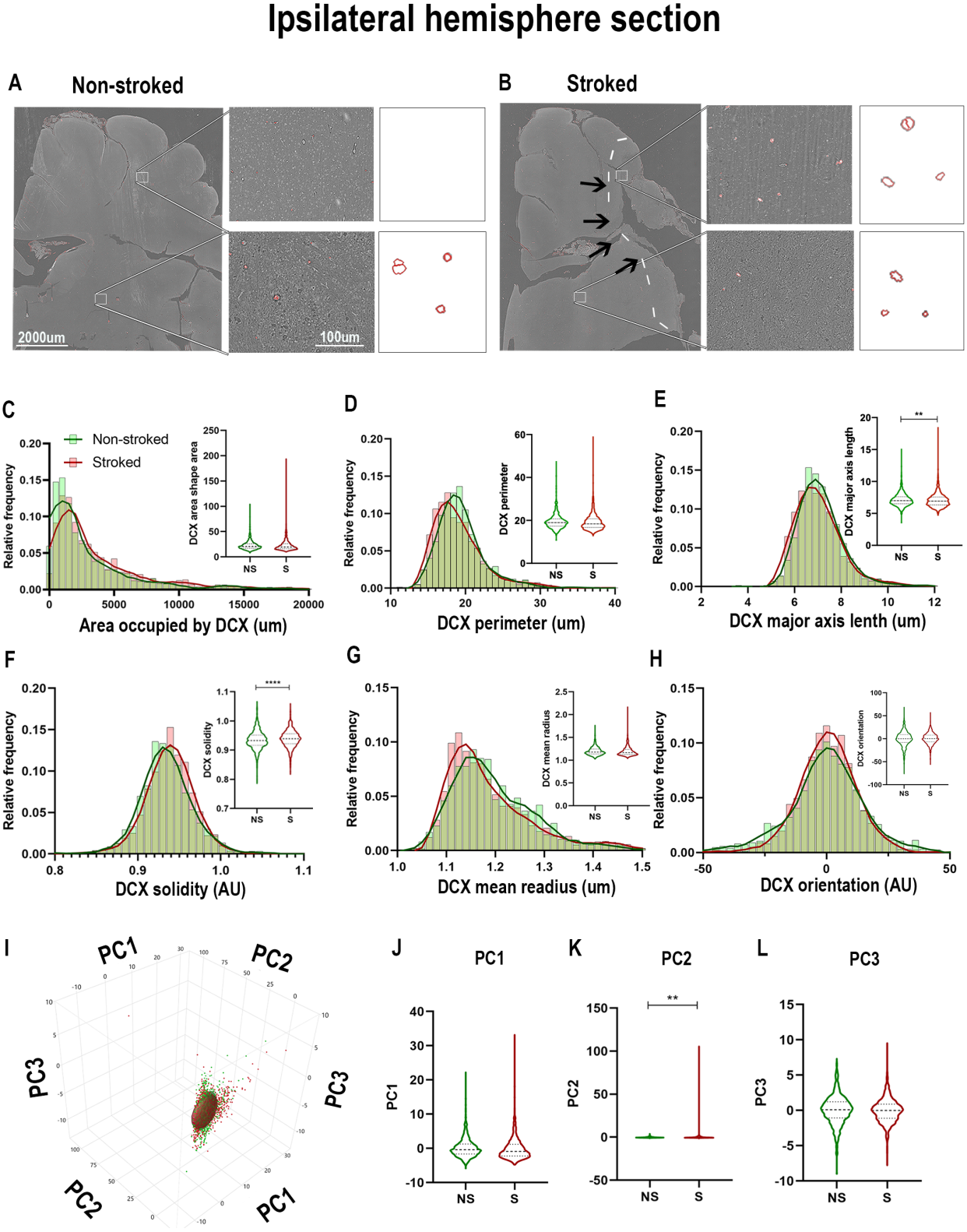
Ipsilateral hemisphere section
A
Non-stroked
B
Stroked
2000um
100um
C
Non-stroked
Stroked
Relative frequency
Area occupied by DCX (um)
DCX area shape area
NS
S
D
DCX perimeter (um)
DCX perimeter
E
DCX major axis lenth (um)
DCX major axis length
**
F
DCX solidity (AU)
DCX solidity
****
G
DCX mean readius (um)
DCX mean radius
H
DCX orientation (AU)
DCX orientation
I
PC1
PC2
PC3
J
PC1
K
PC2
L
PC3

Supplementary Figure 5.1. Stroke resulted in an increase in DCX^+ areas with smaller perimeter in the ipsilateral hemisphere. Visual differences in density and location of DCX^+ areas in ipsilateral hemispheric sections were observed between NS and S animals (**A-B**). Arrows indicate location of stroke lesion (**B**). Significant ($p<0.0001$) increases in area occupied (**C**) and solidity (**F**) were observed between S (n=1,241 ROIs) and NS (n=2,004 ROIs) animals. There was a significant ($p<0.0001$) decrease in perimeter (**D**), major axis length ($p=0.0029$), and (**E**), mean radius ($p=0.3061$) (**G**) observed between S and NS animals. There was no significant difference in orientation ($p=0.3016$) (**H**). PCA **(I)** analysis revealed a significant increase in PC1 (**J**) and PC2 **(K;** $p=0.0025$) in DCX^+ cells in S animals compared to NS animals.

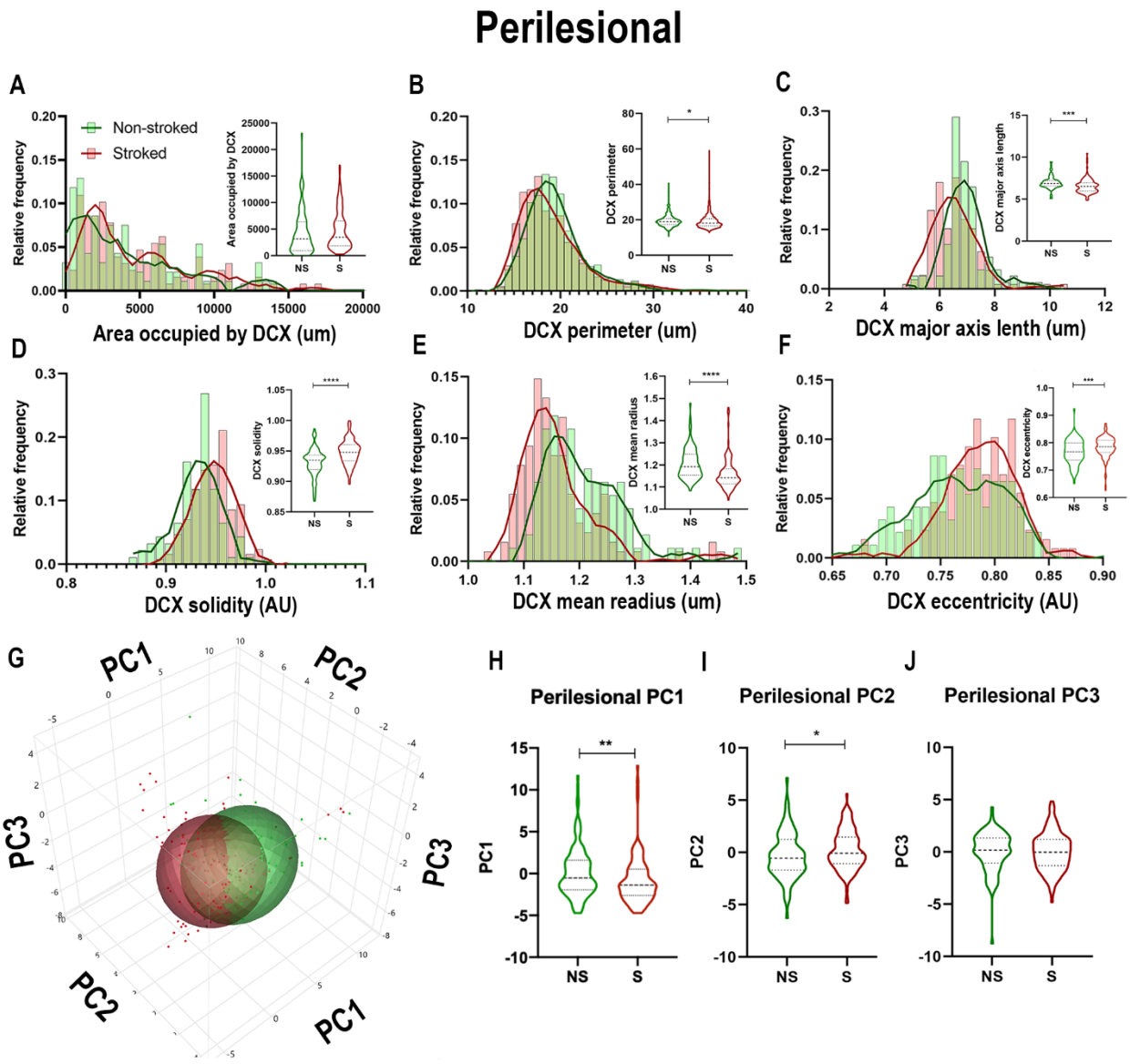

Supplementary Figure 5.2. Stroke resulted in decreased size of DCX$^+$ areas in perilesional tissue. Significant ($p<0.0001$) decreases in perimeter (**B**), major axis length (**C**), and mean radius (**E**) and significant increases in solidity (**D**; $p<0.0001$) and eccentricity (**F**; $p=0.0008$) were observed in S (n=128 ROIs) animals compared NS (n=93 ROIs) animals. There was no significant difference in DCX$^+$ area occupied (**A**). PCA (**G**)

analysis showed a significant decrease in PC1 (**H**; $p<0.0001$), increase in PC2 (**I**; $p=0.0246$), and no difference in PC3 (**J**) between S and NS animals.

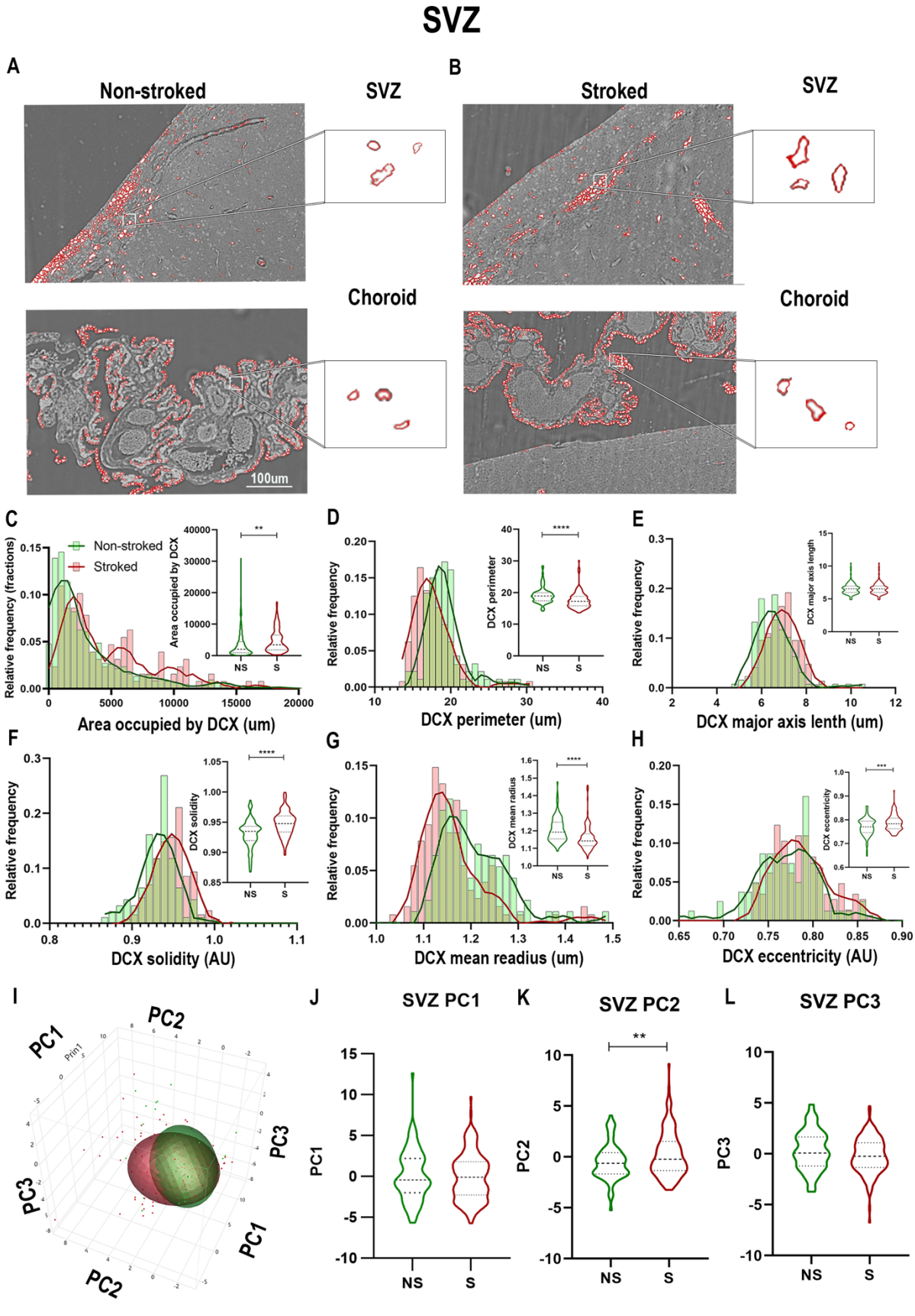
SVZ
A
Non-stroked
SVZ
Choroid
100um
B
Stroked
SVZ
Choroid
C
Non-stroked
Stroked
Relative frequency (fractions)
Area occupied by DCX (um)
Area occupied by DCX
NS
S
D
Relative frequency
DCX perimeter (um)
DCX perimeter
E
Relative frequency
DCX major axis lenth (um)
DCX major axis length
F
Relative frequency
DCX solidity (AU)
DCX solidity
G
Relative frequency
DCX mean readius (um)
DCX mean radius
H
Relative frequency
DCX eccentricity (AU)
DCX eccentricity
I
PC1
PC2
PC3
J
SVZ PC1
K
SVZ PC2
L
SVZ PC3

Supplementary Figure 5.3. Stroke results in an increase of DCX^+ areas in the SVZ. Visual differences in morphology of DCX^+ areas in the SVZ and the choroid plexus were observed between NS (n=128 ROIs) and S (n=93 ROIs) animals (**A-B**). Significant ($p<0.0001$) increases in DCX^+ area occupied (**C**), major axis length (**E**), solidity (**F**), and eccentricity (**H**) were observed in S animals compared NS. There was also a significant ($p<0.0001$) decrease in perimeter (**D**) and mean radius (**G**) in S animals compared to NS animals. PCA (**I**) analysis showed no difference in PC1 (**J**) or PC3 (**L**), but a significant ($p<0.0001$) increase in PC2 (**K**) between S and NS animals.

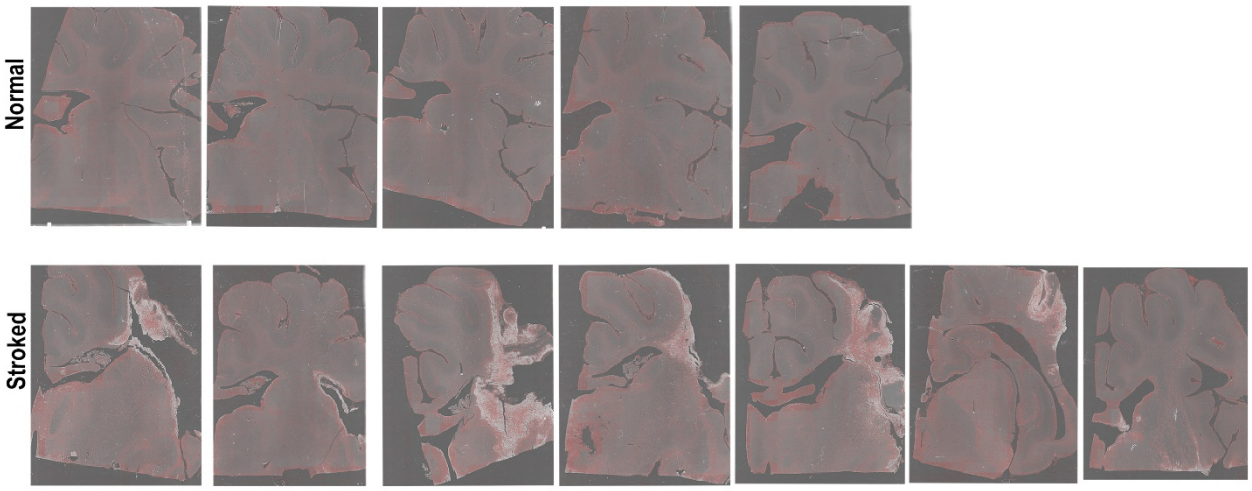

Supplementary Figure 5.4. Processed and stitched IBA1$^+$ sections of normal and stroked animals. IBA1$^+$ areas in each ROI (red) reveal concentrations of microglia/macrophages in ipsilateral sections of normal animals (top row), and after pMCAO stroke (bottom row).

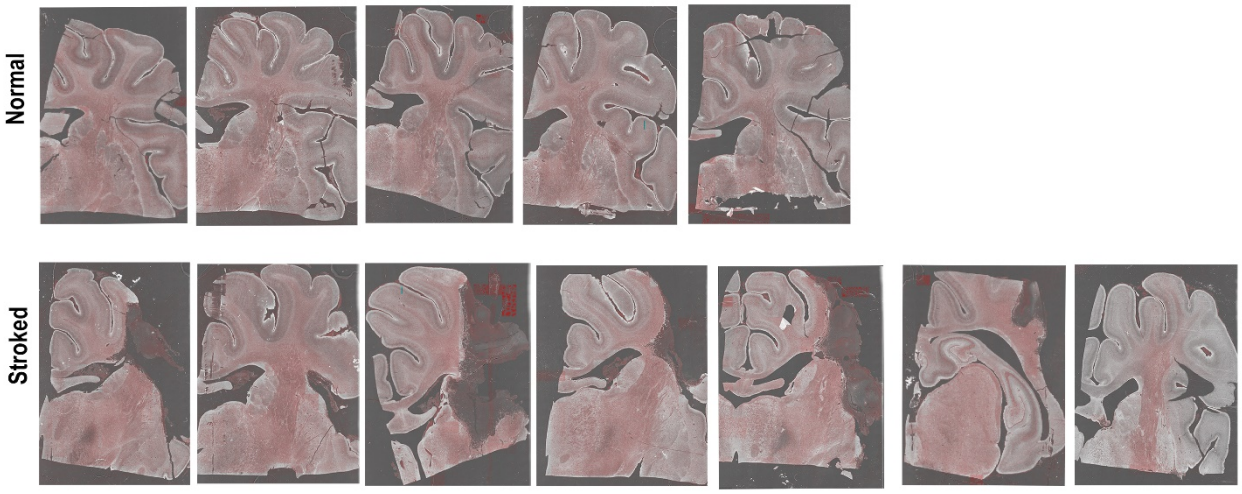

Supplementary Figure 5.5. Processed and stitched GFAP$^+$ sections of normal and stroked animals. GFAP$^+$ areas in each ROI (red) reveal concentrations of astrocytes in ipsilateral sections of normal animals (top row), and after pMCAO stroke (bottom row).

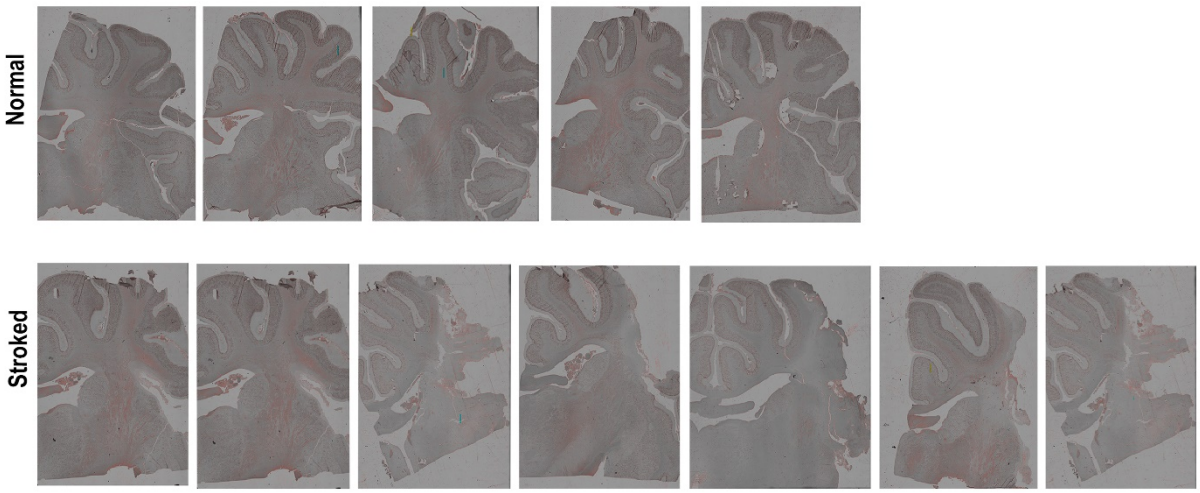

Supplementary Figure 5.6. Processed and stitched NeuN$^+$ sections of normal and stroked animals. NeuN$^+$ areas in each ROI (red) reveal concentrations of neuronal nuclei in ipsilateral sections of normal animals (top row), and after pMCAO stroke (bottom row).

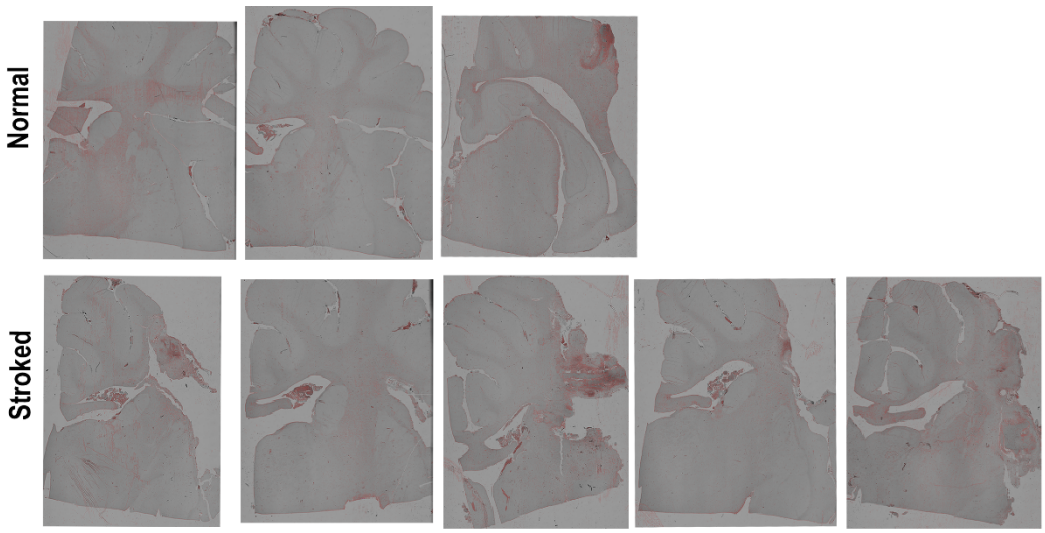

Supplementary Figure 5.7. Processed and stitched FactorVIII^{+} sections of normal and stroked animals. FactorVIII^{+} areas in each ROI (red) reveal concentrations of vasculature in ipsilateral sections of normal animals (top row), and after pMCAO stroke (bottom row).

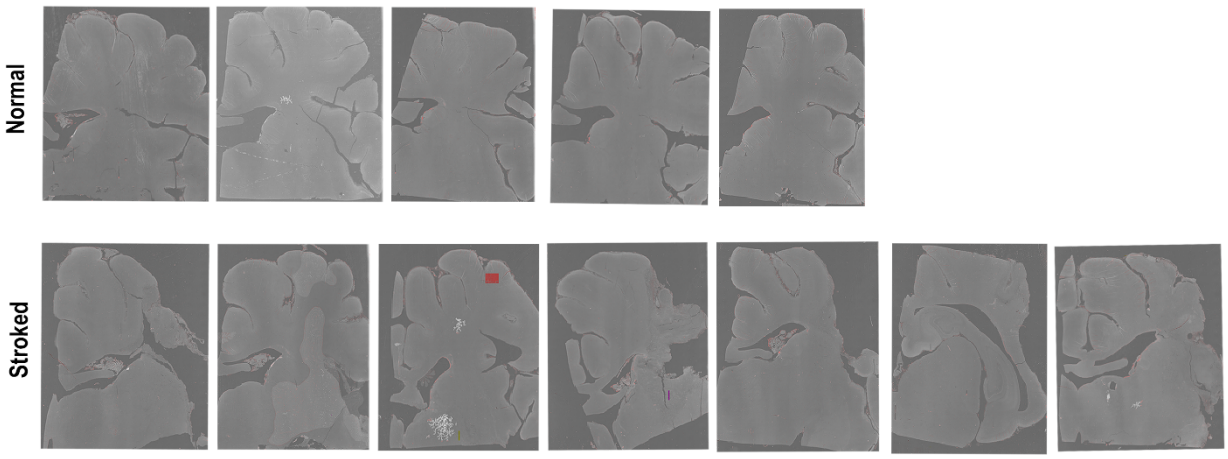

Supplementary Figure 5.8. Processed and stitched DCX$^+$ sections of normal and stroked animals. DCX$^+$ areas in each ROI (red) reveal concentrations of neural progenitors in ipsilateral sections of normal animals (top row), and after pMCAO stroke (bottom row).

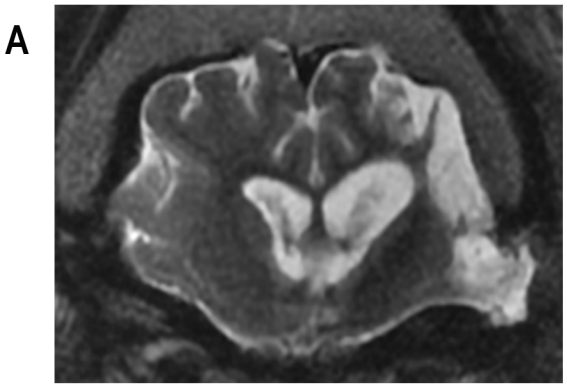
A

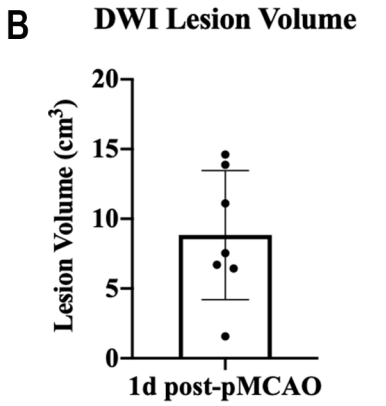
B
DWI Lesion Volume
Lesion Volume (cm3)
20
15
10
5
0
1d post-pMCAO

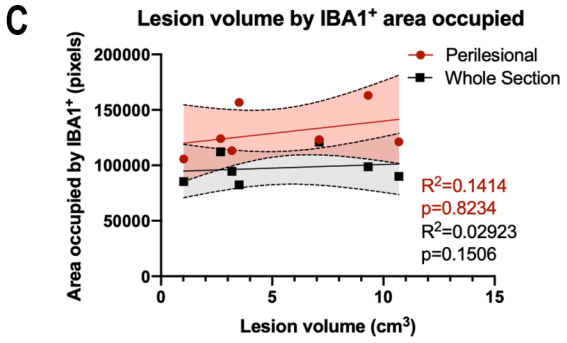
C
Lesion volume by IBA1+ area occupied
Area occupied by IBA1+ (pixels)
200000
150000
100000
50000
0
0
5
10
15
Lesion volume (cm3)
Perilesional
Whole Section
R2=0.1414
p=0.8234
R2=0.02923
p=0.1506

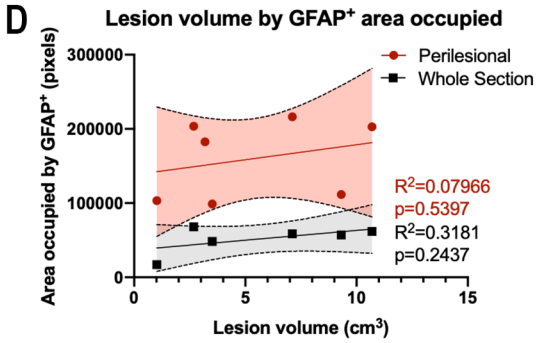
D
Lesion volume by GFAP+ area occupied
Area occupied by GFAP+ (pixels)
300000
200000
100000
0
0
5
10
15
Lesion volume (cm3)
Perilesional
Whole Section
R2=0.07966
p=0.5397
R2=0.3181
p=0.2437

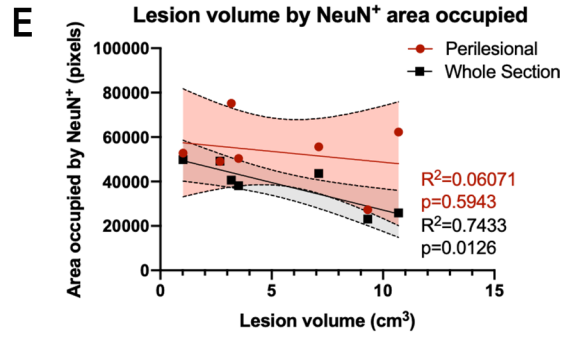
E
Lesion volume by NeuN+ area occupied
Area occupied by NeuN+ (pixels)
100000
80000
60000
40000
20000
0
0
5
10
15
Lesion volume (cm3)
Perilesional
Whole Section
R2=0.06071
p=0.5943
R2=0.7433
p=0.0126

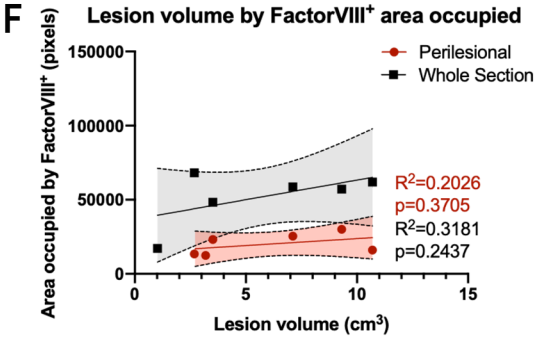
F
Lesion volume by FactorVIII+ area occupied
Area occupied by FactorVIII+ (pixels)
150000
100000
50000
0
0
5
10
15
Lesion volume (cm3)
Perilesional
Whole Section
R2=0.2026
p=0.3705
R2=0.3181
p=0.2437

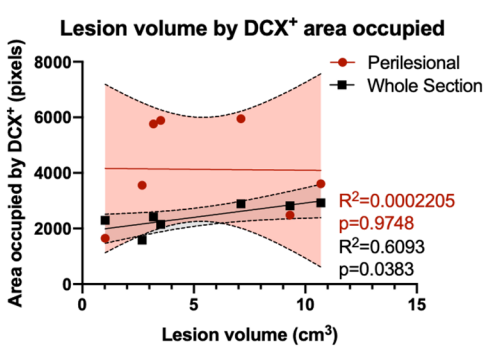
G
Lesion volume by DCX+ area occupied
Area occupied by DCX+ (pixels)
8000
6000
4000
2000
0
0
5
10
15
Lesion volume (cm3)
Perilesional
Whole Section
R2=0.0002205
p=0.9748
R2=0.6093
p=0.0383

Supplementary Figure 5.9. Correlations of lesion volume to positive areas of IBA1, GFAP, NeuN, FactorVIII, and DCX. T2W MRI image depicting lesion volume at 1d post-pMCAO by the hyperintense region in the ipsilateral hemisphere (**A**). DWI corrected lesion volume was measured for all stroked animals and had a mean lesion volume of 5.36 cm^3 with SD of 3.68 cm^3 (**B**). Linear correlations of lesion volume and stained area were evlauated for IBA1 (**C**), GFAP (**D**), NeuN (**E**), FactorVIII (**F**), and DCX (**G**). A significant negative correlation between lesion volume and $NeuN^+$ areas ($p=0.0126$) was observed in whole slice analysis (**E**). Comparatively, a significant positive correlation between lesion volume and DCX^+ areas ($p=0.0383$) was observed in whole slice analysis (**G**).

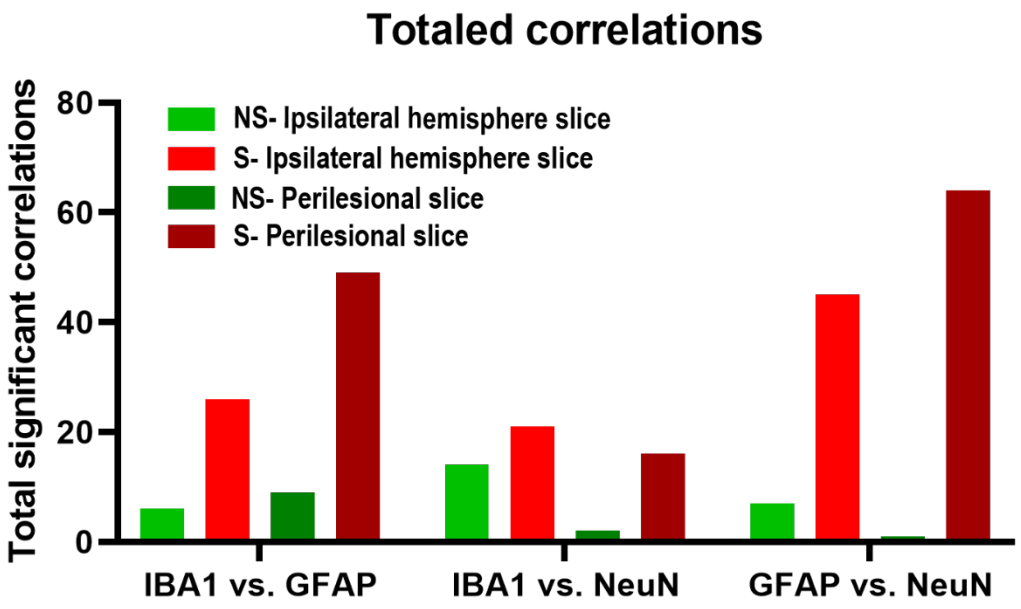

Supplementary Figure 5.10. Quantified significant correlations between stains and treatment groups. Number of significant correlations for IBA1$^+$, GFAP$^+$, and NeuN$^+$ areas were quantified for each treatment group (NS= green, S= red), and locations (Ipsilateral section = lighter shade, Perilesional area = darker shade). Greatest number of correlations were observed between IBA1$^+$ vs. GFAP$^+$ and GFAP$^+$ vs. NeuN$^+$ in S perilesional areas than any other group. Greatest number of correlations between IBA1$^+$ vs. NeuN$^+$ was observed in the ipsilateral hemisphere section of S animals.

CHAPTER 6

CONCLUSION

The use of advanced magnetic resonance imaging (MRI) and histological high-content imaging (HCI) neuroimaging tools in a translational preclinical model have provided important information on 1) lesion topology as it relates to functional deficits, 2) functional connectivity with high spatial resolution following traumatic brain injury (TBI), as well as 3) cellular interactions following ischemic stroke. An ischemic stroke can leave its victims with lifelong injuries. The location of the stroke is largely responsible for the patients' stroke severity and recovery outcomes [1-8]. Following an ischemic stroke, brain injury is initiated by oxygen and energy depletion that triggers inflammatory responses including immune and neural cell disruptions that result in a profound lesion [9, 10]. The lesion can occupy many brain structures vital for necessary everyday actions and movement. Furthermore, the cell-to-cell interactions following an ischemic event also dictate the vitality of the brain tissue. For these reasons and the fact that brain composition and structure in rodent models does not closely resemble the human brain, it is valuable to study the ischemic lesion progression in a brain that closely models the human brain, such as the porcine model. TBI is responsible for a considerable amount of permanent injuries and deaths each year, with the largest affected population being children from 0 to 14 years of age [11]. This age group of children sustained over 500,000 TBIs, which is nearly 50% greater than the incident rate for older adults (greater than 65 years of age). While the developing brain is thought to be resilient, termed

"plastic", when the juvenile brain encounters an insult, the complications may have a profound negative impact on development [12]. Early development in humans is recognized as a period of increased vulnerability to injury that may have life-long effects on brain structure and function [13]. Thus, it is valuable to assess functional connectivity disruptions in a preclinical animal model with similar brain growth and development to human children where noninvasive imaging applications can be observed to assess how an injury and treatment effects critical periods of rapid growth. The studies that comprise this dissertation utilized neuroimaging tools to answer various questions related to ischemic stroke and traumatic brain injury pathophysiology.

The first study in a large animal ischemic stroke model determined brain structures that were consistently affected by the middle cerebral artery occlusion (MCAO) by MRI. Furthermore, this study indicated that the structures responsible for motor coordination showed stronger correlations (higher R values) to functional gait outcomes compared to structures not involved in motor function than traditional MRI metrics such as lesion volume. Determined using a pig brain atlas, damaged structures included the insular cortex, somatosensory cortices, temporal gyri, claustrum, and visual cortices, among others. These structures are also frequently damaged in middle cerebral artery (MCA) strokes in humans [3-8, 14-16]. The neuroanatomical structures that correlated most with functional gait outcomes were putamen, globus pallidus, and primary somatosensory cortex. Logically, these structures having the strongest correlations (highest R values) to functional gait outcomes are reasonable due to their assigned biological function in the brain which is involved in motor function and coordination. This study also further characterized the MCAO model by showing decreased white matter integrity, impaired

spatiotemporal gait outcomes, decreased voluntary movement in open field testing, and higher modified Rankin Scale (mRS) scores at acute timepoints, as well as hemispheric and lesion volumetric changes due to the stroke. The major takeaway from this study supported the notion that individual brain structure function is critical for determining long term outcomes in a preclinical model that could be assumed in clinical populations as well.

The second study presented herein utilized functional MRI (fMRI) to evaluate disruptions in neural networks in TBI and healthy control animals. fMRI can be used to characterize injury severity and predict functional and cognitive deficits in TBI patients [17-20]. Brain resting-state networks are responsible for narrating everyday function including memory, problem-solving ability, language, and personality. It has been previously proven that pigs have homologous resting-state networks to humans [21]. Here, resting-state (rs)-fMRI and task-based (tb)-fMRI were acquired and revealed aberrations in functional connectivity following an injury. Functional connectivity disruptions in the piglet TBI brain were consistently detected in the executive control (EX) and visual (VIS) networks using rs-fMRI, which were determined using two analysis techniques-- independent component analysis (ICA) and sparse dictionary learning (sDL). In response to a tactile stimulus on the hindlimb, functional connectivity disruptions were determined within the EX and sensorimotor (SM) networks using tb-fMRI. This study laid the groundwork for comparisons to be made between healthy and injured brains' functional networks in a translational pediatric porcine model.

Finally, using a semi-automatic cell and tissue analysis pipeline, conclusions were drawn on the cell-to-cell interactions of major immune, neural, and blood vessel cell

types in a healthy and ischemic porcine brain. There is a lack of data surrounding the dynamic morphological changes occurring at later timepoints in the porcine model and this study provides insight on the brain at 4 weeks post-MCAO. In perilesional regions of the stroked brains, $GFAP^+$ and $IBA1^+$ areas showed opposite trends which aligns with an activated immune response morphology [22]. Correlated morphological changes found in the stroked brain between $IBA1^+$, $GFAP^+$, and $NeuN^+$ areas suggest coordinated interactions associated with stroke pathological and recovery responses that were not found as strong in non-stroked brains. In addition, the analysis technique presented in the final study provides a more unbiased approach for more robust quantification, interpretation, and elucidation of morphological cellular features. Overall, dynamic morphological differences in multiple parameters for each cell type (neurons, microglia/macrophages, astrocytes, neuronal precursor cells, and blood vessels) were found using this unbiased tool in stroked brains compared to non-stroked brains.

Animal models of brain injury provide powerful tools to study injury mechanisms in a controlled, reproducible, and cost-effective environment [23]. Animal models serve as a necessary step in the development of drugs and biologics for improving overall patient outcome and recovery. However, there must be an appropriate selection of preclinical species that fits the specific research question, as it is unlikely to be a one-size fits all approach.

Future Directions

Although the studies included in this dissertation lead to significant breakthroughs, there were still a number of limitations. Regarding the studies using MRI,

the pig brain atlas that was developed in 2010 [24] was relied on heavily and provided a coordinate system analogous to those used in humans, such as Montreal Neurological Institute (MNI) space, to place the brain in standardized space [25]. This pig brain atlas that can be co-registered with our individual MRI scans, such as structural anatomical T1 and T2-Weighted, fMRI, and diffusion tensor imaging, lacks major white matter structures including the internal capsules. A strength of using the gyrencephalic pig brain is the similar composition of white matter to the human brain. White matter responds to neural injury differently than gray matter on the biochemical level with evidence of white matter displaying greater metabolic change [26], so the incorporation of these vital white matter structures would improve the overall of translatability of this preclinical model. The refinement of this frequently used atlas would benefit future studies. Furthermore, in preclinical brain injury models and clinical stroke and TBI patients, MRI image registration to neuroanatomical atlases is often imperfect due to hemispheric changes caused by swelling (e.g., midline shifting) and injury related artifacts (e.g., hemorrhage). In our pig model, registration of larger structures demonstrated an acceptable level of atlas registration fidelity, while there was decreased accuracy in the registration of smaller structures. These registration misalignments should be improved in large animal models such as the pig to better account for hemispheric swelling and atrophy. Despite these limitations, the pig brain atlas and registration approach utilized in these studies helped identify lesioned structures involved in motor function related to stroke outcomes and to determine functional network abnormalities following a TBI.

Future studies in our lab will utilize these neuroimaging tools to evaluate the therapeutic efficacy of regenerative and neuroprotective therapies in our translational

large animal porcine model. Stem cell-based therapies are emerging as a new therapeutic approach and as a potential restorative therapy. Preclinical ischemic stroke models have shown promising functional improvements after treatment with various stem cell derivatives, including embryonic stem cells (ESC), pluripotent stem cells (iPSC), neural stem cells (NSC), mesenchymal stem cells (MSC), and mononuclear cells (MNC) cell types [27-31]. Furthermore, the disruption of the bidirectional communication pathway between the brain and the gastrointestinal system, the gut-brain axis, following TBI is being investigated as a novel neuroprotective therapeutic intervention site. Modifications of the gut microbiome result in a type of feedback loop with the brain. This phenomenon has been demonstrated in mice models where changes in gut microbiota were found following experimental stroke and TBI [32]. Phylogenetic changes and alpha diversity were found to be correlated with TBI lesion volume in mice [33]. A fecal microbiota transplantation (FMT) could improve the dysregulation within the gut-brain axis and improve the overall inflammatory response. Our group plans to test both a NSC and FMT therapy in our large animal TBI model and apply the advanced neuroimaging techniques developed and described herein.

References

1. Menezes, N.M., et al., *The real estate factor: quantifying the impact of infarct location on stroke severity.* Stroke, 2007. **38**(1): p. 194-7.
2. Munsch, F., et al., *Stroke Location Is an Independent Predictor of Cognitive Outcome.* Stroke, 2016. **47**(1): p. 66-73.
3. Wu, O., et al., *Role of Acute Lesion Topography in Initial Ischemic Stroke Severity and Long-Term Functional Outcomes.* Stroke, 2015. **46**(9): p. 2438-44.
4. Phan, T.G., et al., *Proof of concept study: relating infarct location to stroke disability in the NINDS rt-PA trial.* Cerebrovasc Dis, 2013. **35**(6): p. 560-5.
5. Laredo, C., et al., *Prognostic Significance of Infarct Size and Location: The Case of Insular Stroke.* Sci Rep, 2018. **8**(1): p. 9498.
6. Timpone, V.M., et al., *Percentage insula ribbon infarction of >50% identifies patients likely to have poor clinical outcome despite small DWI infarct volume.* AJNR Am J Neuroradiol, 2015. **36**(1): p. 40-5.
7. Cheng, B., et al., *Influence of stroke infarct location on functional outcome measured by the modified rankin scale.* Stroke, 2014. **45**(6): p. 1695-702.
8. Payabvash, S., et al., *Acute Ischemic Stroke Infarct Topology: Association with Lesion Volume and Severity of Symptoms at Admission and Discharge.* AJNR Am J Neuroradiol, 2017. **38**(1): p. 58-63.
9. Perego, C., S. Fumagalli, and M.G. De Simoni, *Temporal pattern of expression and colocalization of microglia/macrophage phenotype markers following brain ischemic injury in mice.* J Neuroinflammation, 2011. **8**: p. 174.
10. Zhao, S.C., et al., *Regulation of microglial activation in stroke.* Acta Pharmacol Sin, 2017. **38**(4): p. 445-458.
11. Faul M, X.L., Wald MM, Coronado VG, *Traumatic Brain Injury in the United States: Emergency Department Visits, Hospitalizations and Deaths 2002–2006.* Centers for Disease Control and Prevention, National Center for Injury Prevention and Control, 2010.
12. Anderson, V., et al.,, *Functional Plasticity or Vulnerability After Early Brain Injury?* Pediatr Res, 2006.
13. Conrad, M.S., R.N. Dilger, and R.W. Johnson, *Brain growth of the domestic pig (Sus scrofa) from 2 to 24 weeks of age: a longitudinal MRI study.* Dev Neurosci, 2012. **34**(4): p. 291-8.
14. Nogles, T.E. and M.A. Galuska, *Middle Cerebral Artery Stroke*, in *StatPearls*. 2020: Treasure Island (FL).

15. Payabvash, S., et al., *Location-weighted CTP analysis predicts early motor improvement in stroke: a preliminary study.* Neurology, 2012. **78**(23): p. 1853-9.

16. Payabvash, S., et al., *Regional ischemic vulnerability of the brain to hypoperfusion: the need for location specific computed tomography perfusion thresholds in acute stroke patients.* Stroke, 2011. **42**(5): p. 1255-60.

17. Studerus-Germann, A.M., et al., *Diagnostic approaches to predict persistent post-traumatic symptoms after mild traumatic brain injury - a literature review.* Int J Neurosci, 2016. **126**(4): p. 289-98.

18. Chen, J.K., et al., *A validation of the post concussion symptom scale in the assessment of complex concussion using cognitive testing and functional MRI.* J Neurol Neurosurg Psychiatry, 2007. **78**(11): p. 1231-8.

19. Henry, L.C., et al., *Metabolic changes in concussed American football players during the acute and chronic post-injury phases.* BMC Neurol, 2011. **11**: p. 105.

20. Messe, A., et al., *Specific and evolving resting-state network alterations in post-concussion syndrome following mild traumatic brain injury.* PLoS One, 2013. **8**(6): p. e65470.

21. Simchick, G., et al., *Pig Brains Have Homologous Resting-State Networks with Human Brains.* Brain Connect, 2019. **9**(7): p. 566-579.

22. Wang, Y., et al., *Immunoreactive Cells After Cerebral Ischemia.* Front Immunol, 2019. **10**: p. 2781.

23. Sorby-Adams, A.J., R. Vink, and R.J. Turner, *Large animal models of stroke and traumatic brain injury as translational tools.* Am J Physiol Regul Integr Comp Physiol, 2018. **315**(2): p. R165-R190.

24. Saikali, S., et al., *A three-dimensional digital segmented and deformable brain atlas of the domestic pig.* J Neurosci Methods, 2010. **192**(1): p. 102-9.

25. Mazziotta, J., et al., *A probabilistic atlas and reference system for the human brain: International Consortium for Brain Mapping (ICBM).* Philos Trans R Soc Lond B Biol Sci, 2001. **356**(1412): p. 1293-322.

26. Baker, E.W., et al., *Scaled traumatic brain injury results in unique metabolomic signatures between gray matter, white matter, and serum in a piglet model.* PLoS One, 2018. **13**(10): p. e0206481.

27. Bang, O.Y., *Clinical Trials of Adult Stem Cell Therapy in Patients with Ischemic Stroke.* J Clin Neurol, 2016. **12**(1): p. 14-20.

28. Hao, L., et al., *Stem cell-based therapies for ischemic stroke.* Biomed Res Int, 2014. **2014**: p. 468748.

29. Baker, E.W., et al., *Induced Pluripotent Stem Cell-Derived Neural Stem Cell Therapy Enhances Recovery in an Ischemic Stroke Pig Model.* Sci Rep, 2017. **7**(1): p. 10075.

30. Webb, R.L., et al., *Human Neural Stem Cell Extracellular Vesicles Improve Recovery in a Porcine Model of Ischemic Stroke.* Stroke, 2018. **49**(5): p. 1248-1256.

31. Webb, R.L., et al., *Human Neural Stem Cell Extracellular Vesicles Improve Tissue and Functional Recovery in the Murine Thromboembolic Stroke Model.* Transl Stroke Res, 2018. **9**(5): p. 530-539.

32. Houlden, A., et al., *Brain injury induces specific changes in the caecal microbiota of mice via altered autonomic activity and mucoprotein production.* Brain Behav Immun, 2016. **57**: p. 10-20.

33. Nicholson, S.E., et al., *Moderate Traumatic Brain Injury Alters the Gastrointestinal Microbiome in a Time-Dependent Manner.* Shock, 2019. **52**(2): p. 240-248.